Università degli Studi di Trento

Facoltà di Scienze Matematiche Fisiche e Naturali

Tesi di Dottorato di Ricerca in Fisica

Bose-Einstein Condensates in Rotating Traps and Optical Lattices

Meret Krämer

Dottorato di Ricerca in Fisica, XVI Ciclo
27 Febbraio 2004

Contents

Part I

Bose-Einstein Condensates in rotating traps

Chapter 1

Introduction

Superfluids differ from normal fluids in their behavior under rotation [1] (chapter 6 and 14). Prominent examples are the reduction of the momentum of inertia and the occurrence of quantized vortices. Since the achievement of Bose-Einstein condensation in trapped ultra-cold dilute atomic gases in 1995 [2, 3, 4], exploring the superfluid properties of these systems has been the primary motivation for setting up rotating traps.

One of the experimental methods [5, 6, 7, 8, 9, 10, 11] consists in shining a laser beam along the axis of a cylindrically symmetric magnetic trap

$$V_{\mathrm{mag}} = \frac{m}{2}\left[\omega_r^2\left(x^2+y^2\right)+\omega_z^2 z^2\right]. \tag{1.1}$$

The laser beam axis is moved back and forth very rapidly between two positions symmetric with respect to the z-axis. The atoms feel a time averaged dipole potential which is anisotropic in the xy plane

$$\delta V(\mathbf{r}) = \frac{1}{2} m\omega_r^2\left(\epsilon_x x^2+\epsilon_y y^2\right), \tag{1.2}$$

where ϵ_x and ϵ_y depend on the intensity, the beam waist and on the spacing between the extreme positions of the beam with respect to the z-axis. In addition to the fast movement of the beam the xy axes can be rotated at an angular velocity Ω. In the lab frame the total potential $V = V_{\mathrm{mag}} + \delta V$ is given by

$$V_{\mathrm{lab}} = \frac{m}{2}\left[\omega_\perp^2\left(x^2+y^2\right)+\omega_z^2 z^2\right] + \frac{m}{2}\varepsilon\omega_\perp^2\left[\left(x^2-y^2\right)\cos\left(2\Omega t\right)+2xy\sin\left(2\Omega t\right)\right]. \tag{1.3}$$

Here, ε describes the ellipsoidal deformation of the trapping potential in the rotating xy plane

$$\varepsilon = \frac{\omega_x^2-\omega_y^2}{\omega_x^2+\omega_y^2}, \tag{1.4}$$

where $\omega_{x,y}^2 = \omega_r^2(1\pm\epsilon_{x,y})$, and $\omega_\perp$ is an average transverse oscillator frequency

$$\omega_\perp^2 = \frac{\omega_x^2+\omega_y^2}{2}. \tag{1.5}$$

In a corotating coordinate system the potential takes the form

$$V_{\mathrm{rot}}(\mathbf{r}) = \frac{m}{2}\left[\left(1+\varepsilon\right)\omega_\perp^2 x^2+\left(1-\varepsilon\right)\omega_\perp^2 y^2+\omega_z^2 z^2\right]. \tag{1.6}$$

Using the same experimental scheme a strong anharmonic rotating deformation of the atomic cloud has been used by [12, 11]. Experiments with a potential of the form (1.6) have also been reported in [13, 14]. In these cases the rotation of the trap is achieved by rotating the magnetic trap itself.

This chapter focuses on Bose-Einstein condensates loaded into a trap of the form (1.6). The discussion can be generalized to describe systems in set-ups of the kind used in [12, 11].

Many properties of low temperature dilute-gas Bose-Einstein condensates can be understood assuming zero temperature and working within the framework of Gross-Pitaevskii (GP) theory [1, 15]. Within this framework all atoms are condensed into a single mode $\varphi(\mathbf{r},t)$ often denoted as the condensate wavefunction. The quantity $\Psi(\mathbf{r},t)=\sqrt{N_{\rm tot}}\varphi(\mathbf{r},t)$ constitutes an order parameter. Its modulus and phase S are closely related to the density distribution and the velocity field respectively

$$n(\mathbf{r},t)=|\Psi(\mathbf{r},t)|^2\,, \tag{1.7}$$

$$\mathbf{v}(\mathbf{r},t)=\frac{\hbar}{m}\nabla S(\mathbf{r},t)\,. \tag{1.8}$$

The order parameter's temporal evolution in the external potential $V_{\rm ext}(\mathbf{r},t)$ obeys the Gross-Pitaevskii equation (GPE)

$$i\hbar\frac{\partial\Psi(\mathbf{r},t)}{\partial t}=\left(-\frac{\hbar^2}{2m}\nabla^2+V_{\rm ext}(\mathbf{r},t)+g\,|\Psi(\mathbf{r},t)|^2\right)\Psi(\mathbf{r},t)\,. \tag{1.9}$$

Two-body interaction between atoms is accounted for by the nonlinear term which is governed by the coupling constant

$$g=\frac{4\pi\hbar^2 a}{m}\,, \tag{1.10}$$

where a is the s-wave scattering length.

To describe a condensate in the rotating trap (1.3) we set $V_{\rm ext}=V_{\rm lab}$ in (1.9). The GPE for the order parameter $\Psi_R=\exp(i\Omega\hat{L}_z t/\hbar)\Psi$ in the reference frame rotating with angular velocity Ω around the z-axis takes the form

$$i\hbar\frac{\partial\Psi_R(\mathbf{r},t)}{\partial t}=\left(-\frac{\hbar^2}{2m}\nabla^2+V_{\rm rot}(\mathbf{r})+g\,|\Psi_R(\mathbf{r},t)|^2-\Omega\hat{L}_z\right)\Psi_R(\mathbf{r},t)\,, \tag{1.11}$$

where $\hat{L}_z$ is the z-component of the angular momentum operator and $V_{\rm rot}(\mathbf{r})$ is the *time-independent* potential (1.6). Stationary solutions of (1.11) satisfy the equation $i\hbar\partial\Psi_R/\partial t=\mu\Psi_R$.

A first class of stationary solutions is associated with an irrotational velocity field

$$\nabla\times\mathbf{v}=0\,. \tag{1.12}$$

A condensate in such a state can carry angular momentum. Yet, the circulation of the velocity field is zero everywhere, i.e.

$$\oint d\mathbf{l}\cdot\mathbf{v}=0\,, \tag{1.13}$$

for any closed contour. Such states have been studied theoretically in [16, 17, 18] and investigated experimentally in [10, 14].

The second class of stationary solutions comprises configurations containing vortex lines around which the circulation takes non-zero quantized values

$$\oint d\mathbf{l}\cdot\mathbf{v} = \kappa\frac{2\pi\hbar}{m}\,, \qquad \kappa = \pm 1, \pm 2, \ldots\,. \tag{1.14}$$

The corresponding velocity field is irrotational except on the vortex line, where it is singular. The density on the vortex line is zero, and the radius of the vortex core is of the order of the healing length $\xi = (8\pi a n)^{-1/2}$ [19] (chapter III), where a is the scattering length characterizing 2-body interaction, and n is the density of the condensate in absence of the vortex. The quantization of the circulation is a general property of superfluids. It is the consequence of the existence of a single-valued order parameter [20, 21]. States with $\kappa > 1$ are unstable and fragment into κ vortices each with a unit quantum circulation (see [19], chapter III). In a stationary condensate, a single vortex line passes through the center of the trap while several vortex lines form a regular vortex lattice free of any major distortions, even near the boundary. Such "Abrikosov" lattices were first predicted for superconductors [22]. Tkachenko showed that their lowest energy structure should be triangular for an infinite system [23]. Stationary vortex lattice configurations in dilute-gas Bose-Einstein condensates have for example been studied theoretically in [24, 25, 26] (see also [27] and references therein). The experimental generation of vortex states has been described in [28, 6, 7, 8, 9, 10, 12, 11, 29, 30, 13]. Vortex lattices containing up to ~ 130 vortices have been reported [12]. Their life time can extend up to the one of the condensate itself [13]. In most experiments vortices have been identified by detecting the vortex cores in the density distribution after expansion (see [31, 25, 32] for related theoretical calculations). A visibility of the density reduction of up to 95% [13] has been reported. An alternative technique consists in the measurement of the angular momentum [7, 10, 9]. This method exploits the fact that the quadrupole surface modes with angular momentum $\pm 2\hbar$ are not degenerate in the presence of vortices [64]. In this way it is possible to observe the jump of the angular momentum from 0 to $\hbar$ per particle when a vortex line moves from the edge of the cloud to its stable position at the center of the trap [7]. The angular momentum associated with a single vortex line has also been measured by exciting the scissors mode [33]. Moreover, phase singularities due to vortex excitations have been observed as dislocations in the interference fringes formed by the stirred condensate and a second unterperturbed condensate [34].

In the past years, issues of primary experimental interest have been the nucleation and stabilization of vortices and vortex lattices (see next chapter), the properties of vortex lattices made up of a large number of vortex lines [8, 12, 9, 11, 37, 35], the decay of vortex configurations [6, 8, 12, 37, 13], the bending of vortex lines [11, 36], excitations of vortex lines [38, 29] and of vortex lattices [39] and the behavior of vortex lattices under rapid rotation [40, 41, 42]. The theory of vortices in trapped dilute Bose-Einstein condensates has been reviewed in [27] (see also [1, 15]).

A condensate which is initially in the groundstate of the non-rotating trap will evolve according to (1.9) with $V_{\rm ext}$ given by (1.3). To understand for what value of Ω the system will start responding to the rotation, it is useful to study small perturbations $\delta\Psi(\mathbf{r},t)$ of the groundstate $\Psi_0 = |\Psi_0|\exp(-i\mu_0 t/\hbar)$ in a static axi-symmetric trap ($\Omega = 0$, $\varepsilon = 0$)

$$\Psi(\mathbf{r},t) = \Psi_0 + \delta\Psi(\mathbf{r},t)\,. \tag{1.15}$$

Linearizing the GPE in the small perturbation $\delta\Psi(\mathbf{r},t)$ we can study the conditions under which the system becomes unstable when the rotating trap is switched on. This analysis is done by

looking for solutions of the form

$$\delta\Psi(\mathbf{r},t) = e^{-i\mu_0 t/\hbar} e^{il\phi}\left(u_{nl}(\rho,z)e^{i\omega_{nl}t} + v^*_{nl}(\rho,z)e^{-i\omega_{nl}t}\right) \tag{1.16}$$

corresponding to the collective modes of the initial axi-symmetric state. The modes are labeled by the number of nodes n of the amplitudes u_{nl}, v_{nl} and the angular momentum $\hbar l$. For

$$\int d\mathbf{r}\,(u^*_{nl}u_{n'l'} - v^*_{n'l'}v_{n',l'}) = \delta_{n,n'}\delta_{l,l'} \tag{1.17}$$

they have energy $\hbar\omega_{nl}$ in the lab frame. In the rotating frame the excitation energy associated with the mode $n\,l$ is instead given by

$$\epsilon_{nl}(\Omega) = \hbar\omega_{nl} - \Omega\hbar l\,. \tag{1.18}$$

The initial state is energetically unstable if for some nl

$$\epsilon_{nl}(\Omega) < 0\,. \tag{1.19}$$

This yields a critical angular velocity for the excitation of the mode nl

$$\omega_{cr}(n,l) = \frac{\omega_{nl}}{l} \tag{1.20}$$

corresponding to the Landau criterion for the creation of excitations nl in the rotating trap . It can most easily be satisfied for $n = 0$. The respective excitations are called surface modes since they are associated with a perturbation which is concentrated at the surface of the condensate. They have been investigated experimentally in [5]. In the Thomas-Fermi (TF) limit [1] the critical angular velocities $\omega_{cr,nl}$ for the surface modes take the simple form [43]

$$\omega_{\mathrm{cr,0l}} = \frac{\omega_\perp}{\sqrt{l}}\,. \tag{1.21}$$

In chapter 2 we will discuss the connection between the energetic instability towards the creation of surface modes and the nucleation of a single quantized vortex.

Chapter 2

Vortex nucleation

The problem of the nucleation of quantized vortices in Bose superfluids has been the object of intensive experimental work with dilute gases in rotating traps [6, 7, 8, 12, 10, 11, 9, 13]. It has emerged clearly that the mechanism of nucleation depends crucially on the actual shape of the trap as well as on how the rotation is switched on. A first approach consists of a sudden switch-on of the deformation and rotation of the external potential which generates a non-equilibrium configuration [6, 7, 8, 12, 10, 11, 9]. For sufficiently large values of the angular velocity of the rotating potential one observes the nucleation of one or more vortices. In a second approach either the rotation or the deformation of the trap are switched on slowly [10, 13]. In the case of a sudden switch-on of a small deformation ε and rotation of the trap (1.3), the observed critical angular velocity turns out to be [6, 7, 8, 10, 9] [1]

$$\Omega_c \approx 0.7\omega_\perp \,, \tag{2.1}$$

which is close to the value $\omega_\perp/\sqrt{2}$ of the critical angular velocity (1.21) for the $l = 2$ surface mode in a TF-condensate.

The purpose of this chapter is to gain further insight into the mechanism underlying the nucleation of a single vortex line in this setting. Using a simple semi-analytic model, we investigate the relevance of the quadrupole deformation of the condensate for the nucleation of the quantized vortex in the trap (1.3). In a non-deformed condensate the nucleation process is inhibited by the occurrence of a barrier located near the surface of the condensate. Using the TF-approximation to zero temperature GP-theory we show that this barrier is lowered by the explicit inclusion of ellipsoidal shape deformations and eventually disappears at sufficiently high angular velocities, making it possible for the vortex to nucleate and move to its stable position at the trap center.

This chapter is based on the results presented in:

Vortex nucleation and quadrupole deformation of a rotating Bose-Einstein condensate
M. Krämer, L. Pitaevskii, S. Stringari, and F. Zambelli,
Laser Physics **12**, 113 (2002).

[1] Note that in [6, 8] the rotating trap is actually switched on during the process of evaporative cooling above or around the condensation point. This does not change the results obtained for Ω_c.

2.1 Single vortex line configuration

A quantized vortex is characterized by the appearance of a velocity field associated with a non-vanishing, quantized circulation (see Eq.(1.14)). If we assume that the vortex with $\kappa = 1$ is straight and oriented along the z-axis the quantization of circulation takes the simple form

$$\boldsymbol{\nabla} \times \mathbf{v}_{\rm vortex} = \frac{2\pi\hbar}{m}\,\delta^{(2)}(\mathbf{r}-\mathbf{d})\hat{z} \tag{2.2}$$

for a vortex located at distance $d \equiv |\mathbf{d}|$ from the axis. The general solution of (2.2) can be written in the form

$$\mathbf{v}_{\rm vortex} = \boldsymbol{\nabla}\left(\varphi_{\mathbf{d}} + S\right) \tag{2.3}$$

where $\varphi_{\mathbf{d}}$ is the azimuthal angle around the vortex line at position $\mathbf{d}$ and S is a single-valued function which gives rise to an irrotational component of the velocity field. The irrotational component may be important in the case of a vortex displaced from the symmetry axis and its inclusion permits to optimize the energy cost associated with the vortex line [2]. Considering a straight vortex line is a first important assumption that we introduce in our description [3].

Vortex energy

The energy cost associated with a straight vortex line at the center of the trap is given by [31]

$$E_v(d=0,\varepsilon,\mu) = \frac{4\pi n_0}{3}\frac{\hbar^2}{m}Z\,\log\left(\frac{0.671R_\perp}{\xi_0}\right) = N\hbar\omega_\perp\frac{5}{4}\frac{\hbar\omega_\perp}{\mu}\sqrt{1-\varepsilon^2}\log\left(1.342\frac{\mu}{\hbar\omega_\perp}\right), \tag{2.4}$$

Here, Z is the TF-radius in z-direction, ξ_0 is the healing length calculated with the central density n_0, μ is the TF-chemical potential and ε is the deformation of the trap introduced above (see Eq.(1.6)). The factor $4n_0Z/3$ in (2.4) corresponds to the column density $\int dz\, n(d=0,z)$ evaluated within the TF-approximation at the trap center. Noting that the column density at distance d from the center along the x-axis is given by

$$\int dz\, n(d,z) = \frac{4n_0Z}{3}\left[1-\left(\frac{d}{R_x}\right)^2\right]^{3/2}, \tag{2.5}$$

we introduce the following simple description of the energy of a vortex located at distance d from the center on the x-axis [4]

$$E_v(d/R_x,\varepsilon,\mu) = E_v(d=0,\varepsilon,\mu)\left[1-\left(\frac{d}{R_x}\right)^2\right]^{3/2}, \tag{2.6}$$

where $E_v(d=0,\varepsilon,\mu)$ is given by Eq.(2.4). This expression is expected to be correct within logarithmic accuracy (see [27] and references therein). It could be improved by including an

[2] For a uniform superfluid confined in a cylinder, this extra irrotational velocity field is crucial in order to satisfy the proper boundary conditions and its effects can be exactly accounted for by the inclusion of an image vortex located outside the cylinder. See for example [45].

[3] The inclusion of curvature effects in the description of quantized vortices in trapped condensates has been the subject of recent theoretical studies. See, for example, [46, 47, 48]. See also [27] and references therein.

[4] Our results do not change if d/R_x is replaced by d/R_y. We expect that predicting the preferable direction for a vortex to enter the condensate demands the calculation of the vortex energy beyond logarithmic accuracy.

explicit d-dependence of the healing length inside the logarithm, in order to account for the density dependence of the size of the vortex core.

Eq.(2.6) shows that no excitation energy is carried by the system when $d = R_\perp$. Of course this estimate, being derived using the TF-approximation, is not accurate if we go too close to the border. If the surface of the condensate is described by a more realistic density profile the energy is nevertheless expected to vanish when the vortex line is sufficiently far outside the bulk region. Within the simplifying assumptions made above we can conclude that the configuration with $d = R_\perp$ corresponds to the absence of a vortex, while the transition from $d = R_\perp$ to $d = 0$ describes the nucleation path of the vortex.

Angular momentum of the vortex configuration

The inclusion of vorticity is not only accompanied by an energy cost but also by the appearance of angular momentum. The simplest way to calculate the angular momentum associated with a displaced vortex is to assume axi-symmetric trapping ($\varepsilon = 0$) and to work with the TF-approximation. In this limit the size of the vortex core is small compared to the radius of the condensate so that one can use the vortex-free expression $n(\mathbf{r}) = \mu[1-(r_\perp/R_\perp)^2-(z/Z)^2]/g$ for the density profile of the condensate, where $r_\perp^2 = x^2+y^2$ and $g = 4\pi a\hbar^2/m$ is the coupling constant, fixed by the positive scattering length a. Then, one can write the angular momentum in the form

$$L_z = m\int dz \int dr_\perp r_\perp n(r_\perp, z) \oint \mathbf{v}_{\rm vortex}\cdot d\mathbf{l}\,, \tag{2.7}$$

where the line integral is taken along a circle of radius $r_\perp$. Use of Stokes' theorem gives the result [49]

$$L_z(d/R_\perp) = N\hbar\left[1-\left(\frac{d}{R_\perp}\right)^2\right]^{5/2}, \tag{2.8}$$

where d is the distance of the vortex line from the symmetry axis. Eq. (2.8) shows that the angular momentum per particle is reduced from the value $\hbar$ as soon as the vortex is displaced from the center and becomes zero for $d = R_\perp$.

Vortex energy in the rotating frame

Eq.(2.6) makes evident that a macroscopic energy is required to achieve a transition to a vortex-state. In a rotating trap of the form (1.3) the system may nevertheless like to acquire the vortex configuration. This happens if there is a total energy gain in the rotating frame where the system has energy

$$E(\Omega) = E - \Omega L_z\,. \tag{2.9}$$

Here E is the energy in the laboratory frame, L_z is the angular momentum, and Ω is the angular velocity of the trap around the z-axis.

In an axi-symmetric trap ($\varepsilon = 0$) Eq.(2.9) yields the energy [49, 27]

$$E_v(d/R_\perp,\Omega,\mu) = E_v(d=0,\varepsilon=0,\mu)\left[1-\left(\frac{d}{R_\perp}\right)^2\right]^{3/2} - \Omega N\hbar\left[1-\left(\frac{d}{R_\perp}\right)^2\right]^{5/2}. \tag{2.10}$$

Here, we have used expression (2.6) with $\varepsilon = 0$ for the energy in the laboratory frame and (2.8) for the angular momentum in an axi-symmetric trap.

Some interesting features emerge from Eq. (2.10). First we observe that the occurrence of a vortex at $d = 0$ is energetically favorable for angular velocities satisfying the condition

$$\Omega \geq \Omega_v(\mu) = \frac{E_v(d = 0, \varepsilon = 0, \mu)}{N\hbar} \,. \tag{2.11}$$

This is the well known criterion for the so called thermodynamic stability of the vortex. If it is satisfied the energy $E_v(d/R_\perp, \Omega, \mu)$ exhibits a global minimum at $d = 0$ where the vortex states carries angular momentum $\hbar$ per particle. In contrast the vortex solution at $d = 0$ is energetically unstable if $\Omega \leq 3\,\Omega_v(\mu)/5$, while it is metastable (local minimum) if $3\,\Omega_v(\mu)/5 \leq \Omega \leq \Omega_v(\mu)$ [49, 27].

It is worth noticing that in the TF-limit one should have $\Omega_v(\mu)/\omega_\perp << 1$. In fact, using $\mu = gn_0$ and $\mu = m\omega_\perp^2 R_\perp^2/2$ for the chemical potential we can write

$$\frac{\Omega_v}{\omega_\perp} = \frac{5}{2}\left(\frac{a_\perp}{R_\perp}\right)^2 \log\left(0.671\frac{R_\perp}{\xi_0}\right) , \tag{2.12}$$

which tends to zero when $R_\perp \gg a_\perp$. Here, $a_\perp = \sqrt{\hbar/m\omega_\perp}$ is the radial oscillator length. In the actual experiments the ratio (2.12) is not very small. For example, in the case of Ref. [6]

$$\Omega_v \simeq 0.35\,\omega_\perp \,. \tag{2.13}$$

The angular velocity (2.12) is significantly lower than the minimum value (2.1) needed in the experiments [6, 7, 8, 10, 9] to observe a vortex at small ε.

The fact that the criterion (2.11) is not sufficient to explain vortex nucleation can be understood by further analyzing (2.10): An important feature of (2.10) is the appearance of a barrier. Even if $\Omega \geq \Omega_v(\mu)$ and hence if $E_v(d/R_\perp, \Omega, \mu)$ is negative at $d = 0$, the curve (2.10) exhibits a maximum at intermediate values of d between 0 and $R_\perp$ (see Fig. 2.1). The position d_B and height E_B of the barrier are given by the equations

$$\left(\frac{d_B}{R_\perp}\right)^2 = 1 - \frac{3}{5}\frac{\Omega_v(\mu)}{\Omega} , \tag{2.14}$$

and

$$E_B = \frac{2}{5}E_v(d = 0, \mu)\left[1 - \left(\frac{d_B}{R_\perp}\right)^2\right]^{3/2} = \frac{2}{5}E_v(d = 0, \mu)\left(\frac{3}{5}\frac{\Omega_v(\mu)}{\Omega}\right)^{3/2} , \tag{2.15}$$

showing that the height of the barrier becomes smaller and smaller as Ω increases, but never disappears. Since crossing the barrier costs a macroscopic amount of energy, the system will never be able to overcome it and the vortex cannot be nucleated.

The energy (2.10) can be rewritten as a function of angular momentum rather than of the vortex displacement. This yields the expression

$$E_v(L_z, \Omega, \mu) = N\hbar\left[\Omega_v(\mu)\left(\frac{L_z}{N\hbar}\right)^{3/5} - \Omega\frac{L_z}{N\hbar}\right] . \tag{2.16}$$

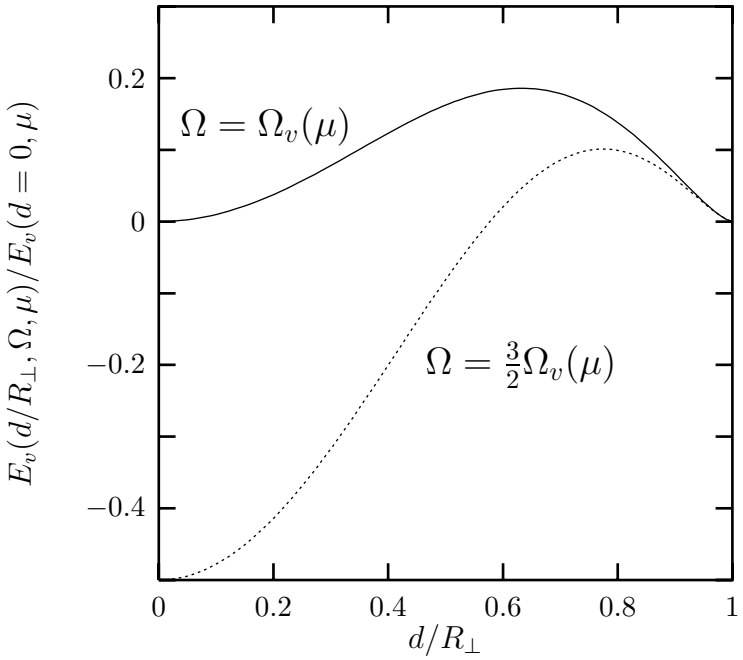

Figure 2.1: Vortex excitation energy in the rotating frame (2.10) for an axisymmetric configuration as a function of the reduced vortex displacement $d/R_\perp$ from the center. The curves refer to two different choices for the angular velocity of the trap: $\Omega = \Omega_v(\mu)$ (solid line), and $\Omega = 3\,\Omega_v(\mu)/2$ (dotted line), where $\Omega_v(\mu) = E_v(d=0,\mu)/N\hbar$. The initial vortex-free state corresponds to $d/R_\perp = 1$. For $\Omega > \Omega_v(\mu)$, the state with a vortex at the center $(d/R_\perp = 0)$ is preferable. However, in this configuration the nucleation of the vortex is inhibited by a barrier separating the vortex-free state $(d/R_\perp = 1)$ from the energetically favored vortex state $(d/R_\perp = 0)$.

Equation (2.16) emphasizes the fact that the nucleation of the vortex is associated with an increase of angular momentum from zero (no vortex) to $N_{\rm tot}\hbar$ (one centered vortex), accompanied by an initial energy increase (barrier) and a subsequent monotonous energy decrease. In this form the TF-result (2.10) can be compared with alternative approaches based on microscopic calculations of the vortex energy.

2.2 Role of Quadrupole deformations

In the previous section we have shown that in order to enter a vortex-state the system has to overcome a barrier associated with a macroscopic energy cost. This barrier exists at any angular velocity $\Omega > \Omega_v$, with Ω_v given by (2.11), if the position d of the vortex line is the only degree of freedom of the system. We need to go beyond this description in order to explain vortex nucleation.

Hints as to what are the crucial degrees of freedom involved are close at hand: The critical angular velocity (2.1) observed in the experiments [6, 7, 8, 10, 9] for small ε turns out to be close to the value associated with the energetic instability of the vortex-free state towards the

excitation of the $l = 2$ quadrupolar surface mode. For a weakly deformed trap this instability sets in at an angular velocity (see Eq.(1.20) with $n = 0, l = 2$)

$$\omega_{\rm cr}(n = 0, l = 2) = \frac{\omega_{0,l=2}}{2}\,, \tag{2.17}$$

where $\omega_{0,l=2}$ is the frequency of the surface oscillation with angular momentum $l = 2\hbar$. In the Thomas-Fermi limit the critical angular velocity takes the simple form (see Eq.(1.21) with $l = 2$)

$$\omega_{\rm cr} = \frac{\omega_\perp}{\sqrt{2}} \approx 0.707\omega_\perp\,. \tag{2.18}$$

The experimental evidence that Eq. (2.17) provides a good estimate for the critical angular velocity for the nucleation of quantized vortices indicates that the quadrupolar shape deformation of the condensate plays a crucial role, in agreement with the theoretical considerations developed in [50, 51, 17, 52, 53, 54]. This is further supported by the observation of strong ellipsoidal deformations observed temporarily during the process of nucleation in the experiments [10, 9, 11, 13] and in simulations (see for example [54, 55, 56]). These observations indicate that the evolution of the shape deformation serves as a mechanism for vortex nucleation.

A quadruplar deformation of the density distribution can be described by the parameter

$$\delta = \frac{\langle y^2 - x^2\rangle}{\langle y^2 + x^2\rangle}\,. \tag{2.19}$$

The expression (2.6) for the vortex energy regards a condensate whose deformation mirrors the one of the trap (1.3). In this case $\delta = \varepsilon$ and hence δ is fixed by the external conditions. When the system becomes unstable towards the creation of quadrupolar surface oscillations it is appropriate to release this constraint and to let the condensate deformation δ be a free parameter. In this way, we allow the system to take deformations different from the trap deformation

$$\delta \neq \varepsilon\,. \tag{2.20}$$

In this section we will derive expressions for the energy and the angular momentum valid for arbitrary condensate deformation δ. This allows us to show that at sufficiently large angular velocities Ω the system can bypass the energy barrier by strongly deforming itself.

Quadrupolar velocity field

In order to describe properly the effects of the quadrupole deformation we introduce, in addition to the vortical field (2.2), an irrotational quadrupolar velocity field given by

$$\mathbf{v}_Q = \alpha\boldsymbol{\nabla}(xy)\,, \tag{2.21}$$

where α is a parameter. Note that $\mathbf{v}_Q$ is the velocity field in the laboratory frame expressed in terms of the coordinates of the rotating frame. The form (2.21) is suggested by the quadrupolar class of irrotational solutions exhibited by the time-dependent Gross-Pitaevskii equation in the rotating frame [16]. In Ref.[16] it has been shown that these solutions are associated with a quadrupole deformation of the density described by the deformation parameter δ (see Eq.(2.19)). The parameters δ and α characterize the quadrupole degrees of freedom that we are including in our picture. In order to provide a simplified description, we fix a relationship

between these two parameters by requiring that the quadrupole velocity field satisfies the condition

$$\boldsymbol{\nabla} \cdot [n(\mathbf{r}) \, (\mathbf{v}_Q - \boldsymbol{\Omega} \times \mathbf{r})] = 0 \, , \tag{2.22}$$

where $\boldsymbol{\Omega} = \Omega \hat{z}$. As a consequence of the equation of continuity, this condition implies that in the rotating frame the density of the gas is stationary except for the motion of the vortex core which involves a change of the density at small length scales. Eq.(2.22) yields the relationship [16]

$$\alpha = -\Omega \delta \tag{2.23}$$

which selects a natural class of paths that will be considered in the present investigation. In the presence of the quadrupole velocity field (2.21), the energy of the condensate in the rotating frame can then be expressed in terms of the deformation parameter δ only. Using the formalism of [16] we find the expression

$$E_Q(\delta, \bar{\Omega}, \varepsilon, \mu) = N\mu \left[\frac{2}{7} \frac{1 - \varepsilon\delta - \bar{\Omega}^2 \delta^2}{\sqrt{1-\varepsilon^2}\sqrt{1-\delta^2}} + \frac{3}{7} \right] \, . \tag{2.24}$$

Here, $\bar{\Omega} = \Omega/\omega_\perp$ and we have neglected the change of the central density caused by the velocity field (2.21). This assumption will be used throughout the paper[5]. Keep in mind that (2.24) is the energy in the rotating frame and hence already includes the angular momentum term $-m \, \boldsymbol{\Omega} \cdot \int d\mathbf{r} \, n(\mathbf{r}) \, [\mathbf{r} \times \mathbf{v}_{\rm Q}]$.

It is useful to expand Eq. (2.24) as a function of δ in the case of axisymmetric trapping ($\varepsilon = 0$). We find the result

$$E_Q(\delta, \bar{\Omega}, \varepsilon = 0, \mu) \simeq N\mu \left[\frac{5}{7} + \delta^2 \left(\frac{1}{7}(1 - 2\bar{\Omega}^2) \right) + \mathcal{O}(\delta^3) \right] \, . \tag{2.25}$$

which explicitly shows that for $\Omega > \omega_\perp/\sqrt{2}$ the symmetric configuration ($\delta = 0$) is energetically unstable against the occurrence of quadrupole deformations.

A quadrupolar deformed vortex state

In order to explore the role of quadrupolar shape deformations for vortex nucleation we assume the presence of a velocity field

$$\mathbf{v} = \mathbf{v}_{\rm vortex} + \mathbf{v}_Q \, , \tag{2.26}$$

where $\mathbf{v}_{\rm vortex}$ is the velocity field (2.3) associated with a straight vortex line at distance d on the x-axis while $\mathbf{v}_Q$ is given by (2.21) (with α chosen according to (2.23)) and gives rise to a quadrupolar shape deformation. The total energy of the condensate in the rotating frame in the presence of the velocity field (2.26) reads

$$E_{\rm tot}(d/R_x, \delta, \bar{\Omega}, \varepsilon, \mu) = E_v(d/R_x, \varepsilon, \mu) + E_Q(\delta, \bar{\Omega}, \varepsilon, \mu) + E_3(d/R_x, \delta, \bar{\Omega}) \, , \tag{2.27}$$

where $E_v(d/R_x, \varepsilon, \mu)$ is the energy (2.4) of the vortex in the lab frame and E_Q is the energy in the rotating frame (2.24) due to the presence of the irrotational velocity field $\mathbf{v}_Q$. The third

[5] Imposing that the energy (2.24) be stationary with respect to δ yields the solutions derived in [16] apart from small corrections due to the changes of the central density not accounted for in the present formalism.

term in (2.27) is the sum of the kinetic energy contribution $m\int d\mathbf{r}\,[\mathbf{v}_{\rm vortex}\cdot\mathbf{v}_Q]\,n(\mathbf{r})$ and the angular momentum term $-m\,\mathbf{\Omega}\cdot\int d\mathbf{r}\,[\mathbf{r}\times\mathbf{v}_{\rm vortex}]\,n(\mathbf{r})$ due to the vortex

$$E_3(d/R_x,\delta,\bar{\Omega}) = m\int d\mathbf{r}\;\mathbf{v}_{\rm vortex}\cdot[\mathbf{v}_Q-\mathbf{\Omega}\times\mathbf{r}]\,n(\mathbf{r})\,. \tag{2.28}$$

It turns out that this contribution can be calculated in a straightforward way. We find

$$E_3(d/R_x,\delta,\bar{\Omega}) = m\int d\mathbf{r}\;\mathbf{v}_{\rm vortex}\cdot[\mathbf{v}_Q-\mathbf{\Omega}\times\mathbf{r}]\,n(\mathbf{r}) = -N\hbar\omega_\perp\bar{\Omega}\sqrt{1-\delta^2}\left[1-\left(\frac{d}{R_x}\right)^2\right]^{5/2}, \tag{2.29}$$

which is consistent with (2.8) in the case of an axi-symmetric condensate ($\delta=0$). In deriving result (2.29) we have used the condition (2.22) for the quadrupole velocity field and we have integrated by parts using the expression (2.3) for $\mathbf{v}_{\rm vortex}$. Note that the irrotational component ∇S of $\mathbf{v}_{\rm vortex}$ does not contribute to (2.29). The result (2.27) generalizes the one given in Ref. [49], which holds in the limit of small $\bar{\Omega}$ where $\delta\sim\varepsilon$.

2.3 Critical angular velocity for vortex nucleation

Within our model, the total energy of a quadrupolar deformed condensate in the presence of a vortex is given by (2.27). The values of the angular velocity Ω, the trap anisotropy ε, the average transverse oscillator frequency $\omega_\perp$, and the chemical potential μ are fixed by the experimental conditions. Hence the degrees of freedom of the system with which one can play in order to identify the optimal path for vortex nucleation are the vortex displacement d and the condensate deformation δ. Note that each of the three energy contributions in (2.27) has a different dependence on the chemical potential resulting in a non-trivial dependence of the critical angular velocity on the relevant parameters of the system (see Eq. (2.31) below).

We assume that the system is initially in the state $d/R_x=1$, $\delta=0$. This assumption adequately describes an experiment in which Ω and ε are switched on suddenly. In this case, the condensate is initially axisymmetric ($\delta=0$) and vortex-free ($d/R_x=1$). Of course this configuration is not stationary and will evolve in time. In the following we will make use of energetic considerations in order to explore the possible paths followed by the system towards the nucleation of the vortex line. These paths should be associated with a monotonous decrease of the energy. In Figs. 2.2 and 2.3 we have plotted the energy surface $E_{\rm tot}$ for two different values of the angular velocity $\bar{\Omega}$ and fixed ε and $\mu/\hbar\omega_\perp$. In both cases the angular velocity is chosen high enough to make the vortex state a global energy minimum. This minimum is surrounded by an energy ridge which, for $\delta=0$, forms a barrier between the initial state ($d/R_x=1$) and the vortex state ($d=0$), as discussed in section 2.1. Moreover, the energy ridge exhibits a saddle point at non-zero deformation δ. The height of this saddle depends on $\bar{\Omega}$, ε, and $\mu/\hbar\omega_\perp$. In Fig. 2.2 the energy at the saddle point is higher than the energy of the initial state and the ridge can not be surpassed. However, at higher angular velocities $\bar{\Omega}$ the situation changes. In Fig. 2.3 the saddle lies lower than the initial state. Hence in this case the system can bypass the barrier by crossing the saddle. The corresponding path is always associated with the occurrence of a strong intermediate deformation of the condensate.

The critical angular velocity for the nucleation of vortices naturally emerges as the angular velocity $\bar{\Omega}_c$ at which the energy on the saddle point $((d/R_x)_{\rm sp},\delta_{\rm sp})$ is the same as the energy

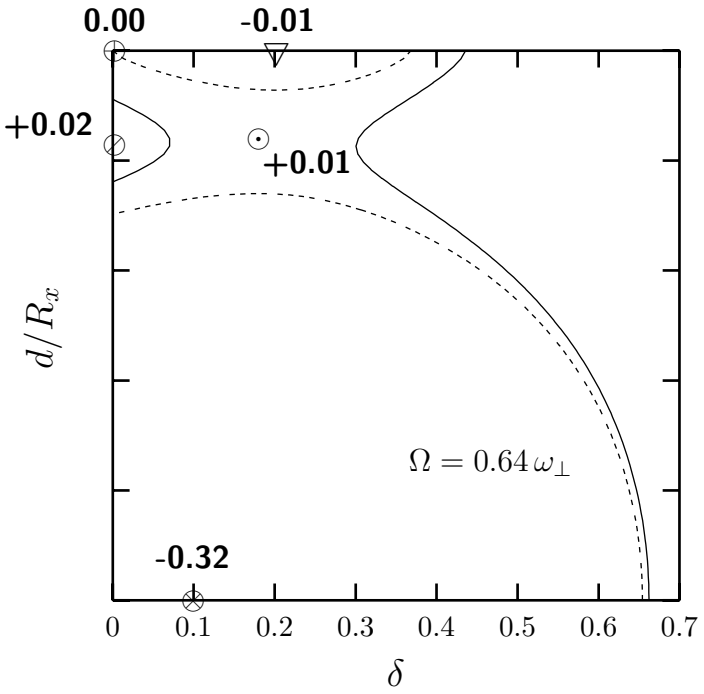

Figure 2.2: Below the critical angular velocity of vortex nucleation the plot shows the dependence of the total energy (2.27) minus the energy of the initial non-deformed vortex-free state $E(d/R_x = 1, \delta = 0)$ on the quadrupolar shape deformation δ and on the vortex displacement d/R_x from the center. Energy is given in units of $N\hbar\omega_\perp$. The dashed line corresponds to $E_{\rm tot} - E(d/R_x = 1, \delta = 0) = 0$, while the solid curve refers to $E_{\rm tot} - E(d/R_x = 1, \delta = 0) = 0.015 N\hbar\omega_\perp$. This plot has been obtained by setting $\varepsilon = 0.04$, $\mu = 10\,\hbar\omega_\perp$ and $\Omega = 0.64\omega_\perp$. The initial state is indicated with $\oplus$, while $\otimes$ corresponds to the energetically preferable centered vortex state. The barrier $\oslash$ inhibits vortex nucleation in a non-deforming condensate ($\delta = 0$). The saddle point $\odot$ lies lower than the barrier $\oslash$. However, at the chosen Ω the energy on the saddle is still higher than the one of the initial state $\oplus$. Note that the preferable vortex state is associated with a shape deformation $\delta > \varepsilon$ (see section 2.4). Note also the existence of a favorable deformed and vortex-free state labeled by $\bigtriangledown$ [16].

of the initial state $(d/R_x = 1, \delta = 0)$:

$$E((d/R_x)_{\rm sp}, \delta_{\rm sp}, \bar{\Omega}_c, \varepsilon, \mu) = E(d/R_x = 1, \delta = 0, \bar{\Omega}_c, \varepsilon, \mu)\,. \tag{2.30}$$

It is worth mentioning that crossing the saddle point is not the only possibility for the system to lower its energy. In fact Figs. 2.2 and 2.3 show the existence of stationary deformed vortex-free states which can be reached starting from the initial state. These are the states predicted in [16] and experimentally studied in [10, 13] through an adiabatic increase of either Ω or ε instead of doing a rapid switch-on. The energy ridge separates these configurations from the vortex state. Still, under certain conditions this stationary vortex-free state becomes dynamically unstable and a vortex can be nucleated starting out from it [10, 13, 17]. The study of this type of vortex nucleation is beyond the scope of the present discussion.

The actual value of the critical angular velocity $\bar{\Omega}_c$ for vortex nucleation depends on the

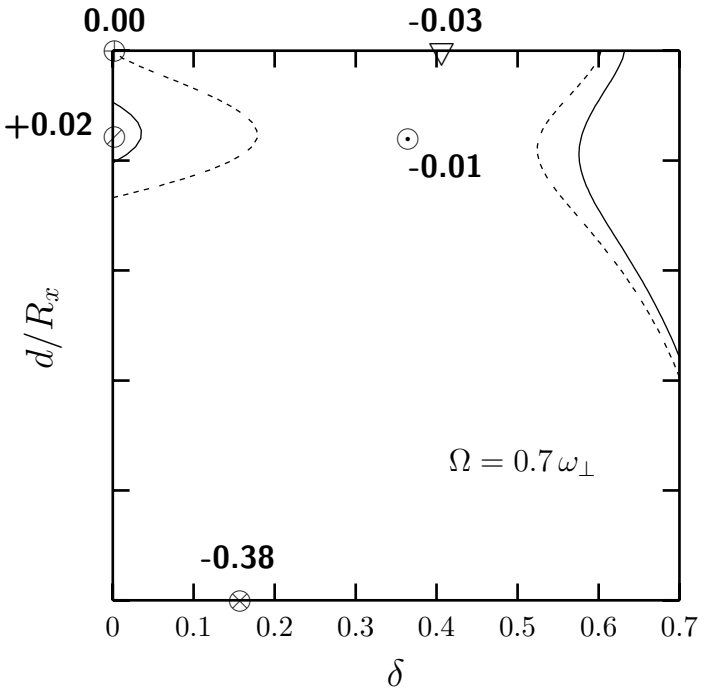

Figure 2.3: Above the critical angular velocity of vortex nucleation: the plot shows the dependence of the total energy (2.27) minus the energy of the initial non-deformed vortex-free state $E(d/R_x = 1, \delta = 0)$ on the quadrupolar shape deformation δ and on the vortex displacement d/R_x from the center. Energy is given in units of $N\hbar\omega_\perp$. The dashed line corresponds to $E_{\rm tot} - E(d/R_x = 1, \delta = 0) = 0$, while the solid curve refers to $E_{\rm tot} - E(d/R_x = 1, \delta = 0) = 0.015 N\hbar\omega_\perp$. In this plot $\varepsilon = 0.04$, $\mu = 10\,\hbar\omega_\perp$, as in Fig. 2.2, and $\Omega = 0.7\omega_\perp$. Important states are indicated as in Fig. 2.2. At the chosen Ω, the saddle $\odot$ lies lower than the initial state $\oplus$ allowing the system to bypass the barrier $\oslash$ by taking a quadrupolar deformation δ and reach the preferable vortex state $\otimes$. Note also the existence of a favorable deformed and vortex-free state labeled by $\bigtriangledown$ [16].

parameters ε and $\mu/\hbar\omega_\perp$. Fig. 2.4 shows the dependence of $\bar{\Omega}_c$ on ε for different choices of $\mu/\hbar\omega_\perp$. To lowest order in ε and $\hbar\omega_\perp/\mu$ the dependence is given by

$$\bar{\Omega}_{\rm c}(\varepsilon) - \frac{1}{\sqrt{2}} \;\approx\; \frac{1}{\sqrt{2}} \left[\frac{(A\eta)^{1/2}}{4} - \frac{\varepsilon}{(A\eta)^{1/4}} \right], \tag{2.31}$$

where

$$\eta = \left[\log\left(1.342\, \frac{\mu}{\hbar\omega_\perp} \right) \right]^{5/2} \left(\frac{\hbar\omega_\perp}{\mu} \right)^{7/2},$$

and $A = 2^{-5/4} 21\sqrt{3}$. This formula shows that the relevant parameters of the expansion are $\eta^{1/2}$ and $\varepsilon/\eta^{1/4}$. Fig. 2.4 demonstrates that it is applicable also at rather small values of the chemical potential.

At $\varepsilon = 0$ the vortex nucleation, according to the present scenario, is possible only at angular velocities slightly higher than the value $\omega_\perp/\sqrt{2}$. For non-vanishing ε the preferable configuration will be always deformed even for small values of $\bar{\Omega}$ where δ depends linearly on ε. At higher $\bar{\Omega}$ the condensate gains energy by increasing its deformation in a nonlinear way

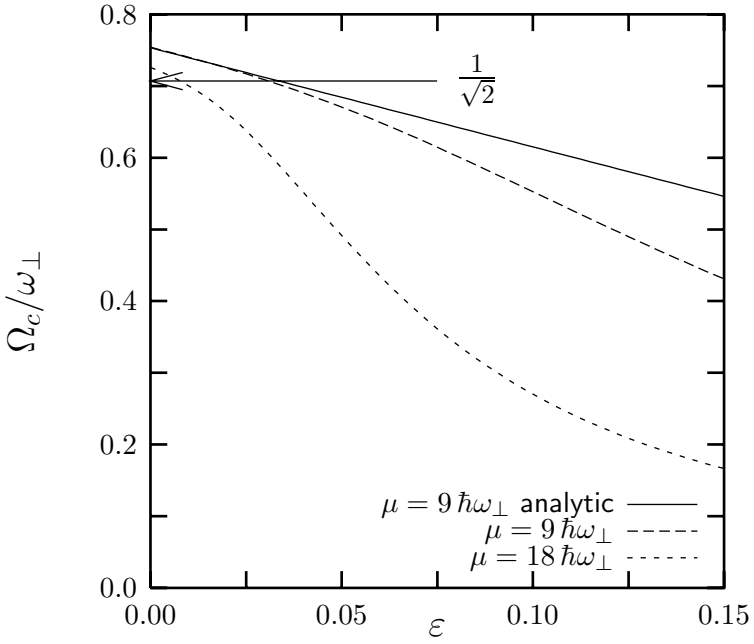

Figure 2.4: Critical angular velocity of vortex nucleation in units of $\omega_\perp$ as a function of the trap deformation ε. The long dashed and short dashed curves correspond to the numerical calculation satisfying condition (2.30) for $\mu = 9\,\hbar\omega_\perp$ and $\mu = 18\,\hbar\omega_\perp$ respectively, while the solid line is the analytic prediction (2.31) evaluated with $\mu = 9\,\hbar\omega_\perp$. The arrow indicates the angular velocity at which the quadrupole surface mode becomes unstable in the case $\varepsilon = 0$. The value $\mu = 9\,\hbar\omega_\perp$ is close to the experimental setting of [6].

(see [16]). Eq. (2.31) and Fig. 2.4 show that for non-vanishing ε the saddle point on the energy ridge can be surpassed at angular velocities smaller than $\omega_\perp/\sqrt{2}$. The critical angular velocity can be lowered further by increasing the value of $\mu/\hbar\omega_\perp$.

The above exemplified scenario is in reasonable agreement with the experiments. For example, for $\varepsilon = 0.045\,, \mu = 8.71\hbar\omega_\perp$[6] a critical angular velocity $\Omega_c = 0.64\omega_\perp$ is obtained from the measurement of the angular momentum (see data reported in Fig. 2 of [7]). For this value of ε and $\mu = 9\hbar\omega_\perp$ we find $\Omega_c = 0.68\omega_\perp$ (see Fig.2.4). Further on, increasing the value of ε is found to lower the critical angular velocity: In [9] a decrease of $\approx 6\%$ of Ω_c is observed when increasing ε from 0.01 to 0.019. For this setting we find a decrease of 2%. Several papers note that the nucleation range extends to lower Ω for larger ε or longer stirring times [12, 10, 11, 9]. The experiment [11] demonstrates particularly clearly that a strong stirrer with $l = 2$-symmetry corresponding to a large ε shifts Ω_c to angular velocities significantly ($\approx 30\%$) below $\omega_\perp/\sqrt{2}$.

The data reported in the experimental papers is not sufficient to verify our prediction for the dependence of Ω_c on $\mu/\hbar\omega_\perp$. For the small values of ε used in the experiments [6, 7, 8, 10, 9] the calculated dependence on $\mu/\hbar\omega_\perp$ is in fact very weak. This seems in agreement with

[6] Note that in this experiment the static magnetic trap has an anisotropy of $\varepsilon \approx 0.01$ which is not taken into account in our comparison.

a comment made in [7] saying that a change of the total particle number by a factor of 2 (corresponding to a change of μ by about 32% if all other quantities are fixed) brings about a 5% change in Ω_c only. A more systematic comparison with the expected dependence of $\bar{\Omega}_c$ on the trap deformation ε and on the chemical potential μ would be crucial in order to assess the validity of the model.

The energy diagram we employed to calculate the critical angular velocity is based on the Thomas-Fermi approximation to the vortex energy. This approximation is expected to become worse as the vortex line approaches the surface region [57, 31]. Since the main mechanism of nucleation takes place near the surface, we expect that the quantitative predictions concerning the dependence of the critical angular velocity on the trap deformation and on the chemical potential would be improved by using a microscopic evaluation of the vortex energy, beyond the Thomas-Fermi approximation. This should include, in particular, the density dependence of the size of the vortex core. Moreover, the expression for the energy (2.6) can be improved by including image vortex effects on the velocity field associated with a vortex displaced from the center. This amounts to optimizing the choice for the function S in Eq.(2.3). Note that in [55] the critical value of ε at a given angular velocity Ω is obtained by numerically solving the GP-equation. The authors find reasonable agreement between their data and our analytical result (2.31).

Our treatment is based on zero temperature GP-theory and hence does not take account of modes other than the condensate mode. Yet clearly, some dissipative mechanism is required to remove the energy liberated when the vortex state is formed. Finite temperature theories including such processes have been presented in [58, 59]. Others [56] have argued that a zero temperature theory suffices to explain the irreversible transfer of energy from the vortex state to other modes of the system.

We emphasize that the discussion of vortex nucleation presented in this chapter concerns the particular nucleation mechanism relevant when using a rotating trap of the form (1.3) characterized by a $l = 2$-symmetry. The model developed here could be modified to describe systems in rotating traps with $l = 3$ or $l = 4$-symmetry as used in the experiment [11]. In these cases vortex nucleation is connected with the instability of the $l = 3$ and $l = 4$ surface modes respectively and the critical angular velocity is therefore shifted to lower values. Generally, the use of rotating traps with specific symmetries leads to distinct resonance frequencies for vortex nucleation reflecting the existence of the discrete spectrum of surface modes [11]. Strongly deformed traps excite a broad range of surface modes [12]. In this case, vortices are first observed at an angular velocity which approximately corresponds to the minimal critical angular velocity (1.21) for the range of l excited ($l \approx 18$ in the experiment [12]). A very different behavior has been observed when letting a laser beam of a size smaller than the cloud's radius rotate around the condensate [11]: In this case vortices are already detected at the angular velocity Ω_v at which a vortex configuration becomes energetically favourable (see Eq.(2.11)). The number of vortices is a monotonically increasing function of Ω and does not exhibit any resonances associated with the excitation of surface modes. In this experiment, the nucleation of vortices is attributed to the creation of local turbulence by the stirring beam rather than to the excitation of surface modes. A further, very different, way of nucleating vortices is offered by the phase imprinting method proposed by [60] and successfully implemented in the experiment [28] (see also [61, 62] for further imprinting methods). Moreover, vortex lattices have been generated by evaporatively cooling a rotating vapor of cold atoms [30]. Vortices have also been generated by slicing through the cloud with a perturbation above the critical

velocity of the condensate [12, 34]. Finally, vortex rings have been observed as a decay product of dark solitons [63].

2.4 Stability of a vortex-configuration against quadrupole deformation

Once the energy barrier is bypassed, the vortex moves to the center of the trap ($d/R_x = 0$) where the energy has a minimum. In an axisymmetric trap ($\varepsilon = 0$) this configuration will be in general stable against the formation of quadrupole deformations of the condensate unless the angular velocity Ω of the trap becomes too large. The criterion for instability is easily obtained by studying the δ-dependence of the energy of the system in the presence of a single quantized vortex located at $d/R_x = 0$. Considering the total energy (2.27) we find

$$E_{\rm tot}(d/R_x = 0, \delta, \bar{\Omega}, \varepsilon = 0, \mu) \simeq E_{\rm tot}(d/R_x = 0, \delta = 0, \bar{\Omega}, \varepsilon = 0, \mu) + \delta^2 N\mu \left(\frac{1}{7}(1 - 2\bar{\Omega}^2) + \frac{\bar{\Omega}}{2}\frac{\hbar\omega_\perp}{\mu} \right) + \mathcal{O}(\delta^3) \, . \quad (2.32)$$

Comparing Eqs. (2.32) with the analog expression (2.25) holding in the absence of the vortex line one observes that in the presence of the vortex the instability against quadrupole deformation occurs at a higher angular velocity given by

$$\Omega = \omega_\perp \left(\frac{1}{\sqrt{2}} + \frac{7}{8}\frac{\hbar\omega_\perp}{\mu} \right) \, . \quad (2.33)$$

If the angular velocity is smaller than (2.33) the vortex is stable in the axisymmetric configuration while at higher angular velocities the system prefers to deform, giving rise to new stationary configurations. The critical angular velocity (2.33) can also be obtained by applying the Landau criterion (2.17) to the quadrupole collective frequencies in the presence of a quantized vortex. These frequencies were calculated in [64] using a sum rule approach. For the $l = \pm 2$ quadrupole frequencies the result reads

$$\omega_{\pm 2} = \omega_\perp \sqrt{2} \pm \frac{\Delta}{2} \, , \quad (2.34)$$

where

$$\Delta = \omega_\perp \left(\frac{7}{2}\frac{\hbar\omega_\perp}{\mu} \right) \quad (2.35)$$

is the frequency splitting between the two modes. Applying the condition (2.17) to the $l = +2$ mode one can immediately reproduce result (2.33) for the onset of the quadrupole instability in the presence of the quantized vortex.

In an anisotropic trap ($\varepsilon \neq 0$), the stable vortex state will generally be associated with a non-zero deformation δ of the condensate. It is interesting to note that δ increases with the angular velocity of the trap and easily exceeds ε (see Figs. 2.2 and 2.3). This behaviour is analogous to the properties of the deformed stationary states in the absence of vortices [16].

Part II

Bose-Einstein condensates in optical lattices

Chapter 3

Introduction

Since the achievement of Bose-Einstein condensation in trapped ultra-cold dilute atomic gases in 1995 [2, 3, 4], condensates have proven to be extraordinarily robust samples for the study of a wide class of phenomena [1, 15]. A great advantage of these systems is provided by the fact that they are very well isolated and can be controlled and manipulated with high precision by means of electromagnetic fields. This opens up the possibility to design external potentials which change the statics and the dynamics of the gas in a well-defined manner and offer new ways of controlling its properties. Regular lattice potentials produced by light fields provide a prominent example. They allow for the external control of the effect of interactions, the transport properties and the dimensionality of the sample. Situations well known from solid state and condensed matter physics can be mimicked and new types of systems can be engineered.

The tailoring of optical potentials of various forms in space and time is based on the efficient exploitation of the interaction of atoms with laser fields. In the dipole approximation, the interaction Hamiltonian is given by

$$\hat{V}(\mathbf{r},t) = -\hat{\mathbf{d}} \cdot \mathbf{E}(\mathbf{r},t)\,, \tag{3.1}$$

where $\hat{\mathbf{d}}$ is the electric dipole operator of an atom and

$$\mathbf{E}(\mathbf{r},t) = \mathbf{E}(\mathbf{r})e^{-i\omega t} + c.c. \tag{3.2}$$

is a classical time-dependent electric field oscillating with frequency ω. The energy change of each atom associated with the dipolar polarization can be accounted for by the effective potential

$$V(\mathbf{r}) = -\frac{1}{2}\alpha(\omega)\langle \mathbf{E}^2(\mathbf{r},t)\rangle\,, \tag{3.3}$$

where $\alpha(\omega)$ is the dipole dynamic polarizability of an atom and the brackets $\langle \ldots \rangle$ indicate a time average. Here, the response of the atom is assumed to be linear and energy absorption is excluded implying that $\alpha(\omega)$ is real. This can be ensured by detuning the laser sufficiently far away from the atomic resonance frequencies. The time averaging of the potential in (3.3) is justified because the time variation of the laser field is much faster than the typical frequencies of the atomic motion. If the response is dominated by a single resonance state $|R\rangle$ the polarizability behaves like

$$\alpha(\omega) = \frac{|\langle R|\hat{d}_{\mathbf{E}}|0\rangle|^2}{\hbar(\omega_R - \omega)}\,, \tag{3.4}$$

where $|0\rangle$ denotes the unperturbed state of the atom, $\hat{d}_{\mathbf{E}}$ is the dipole operator component in the direction of the electric field and $\hbar\omega_R$ is the energy difference between $|0\rangle$ and $|R\rangle$. Hence, a blue ($\omega > \omega_R$) and red detuned field ($\omega < \omega_R$) lead to repulsion and attraction of the atom respectively.

By illuminating an atom with a standing wave field

$$E(\mathbf{r},t) = E\sin(qz)e^{-i\omega t} + c.c.\,, \tag{3.5}$$

an effective potential (3.3) of the form

$$V(z) = sE_R \sin^2\left(\frac{\pi z}{d}\right)\,, \tag{3.6}$$

is created, corresponding to a potential of period $d = \pi/q$ along the z-direction. Here and in the following, s is the lattice depth $-\alpha(\omega)E^2$ in units of the recoil energy $E_R = \hbar^2\pi^2/2md^2$, which corresponds to the energy an atom gains by absorbing a photon from the standing wave field (3.5). The standing wave can be produced by two laser beams of the same intensity with zero relative detuning and wavevector difference q oriented along the z-direction. For counterpropagating beams, the lattice period is given by half the laser wavelength. The lattice potential can be set into motion by choosing a nonzero relative detuning ω, corresponding to the potential

$$V(z) = \frac{1}{2}sE_R\cos\left(2\frac{\pi z}{d} - \omega t\right)\,. \tag{3.7}$$

A constant ω makes the lattice move at constant velocity. It is accelerated by increasing ω, while it shakes if ω oscillates. With additional laser beams, two- and three-dimensional lattices can be generated. In the simplest case, the resulting structures have cubic symmetry, but also more complicated patterns can be attained.

The most important tunable parameter is the lattice depth s which is proportional to the laser intensity. In addition, the lattice period can be tuned by changing the angle between the beams, while the motion of the lattice can be controlled through the detuning of the lasers.

In most current experiments, the lattice period d is of the order of $0.5\mu m$ associated with a recoil energy of several kHz for ^{87}Rb and ^{23}Na. The lattice potential is usually superimposed to the harmonic potential of a magnetic trap. Typically, the size of the condensate without lattice is much larger than the lattice period d. As a consequence, the atoms are distributed over many sites of the added optical potential.

Many properties of low temperature dilute-gas Bose-Einstein condensates can be understood assuming zero temperature and working within the framework of Gross-Pitaevskii (GP) theory [1, 15]. Within this framework all atoms are condensed into a single mode $\varphi(\mathbf{r},t)$ often denoted as the condensate wavefunction. The quantity $\Psi(\mathbf{r},t) = \sqrt{N_{\rm tot}}\varphi(\mathbf{r},t)$ constitutes an order parameter, where $N_{\rm tot}$ is the total number of particles. Modulus and phase S of the order parameter are closely related to the density distribution and the velocity field respectively

$$n(\mathbf{r},t) = |\Psi(\mathbf{r},t)|^2\,, \tag{3.8}$$

$$\mathbf{v}(\mathbf{r},t) = \frac{\hbar}{m}\nabla S(\mathbf{r},t)\,. \tag{3.9}$$

The order parameter's temporal evolution in the external potential $V(\mathbf{r},t)$ obeys the Gross-Pitaevskii equation (GPE)

$$i\hbar\frac{\partial\Psi(\mathbf{r},t)}{\partial t}=\left(-\frac{\hbar^2}{2m}\nabla^2+V(\mathbf{r},t)+g\left|\Psi(\mathbf{r},t)\right|^2\right)\Psi(\mathbf{r},t)\,. \tag{3.10}$$

Two-body interaction between atoms is accounted for by the nonlinear term which is governed by the coupling constant

$$g=\frac{4\pi\hbar^2 a}{m}\,, \tag{3.11}$$

where a is the s-wave scattering length. Throughout this thesis, we will focus on repulsively interacting atoms ($a>0$). The criterion for the diluteness of the gas reads

$$na^3\ll 1\,, \tag{3.12}$$

with n the density.

With the external potential $V(\mathbf{r},t)$ given by an optical lattice, the GP-equation differs from the Schrödinger equation of a particle in a crystal structure by the nonlinear mean field term, opening up the possibility to explore analogies and differences with respect to solid state physics.

A dilute-gas condensate in a lattice at very low temperatures is well described by GP-theory only if the potential is not too deep. An increase of the lattice depth is in fact accompanied by a drop of the condensate fraction and a loss of coherence. This is due to the enhanced role played by correlations between the particles. The gas can even loose its superfluid properties: At a critical value of the lattice depth at zero temperature the gas undergoes a quantum phase transition to an insulating phase. Complete insulation is achieved provided the number of particles is a multiple of the number of sites.

The different physical regimes experienced by a cold atomic gas in an optical lattice can be described using a Bose-Hubbard Hamiltonian (for a review see [65]). This Hamiltonian is obtained by expanding the atomic field operators of the many-body Hamiltonian in the single particle Wannier basis. Terms due to higher bands are omitted. From the lowest band, only on-site and nearest-neighbour contributions are retained. In this framework, the state of the system is expressed in the Fock basis $\{|N_1,\ldots,N_l,\ldots\rangle\}$ where l labels the Wannier functions, or equivalently, the lattice sites and the numbers N_l give the number of atoms at site l. With $\hat{b}_l^\dagger$ as the creation operator for an atom at site l and $\hat{n}_l$ the associated number operator, the Bose-Hubbard Hamiltonian reads

$$\hat{H}=-\delta\sum_{l,l'=l\pm1}\hat{b}_l^\dagger\hat{b}_{l'}+\frac{U}{2}\sum_l\hat{n}_l(\hat{n}_l-1)\,. \tag{3.13}$$

The parameters U and δ govern the on-site interaction and the tunneling of particles to neighbouring sites respectively. They are associated with two competing tendencies of the system: On one side, the atoms try to reduce their interaction energy by localizing at different lattice sites thereby reducing occupation number fluctuations. On the other side, they tend to spread over many sites in order to minimize the kinetic energy. The physical characteristics of the zero temperature groundstate depends on the ratio U/δ between tunneling and on-site interaction: For $U/\delta\ll 1$, the particles are delocalized over all sites. In this case, all particles occupy the

same condensate wavefunction given by the groundstate solution of the GP-equation in the tight binding regime and the state of the system can approximately be written as a coherent state in the Fock basis $|N_1, \ldots, N_l, \ldots\rangle$ associated with Poissonian fluctuations of the occupation numbers. In this limit, the gas exhibits superfluidity, the excitation spectrum is gapless and is characterized by a phononic excitations at low energies. In the opposite limit $U/\delta \to \infty$, most particles are localized at certain sites. For comensurate filling, the groundstate can be written as a Fockstate $|N_1, \ldots, N_l, \ldots\rangle$ and exhibits zero occupation number fluctuations. The excitation spectrum is then characterized by a gap of magnitude U. The gas is an insulator and is incompressible $\partial n/\partial \mu = 0$. For non-commensurate filling, some particles are still delocalized. This portion of the gas remains superfluid and gives rise to a finite compressibility. When moving between the two limits, a quantum phase transition between the superfluid phase and the insulating phase is encountered at a critical value of U/δ. In the case of cold atoms in an optical lattice, the parameters U and δ can be tuned by changing the lattice depth s: The ratio U/δ increases in fact as a function of s since δ decays exponentially with increasing s and U features a power law increase.

The Bose-Hubbard Hamiltonian offers an adequate description if the motion of the atoms is confined to the lowest band and if the lattice is deep enough to permit only nearest neighbour hopping. This implies that the $U/\delta \ll 1$-limit as described by the Bose-Hubbard Hamiltonian coincides with the tight binding regime of GP-theory in the presence of a lattice. Hence, a complete description of the zero temperature behavior is obtained by using GP-theory at relatively low lattice depth and the Bose-Hubbard Hamiltonian at larger lattice depth when effects going beyond GP theory become crucial. This is the case even when the system is still superfluid. Note that if the number of particles at each site is large an alternative way to go beyond the GP-regime is offered by the use of a suitable Quantum Josephson Hamiltonian.

In order for GP-theory to be valid, the depletion of the condensate, due to quantum or thermal fluctuations, must be small. There is in fact a large range of lattice depths for which almost all particles are in the condensate provided the number of particles per site is large. In practise, this implies that in the case of three-dimensional lattices the range of lattice depth at which GP-theory is valid is very small since the occupation of each site is of order one.

The first experimental investigation of a condensate in an optical lattice was done by Anderson and Kasevich [66]. These authors observed the coherent tunneling of atoms from individual lattice sites into the continuum where they accelerate due to gravity, giving rise to visible interference patterns. Subsequently, many further experiments were devoted to the study of these systems in the regime where the atomic cloud is coherent: In an accelerated lattice, Bloch oscillations [67] and Landau-Zener tunneling out of the lowest Bloch band [67, 68, 69] were observed. The screening effect of mean field interaction was explored in [67]. The interference pattern in the density distribution after a time of free flight was studied in [70], demonstrating that in the groundstate coherence is maintained across the whole system. In [71] the density distribution after free expansion was analyzed to determine the increase of the chemical potential and the radial size due to the lattice. A further experiment demonstrated the slow-down of the expansion if the optical lattice is kept on and only the harmonic trap is switched off [72]. The realization of an array of Josephson Junction was reported in [73]. Also the changes in the frequencies of collective excitations due to the combined presence of lattice and harmonic trap have been observed [74, 73, 75]. Due the presence of interactions, the motion of the cloud through the lattice can lead to the occurrence of instability phenomena [74, 76, 77]. The coherent transfer of population within the band structure and methods for

band spectroscopy were described in [79]. In [72, 79, 80] effects related to the non-adiabatic loading of the sample into the lattice were explored. The motion of the lattice was used to do dispersion management of matter wave packets [81]. It was found to have a lensing effect on the condensate [82] and was applied recently to generate bright solitons [83, 84]. Finite temperature effects were studied in [85, 86]. In particular, a change of the critical temperature of Bose-Einstein condensation was observed reflecting the two-dimensional nature of the cloud in each well of a deep potential [85], while in [86] the temperature-dependent transport properties of the system were demonstrated. The phase coherence of a condensate loaded into a two-dimensional lattice was investigated in [87]. Recently, a two-dimensional lattice was used successfully to prepare a one-dimensional Bose gas [88].

Remarkable progress has been made also in the study of regimes where the GP-description breaks down: A first advance in this direction was the observation of number squeezing in a superfluid ultracold atomic gas in a one-dimensional lattice [89]. Further on, the superfluid-insulator transition of cold atoms in a three-dimensional lattice was observed [90, 91]. The transition to the insulating phase has been used to demonstrate the collapse and revival of the matter wave field of a Bose-Einstein condensate [92]. Atoms in the insulating phase promise to be a precious resource for quantum computing: Their spin-dependent coherent transport between lattice sites and the controlled creation of entanglement have already been achieved [93, 94, 95].

This thesis deals with repulsively interacting three-dimensional dilute-gas Bose-Einstein condensates in optical lattices at zero temperature. We concentrate on the range of lattice depths where GP-theory is valid, i.e. the gas is almost completely condensed and exhibits full coherence. We deal with one-dimensional lattices in the first place. The generalization of many of the results to cubic two-dimensional lattices is straightforward and will be commented on. As a general strategy, we first exclude harmonic trapping from our considerations. Since typically, the particles are distributed over many lattice sites in the presence of harmonic trapping, its effects can be included in a second step, as will be shown in detail. In so far as we neglect harmonic trapping effects and concentrate on one-dimensional optical lattices, we study the properties of condensates as described by the Gross-Pitaevskii equation

$$i\hbar\frac{\partial\Psi(z,t)}{\partial t}=\left(-\frac{\hbar^2}{2m}\frac{\partial^2}{\partial z^2}+sE_R\sin^2\left(\frac{\pi z}{d}\right)+g\left|\Psi(z,t)\right|^2\right)\Psi(z,t)\,, \tag{3.14}$$

where the order parameter Ψ fulfills the normalization condition

$$\int d\mathbf{r}\left|\Psi(z,t)\right|^2=N_{\rm tot}\,, \tag{3.15}$$

with $N_{\rm tot}$ the total number of particles. Because we assume the system to be confined in a box of length L along x,y and we exclude dynamics involving these transverse directions, the order parameter Ψ depends only on z. The dependence of Ψ on x,y comes into play only once we allow for the effects of harmonic trapping.

The linear response of the system and the depletion of the condensate are treated within Bogoliubov theory (see [1]). In the latter case, also elementary excitations in the transverse directions have to be taken into account.

Particular attention is paid to the analogies and differences with respect to the single particle case and with respect to the case of a uniform or harmonically trapped condensate.

We develop simple theoretic frameworks for the description of statical and dynamical properties and discuss quantities which are crucial for their characterization. We also evaluate the validity of GP-theory in order to demonstrate the applicability of our results.

In particular, after a short review of some standard results concerning a single particle in a one-dimensional periodic potential, we will discuss

- the groundstate with and without harmonic trap (chapter 5)
- stationary states of Bloch form (chapter 6)
- the Bogoliubov excitations of the groundstate (chapter 7)
- the linear response to a density perturbation (chapter 8)
- the macroscopic dynamics with and without harmonic trap (chapter 9)
- the description of the system as an array of Josephson junctions (chapter 10)
- the propagation of sound signals (chapter 11)
- the quantum depletion (chapter 12)

Here is a more detailed overview of the thesis:

Chapter 5 discusses the groundstate of a condensate confined in a one-dimensional optical lattice. We first consider a system without harmonic trapping which is uniform in the direction transverse to the lattice. We study the chemical potential, the energy, the density profile and the compressibility as a function of lattice depth s and the interaction parameter gn, where g is the two-body coupling constant (3.11) and n is the average density. In a second step, we allow for the additional presence of radial and axial harmonic trapping. We use the results obtained for the purely periodic potential as an input to calculate the groundstate properties in the combined trap.

In chapter 6, we extend the discussion of stationary condensates in a one-dimensional lattice to non-groundstate solutions of the GP-equation. We focus on solutions which take the form of Bloch states and investigate the associated band spectra for the energy and the chemical potential in dependence on lattice depth and interaction strength carrying out a detailed comparison both with the non-interacting and the uniform cases. The energy Bloch band spectrum determines the current and therefore the group velocity and the effective mass. In the tight binding regime, the energy and chemical potential bands take a simple analytic form. From the expression for the Bloch energy bands we find equations for the current and the group velocity. Exploiting the tight binding formalism, we also derive simple expressions for the compressibility of the groundstate.

Chapter 7 deals with small perturbations of a stationary Bloch state condensate in the periodic potential. We study in detail the Bogoliubv band spectrum of the groundstate both numerically for all lattice depths and analytically in the tight binding regime. Special attention is paid to the behavior of the sound velocity both for the groundstate and for a condensate moving with non-zero group velocity.

The Bogoliubov band structure can be probed by studying the linear response of the condensate to a weak external perturbation. In chapter 8 we consider the particular case in which

the external probe generates a density perturbation in the system. We present results for the dynamic structure factor and the static structure factor of a condensate loaded into a one-dimensional lattice pointing out the striking effect of the periodic potential.

In chapter 9, we show how to describe the long length scale GP-dynamics of a condensate in a one-dimensional optical lattice by means of a set of hydrodynamic equations for the density and the velocity field. Within this formalism, we can account for the presence of additional external fields, as for example a harmonic trap, provided they vary on length scales large compared to the lattice spacing d. As an application we derive an analytic expression for the sound velocity in a Bloch state condensate. In the combined presence of optical lattice and harmonic trap, the hydrodynamic equations can be solved for the frequencies of small amplitude collective oscillations. The results are compared with recent experimental data. We also discuss the large amplitude center-of-mass motion.

In chapter 10 we describe the dynamics of the system in terms of the dynamics of the number of particles and the condensate phase at each lattice site. From this point of view, the system constitutes a realization of an array of Josephson junctions.

The effect of a one-dimensional optical lattice on the propagation of sound signals is discussed in chapter 11. We devote special attention to the propagation in the nonlinear regime and distinguish different nonlinear effects in dependence on lattice depth.

Finally, in chapter 12 we discuss the effect of the lattice on the condensate fraction within the framework of Bogoliubov theory. We provide estimates for the depletion, discuss the effective change of geometry induced by the lattice and set the limit of validity of our methods.

This part of the thesis is essentially based on the following papers:

- *Macroscopic dynamics of a trapped Bose-Einstein condensate in the presence of 1D and 2D optical lattices*
  M. Krämer, L. Pitaevskii and S. Stringari,
  Phys. Rev. Lett. **88**, 180404 (2002).

- *Dynamic structure factor of a Bose-Einstein condensate in a 1D optical lattice*
  C. Menotti, M. Krämer, L. Pitaevskii, and S. Stringari:
  Phys. Rev. A **67**, 053609 (2003).

- *Bose-Einstein condensates in 1D optical lattices: Compressibility, Bloch bands and elementary excitations*
  M. Krämer, C. Menotti, L. Pitaevskii and S. Stringari,
  Eur. Phys. J. D **27**, 247 (2003).

- *Sound propagation in presence of a one-dimensional optical lattice*
  in preparation, with C. Menotti, A. Smerzi, L. Pitaevskii and S. Stringari

Chapter 4

Single particle in a periodic potential

This chapter reviews some standard results (see for example [19, 96]) concerning a single particle in one dimension subject to an external potential $V(x)$ which is periodic in space with period d

$$V(x) = V(x+d)\,. \tag{4.1}$$

The aim of this chapter is to provide some basic concepts such as quasi-momentum, band structure, Brillouin zone, Bloch functions and Wannier functions. Starting from the single particle case we can then conveniently extend and generalize these notions to the case of a Bose-Einstein condensate in the following chapters.

4.1 Solution of the Schrödinger equation

Bloch states and Bloch bands

The one-dimensional motion of a particle in the periodic potential (4.1) is described by the Schrödinger equation

$$i\hbar\frac{\partial\varphi(x)}{\partial t} = \left(-\frac{\hbar^2}{2m}\frac{\partial^2}{\partial x^2} + V(x)\right)\varphi(x)\,. \tag{4.2}$$

Due to the periodicity of the potential this equation is invariant under any tranformation $x \to x+ld$ where l is any integer. Thus, if $\varphi(x)$ is the wavefunction of a stationary state, then $\varphi(x+ld)$ is also a solution of the Schrödinger equation. This means that the two functions must be the same apart from a constant factor: $\varphi(x+ld) = \text{constant} \times \varphi(x)$. It is evident that the constant must have unit modulus; otherwise, the wave function would tend to infinity when the displacement through ld was repeated infinitely. The general form of a function having this property is

$$\varphi_{jk}(x) = e^{ikx}\tilde{\varphi}_{jk}(x)\,, \tag{4.3}$$

where $\hbar k$ is the quasi-momentum and $\tilde{\varphi}_{jk}(x)$ is a periodic function

$$\tilde{\varphi}_{jk}(x) = \tilde{\varphi}_{jk}(x+d)\,. \tag{4.4}$$

To satisfy periodic boundary conditions, $\varphi(-L/2) = \varphi(L/2)$, where L is the length of the system, k must be restricted to the spectrum

$$k = \frac{2\pi}{L}\nu\,, \qquad \nu = 0, \pm 1, \pm 2, \ldots \qquad . \tag{4.5}$$

Solutions of the form (4.3) are called Bloch functions. The functions $\tilde{\varphi}_{jk}(x)$ are referred to as Bloch waves.

From the translational properties of the wavefunction

$$\varphi_{jk}(x+d) = e^{ikd}\varphi_{jk}(x)\,, \tag{4.6}$$

it follows that values $k + l\,2\pi/d$ with l integer label the same physical state of the particle. We can say that the Bloch functions $\varphi_{jk}(x)$ and their energy are periodic with respect to k

$$\varphi_{jk}(x) = \varphi_{jk+l2\pi/d}(x)\,, \tag{4.7}$$

$$\varepsilon_j(k) = \varepsilon_j(k + l\frac{2\pi}{d})\,. \tag{4.8}$$

In order to find all physically different states of the particle it is thus sufficient to consider values of k in the range $-\pi/d, \ldots \pi/d$, i.e. in the so called first Brillouin zone. In the following we will refer to the momentum

$$q_B = \frac{\hbar\pi}{d} \tag{4.9}$$

corresponding to the boundary of the first Brillouin zone as the Bragg momentum. The associated energy scale is provided by the recoil energy $E_R = \hbar^2\pi^2/2md^2$.

For a given value of k, the Schrödinger equation has an infinite set of discrete solutions $\varepsilon_j(k)$ labeled by the index j. For fixed j, the energy as a function of k takes values in a certain finite range called an energy band. For this reason, the label j is referred to as the band index.

The Bloch functions φ_{jk} with k belonging to the first Brillouin zone form an orthonormal set. Since the Bloch waves $\tilde{\varphi}_{jk}$ are periodic it is common to impose the normalization condition over one period

$$\int_{-d/2}^{d/2} dx\; \tilde{\varphi}^*_{jk}\tilde{\varphi}_{j'k} = \delta_{jj'}\,. \tag{4.10}$$

Note that that to get orthogonality of Bloch functions with different quasi-momenta the integration over all space and the correct boundary conditions are required. Accordingly, the energy is calculated by integrating over one lattice period

$$\varepsilon_j(k) = \int_{-d/2}^{d/2} dx\; \varphi^*_{jk}(x)\left(-\frac{\hbar^2}{2m}\frac{\partial^2}{\partial x^2} + V(x)\right)\varphi_{jk}(x)\,. \tag{4.11}$$

Each energy level is doubly degenerate with respect to the sign of k

$$\varepsilon_j(k) = \varepsilon_j(-k)\,. \tag{4.12}$$

This property is a consequence of the symmetry under time reversal: Because of this symmetry, if φ_{jk} is the wave function of a stationary state, the complex conjugate function φ^*_{jk} describes a state with the same energy and quasi-momentum $-\hbar k$. It is worth noting that in one-dimensional motion no degree of degeneracy higher than (4.12) is possible. As a consequence,

different bands are always separated by energy gaps. Moreover, in the one-dimensional case, the minimum and maximum values of each band $\varepsilon_j(k)$ are found at $k = 0$ and $k = \pi/d$.

If the potential $V(x)$ is weak, one can apply first order perturbation theory to calculate the energy bands $\varepsilon_j(k)$. For this purpose, it is useful to expand the function V in a Fourier series $V(x) = \sum_{l=-\infty}^{\infty} V_l \, e^{il2\pi x/d}$. One finds that all bands are shifted by the constant V_0 and that the energy gap between the band j and the band $j+1$ equals to $2|V_j|$. In the particular case of an optical lattice $V = sE_R\sin^2(\pi x/d)$, only V_0 and V_1 are nonzero. Hence, the energy gaps are found to be zero except for the one between the lowest and the first excited band. Higher order perturbation theory is needed to resolve the gaps between the higher bands. The opposite extreme of a deep potential is discussed below in section 4.2.

In Fig. 4.1, we plot the first three energy bands for a single particle in the optical lattice potential $V = sE_R\sin^2(\pi x/d)$ for $s = 0, 1, 5$ as obtained from the numerical solution of the Schrödinger equation. For $s = 0$ we are dealing with a free particle with energy spectrum $\varepsilon(k) = \hbar^2k^2/2m$. The corresponding "band spectrum" is obtained by mapping to the jth band energies with wave numbers k belonging to the jth Brillouin zone ($(j-1)q_B \leq |k| \leq jq_B$). Fig. 4.1 illustrates that energy gaps become larger while the heights of the bands decrease as the lattice is made deeper. These effects become most clearly visible by looking at the lowest band: In fact, the energy gap between first and second band is already large at a lattice depth of $s = 1$, while the gaps between higher bands are hardly visible. Also, the height of the lowest band decreases much more rapidly as a function of s than the ones of the higher bands.

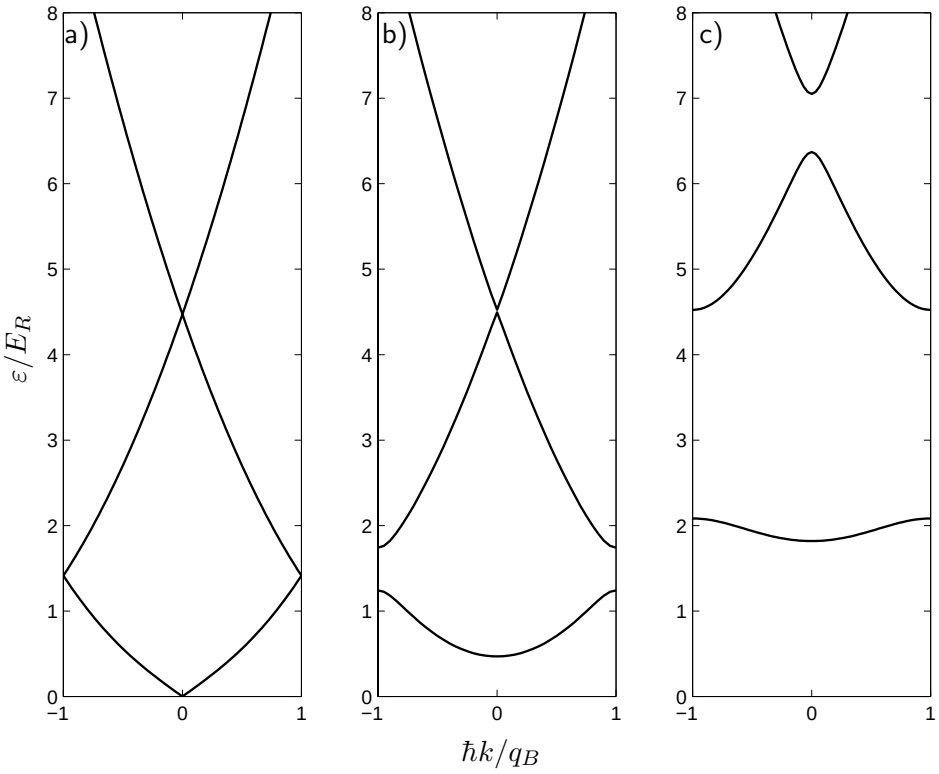

Figure 4.1: Lowest three Bloch bands (4.11) in the first Brillouin zone of a particle in the optical lattice potential $V = sE_R\sin^2(\pi x/d)$ for a) $s = 0$, b) $s = 1$ and c) $s = 5$.

In Fig. 4.2, we plot the quantity $|\varphi_{jk}|^2$ for different values of the quantum numbers j and k in the case of the optical lattice potential $V = sE_R\sin^2(\pi x/d)$ with $s = 5$. In the lowest band the particle tends to be concentrated close to the potential minima. The higher the band index the more probable it becomes to find the particle in high potential regions. This is because the particle is less affected by the presence of the lattice and its wavefunction resembles more the free particle delocalized plane wave solution. Moreover, the flatter a band the less the distribution changes when varying k.

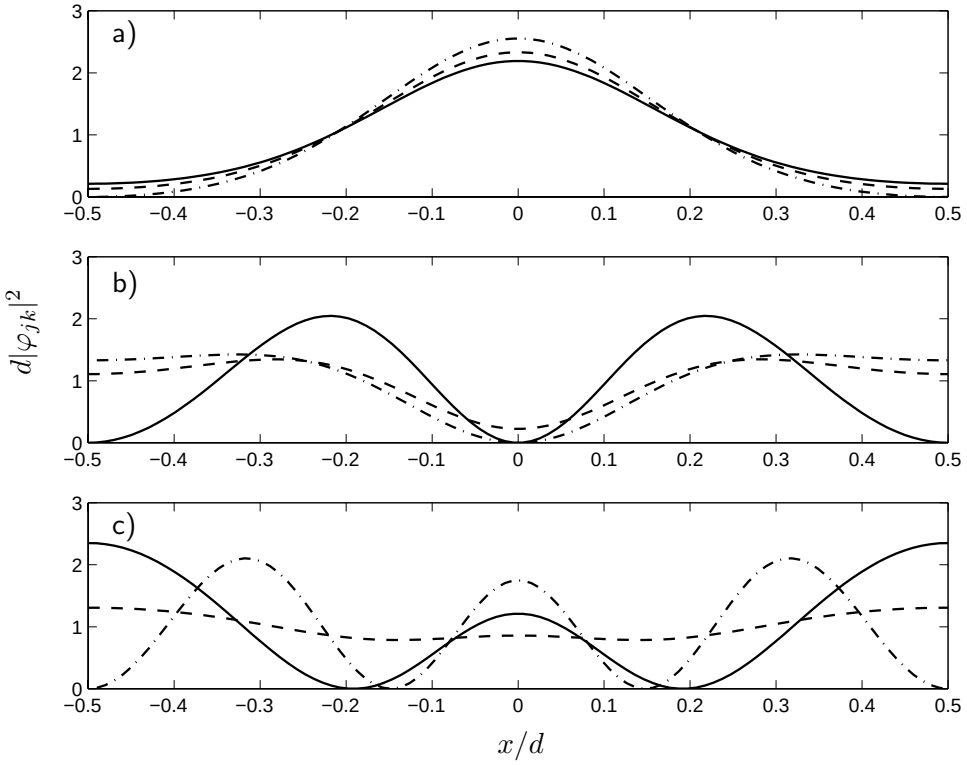

Figure 4.2: Modulus squared of the Bloch function φ_{jk} (4.3) at $k = 0$ (solid line), $\hbar k = 0.5q_B$ (dashed line) and $\hbar k = q_B$ (dash-dotted line) with a) $j = 1$, b) $j = 2$ and c) $j = 3$ of a particle in the optical lattice potential $V = sE_R\sin^2(\pi x/d)$ for $s = 5$.

Momentum and Quasi-momentum

The Bloch functions (4.3), being characterized by a certain constant wave number k, have a certain similarity with the plane wave states of a free particle of momentum $p = \hbar k$. For this reason, the quantity $\hbar k$ is often called quasi-momentum. It is however important to point out that due to the presence of the external potential, which has only a discrete translational invariance, there is no conserved momentum. In fact, in a stationary state with a given quasi-momentum $\hbar k$, the momentum can have values $\hbar(k+l\,2\pi/d)$ with l integer. The corresponding

probabilities are obtained from the Fourier expansion of the periodic function $\tilde{\varphi}_{jk}(x)$

$$\tilde{\varphi}_{jk}(x) = \sum_l a_{jkl}\, e^{il2\pi x/d}\,. \tag{4.13}$$

Inserting this expression into (4.3) yields the expansion of the Bloch function in plane waves

$$\varphi_{jk}(x) = \sum_l a_{jkl}\, e^{i(l2\pi/d+k)x}\,. \tag{4.14}$$

Hence the probability for the particle to have momentum $\hbar(k+l\,2\pi/d)$ is given by $d|a_{jkl}|^2$. In the case of the groundstate $(j=1, k=0)$, the more the function $\tilde{\varphi}_{jk}(x)$ is modulated by the presence of the external potential, the more momentum components $p = \hbar l\, 2\pi/d$ with $l \neq 0$ are important.

In Figs.4.3 and 4.4, we plot the probabilities $|a_{jkl}|^2$ with $j=1$ and $\hbar k = 0,\, 0.5q_B,\, q_B$ for a particle in the optical lattice potential $V = sE_R\sin^2(\pi x/d)$ for $s=1$ and $s=5$ respectively. Note that non-zero values of l become more important as s is increased. When tuning k to non-zero values, the distribution $|a_{jkl}|^2$ becomes asymmetric with respect to $l=0$ because $\tilde{\varphi}_{jk}$ can not be written as a real function, indicating the presence of a nonzero velocity distribution within each well.

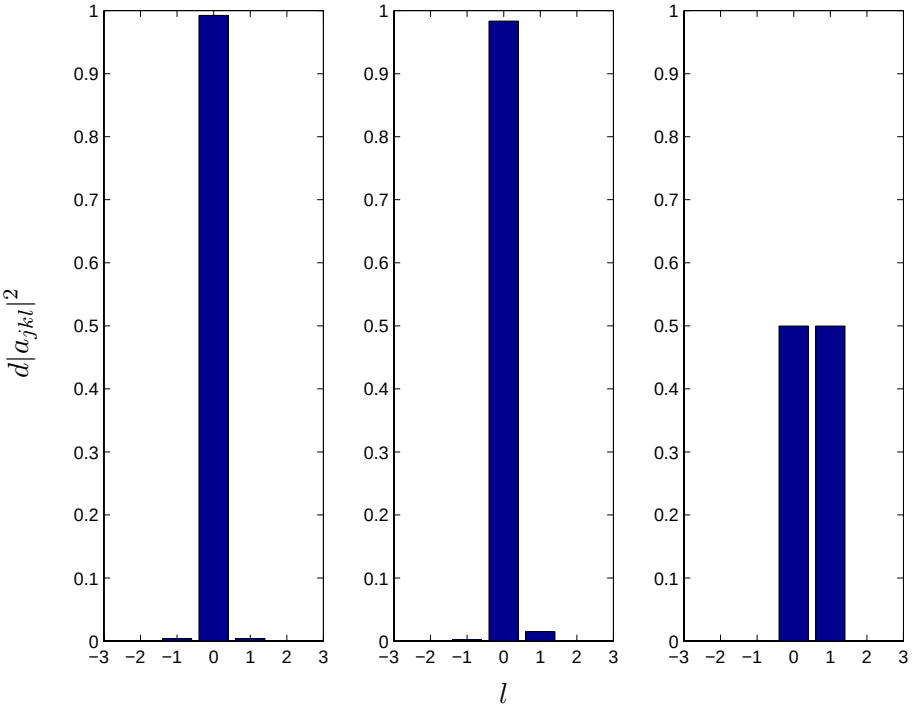

Figure 4.3: Probabilities $|a_{jkl}|^2$ of momentum components $p = \hbar k + l\,2\pi/d$ in the state with band index $j=1$ and quasi-momentum $\hbar k = 0$ (left), $\hbar k = 0.5q_B$ (middle), and $\hbar k = q_B$ (right) for a particle in the optical lattice potential $V = sE_R\sin^2(\pi x/d)$ with $s=1$.

Group velocity, current and effective mass

A further analogy between quasi-momentum and actual momentum is revealed by calculating the mean velocity $\bar{v}_j(k)$ of a particle in the Bloch state $\varphi_{jk}(x)$. One finds

$$\bar{v}_j(k) \equiv \langle \varphi_{jk} | \hat{\dot{x}} | \varphi_{jk} \rangle = \frac{\partial \varepsilon_j(k)}{\hbar \partial k} \,. \tag{4.15}$$

This quantity is referred to as the group velocity. According to relation (4.15) the particle remains at rest on average when $k = l\pi/d$ since at these values of the quasi-momentum the energy bands exhibit local minima or maxima. Furthermore, the particle mean velocity decreases as the potential is made deeper due the flattening of the bands. The dependence of the group velocity on the quasi-momentum for different potential depths is illustrated in Fig. 4.5 for a particle in the optical lattice potential $V = sE_R \sin^2(\pi x/d)$.

A closely related quantity is the current density associated with a certain Bloch state

$$I_j(k) = \frac{i\hbar}{2m} \left(\varphi_{jk} \frac{\partial}{\partial x} \varphi^*_{jk} - \varphi^*_{jk} \frac{\partial}{\partial x} \varphi_{jk} \right) . \tag{4.16}$$

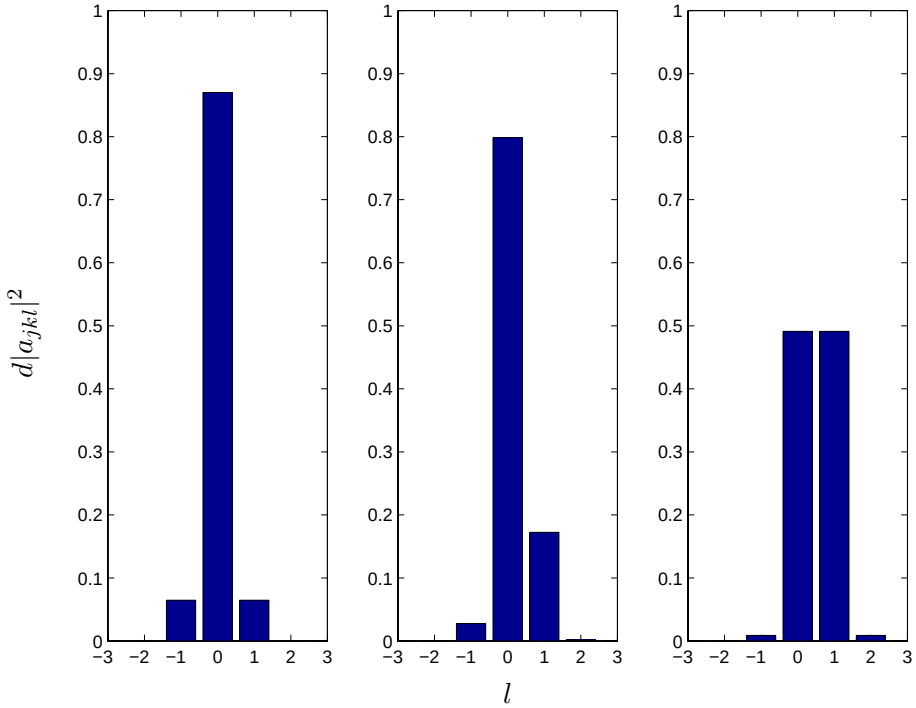

Figure 4.4: Probabilities $|a_{jkl}|^2$ of momentum components $p = l\,2\pi/d$ in the state with band index $j = 1$ and quasi-momentum $\hbar k = 0$ (left), $\hbar k = 0.5 q_B$ (middle), and $\hbar k = q_B$ (right) for a particle in the optical lattice potential $V = sE_R \sin^2(\pi x/d)$ with $s = 5$.

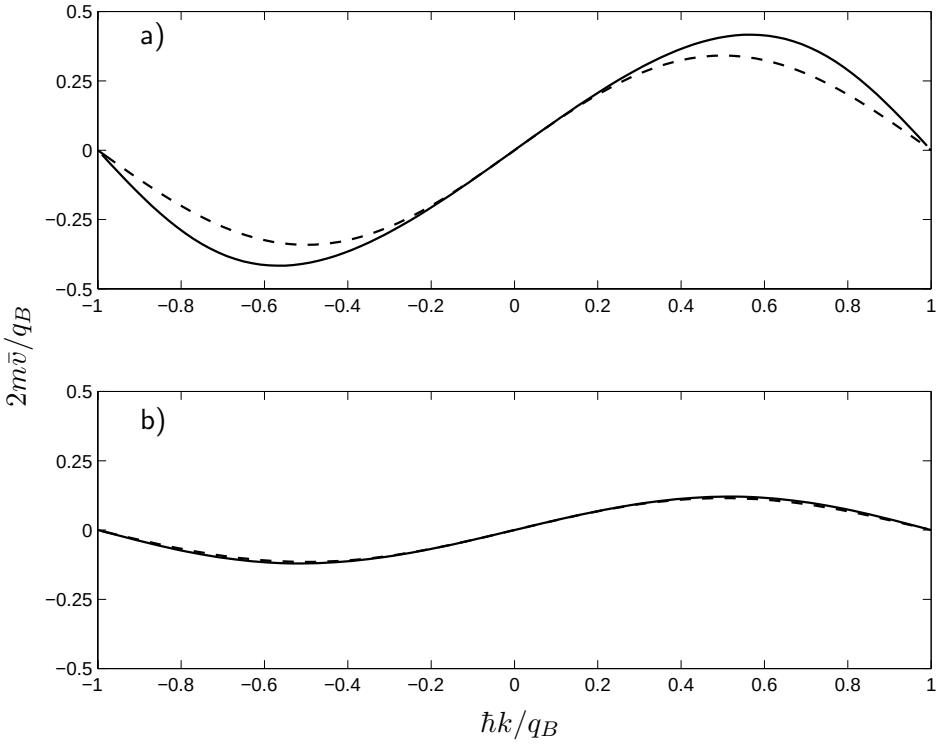

Figure 4.5: Group velocity (4.15) as function of quasi-momentum $\hbar k$ of a particle in the optical lattice potential $V = sE_R \sin^2(\pi x/d)$ with a) $s = 1$ and b) $s = 5$. Solid lines: Exact numerical results. Dashed lines: Tight binding result (4.31) with δ as obtained from (4.33) using the numerical data for m^* (4.18).

The current density does not depend on the spatial coordinate x since we are dealing with a stationary state solution of the Schrödinger equation. Hence, each Bloch state is characterized by a certain value of the current density $I_j(k)$. One can show easily (see discussion in chapter 6.1) that

$$I_j(k) = \frac{1}{L}\frac{\partial \varepsilon_j(k)}{\hbar \partial k}\,, \tag{4.17}$$

where L is the length of the system. It is interesting to note that Eq.(4.17) implies the result (4.15) since the group velocity must fulfill the equation $\bar{v}_j(k) = IL$.

For small quasi-momenta $k \to 0$, the lowest energy band depends quadratically on k, its curvature defining the effective mass

$$\frac{1}{m^*} := \left.\frac{\partial^2 \varepsilon_j(k)}{\hbar^2 \partial k^2}\right|_{k=0}\,. \tag{4.18}$$

With this defintion, current and group velocity for $k \to 0$ are given by

$$I_{j=1}(k) \;\to\; \frac{1}{L}\frac{\hbar k}{m^*} \tag{4.19}$$

$$\bar{v}_{j=1}(k) \;\to\; \frac{\hbar k}{m^*} \tag{4.20}$$

Hence, at small quasi-momenta, the change in current and average velocity brought about by the periodic potential can be understood in terms of the change in the effective mass. In Fig.4.6 we plot the effective mass (4.18) as a function of potential depth in the case of the optical lattice potential $V = sE_R \sin^2(\pi x/d)$. The increase of m^* as a function of lattice depth s reflects the slow-down of the particle by the potential barriers. In fact, in a sufficiently deep lattice, the particle has to tunnel through the barriers. The exponential increase of the effective mass encountered in this regime can be understood in terms of the tunneling properties of the system, as is shown in the next section.

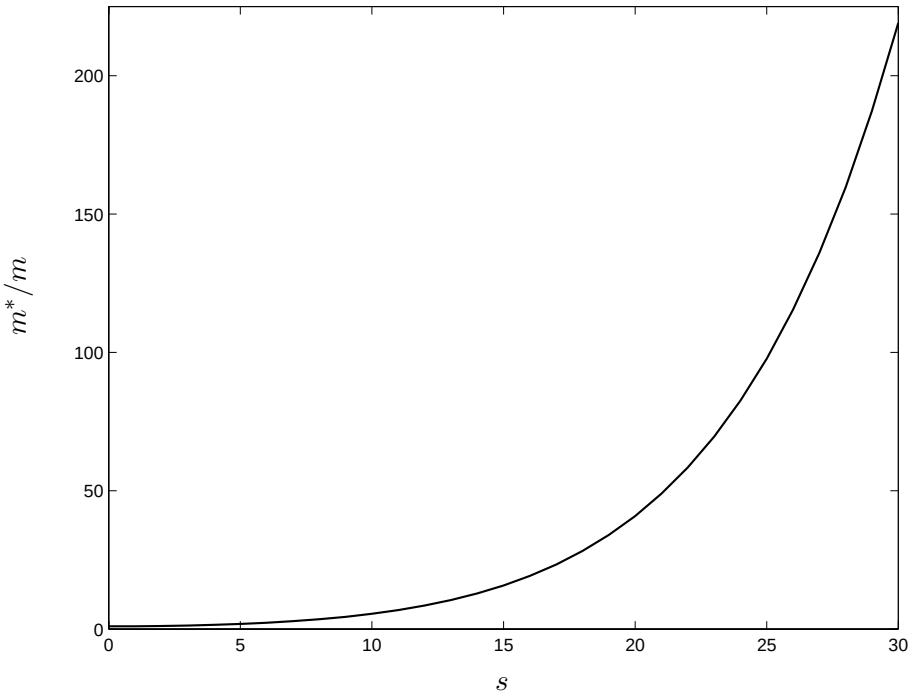

Figure 4.6: Effective mass (4.18) as a function of potential depth in the case of the optical lattice potential $V = sE_R \sin^2(\pi x/d)$.

It is common to generalize the definition of the effective mass (4.18) to any band and quasi-momentum

$$\frac{1}{m_j^*(k)} := \frac{\partial^2 \varepsilon_j(k)}{\hbar^2 \partial k^2} \,. \tag{4.21}$$

The k-dependent effective mass and the group velocity (4.15) are useful concepts to describe Bloch-oscillations experiments with cold (non-interacting) atoms in which the atoms are exposed to a constant small acceleration a [97, 98]. This can for example be achieved by accelerating the potential or by exploiting gravity in a vertical set up. The state of the system can be described by $\varphi_{jk(t)}$ where the quasi-momentum $\hbar k(t)$ increases linearly in time. As a consequence, the instantaneous group velocity $\bar{v}(k(t))$ (4.15) clearly oscillates in time with a period $2q_B/ma$ determined by the time needed to cross a Brillouin zone. Regions of positive

and negative acceleration $m\dot{\bar{v}}$ correspond to regions of positive and negative effective mass respectively.

Wannier functions

Due to their periodicity in k-space, the Bloch functions $\varphi_{jk}(x)$ can be expanded in the Fourier series

$$\varphi_{jk}(x) = \sum_l f_{j,l}(x) e^{ikld}\,, \tag{4.22}$$

where l labels the sites of the periodic potential. The quantities $f_{j,l}(x)$ are the Fourier coefficients of the expansion at x fixed. The inverse expansion reads

$$f_{j,l}(x) = \frac{1}{N_w} \sum_k e^{-ikld} \varphi_{jk}(x)\,, \tag{4.23}$$

where the quasi-momenta k belong to the first Brillouin zone and $N_w = L/d$ is the number of wells. Calculating the coefficients $f_{j,l}(x)$ for x varying across the whole length of the system, allows the construction of the so called Wannier functions $f_{j,l}(x)$. In contrast to the Bloch functions, the Wannier functions do not depend on quasi-momentum, but are instead labeled by the band index j and the site index l where they are centered. They are orthonormal

$$\int_{-L/2}^{L/2} dx\; f^*_{j,l}(x) f_{j',l'}(x) = \delta_{j,j'}\delta_{l,l'} \tag{4.24}$$

and form a complete set. Eq.(4.22) the expansion of the Bloch function φ_{jk} in the Wannier basis with coefficients e^{ikld}.

An important property of the Wannier functions consists in the fact that they can be obtained from each other by a simple displacement

$$f_{l,j}(x) = f_j(x - ld)\,, \tag{4.25}$$

where here and in the following f_j denotes the Wannier function with $l = 0$. As a consequence of (4.25), a single function f_j suffices in characterizing band j, since all other Wannier functions are obtained by simply displacing f_j by ld.

Wannier functions are a useful basis because they tend to be localized in the vicinity of the site l by which they are labelled. This makes them especially suited for describing a particle in a potential with deep wells where the tunneling probability is small. When the tunneling probability becomes zero, the Wannier functions coincide with the wavefunction of particles confined in single wells. In the particular case of an electron in a crystal, the respective solutions are given by the atomic orbitals. Yet, Wannier functions are well defined at arbitrary depth and might spread out over several wells, their orthogonality being ensured by oscillating tails.

An interesting connection can be found between the spatial extent of the Wannier functions and the form of the respective energy band: The matrix elements of the Hamiltonian in the Wannier basis read

$$\begin{aligned} \langle f_{l,j}|\hat{H}|f_{l',j'}\rangle &= \int dx\; f^*_j(x - ld) H f_{j'}(x - l'd) \\ &= \delta_{j,j'} \mathcal{E}_j((l' - l)d)\,, \end{aligned} \tag{4.26}$$

where the quantities $\mathcal{E}_j((l'-l)d)$ fulfill the condition

$$\mathcal{E}_j(ld) = \mathcal{E}_j(-ld)\,, \tag{4.27}$$

as a consequence of Eq.(4.12). Note that the matrix elements involving Wannier functions of different bands are zero. The matrix elements $\mathcal{E}_j((l'-l)d)$ have a straight forward meaning: They are the coefficients of the Fourier expansion of the energy band $\varepsilon_j(k)$

$$\varepsilon_j(k) = \sum_l e^{ikld}\mathcal{E}_j(ld)\,. \tag{4.28}$$

This is an interesting point: A Fourier analysis of the energy bands allows us to extract the matrix elements $\mathcal{E}_j(ld)$ and hence tells us something about the spatial extent of the Wannier functions. If the Wannier functions extend only over nearest neighbouring sites, the coefficients $\mathcal{E}_j(ld)$ are zero for $|l| > 1$ and hence the band $\varepsilon_j(k)$ has the k-dependence $\cos(kd)$.

In the scope of this thesis, the Wannier basis mainly serves to derive analytic results in the tight binding regime (see next section and applications to Bose-Einstein condensate in sections 6.2 and 7.3).

4.2 Tight binding regime

A particle subject to a strong periodic potential concentrates in the potential wells. The periodic part $\tilde{\varphi}_{jk}$ of the Bloch function (4.3) is strongly modulated and the Wannier functions $f_j(x-ld)$ are highly localized at the sites l. One can say that the particle is tightly bound to the sites created by the potential. For a given depth of the potential, the particle is less localized in higher bands.

Bloch states and Bloch bands

In a sufficiently deep potential, the Wannier functions exhibit only nearest-neighbour contact, implying that f_l extends only over the sites l and $l \pm 1$ with its main contributions arising from the site l. Throughout this thesis, we will use the term tight binding to denote such a situation. The range of potential strength for which only nearest-neighbour contact is present will be referred to as the tight binding regime. In this regime, a simple analytical expression can be found for the energy bands which can be understood in terms of the tunneling properties of the system.

In order to find the expression for the energy band $\varepsilon_j(k)$, we note that the matrix elements (4.26) are zero except for $\mathcal{E}_j((l'-l)d)$ with $l'-l = 0, \pm 1$. Hence, the Fourier expansion (4.28) of the energy band takes the form

$$\varepsilon(k) = \mathcal{E}_j(0) - \delta_j \cos(kd)\,, \tag{4.29}$$

where we have introduced the tunneling parameter $\delta_j := -2\mathcal{E}_j(d)$

$$\delta_j \;=\; -2\int dx\, f_j^*(x)\left(-\frac{\hbar^2}{2m}\frac{\partial^2}{\partial x^2} + V(x)\right) f_j(x-d)\,, \tag{4.30}$$

describing the capability of a particle to tunnel through the barriers of the potential. As the potential is made deeper, the smaller becomes the tunneling parameter δ_j and hence the flatter becomes the band (4.29).

For exactly zero tunneling ($\delta_j = 0$), i.e. when the Wannier function does not extend over neighbouring wells, all Bloch states of a band are degenerate and the Wannier functions are also eigenstates of the Schrödinger equation. In the case of an electron in a crystal, they coincide with the atomic orbitals in this limit.

When tunneling is possible, the degeneracy between the Bloch states is lifted and the particle can gain energy δ_j by spreading over the wells of the potential. This is analogous to the case of a particle in a double-well: When tunneling contact is established the two, initially degenerate, energy levels split by 2δ. The new groundstate corresponds to the symmetric combination of the single-well solutions and its energy is lowered by δ.

The value of δ_j can be calculated using the semi-classical form of the single-well wavefunction in the region of the barrier (see [99], §50). The exponential decay of the semi-classical wavefunction as a function of the height of the potential barrier gives rise to an exponential decay of δ_j in s (see also section 4.2 below).

Group velocity, current and effective mass

The knowledge of the form of the energy band (4.29) considered in the tight binding regime, immediately permits to write down explicit expressions for the group velocity (4.15), the current density (4.17) and the effective mass (4.18).

The group velocity (4.15) takes the simple form

$$\bar{v}_j(k) = \frac{d\delta_j}{\hbar} \sin(kd)\,, \tag{4.31}$$

and correspondingly, the current density reads

$$I_j(k) = \frac{d\delta_j}{\hbar L} \sin(kd)\,. \tag{4.32}$$

The two quantities (4.31) and (4.32) are proportional to the tunneling parameter δ_j. Hence they decrease in the same manner as δ_j when the potential depth is increased.

The effective mass (4.18) turns out to be inversely proportional to the tunneling parameter of the lowest band

$$\frac{1}{m^*} = \frac{d^2\delta}{\hbar^2}\,. \tag{4.33}$$

Thus, the exponential increase of m^* as a function of s in an optical lattice (see Fig.4.6) reflects the exponential decrease of the tunneling parameter.

The generalized k-dependent effective mass (4.21) takes the form

$$\frac{1}{m_j^*} = \frac{d^2\delta_j}{\hbar^2} \cos(kd)\,. \tag{4.34}$$

In Figs. 4.5 and 4.7 we compare the tight binding expressions for the lowest energy band and the associated group velocity with the respective numerical solution in the case of an optical lattice. To evaluate the tight binding expressions we use the tunneling parameter (4.33) obtained from the numerical results for m^*. For this reason the curvature of the tight binding and the numerical result match automatically.

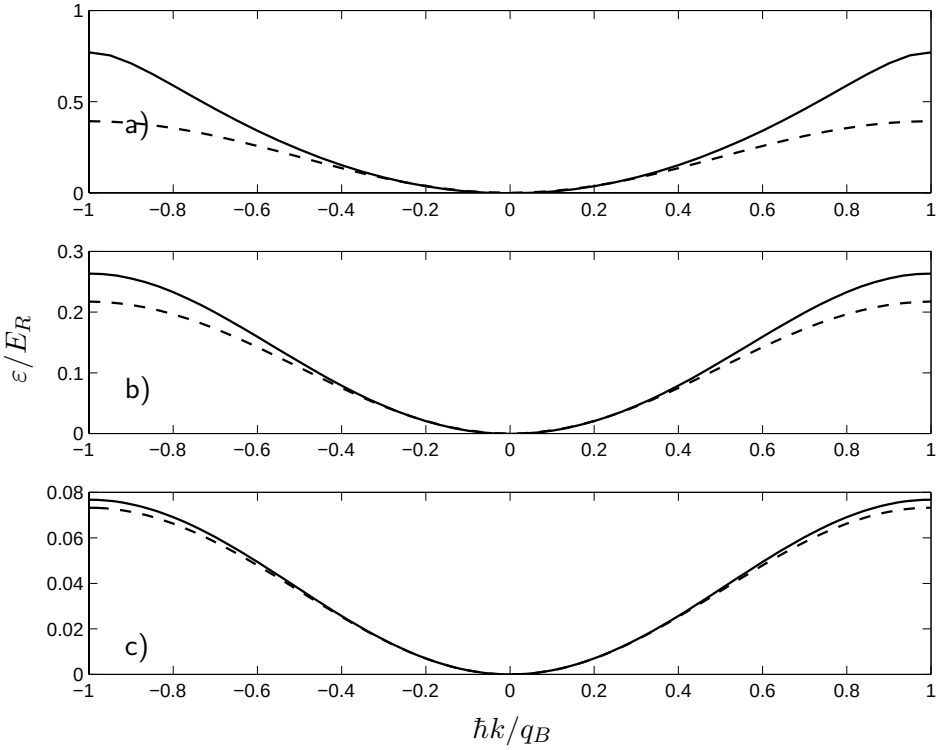

Figure 4.7: Comparison of the tight binding expression (4.29) for the lowest energy band of a single particle (dashed lines) with the respective numerical solution (solid lines) in the case of an optical lattice for a) $s = 1$, b) $s = 5$ and c) $s = 10$.

Tunneling parameter of the 1D Mathieu problem

The tunneling parameter (4.30) plays a crucial role in the tight binding regime and it is hence desirable to know its dependence on the experimental parameters of the problem. This depends, of course, on the particular form of the periodic potential. In the case of an optical lattice $V = sE_R \sin^2(\pi x/d)$, the potential depth sE_R is proportional to the intensity of the lasers and thus can be tuned freely.

The problem of a particle in a periodic potential of the form $V = V_0 \sin^2(\pi x/d)$ is known as the 1D Mathieu problem. Analytic solutions for the respective Wannier functions were investigated in [100]. An approximate analytic expression can be derived for the tunneling

parameter (4.30) (see for example [101]). The result reads

$$\delta_j = E_R \frac{1}{2} (-1)^j \left(\frac{2}{\pi}\right)^{1/2} \left(\frac{s}{4}\right)^{(j-1)/2+3/4} \left(\frac{2^{4(j-1)+5}}{(j-1)!}\right) e^{-2\sqrt{s}}, \tag{4.35}$$

where $j = 1, 2, ...$ is the index of the band for which the tight binding regime is considered. In order for expression (4.35) to be valid, the considered energy band must be a slowly varying function of the quasi-momentum. Hence, the potential depth s must be sufficiently large.

Fig. 4.8 depicts (4.35) as a function of potential depth for the bands $j = 1, 2$. The tunneling parameter $\delta_{j=1}$ of the lowest band is much smaller than $\delta_{j=2}$. This reflects the fact that the Wannier functions of the lowest band concentrate at one site more easily than those of higher bands.

In Fig.4.9 we also plot the ratio between the approximative δ (4.35) for $j = 1$ and the exact δ as obtained from Eq.(4.33) using the numerical data for m^*. We find that for $s > 30$ (4.35) differs from the numeric result by less than 10%.

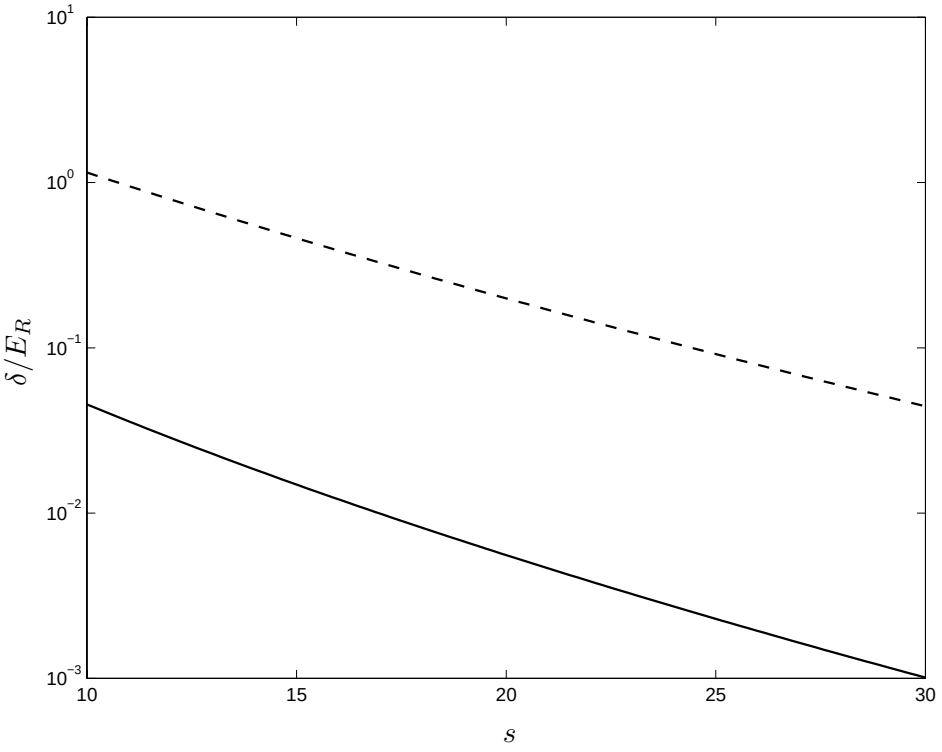

Figure 4.8: Tunneling parameter (4.35) of the 1D Mathieu problem as a function of potential depth for the bands $j = 1$ (solid line) and $j = 2$ (dashed line).

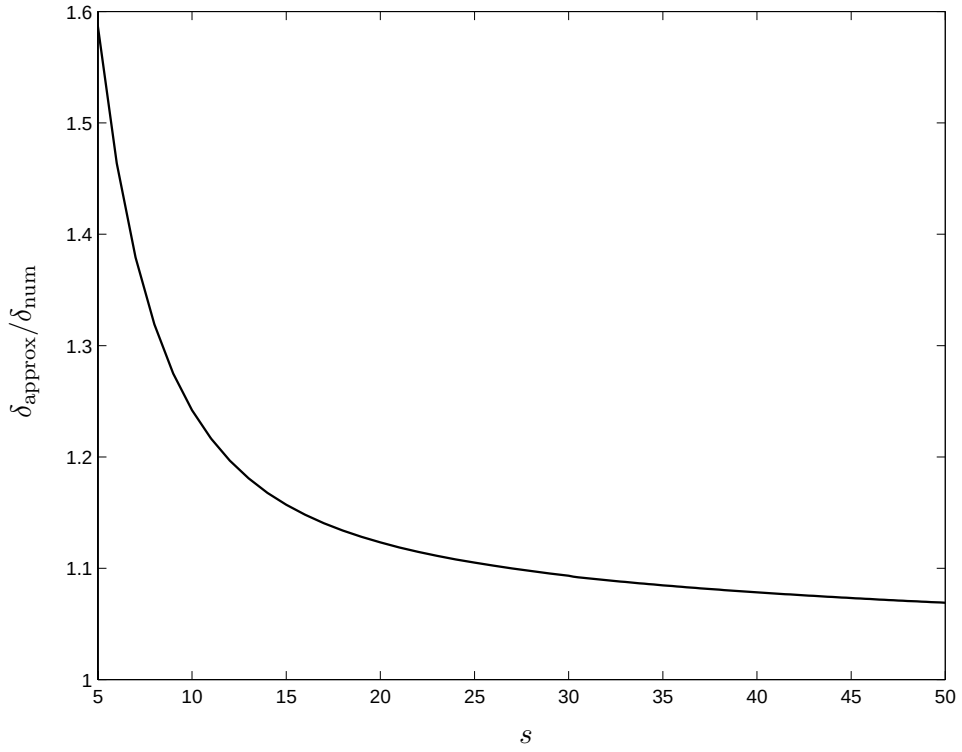

Figure 4.9: Ratio between the approximative δ (4.35) for $j = 1$ and the exact δ as obtained from Eq.(4.33) using the numerical data for m^* in the case of the lattice potential $V = sE_R\sin^2(\pi x/d)$.

Chapter 5

Groundstate of a BEC in an optical lattice

We explore the groundstate of a condensate confined in a one-dimensional optical lattice within GP-theory.

First, we consider a system which is uniform in the transverse direction (section 5.1,5.2 and 5.3). In this case, there are two tunable parameters: the lattice depth sE_R and the interaction parameter gn where n is the average density. In the lattice direction the density profile is strongly modulated by the periodic potential reflecting the concentration of the atoms at the bottom of the potential wells. Energy and chemical potential are significantly increased with respect to the uniform case, while the combined presence of lattice and repulsive interactions between atoms leads to a decrease in the compressibility. The inverse compressibility has a nonlinear dependence on average density since interactions counteract the compression of the atoms by the external potential. In a deep lattice however, the equation of state of the system takes the same linear dependence on density as in the uniform case and is charcterized by an effective coupling constant $\tilde{g}$ which grows as a function of lattice depth.

The presence of repulsive interactions produces a screening effect since the particles resist more to being squeezed in the potential wells than in the absence of interaction. We find that increasing the interaction parameter gn corresponds to an effective decrease of the lattice depth s.

In a second step, we allow for the additional presence of radial and axial harmonic trapping (section 5.4). We use the results obtained for the purely periodic potential as an input to calculate the groundstate properties in the combined trap. The scheme we develop adequately describes current experimental settings in which the optical potential is superimposed to a harmonically trapped TF-condensate leading to a distribution of atoms over many lattice sites. We derive simple analytic expressions for the chemical potential and the density profile averaged over each lattice period by using the effective coupling constant description. These expressions allow us to explicitly calculate the occupation of each site and the radius of the cloud. We discuss the dependence on lattice depth of the chemical potential, the condensate size and the density at the center of the harmonic trap averaged over one lattice period.

Our results for the groundstate energy, chemical potential, compressibility and regarding

the effects of harmonic trapping have been presented in [102]. In this thesis, also results for the density profile are included and the dependence on lattice depth of the density at the center of the harmonic trap averaged over one lattice period is described. We briefly comment on the generalization to 2D lattices. Based on an ansatz for the order parameter valid in deep lattices, the effective coupling constant $\tilde{g}$ and its effect on the harmonically trapped system have been previously discussed in [70].

5.1 Density profile, energy and chemical potential

When looking for stationary solutions, the GP-equation (3.14) takes the form

$$\left(-\frac{\hbar^2}{2m}\frac{\partial^2}{\partial z^2} + sE_R \sin^2\left(\frac{\pi z}{d}\right) + g\left|\Psi(z)\right|^2\right)\Psi(z) = \mu\Psi(z)\,. \tag{5.1}$$

The groundstate is given by the solution of this equation with the lowest energy.

Let us rewrite Eq.(5.1) in a more convenient form. First, we introduce the rescaled order parameter

$$\varphi(z) = \sqrt{\frac{L^2}{N}}\Psi(z)\,, \tag{5.2}$$

with L the transverse size of the system and N the number of particles per lattice site such that

$$\int_{-d/2}^{d/2} dx\,|\varphi(z)|^2 = 1\,. \tag{5.3}$$

The GPE (5.1) then reads

$$\left(-\frac{\hbar^2}{2m}\frac{\partial^2}{\partial z^2} + sE_R \sin^2\left(\frac{\pi z}{d}\right) + d\,gn\left|\varphi(z)\right|^2\right)\varphi(z) = \mu\varphi(z)\,, \tag{5.4}$$

where we have introduced the average density

$$n = \frac{N}{dL^2}\,. \tag{5.5}$$

Casting Eq. (5.4) in dimensionless form, in dimensionless form it is possible to identify the governing parameters of the problem. We shall measure length in units of d/π, momentum in units of the Bragg-momentum $q_B = \hbar\pi/d$ and energy in units of the recoil energy $E_R = \hbar^2\pi^2/2md^2$. In this way, we obtain the dimensionless GPE

$$\left(-\frac{\partial^2}{\partial z^2} + s\sin^2(z) + \pi\frac{gn}{E_R}\left|\varphi(z)\right|^2\right)\varphi(z) = \frac{\mu}{E_R}\varphi(z)\,. \tag{5.6}$$

In contrast to the case of a single particle discussed in chapter 4, there are now two governing parameters: the lattice depth s and the interaction parameter gn/E_R. The latter quantity can be changed by varying the average density or the scattering length by means of a Feshbach resonance.

Typical values of gn/E_R in current experiments can be estimated by taking the density at the center of the harmonic trap in absence of the lattice and evaluating $E_R = \hbar^2\pi^2/2md^2$ for the lattice period d used in the respective experiment. In this way, one finds values ranging from $gn = 0.02E_R$ to $gn = 1.1E_R$ in the experiments [79, 73, 71, 87, 66].

For each choice of parameter s and gn/E_R, we obtain a different groundstate wave function $\varphi(z)$ and chemical potential

$$\mu = \int_{-d/2}^{d/2} \varphi^*(z) \left(-\frac{\hbar^2}{2m}\frac{\partial^2}{\partial z^2} + sE_R \sin^2\left(\frac{\pi z}{d}\right) + gnd|\varphi(z)|^2 \right) \varphi(z) dz \tag{5.7}$$

and groundstate energy per particle

$$\varepsilon = \int_{-d/2}^{d/2} \varphi^*(z) \left(-\frac{\hbar^2}{2m}\frac{\partial^2}{\partial z^2} + sE_R \sin^2\left(\frac{\pi z}{d}\right) + \frac{gnd}{2}|\varphi(z)|^2 \right) \varphi(z) dz\,. \tag{5.8}$$

Calculating these quantities for different choices of s and gn/E_R allows us to elucidate the role played by mean field interaction: Under what conditions does it play an important role ? How does it alter the effects produced by the lattice?

Let us first discuss some solutions for the groundstate wavefunction $\varphi(z)$ or, equivalently, the density $nd\,|\varphi(z)|^2$. In Fig. 5.1, we report the results obtained at different values of lattice depth and interaction parameter. When s is increased for fixed gn/E_R, the density becomes more and more modulated by the optical potential. Instead, when s is kept fixed while gn/E_R is increased, the modulation of the density is reduced. Repulsive interactions screen off the lattice as mentioned above. In fact, at low lattice depth explicit formulas for the effective potential can be derived [103] and are found to be in agreement with experimental results [67].

Let us now proceed to the results obtained for the chemical potential and the energy per particle. In Fig. 5.2, we report the results obtained as a function of lattice depth s for different values of the interaction parameter gn/E_R.

Chemical potential and energy per particle coincide only in the absence of interactions. In general, they are linked by the relation

$$\mu = \frac{\partial\,(n\varepsilon)}{\partial n} = \varepsilon + gn\frac{\partial\varepsilon}{\partial\,(gn)}\,. \tag{5.9}$$

The second term is necessarily positive for repulsive interactions and hence the chemical potential is always larger than the energy per particle (see Fig.5.2).

When plotting the relative difference $(\mu-\varepsilon)/\varepsilon$ as a function of gn at fixed high s, we observe that the curve is proportional to gn for sufficiently small gn (see Fig.5.3). The deviation from the linear behavior (see dotted line) for larger gn is due to the density dependence of φ. For gn small enough, the derivative $\partial\varepsilon/\partial\,(gn)$ is essentially given by its $gn = 0$-limit

$$\frac{\partial\varepsilon}{\partial\,(gn)} \approx \frac{d}{2}\int_{-d/2}^{d/2} |\varphi_{gn=0}(z)|^4 dz\,, \tag{5.10}$$

where $\varphi_{gn=0}(z)$ is the groundstate solution in absence of interactions ($gn = 0$). In the next section, we will show that the quantity (5.10) is closely related to the compressibility of the system.

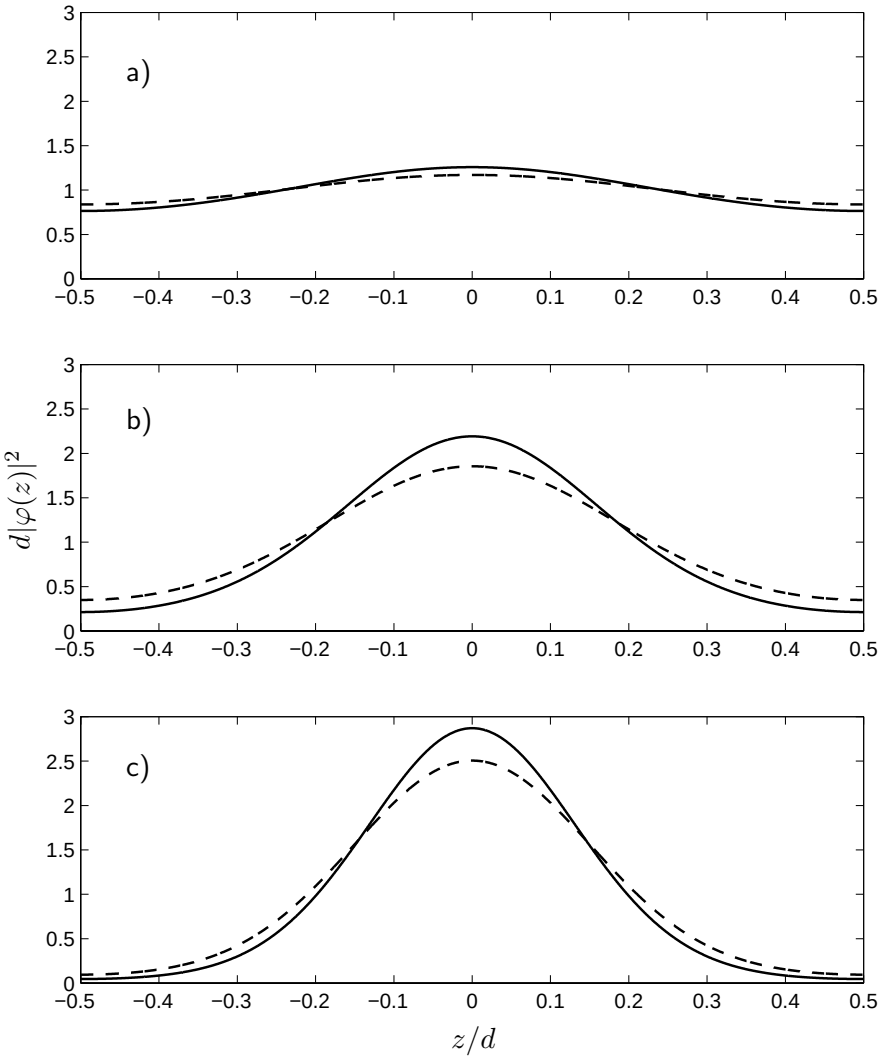

Figure 5.1: Groundstate density $d|\varphi(z)|^2$ as obtained from (5.4) at a) $s = 1$, b) $s = 5$ and c) $s = 10$ with $gn = 0$ (solid line) and $gn = 1E_R$ (dashed line).

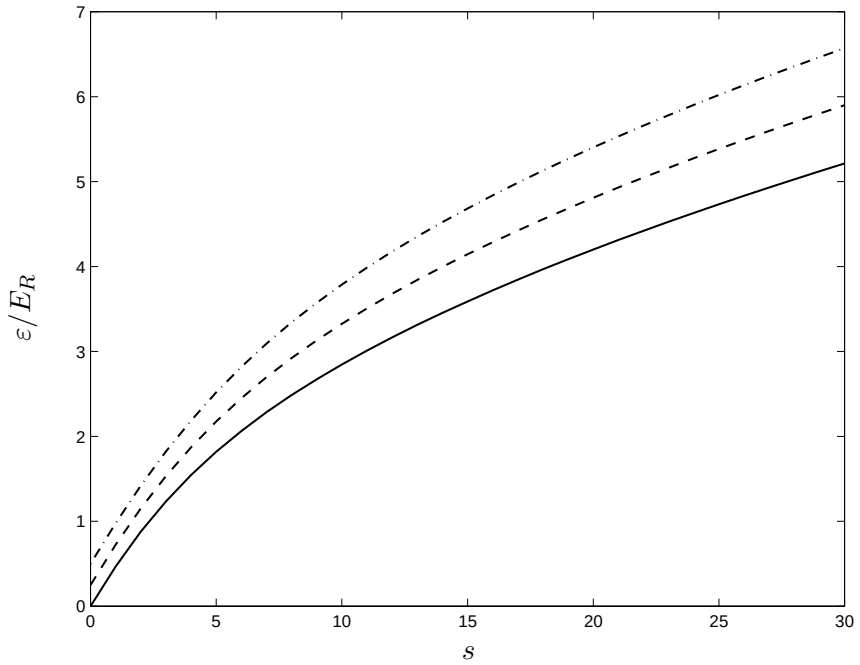

Figure 5.2: Results obtained for the chemical potential (5.7) (dash-dotted line) and the energy per particle (5.8) (dashed line) as a function of lattice depth s for $gn/E_R = 0.5$. The solid line is the single particle energy ($gn/E_R = 0$).

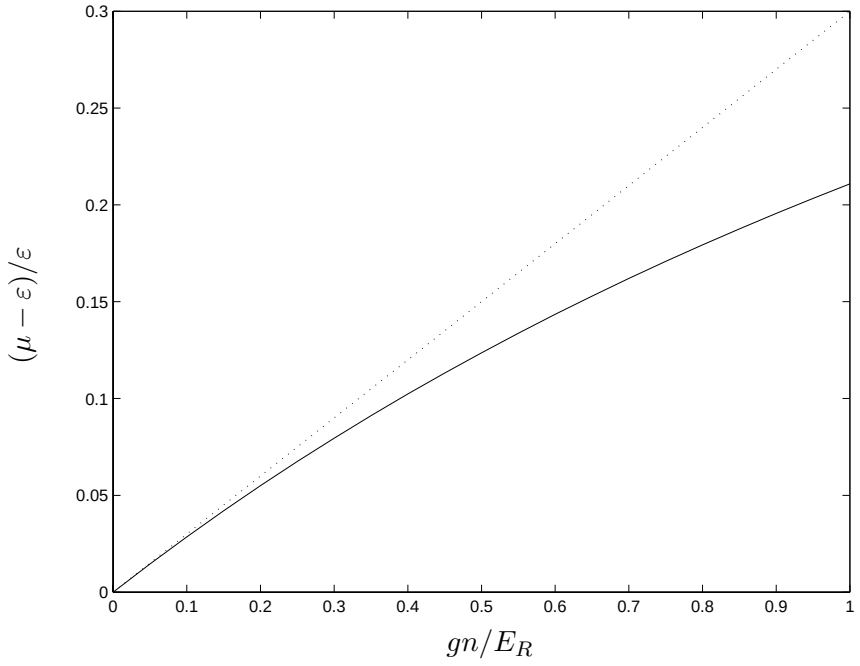

Figure 5.3: Relative difference $(\mu - \varepsilon)/\varepsilon$ as a function of gn/E_R at $s = 20$ (solid line). The dotted line extrapolates the linear behavior at small gn.

5.2 Compressibility and effective coupling constant

From the solutions $\mu(s, gn)$ for the chemical potential, the compressibility κ of the system can be immediately calculated using the relation

$$\kappa^{-1} = n\frac{\partial \mu}{\partial n} \tag{5.11}$$

It is useful to evaluate this quantity in order to understand better the combined effects of lattice and interactions. In particular, analyzing the behavior of the compressibility helps to study in more detail the dependence of the chemical potential on density in a lattice of fixed depth. Knowing the form of this density-dependence is crucial to determine for example the frequencies of collective oscillations, the density profile and the chemical potential obtained when adding a harmonic trap to the optical lattice (see sections 5.4 and 9). In the uniform system, the chemical potential is simply linear in the density $\mu = gn$ leading to an increase of the inverse compressibility that is proportional to the density $\kappa^{-1} = gn$. In the presence of the lattice, we expect deviations from this behaviour due to the localization of the particles near the bottom of the well centers.

In Fig.5.4, the inverse compressibility κ^{-1} is plotted as a function of gn for different potential depths s. As a general rule, the condensate becomes more rigid as gn/E_R or s is increased. Yet, in contrast to the uniform case, the monotonic growth of κ^{-1} is linear only at small densities. At larger values of gn/E_R, the slope of the curve tends to decrease and develop a non-linear functional dependence.

At small values of gn where the inverse compressibility is approximately linear in gn, let us denote the proportionality constant by $\tilde{g}$ such that

$$\kappa^{-1} = \tilde{g}(s)n\,. \tag{5.12}$$

corresponding to the chemical potential

$$\mu = \mu_{gn=0} + \tilde{g}(s)n\,, \tag{5.13}$$

where $\mu_{gn=0}$ depends on the lattice depth, but not on density. Since the condensate is more rigid in the lattice relative to the uniform case, we have $\tilde{g} > g$. Actually, $\tilde{g}$ is a monotonically increasing function of s (see increase of the slopes at $gn = 0$ for increasing s in Fig. 5.4).

The quantity $\tilde{g}$ can be considered as an effective coupling constant: In a situation in which Eq.(5.12) is valid, the compressibility of the condensate in the lattice with coupling constant g is the same as the compressibility of a uniform condensate with coupling constant $\tilde{g}$. So, as far as the compressibility is concerned we can deal with the problem as if there was no lattice by simply replacing $g \to \tilde{g}$. Below, we will see that this is a useful approach when describing macroscopic properties, both static (see section 5.4) and dynamic (see section 9), which do not require a detailed knowledge of the behavior on length scales of the order of the lattice spacing d. In fact, the properties of the compressibility discussed in this section will prove useful in devising a hydrodynamic formalism for condensates in a lattice.

The concept of an effective coupling constant $\tilde{g}$ is applicable when the influence of 2-body interaction on the wavefunction $\varphi(z)$ is negligible in the calculation of the chemical potential (5.7). Provided this condition is fulfilled, we obtain using Eq.(5.7)

$$\kappa^{-1} = n\frac{\partial \mu}{\partial n} = gnd\int_{-d/2}^{d/2} |\varphi_{gn=0}(z)|^4 dz\,, \tag{5.14}$$

where $\varphi_{gn=0}(z)$ is the groundstate solution in absence of interactions ($gn = 0$). Comparison with Eq.(5.12) yields

$$\boxed{\tilde{g} = gd \int_{-d/2}^{d/2} |\varphi_{gn=0}(z)|^4 dz\,.} \tag{5.15}$$

This explicit formula makes again visible that the decrease of the compressibility described by $\tilde{g}$ is due to the concentration of the particles close to the well centers.

In Fig.5.5 we compare the exact results for κ^{-1} with the approximate formula (5.12) as a function of s for different values of gn/E_R. This plot allows to determine how deep the lattice has to be made for a given value of gn/E_R in order to be able to use the effective coupling constant description. Given, for example, $gn = 0.5E_R$ we find that at $s = 10$ and $s = 20$ the expression (5.12) is valid within $\approx 10\%$ and $\approx 7\%$ respectively. A larger value of gn requires larger values of s to achieve the same accuracy.

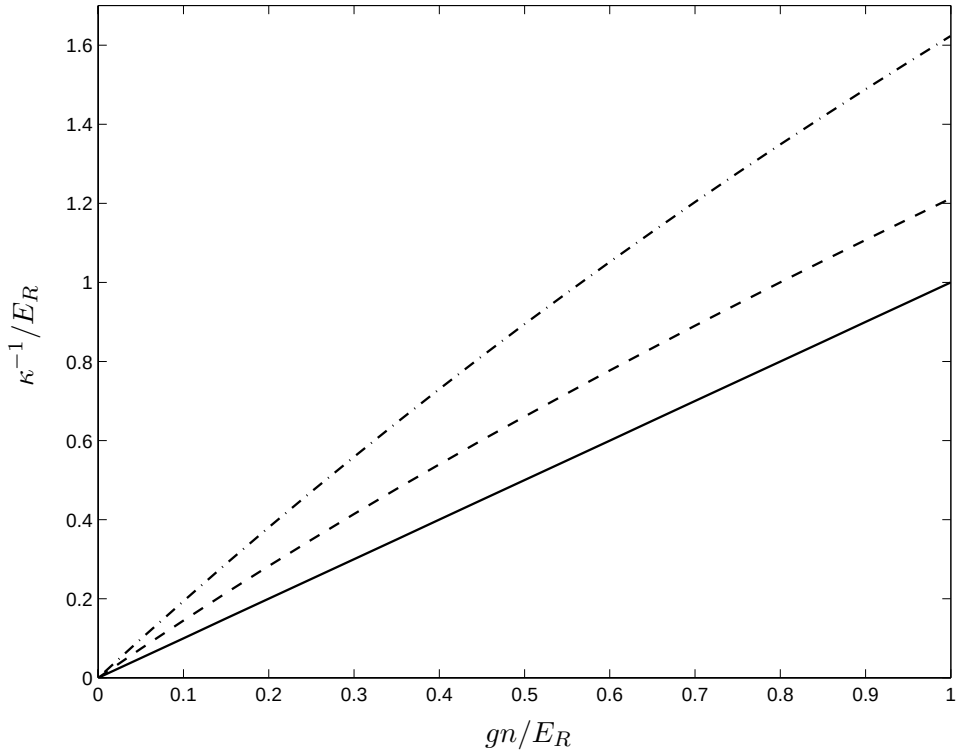

Figure 5.4: The inverse compressibility (5.11) as a function of gn/E_R for $s = 0$ (solid line), $s = 5$ (dashed line) and $s = 10$ (dash-dotted line).

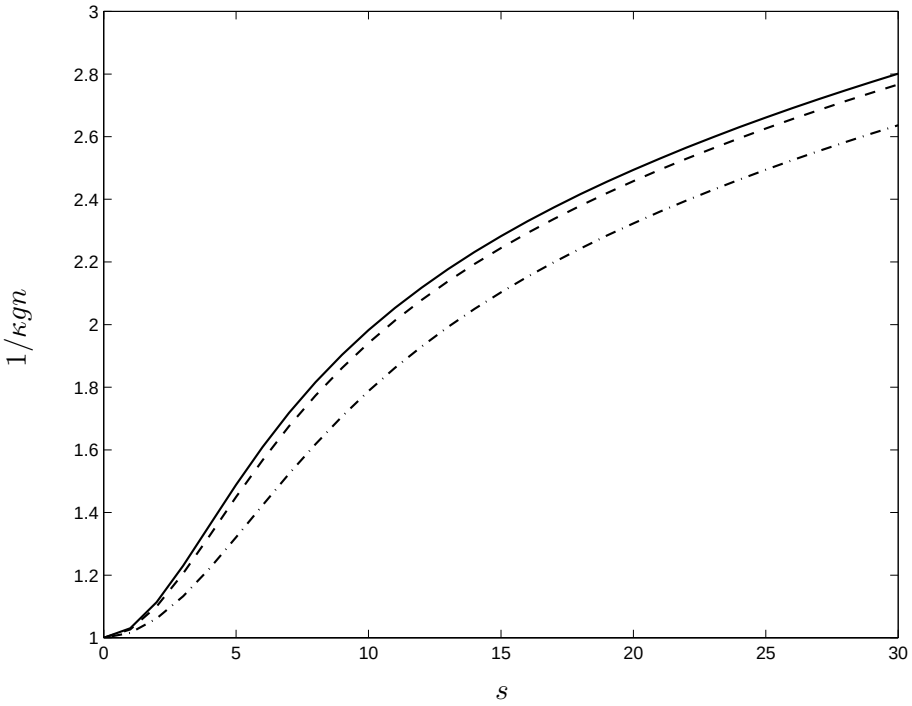

Figure 5.5: Comparison of κ^{-1}/gn as obtained from Eq.(5.11) for $gn = 0.1E_R$ (dashed line) and $gn = 0.5E_R$ (dash-dotted line) with the approximate formula (5.12) (solid line) evaluated using (5.15) as a function of s.

5.3 Momentum distribution

Since the groundstate solution of the GPE (5.4) is periodic with period d, it can be expanded in the Fourier series

$$\varphi(z) = \sum_l a_l \, e^{il2\pi z/d} \,, \tag{5.16}$$

showing that the contributing momenta are multiples of $2q_B$ just as for a single particle in a periodic potential (see discussion section 4.1). The values of the coefficients a_l involve interaction effects: The contribution of momenta with $l \neq 0$ is slightly reduced in the presence of repulsive interactions, due to the screening effect on the lattice.

The fact that the momentum distribution in the direction of the lattice is characterized by several momentum components is an interesting difference with respect to the uniform system where the presence of a BEC is associated with a single peak in the momentum distribution. This feature governs the expansion of atoms released from an optical lattice: During the time of flight the different momentum components are separated spatially resulting in a density distribution featuring several peaks (see Fig. 5.6). Due to the large kinetic energy contained in (5.8) the role of interactions can be neglected after the potential has been switched off, in contrast to a situation without lattice where the expansion is governed by mean-field effects. This issue has been discussed in [70] with regard to both theory and experiment.

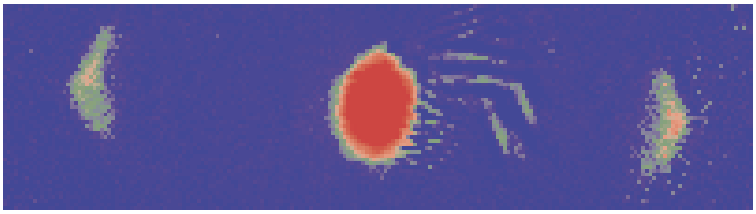

Figure 5.6: Density distribution after a time of free flight in the experiment [70]: Separation of momentum components $p = 0$ (central peak) and $p \pm 2q_B$ (lateral peaks). Figure taken from [70].

5.4 Effects of harmonic trapping

The results obtained in the previous section can be used to describe the groundstate of a condensate in the combined potential of optical lattice and harmonic trap

$$V = sE_R \sin^2\left(\frac{\pi z}{d}\right) + \frac{m}{2}\left(\omega_z^2 z^2 + \omega_\perp^2 r_\perp^2\right), \tag{5.17}$$

where we have assumed radial symmetry of the harmonic trap $\omega_\perp = \omega_x = \omega_y$ in order to simplify notation. The generalization of the results to anisotropic traps is immediate. For convenience, we will denote the lattice site at the trap center by $l = 0$. The combined potential (5.17) is depicted in Fig.5.7.

In the presence of the potential (5.17), the GPE for the groundstate takes the form

$$\left(-\frac{\hbar^2}{2m}\frac{\partial^2}{\partial z^2} + sE_R \sin^2\left(\frac{\pi z}{d}\right) + \frac{m}{2}\left(\omega_z^2 z^2 + \omega_\perp^2 r_\perp^2\right) + g\left|\Psi(r_\perp, z)\right|^2\right)\Psi(r_\perp, z) = \mu\Psi(r_\perp, z)\,. \tag{5.18}$$

The groundstate density profile

$$n(r_\perp, z) = \left|\Psi(r_\perp, z)\right|^2 \tag{5.19}$$

varies rapidly on the length-scale d in the z-direction as discussed in the previous section. Yet, due to the harmonic trap an additional length scale can come into play: If the axial size of the condensate Z is much larger than the lattice period d, then the density profile (5.19) varies on the scales d and Z. Provided the condensate is well described by the TF-approximation in the absence of the lattice, then we have

$$d << Z\,, \tag{5.20}$$

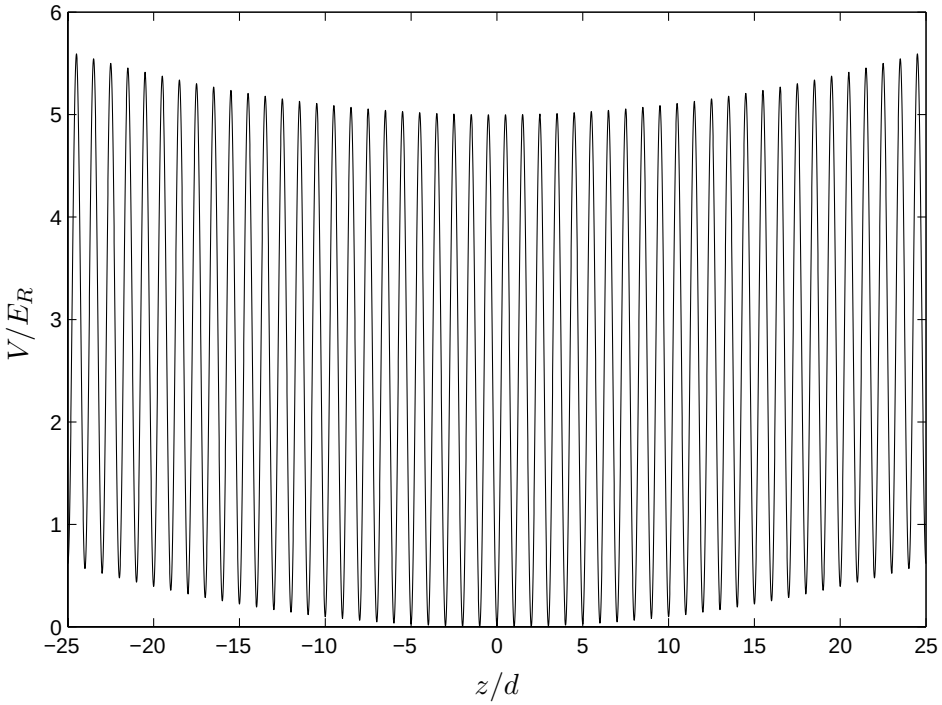

Figure 5.7: The z-dependence of the combined potential of optical lattice and harmonic trap (5.17) with a lattice depth of $s = 5$ and $\hbar\omega_z = 0.02E_R$.

and the variation on the scale Z is slow. Situation (5.20) is typical of current experiments. It implies that many sites of the lattice are occupied and that the site occupation numbers vary slowly as a function of the site index. For example, in the experiment [70] atoms are loaded into ~ 200 sites.

Local Density Approximation

Given (5.20), one can generalize the local density approximation (LDA) to describe harmonically trapped condensates in a lattice. This procedure avoids the solution of the full problem (5.18).

Let us consider the average density at site l

$$n_l(r_\perp) = \frac{1}{d}\int_{ld-d/2}^{ld+d/2} n(r_\perp, z)\, dz \ , \tag{5.21}$$

where $n(r_\perp, z) = |\Psi(r_\perp, z)|^2$ is the density obtained by solving the GP-equation (5.18). With l replacing the continous variable z, expression (5.21) defines an average density profile of the condensate in the trap. It is a smooth function of $r_\perp$ and varies slowly as a function of the index l since many sites are occupied as a consequence of condition (5.20). Basically, the idea is now to apply a LDA to the average profile $n_l(r_\perp)$.

Within this generalized LDA, the chemical potential at site l is given by

$$\mu_l = \mu_{\rm opt}(n_l(r_\perp)) + \frac{m}{2}(\omega_z^2 l^2 d^2 + \omega_\perp^2 r_\perp^2)\,, \tag{5.22}$$

where $\mu_{\rm opt}(n_l(r_\perp))$ is the chemical potential calculated at the average density $n_l(r_\perp)$ in the presence of the optical lattice potential only. The effect of axial trapping is accounted for by the term $m\omega_z^2 l^2 d^2/2$ since the harmonic potential varies slowly on the scale d. Eq.(5.22) fixes the radial density profile $n_l(r_\perp)$ at the l-th site once the value of μ_l or, equivalently, the number of atoms at well l

$$N_l = 2\pi d \int_0^{R_l} r_\perp dr_\perp n_l(r_\perp)\,, \tag{5.23}$$

is known. In Eq.(5.23), R_l is the radial size of the condensate at the l-th site, which is fixed by the value of $r_\perp$ where the density $n_l(r_\perp)$ vanishes.

When equilibrium is established across the whole sample we have $\mu_l = \mu$ for all l. Making use of this fact and employing that $\sum_l N_l = N_{\rm tot}$, we can find the dependence of μ on the total number of particles $N_{\rm tot}$. This procedure also yields the single well occupation numbers N_l and the number of sites occupied in the groundstate.

In the simple case in which the chemical potential without harmonic trap exhibits the linear dependence on density $\mu_{\rm opt} = \mu_{gn=0} + \tilde{g}(s)n$ (see Eq.(5.13)), one obtains for the radial density profile

$$n_l(r_\perp) = \frac{1}{\tilde{g}}\left(\mu - \mu_{gn=0} - \frac{m}{2}\omega_z^2 l^2 d^2 - \frac{m}{2}\omega_\perp^2 r_\perp^2\right)\,. \tag{5.24}$$

The well occupation numbers and transverse radii are given by

$$N_l \;=\; N_0\left(1 - \frac{l^2}{l_m^2}\right)^2\,, \tag{5.25}$$

$$R_l \;=\; R_0\left(1 - \frac{l^2}{l_m^2}\right)^{1/2}\,, \tag{5.26}$$

where

$$\boxed{l_m = \sqrt{\frac{2(\mu - \mu_{gn=0})}{m\omega_z^2 d^2}}} \tag{5.27}$$

is the outer most occupied site and fixes the total number $2l_m + 1$ of occupied sites, and

$$\boxed{R_0 = \sqrt{\frac{2(\mu - \mu_{gn=0})}{m\omega_\perp^2}}} \tag{5.28}$$

is the radial size at the trap center. To obtain an explicit expression for the chemical potential μ and the occupation N_0 of the central site, we apply the continuum approximation $\sum_l \to 1/d\int dz$ to the normalization condition $\sum_l N_l = N_{\rm tot}$. This yields

$$\boxed{\mu = \frac{\hbar\bar{\omega}}{2}\left(15 N_{\rm tot}\frac{a}{a_{ho}}\,\frac{\tilde{g}}{g}\right)^{2/5} + \mu_{gn=0}} \tag{5.29}$$

and

$$N_0 = \frac{15}{16}\frac{N_{\rm tot}}{l_m}\,, \tag{5.30}$$

with $\bar{\omega} = (\omega_x\omega_\perp^2)^{1/3}$, $a_{ho} = \sqrt{\hbar/m\bar{\omega}}$. The profile (5.24) has the usual parabolic TF-form. The presence of the lattice is accounted for by the dependence of the effective coupling constant $\tilde{g}$ on s.

The increase of $\mu - \mu_{gn=0}$ (see Eq.(5.29)) due to the optical lattice (recall $\tilde{g} > g$) implies an increase of the radii R_l (see Eqs.(5.26) and (5.28)) with respect to the absence of the lattice. It is worth pointing out that the axial size increases in the same manner as the radial size, so that the aspect ratio R/Z is not affected by the optical lattice: The outermost occupied sites l_m, as given by Eq. (5.27), depend on $\mu - \mu_{gn=0}$ in the same way as the radius R_0 at the central well (see Eq.(5.28)). The increase in size of the condensate is illustrated in Fig. 5.8 where we plot the radius R_0 as a function of s. By tuning the lattice depth to $s = 20$, the condensate grows by about 20%. Hence, the effect is not dramatic. In chapter 6.2 we will show that $\tilde{g}/g \sim s^{1/4}$ in a deep lattice, implying that R_0 and Z increase like $\sim s^{1/20}$.

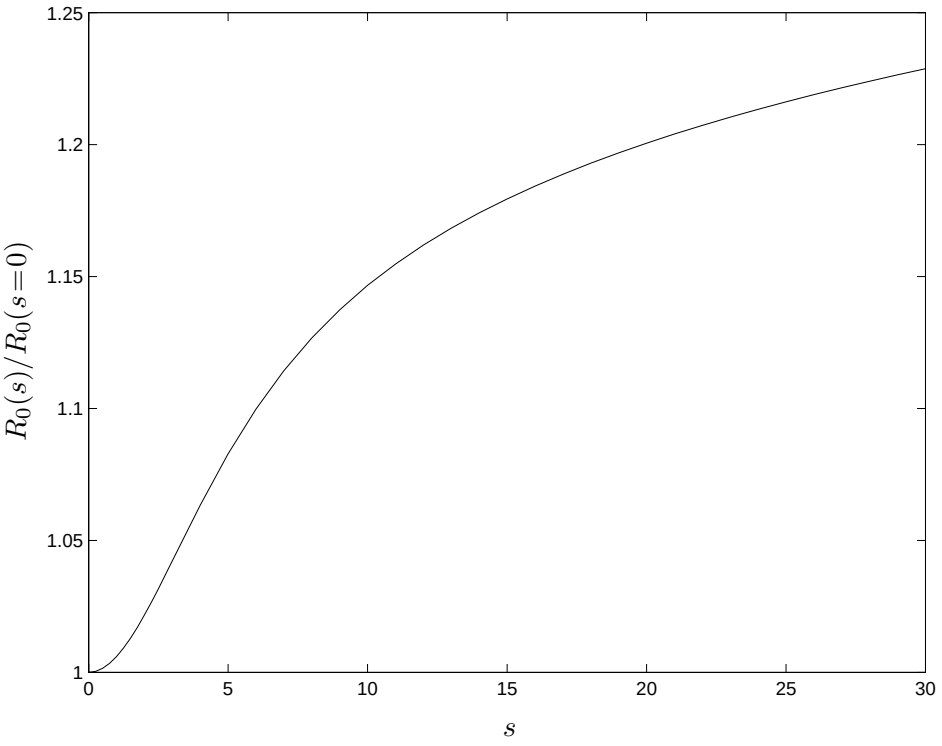

Figure 5.8: The condensate radius R_0 (5.28) divided by $R_0(s = 0)$ as a function of lattice depth s.

As a consequence of the increasing size of the condensate, the average density at the trap center drops as a function of lattice depth: To evaluate to what degree this happens, recall

that the density at the center of a TF-condensate without lattice is given by μ/g, where the chemical potential is given by Eq.(5.29) with $\tilde{g}/g = 1$ and $\mu_{gn=0} = 0$. Hence, at the center of the trap the ratio between the average density with lattice (5.24) and the density without lattice is given by

$$\frac{n_{l=0}(r_\perp = 0; s)}{n(r_\perp = 0, z = 0; s = 0)} = \left(\frac{\tilde{g}}{g}\right)^{-3/5} . \tag{5.31}$$

In Fig.5.9, we display this ratio as a function of lattice depth. Again, the effect is not very dramatic, since the dependence of $\tilde{g}/g$ on s is weak. The estimate $\tilde{g}/g \sim s^{1/4}$ valid in a deep lattice (see chapter 6.2 below) implies that the average density at the trap center drops like $\sim s^{-3/20}$.

The decrease of the *average* density at the trap center (5.31) is to be contrasted with an increase of the non-averaged density (5.19) at $r_\perp = 0, z = 0$ (peak density). This increase arises due to the modulation of the density on the scale d which overcompensates the drop of the average density (5.31). This effect will be evaluated quantitatively in chapter 6.2. It turns out that the peak density grows like $(\tilde{g}/g)^{2/5}$ corresponding to an increase $\sim s^{1/10}$.

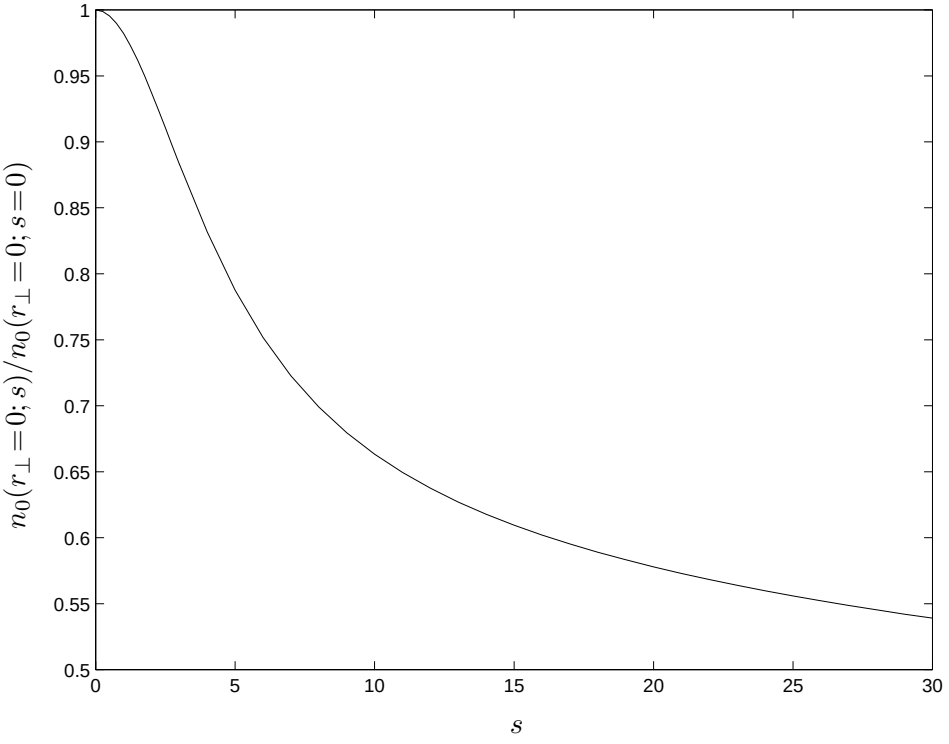

Figure 5.9: The average density at the central site $l = 0$ divided by its value at $s = 0$ as a function of lattice depth (see Eq.(5.31)).

It is interesting to note that the integration (5.23) over the radial profile is crucial to obtain the correct distribution (5.25). In a 1D system with the linear equation of state $\mu_{\rm opt} = \mu_{gn=0} + \tilde{g}(s)n$, one would instead obtain the expression $N_l = N_0\left(1 - l^2/l_m^2\right)$. This difference

is related to the fact that in a 1D system one has $\mu \propto N_l$. In contrast, for a 3D system with radial trapping one obtains $\mu \propto \sqrt{N_l}$ from Eq.(5.23).

As mentioned above, the average density profile $n_l(r_\perp)$ varies slowly as a function of the site index l. We obtain a smooth macroscopic density profile $n_M(r_\perp, z)$ by replacing the discrete index l by the continous variable $z = ld$ This is convenient in devising a hydrodynamic formalism (see section 9): The particular profile (5.24) becomes

$$\boxed{n_M(r_\perp, z) = \frac{1}{\tilde{g}} \left(\mu - \mu_{gn=0} - \frac{m}{2}\omega_z^2 z^2 - \frac{m}{2}\omega_\perp^2 r_\perp^2 \right) ,} \tag{5.32}$$

with μ given by Eq.(5.29). The extension of the condensate along z is given by

$$Z = \sqrt{\frac{2(\mu - \mu_{gn=0})}{m\omega_z^2}} . \tag{5.33}$$

Obviously, the profile (5.32) mimics a TF-profile of a condensate without lattice. This confirms the statement made in section 5.2 that if $\mu_{\rm opt} = \tilde{g}n + \mu_{gn=0}$ the system can be described as if there was no lattice as long as g is replaced by $\tilde{g}$.

Before concluding this section, we would like to emphasize that it is important to do the average (5.21) before applying the LDA. The strong modulation of the wavefunction generated by the lattice contributes a large kinetic energy which would be, mistakenly, discarded within a LDA. The situation is different in a system made up of only very few wells (produced for example by raising a few barriers in a TF-condensate). In this case, the condensate in *each* well might be well described by the TF-approximation (see for example [57]). In the LDA proposed in this section, the large kinetic energy caused by the lattice, is contained in the chemical potential $\mu_{\rm opt}(n_l(r_\perp))$.

The effects described in this section, in particular the dependence of μ (5.29) and R_0 (5.28) on s, have been investigated by [71]. In this experiment, the chemical potential and the radius of the groundstate in the combined potential of harmonic trap and one-dimensional optical lattice is determined from the measurement of the radial size of the cloud after a time of free flight. The results for the chemical potential are depicted in Fig.5.10 together with the theoretical prediction (5.29).

The generalization of the results presented in this section to two-dimensional cubic lattices is straightforward. For a two-dimensional lattice in the x, y-directions, the smoothed macroscopic density profile is given by

$$n_M(r_\perp, z) = \frac{1}{\tilde{g}} \left(\mu - \mu_{gn=0} - \frac{m}{2}\omega_z^2 z^2 - \frac{m}{2}\omega_\perp^2 r_\perp^2 \right) , \tag{5.34}$$

with the effective coupling constant

$$\tilde{g} = g d^2 \int_{-d/2}^{d/2} |\varphi_{gn=0}(x, y)|^4 dx dy , \tag{5.35}$$

and

$$\mu = \frac{\hbar\bar{\omega}}{2} \left(15 N_{\rm tot} \frac{a}{a_{ho}} \frac{\tilde{g}}{g} \right)^{2/5} + \mu_{gn=0} , \tag{5.36}$$

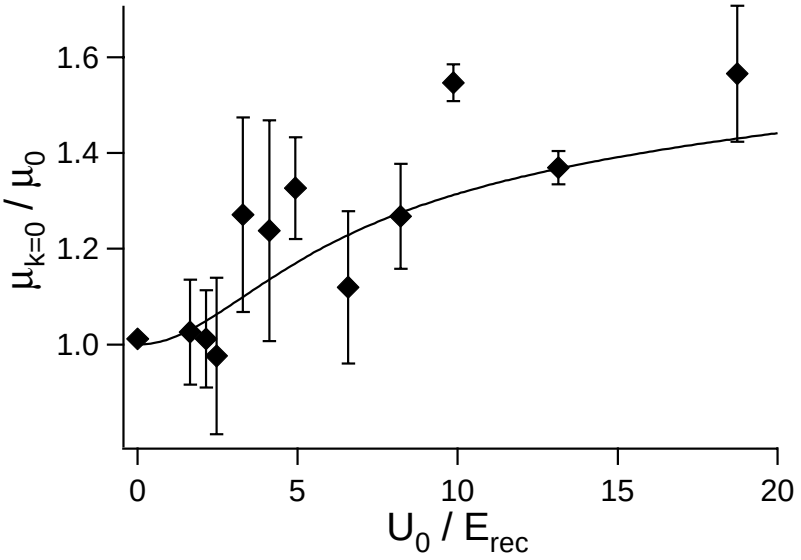

Figure 5.10: The density-dependent contribution to the chemical potential $\mu - \mu_{gn=0}$ of a condensate in the combined potential of harmonic trap and one-dimensional optical lattice divided by its value in the absence of the lattice as a function of lattice depth $U_0 \equiv s$. Experimental data from [71] together with the theoretical prediction (5.29) (solid line). Figure taken from [71].

in complete analogy to the case of a one-dimensional lattice. Yet, note that the 2D effective coupling constant (5.35) increases more strongly with s since the condensate is compressed in two directions.

These predictions have proved useful in the preparation of a one-dimensional Bose gas [88]: They allow to estimate the 1D density in the tubes produced by a two-dimensional lattice which is superimposed to a harmonically trapped condensate. Moreover, the calculation of the chemical potential allows to determine the lattice depth needed to satisfy the condition

$$\mu \ll \hbar\tilde{\omega}_r \,, \tag{5.37}$$

for the one-dimensionality of the gas in the tubes, where $\tilde{\omega}_r$ is the characteristic radial trapping frequency in each tube.

Chapter 6

Stationary states of a BEC in an optical lattice

In this chapter, we extend the discussion of stationary condensates in a one-dimensional lattice to non-groundstate solutions of the GP-equation without harmonic trapping. All such states are characterized by a spatially uniform, time-independent current

$$I = constant \tag{6.1}$$

of atoms through the lattice. In the following, we will be dealing with states in which the current is not generally constrained to the value zero, in contrast to the particular case of the groundstate discussed in the previous section.

We concentrate on states associated with a condensate wavefunction of Bloch form labeled by the band index j and the condensate quasi-momentum $\hbar k$. Such states form the class of solutions associated with a density profile of the same periodicity as the lattice. They are associated with two types of band spectra: the energy per particle Bloch band spectrum and the chemical potential Bloch band spectrum (see section 6.1) which depend on lattice depth sE_R and the interaction parameter gn. The two spectra coincide only in the absence of interactions ($gn = 0$; see discussion of the single particle case chapter 4 above). We show that it is the energy Bloch band spectrum which determines the current and therefore the group velocity and the effective mass. We analyze the dependence of the group velocity and the effective mass on the lattice depth s and the interaction parameter gn. At a given lattice depth, the group velocity of a certain Bloch state increases with increasing gn. Correspondingly, the effective mass is lowered by interactions. Yet, it remains an exponentially growing function of potential depth as in the single particle case. The effect of interactions on the group velocity and the effective mass can be understood in terms of the screening of the lattice by repulsive interactions.

In the tight binding regime (see section 6.2), the energy and chemical potential bands take a simple analytic form. They are characterized by different density-dependent tunneling parameters δ and δ_μ. The effective mass is inversely proportional to the density-dependent tunneling parameter of the lowest energy Bloch band. From the expression for the Bloch energy bands we also find equations for the current and the group velocity. We compare the tight binding predictions with the respective results obtained from the numerical solution of the GP-equation.

Exploiting the tight binding formalism, we also derive simple expressions for the compressibility of the groundstate and the effective coupling constant introduced in chapter 5. Explicit formulars for the groundstate energy, chemical potential and compressibility in a very deep lattice are obtained based on a gaussian ansatz for the Wannier function of the lowest band. Using this ansatz, we also estimate the dependence on lattice depth of the peak density at the center of a harmonic trap added to the optical lattice.

In [102], we have reported our numerical results for the Bloch band spectra, the group velocity, the effective mass and their analytical tight binding expressions, as well as the tight binding expressions for the groundstate compressibility. In this thesis, results for the Bloch state density profiles and the gap between first and second energy and chemical potential Bloch band are included. Also, the proof of the relation between the current of a Bloch state and the energy Bloch bands is added, as well as the discussion of the peak density and the on-site energy and chemical potential within the gaussian approximation to the Wannier function of the lowest Bloch band.

6.1 Bloch states and Bloch bands

As discussed in chapter (4), the stationary state of a single particle in a periodic potential is described by a Bloch function (see Eq.(4.3)). Within GP-theory, the difference between a single particle and an interacting condensate is accounted for by the nonlinear term in the GPE (5.4). Now, suppose we are dealing with a solution whose density has period d. Under this condition, the GPE is invariant under any transformation $z \to z + ld$ and we can use the same arguments as in section (4.1) to show that the respective solution has the form of a Bloch function

$$\varphi_{jk}(z) = e^{ikz}\tilde{\varphi}_{jk}(z)\,, \tag{6.2}$$

with the periodic Bloch wave $\tilde{\varphi}_{jk}(z) = \tilde{\varphi}_{jk}(z+ld)$. Stationary states can be of this kind, but, due to the presence of the nonlinear term, they do not have to: Other classes of solutions are associated with density profiles of periodicity $2d$, $4d$, ... Such solutions have recently been found in [104, 105]. The groundstate discussed above in chapter 5 is of the form (6.2) with $j = 1$, $k = 0$. In the following we explore condensates in Bloch states (6.2).

It is convenient to solve the GPE (5.4) for the periodic Bloch waves $\tilde{\varphi}_{jk}$

$$\left[\frac{1}{2m}\left(-i\hbar\partial_z + \hbar k\right)^2 + s\,E_R\sin^2\left(\frac{\pi z}{d}\right) + gnd|\tilde{\varphi}_{jk}(z)|^2\right]\tilde{\varphi}_{jk}(z) = \mu_j(k)\tilde{\varphi}_{jk}(z). \tag{6.3}$$

From the solution of Eq.(6.3) one gets the functions $\tilde{\varphi}_{jk}(z)$ and the corresponding chemical potentials $\mu_j(k)$. This section is devoted to such solutions.

Density profile

Let us first discuss some solutions for the density $|\varphi_{jk}(z)|^2$. In Figs. 6.1 and 6.2, we report results obtained at $s = 5, gn = 0.5E_R$ and $s = 10, gn = 0.5E_R$ respectively for different bands and quasi-momenta ($j = 1, 2, 3$, $\hbar k = 0,\, 0.5q_B, 1q_B$). Density profiles of higher bands are more modulated and tend to allow for larger particle densities in high potential regions.

Note also the qualitative resemblance of the profiles with the probability amplitude of a single particle in a harmonic oscillator potential. When the lattice is made deeper, density profiles of states within a certain band become more and more similar. This effect is more obvious the lower the band index. Overall, the behavior of the density profile for varying j and k is analogous to the single particle case. Fig.6.3 compares the density profiles at $k = 0.5q_B$ for $gn = 0$ and $gn = 1E_R$. This shows that a change in gn/E_R has the same screening effect as in the case of the groundstate ($k = 0$).

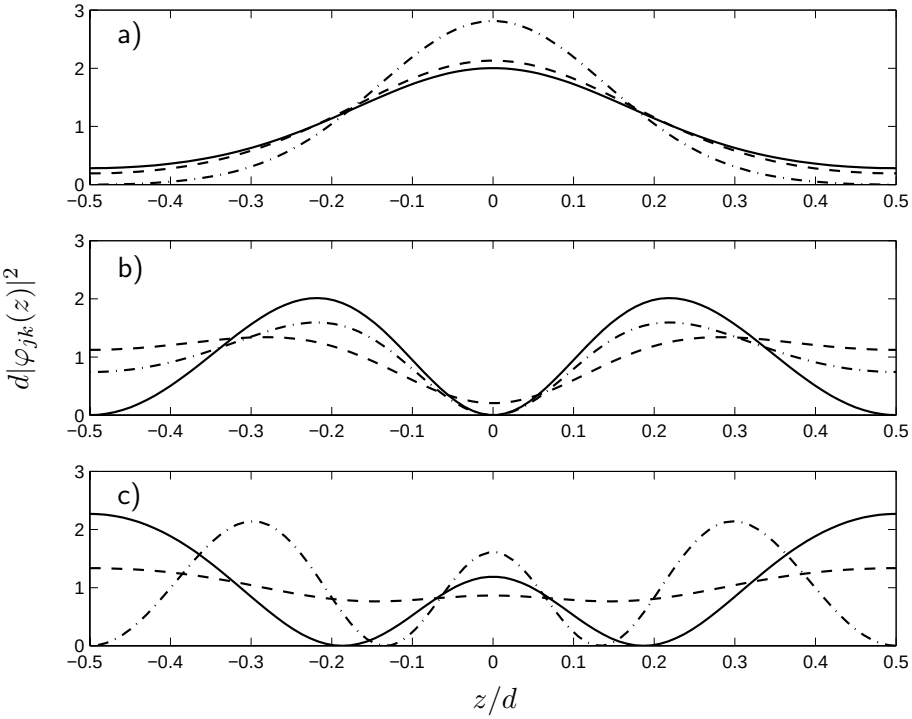

Figure 6.1: Density profiles $d|\varphi_{jk}(z)|^2$ obtained from (6.3) at $s = 5$, $gn = 0.5E_R$ for band index a) $j = 1$, b) $j = 2$ and c) $j = 3$ at $\hbar k = 0$ (solid lines), $\hbar k = 0.5q_B$ (dashed lines) and $\hbar k = q_B$ (dash-dotted lines)).

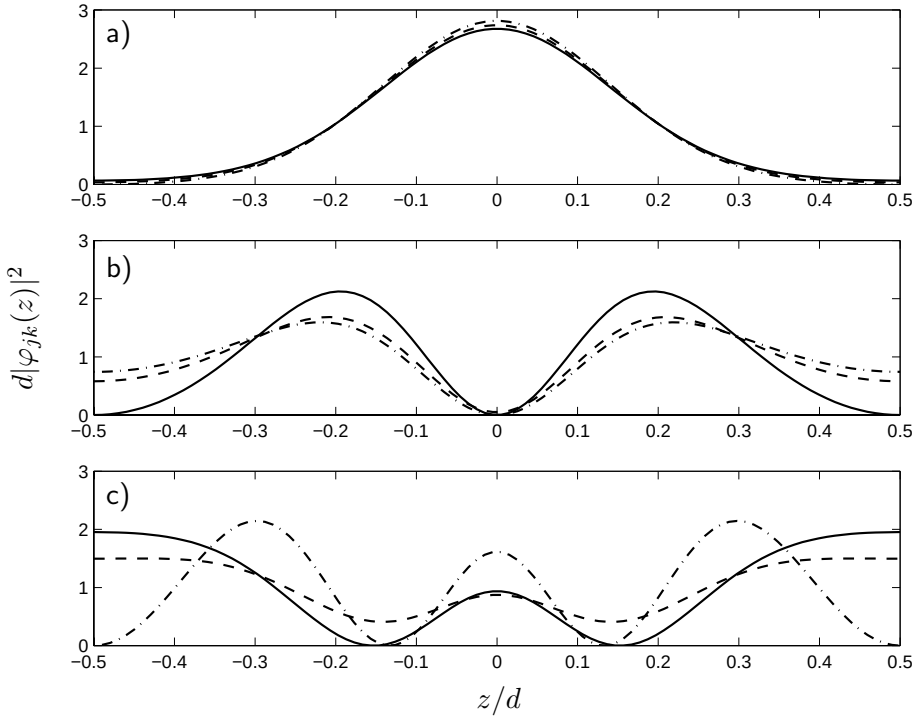

Figure 6.2: Density profiles $d|\varphi_{jk}(z)|^2$ obtained from (6.3) at $s = 10$, $gn = 0.5E_R$ for band index a) $j = 1$, b) $j = 2$ and c) $j = 3$ at $\hbar k = 0$ (solid lines), $\hbar k = 0.5q_B$ (dashed lines) and $\hbar k = q_B$ (dash-dotted lines)).

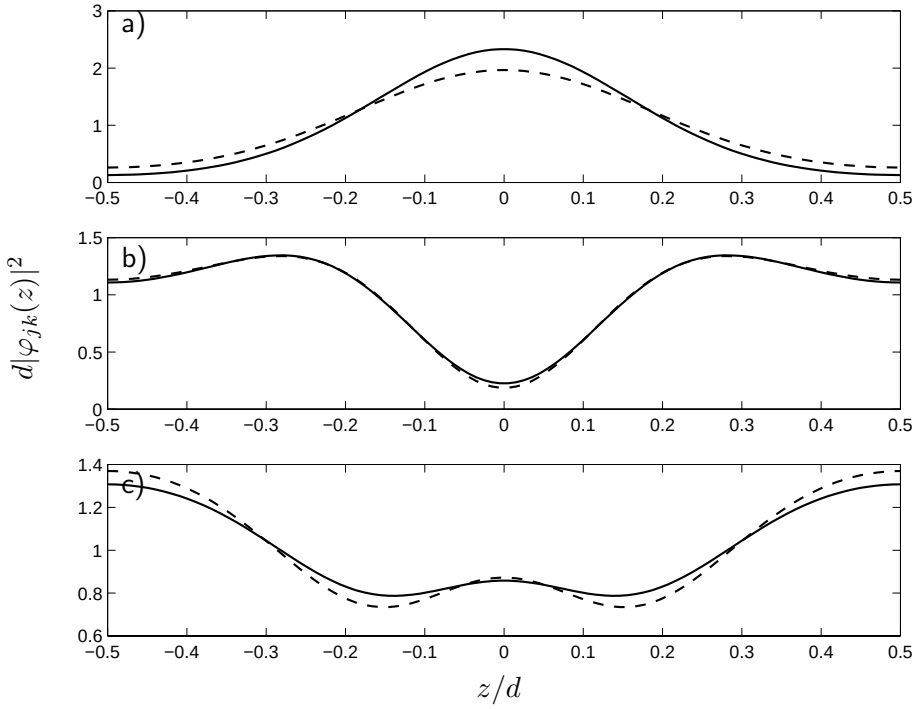

Figure 6.3: Density profiles $d|\varphi_{jk}(z)|^2$ obtained from (6.3) at $s = 5$, $gn = 0E_R$ (solid lines) and $s = 5$, $gn = 1E_R$ (dashed lines) for band index a) $j = 1$, b) $j = 2$ and c) $j = 3$ at $\hbar k = 0.5q_B$.

Chemical potential and energy band spectra

Given a solution $\tilde{\varphi}_{jk}$ of the GPE (6.3), the energy per particle $\varepsilon_j(k)$ can be calculated using the expression

$$\varepsilon_j(k) = \int_{-d/2}^{d/2} \tilde{\varphi}^*_{jk}(z) \left[\frac{1}{2m} \left(-i\hbar\partial_z + \hbar k\right)^2 + s\, E_R \sin^2(z) + \frac{1}{2} gnd|\tilde{\varphi}_{jk}(z)|^2 \right] \tilde{\varphi}_{jk}(z) dz \quad (6.4)$$

and differs from the chemical potential $\mu_j(k)$

$$\mu_j(k) = \int_{-d/2}^{d/2} \tilde{\varphi}^*_{jk}(z) \left[\frac{1}{2m} \left(-i\hbar\partial_z + \hbar k\right)^2 + s\, E_R \sin^2(z) + gnd|\tilde{\varphi}_{jk}(z)|^2 \right] \tilde{\varphi}_{jk}(z) dz. \quad (6.5)$$

by the term $(gnd/2)\int_{-d/2}^{d/2} |\tilde{\varphi}_{jk}(z)|^4$. The chemical potential coincides with the energy per particle only in absence of the interaction term. In general, μ_j and ε_j are linked to each other by the relation

$$\mu_j(k) = \frac{\partial[n\varepsilon_j(k)]}{\partial n}\,. \quad (6.6)$$

In the uniform interacting system, a condensate in a stationary state is characterized by an energy per particle and by a chemical potential. These two quantities differ from each other due to interaction. Stationary states are plane waves and the GPE yields

$$\varepsilon(k; s=0) \;=\; \frac{gn}{2} + \frac{\hbar^2 k^2}{2m}\,, \quad (6.7)$$

$$\mu(k; s=0) \;=\; gn + \frac{\hbar^2 k^2}{2m}\,, \quad (6.8)$$

showing that *both* energy and chemical potential have the same free-particle k-dependence. Going from $k = 0$ to $k \neq 0$ changes the wavefunction by just the phase factor $\exp(ikz)$, which physically corresponds to imparting a constant velocity $\hbar k/m$ to the condensate. The "excitation" to a state with $k \neq 0$ corresponds to a simple Galileo transformation which adds energy $\hbar^2 k^2/2m$ to each particle and thus to the chemical potential. Hence, in the absence of a lattice the two spectra $\varepsilon(k)$ and $\mu(k)$ differ from each other only by an off-set due to the groundstate interaction energy and don't exhibit a different k-dependence.

In the presence of a lattice, analogously to the uniform case one can associate to each stationary state φ_{jk} an energy per particle and a chemical potential which form two different band spectra. However, in the presence of a lattice, the situation is very different from the uniform case: Going from $k = 0$ to $k \neq 0$ does not just correspond to a simple change of reference frame since the barriers of the potential remain fixed. The consequence is a dependence of the Bloch wave $\tilde{\varphi}_{jk}$ on k which gives rise in general also to a difference between the k-dependence of energy and chemical potential.

In Fig.6.4 we plot the band spectra (6.4,6.5) for $gn = 0.5E_R$ at different lattice depth s. For any j, k the value of the chemical potential is always larger than the energy per particle. In analogy to the properties of the single particle Bloch band spectrum, increasing s has three major effects: The energy per particle and the chemical potential are shifted to larger values. The gaps between the bands become larger while each band becomes flatter.

In Figs.6.5, we plot the band spectra (6.4,6.5) at depth $s = 5$ for $gn = 0$ and $gn = 1E_R$. Fig. 6.5 a) shows again the upward shift of the energy (6.4) and even more of the chemical

potential (6.5) due to interactions. In order to have a look at the change of the k-dependence brought about by interactions, we plot in Fig. 6.5 b) the same data as in Fig. 6.5 a), but from each data set we subtract the respective groundstate value. We observe that interactions most affect the k-dependence of the lowest bands, especially in a deep lattice where higher bands are almost identical to the single particle case.

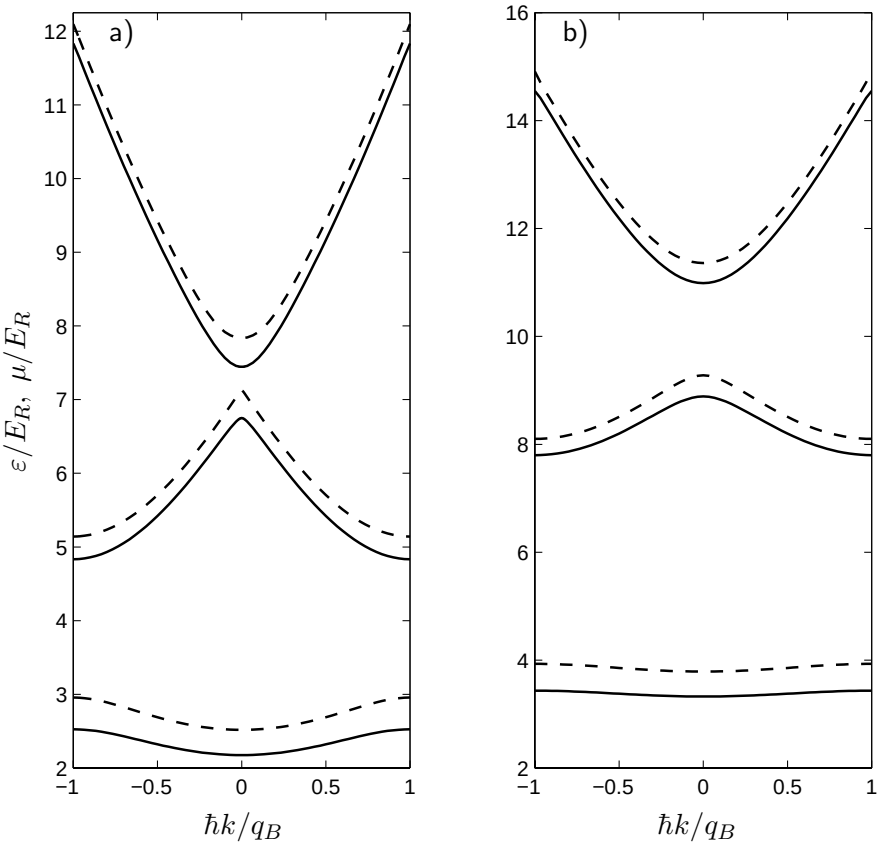

Figure 6.4: Bloch band spectra $\varepsilon_j(k)$ (6.4) (solid lines) and $\mu_j(k)$ (6.5) (dashed lines) for $gn = 0.5E_R$ at lattice depth a) $s = 5$ and b) $s = 10$.

Gap in the band spectra

The opening up of gaps between the bands is a feature that physically characterizes a system in presence of a periodic potential. Fig.6.6 displays this gap between first and second band as a function of lattice depth for different values of gn/E_R for both the energy per particle (6.4) and the chemical potential (6.5). At fixed s, the gap becomes smaller when gn/E_R is increased which again can be understood as a screening effect. Yet, quantitatively the effect is not very large. For large s the gap very slowly approaches the value $2\sqrt{s}E_R$ given by the harmonic approximation of the potential well. Note that in Fig. 6.6 we do not include the range of small potential depths where swallow tails exist (see comments at the end of this section).

The gap in the energy spectrum has been studied experimentally in [67, 68, 69]

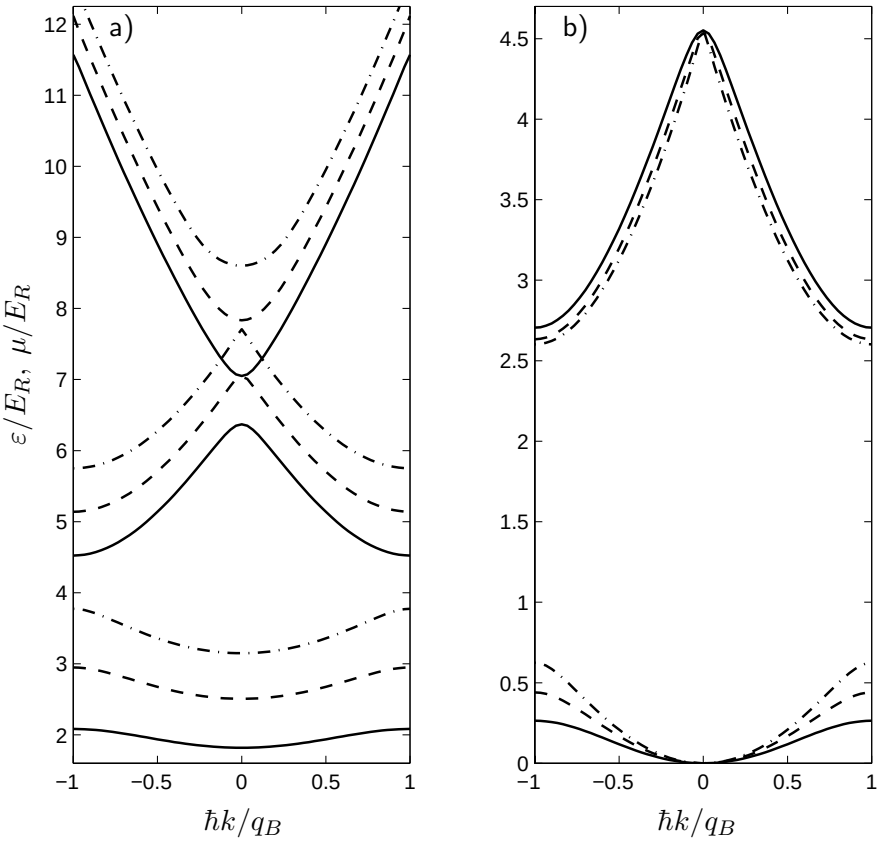

Figure 6.5: Bloch band spectra $\varepsilon_j(k)$ (6.4) (dashed lines) and $\mu_j(k)$ (6.5) (dash-dotted lines) at $s = 5$ for $gn = 1E_R$. Solid lines: Single particle Bloch band spectrum at $s = 5$ ($gn = 0$ where $\varepsilon_j(k) = \mu_j(k)$). In b) the groundstate value has been subtracted for each data set.

Current, group velocity and effective mass

A stationary state is characterized by a spatially uniform, time-independent current. In the following, we will show that the current density

$$I_j(k) = nd\frac{i\hbar}{2m}\left(\varphi_{jk}\frac{\partial}{\partial x}\varphi^*_{jk} - \varphi^*_{jk}\frac{\partial}{\partial x}\varphi_{jk}\right) \tag{6.9}$$

associated with a certain condensate Bloch state is determined by the energy band structure in the same way as in the single particle case. Let us consider the modified GP-equation

$$\left(-\frac{\hbar^2}{2m}\left(\frac{\partial}{\partial z} + iA\right)^2 + V(z) + g\left|\Psi\right|^2\right)\Psi = \mu\Psi\,, \tag{6.10}$$

which is obtained by replacing the momentum operator $-i\hbar\partial/\partial z$ by $-i\hbar\partial/\partial z + \hbar A$, where A is a constant. The presence of A does not violate periodicity so we can look for solutions of Bloch form

$$\Psi_{jk}(z, A) = e^{ikz}\tilde{\Psi}_{jk}(z, A)\,, \tag{6.11}$$

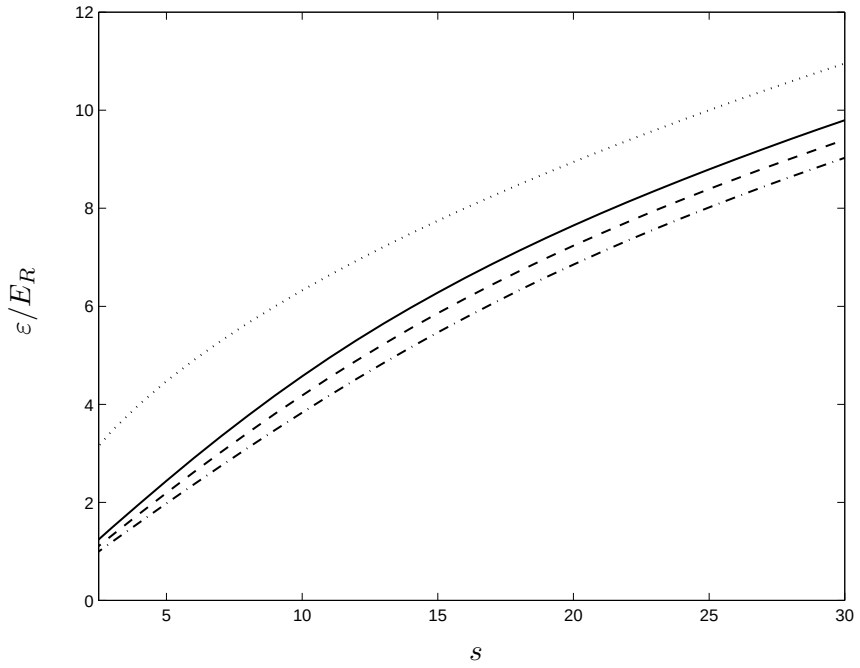

Figure 6.6: Gap between first and second Bloch band of the spectra (6.4) and (6.5) at $\hbar k = q_B$ as a function of lattice depth s for $gn = 0$ (solid line) and $gn = 1E_R$ (dashed and dash-dotted lines respectively). The dotted line indicates the value $2\sqrt{s}E_R$ given by the harmonic approximation of the potential well.

where $\hbar k$ is the quasimomentum and j the band index. The corresponding energy functional yields the "energy per particle"

$$\varepsilon_j(k,A) = \int_{-d/2}^{d/2} \varphi_{jk}^*(z) \left[\frac{1}{2m} \left(-i\hbar\partial_z + \hbar A\right)^2 + s\, E_R \sin^2(z) + \frac{1}{2} gnd|\varphi_{jk}(z)|^2 \right] \varphi_{jk}(z) dz. \tag{6.12}$$

Differentiation with respect to A gives

$$\frac{1}{\hbar}\left[\frac{\partial\varepsilon_j(k,A)}{\partial A}\right]_{A=0} = \frac{i\hbar}{2m}\int_{-d/2}^{d/2} dz \left[\varphi_{jk}\partial_z\varphi_{jk}^* - \varphi_{jk}^*\partial_z\varphi_{jk}\right] . \tag{6.13}$$

It is important that φ_{jk} need not be differentiated because $\delta\varepsilon/\delta\varphi = 0$. The integrand is $I_j(k)/nd$ where $I_j(k)$ is the current density (6.9). Hence, we have

$$\frac{1}{\hbar}\left[\frac{\partial\varepsilon_j(k,A)}{\partial A}\right]_{A=0} = \frac{I_j(k)}{n} . \tag{6.14}$$

However, the dependence of ε on A is completely fictional. Due to the gauge invariance of the GP-equation, A can be excluded from the equation by the substitution

$$\phi_{jk} = e^{iAz}\varphi_{jk}(z,A) = e^{i(A+k)z}\tilde{\varphi}_{jk}(z,A) . \tag{6.15}$$

The function ϕ_{jk} satisfies the usual GP-equation. This means that the energy Bloch bands for the modified GP-equation (6.10) are the same as for the usual one. However, the function

ϕ_{jk} according to (6.15) corresponds to a Bloch state with quasi-momentum $\hbar(k+A)$! This implies that

$$\varepsilon_j(k,A) = \varepsilon_j(k+A)\,, \tag{6.16}$$

where $\varepsilon_j(k)$ are the usual energy Bloch bands. Comparing with (6.14) we find finally that

$$\boxed{I_j(k) = n\frac{\partial\varepsilon_j(k)}{\hbar\partial k}\,,} \tag{6.17}$$

in analogy with the single particle case (see section 4.15). Hence, the group velocity $\bar{v}_j(k)$ is given by

$$\bar{v}_j(k) \;=\; \frac{\partial\varepsilon_j(k)}{\hbar\partial k}\,. \tag{6.18}$$

The effective mass m^* is defined by

$$\boxed{\frac{1}{m^*} := \left.\frac{\partial^2\varepsilon_{j=1}(k)}{\hbar^2\partial k^2}\right|_{k=0}\,,} \tag{6.19}$$

and characterizes current and group velocity at small quasi-momenta in the lowest band

$$I_{j=1}(k) \to n\frac{\hbar k}{m^*}\,, \tag{6.20}$$

$$\bar{v}_{j=1}(k) \to \frac{\hbar k}{m^*}\,. \tag{6.21}$$

The generalization of the definition of the effective mass (6.19) to any value of band index and quasi-momentum reads the same as in the single particle case

$$\frac{1}{m_j^*(k)} := \frac{\partial^2\varepsilon_j(k)}{\hbar^2\partial k^2}\,. \tag{6.22}$$

The fact that the expressions (6.17,6.18,6.19) are the same as for a single particle is not trivial: It shows that it is the energy band spectrum which determines these quantities and not the chemical potential band spectrum! Formally, we can of course define an effective mass associated with the lowest chemical potential at small k

$$\frac{1}{m_\mu^*} \;:=\; \left.\frac{\partial^2\mu_j(k)}{\hbar^2\partial k^2}\right|_{k=0}\,, \tag{6.23}$$

in analogy to definition (6.19). In fact, in section 7 we will find that the k-dependence of the chemical potential and in particular the effective mass (6.23) play a role in the description of the spectrum of the Bogoliubov excitations of the condensate in a stationary state of the Bloch-form (6.2). The energy and chemical potential effective mass are linked by the relation

$$\boxed{\frac{1}{m_\mu^*} := \frac{\partial}{\partial n}\left(\frac{n}{m^*}\right)\,,} \tag{6.24}$$

which follows from $\mu(k) = \partial(n\varepsilon(k))/\partial n$. The two effective masses are in general different from each other reflecting the difference in the Bloch band spectra. To give an example, for $s = 10$, $gn = 0.5E_R$ one finds that m^* is about 28% larger than m^*_μ.

Even though the expressions (6.17,6.18,6.19) are the same as for a single particle, the results obtained are generally different since the energy Bloch bands do change in the presence of interactions. Consequently, current, group velocity and effective mass not only depend on lattice depth, but also on density.

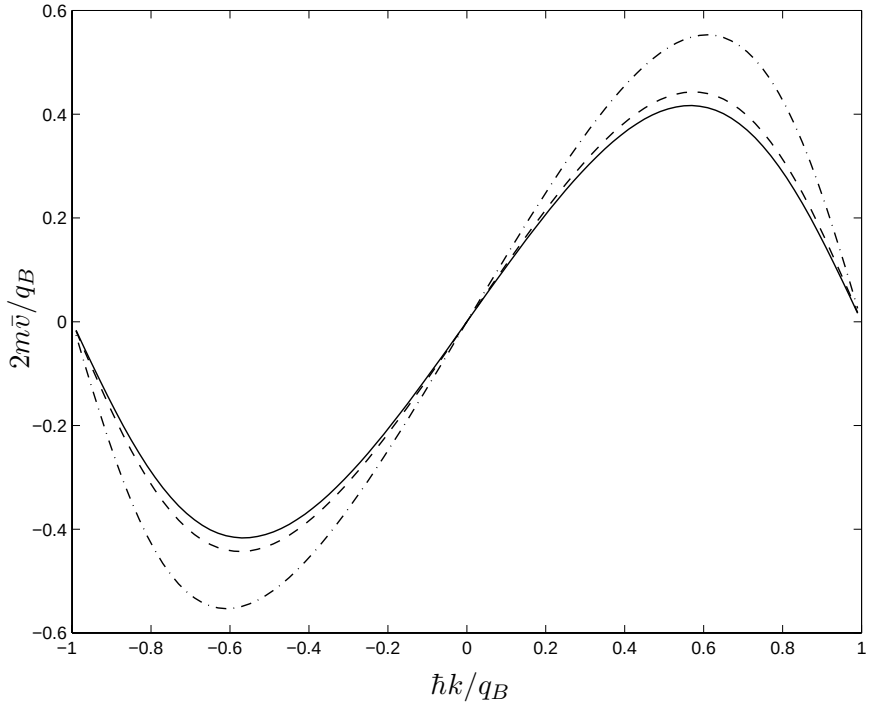

Figure 6.7: Group velocity (6.18) in the lowest band as a function of condensate quasi-momentum k at $s = 5$ for $gn = 0$ (solid line), $gn = 0.1E_R$ (dashed line) and $gn = 0.5E_R$ (dash-dotted line).

The effect of interactions on the group velocity (6.18) is most evident in the lowest band: Its dependence on the condensate quasi-momentum k for different densities in the lowest band is illustrated in Fig. 6.7 for $s = 5$. The larger gn/E_R the larger are the group velocities the condensate can achieve at fixed lattice depth. For example, a change from $gn = 0$ to $gn = 0.5E_R$ increases the maximal group velocity by about 30%. Again, the underlying physical reason is the effective lowering of the potential achieved by an increase of gn/E_R (screening): In a shallower lattice the lowest energy Bloch band is broader implying larger values of the group velocity (6.18).

At small quasi-momenta, the change in current and group velocity brought about by the optical lattice can be understood in terms of the change in the effective mass. In Fig.6.8, we plot the effective mass (6.19) as a function of potential depth for different values of gn/E_R. As in the single particle case, the exponential increase of m^* as a function of lattice

depth s reflects the slow-down of the particles by the tunneling through the potential barriers. Qualitatively, this effect is unaltered in the presence of interactions: The effective mass still features an exponential increase, yet this increase is weaker than for a single particle. At a given potential depth, the effective mass is lowered by increasing gn/E_R due to the screening effect of interactions. This is illustrated in Fig.6.9 where we depict the ratio between condensate and single particle effective mass at different densities. At $gn = 0.5E_R$, the condensate effective mass is about 30% smaller than the one of a single particle at $s = 15$. It is interesting to note that the ratio between $m^*(gn)$ and the single particle effective mass plotted in Fig. 6.9 saturates when s is tuned to large values. This property of the effective mass will become clear in the next section once we relate m^* with the tunneling parameter δ.

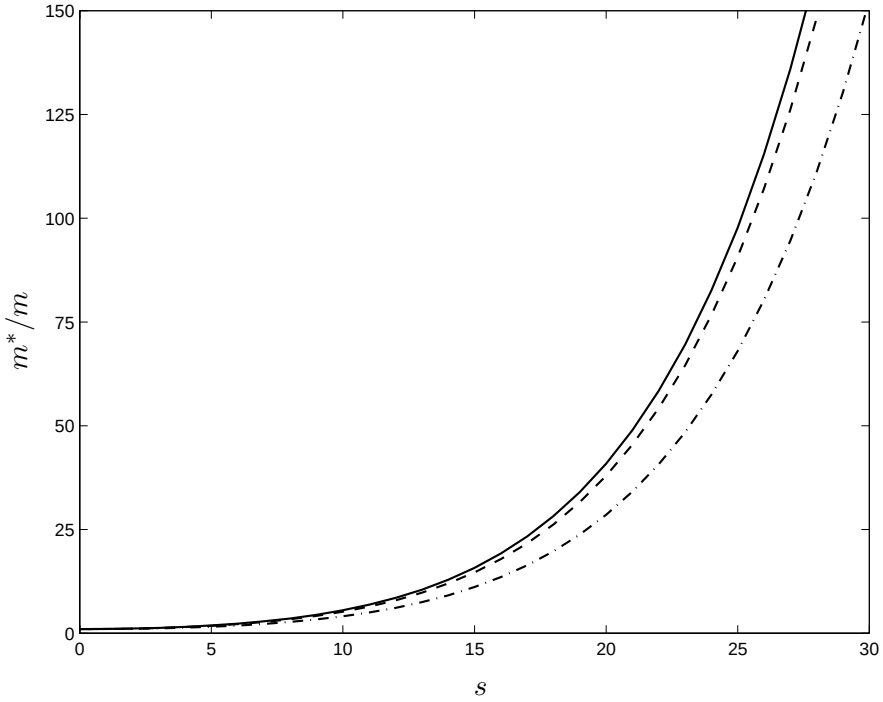

Figure 6.8: Effective mass (6.19) as a function of lattice depth s for $gn = 0$ (solid line), $gn = 0.1E_R$ (dashed line) and $gn = 0.5E_R$ (dash-dotted line) (a) $s \leq 30$, b) $s \leq 10$).

Wannier functions

In analogy to the case of a single particle (see section 4.1), we can introduce the Wannier functions

$$f_{j,l}(x) = \frac{1}{N_w} \sum_k e^{-ikld} \varphi_{jk}(x)\,, \tag{6.25}$$

where φ_{jk} is a Bloch function solution of the stationary GPE (5.4). The inverse relation reads

$$\varphi_{jk}(z) = \sum_l f_{j,l}(z) e^{ikld}\,. \tag{6.26}$$

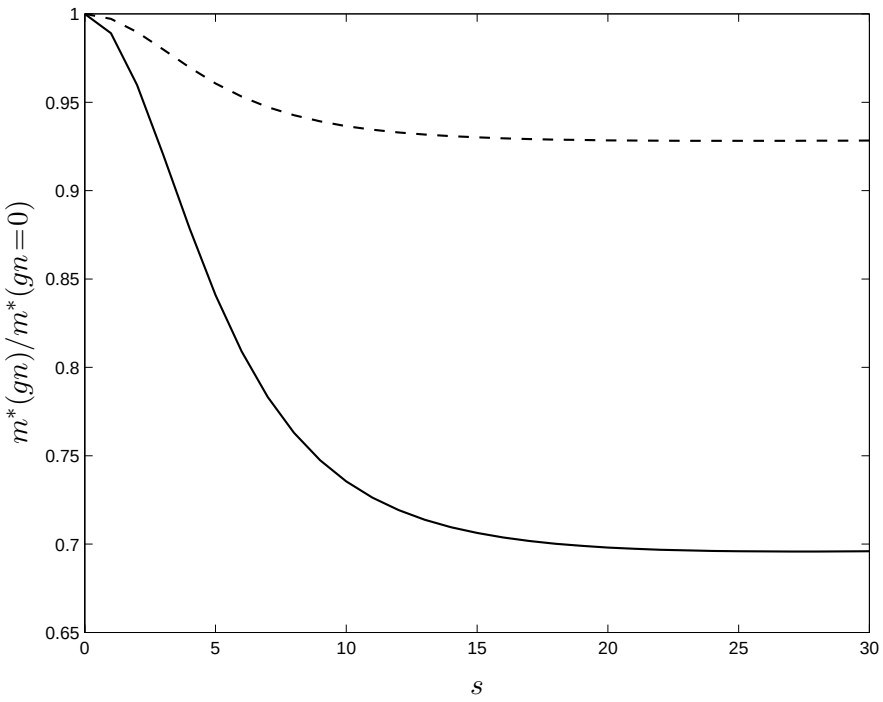

Figure 6.9: Ratio between the effective mass $m^*(gn)$ and the single particle effective mass for $gn = 0.5E_R$ (solid line) and $gn = 0.1E_R$ (dashed line) as a function of lattice depth s.

'The condensate Wannier functions (6.25) form a complete orthonormal set and fulfill the relation

$$f_{j,l}(x) = f_j(x - ld)\,. \tag{6.27}$$

As in the single particle case, the Wannier function $f_{j,l}$ of a condensate is localized at site l and spreads less and less over other sites the deeper the lattice. For convenience, we choose the Wannier functions to be real in the following.

Momentum and quasi-momentum

The momentum distribution of a Bloch state is obtained in complete analogy to the single particle case (see chapter 4.1). In fact, we find that apart from a slight screening effect interactions do not have a strong effect for typical values of gn.

Swallow tails

For $gn \geq s$ one encounters Bloch state solutions which lead to loops ("swallow tails") at the edge of the lowest energy Bloch band [107, 106, 108, 109, 110, 111]. The appearance of these states goes along with a non-zero group velocity of the Bloch state at $k = \hbar q_B$, in sharp contrast with the typical behavior of a single particle. For smaller values of $gn > 0$ such loops can also be found at the center of the first excited band [107]. For the values of gn we have

considered, these swallow tails exist only for very small values of the lattice depth s and we will not discuss them in the following.

Stability of condensate Bloch states

It is important to note that Bloch states can be energetically or dynamically unstable. The stability can be analyzed by calculating the Bogoliubov excitation spectrum of a given φ_{jk} (see [1] chapter 5.6 and comments in section 7.1 below). Two types of instabilities can be encountered: An energetic instability is present if a small perturbation of the stationary solution φ_{jk} leads to a decrease of the energy. Hence in the presence of dissipative terms the system is driven to configurations with lower energy. In contrast, a dynamic instability is associated with the exponential growth in time of a small perturbation which does not require the inclusion of dissipation.

As a general rule, for a given s and nonzero gn, Bloch states in the lowest band are stable for sufficiently small k. Then, there is a range of $k < \hbar q_B$ in which they are energetically unstable, but dynamically stable. For further increasing k, the states also become dynamically unstable. This issue has been the subject of extensive theoretical work (see for example [112, 113, 114, 115, 107, 116, 117, 118]) and has important experimental consequences [74, 76, 77]. The onset of dynamical instabilities leads to a breakdown of the center-of-mass oscillations of a condensate in the combined potential of optical lattice and harmonic trap [115, 76] (see also discussion at the end of chapter 9.6). Recently [104], a connection has been established between the quasi-momentum $\hbar k$ at which dynamical instabilities are first encountered and the appearance of period doubled stationary state solutions of the GP-equation in the band spectrum. The stability of a condensate in the vicinity of the Brillouin zone edge has recently been investigated by controlling the the quasi-momentum through an acceleration of the lattice [77]. The presence of instabilities at the zone edge is confirmed. The growth rates are found to be in agreement with theoretical predictions.

6.2 Tight binding regime

In a sufficiently deep potential, the Wannier functions of a band exhibit only nearest-neighbour contact, as in the single particle case. This means that f_l extends only over the sites l and $l \pm 1$ with its main contributions arising from the site l. This fact can be exploited to derive simple analytic expressions for the energy and chemical potential Bloch bands, and hence for the current, the group velocity and the effective mass, allowing to link these quantities with the tunneling properties of the system.

Bloch states and Bloch bands

Let us write down the energy of the condensate in the Bloch state $\varphi_{jk}(z)$ with only next-neighbour contact Wannier functions of the respective band. We neglect next-neighbour terms of the form $\int_0^L dz f_l^2 f_{l\pm1}^2$ which are much smaller than contributions involving $\int_0^L dz f_l^3 f_{l\pm1}$.

As a consequence of the displacement property of the Wannier functions (6.27), we have

$$\int_{-L/2}^{L/2} f_j^3(z) f_j(z \pm d) dz = \int_{-L/2}^{L/2} f_j(z) f_j^3(z \pm d) dz \,, \tag{6.28}$$

and we obtain the result

$$\begin{aligned} \varepsilon_j(k) \;&=\; \int_{-L/2}^{L/2} f_j(z) \left(-\frac{\hbar^2}{2m}\frac{\partial^2}{\partial z^2} + sE_R \sin^2\left(\frac{\pi z}{d}\right) + \frac{gnd}{2} f_j^2(z) \right) f_j(z) dz \\ &+\; 2\cos(kd) \int_{-L/2}^{L/2} f_j(z) \left(-\frac{\hbar^2}{2m}\frac{\partial^2}{\partial z^2} + sE_R \sin^2\left(\frac{\pi z}{d}\right) + 2gnd f_j^2(z) \right) f_j(z-d) dz \\ &=\; \varepsilon_{0j} - \delta_j \cos(kd) \,, \end{aligned} \tag{6.29}$$

where in the last step we have defined the quantities

$$\varepsilon_{0j} \;=\; \int_{-L/2}^{L/2} f_j(z) \left(-\frac{\hbar^2}{2m}\frac{\partial^2}{\partial z^2} + sE_R \sin^2\left(\frac{\pi z}{d}\right) + \frac{gnd}{2} f_j^2(z) \right) f_j(z) dz \,, \tag{6.30}$$

$$\boxed{\delta_j = -2 \int_{-L/2}^{L/2} f_j(z) \left(-\frac{\hbar^2}{2m}\frac{\partial^2}{\partial z^2} + sE_R \sin^2\left(\frac{\pi z}{d}\right) + 2gnd f_j^2(z) \right) f_j(z-d) dz \,.} \tag{6.31}$$

Comparison of Eq.(6.29) with Eq.(4.29) reveals that in the tight binding regime, the energy bands of a condensate have the same form as in the single particle case. The first term ε_{0j} is an off-set, while the second describes the formation of a band of height $2\delta_j$ and a $\cos(kd)$-dependence on the quasi-momentum. In particular, expression (6.31) generalizes the definition of the tunneling parameter (4.30) to a condensate in presence of interactions.

In contrast to the single particle case, the off-set ε_{0j} and the tunneling parameter δ_j do not only depend on lattice depth, but also on density. This density-dependence shows up in two ways: implicitly through the density-dependence of the Wannier function f_j, which can often be neglected, and explicitly through the interaction term.

We can apply the same considerations to the calculation of the chemical potential in the tight binding regime. In this way, we obtain

$$\begin{aligned} \mu_j(k) \;&=\; \int_{-d/2}^{d/2} \varphi_{jk}^*(z) \left(-\frac{\hbar^2}{2m}\frac{\partial^2}{\partial z^2} + sE_R \sin^2\left(\frac{\pi z}{d}\right) + gnd|\varphi_{jk}(z)|^2 \right) \varphi_{jk}(z) dz \\ &=\; \mu_{0j} - \delta_{\mu,j} \cos(kd) \,, \end{aligned} \tag{6.32}$$

where we have defined the quantities

$$\mu_{0j} \;=\; \int_{-L/2}^{L/2} f_j(z) \left(-\frac{\hbar^2}{2m}\frac{\partial^2}{\partial z^2} + sE_R \sin^2\left(\frac{\pi z}{d}\right) + gnd f_j^2(z) \right) f_j(z) dz \,, \tag{6.33}$$

$$\delta_{\mu,j} \;=\; -2 \int_{-L/2}^{L/2} f_j(z) \left(-\frac{\hbar^2}{2m}\frac{\partial^2}{\partial z^2} + sE_R \sin^2\left(\frac{\pi z}{d}\right) + 4gnd f_j^2(z) \right) f_j(z-d) dz \,. \tag{6.34}$$

Comparison of Eqs.(6.30,6.33) and Eqs.(6.31,6.34) shows that

$$\mu_{0j} - \varepsilon_{0j} = \frac{gnd}{2} \int_{-L/2}^{L/2} f_j^4(z)\,, \tag{6.35}$$

$$\delta_{\mu,j} - \delta_j = -4gnd \int_{-L/2}^{L/2} f_j^3(z) f_j(z-d) dz\,. \tag{6.36}$$

Using this result and the general relation $\mu = \partial(n\varepsilon)/\partial n$, we identify

$$n\frac{\partial \varepsilon_0}{\partial n} = \frac{gnd}{2} \int_{-L/2}^{L/2} f_j^4(z)\,, \tag{6.37}$$

$$n\frac{\partial \delta_j}{\partial n} = -4gnd \int_{-L/2}^{L/2} f_j^3(z) f_j(z-d) dz\,. \tag{6.38}$$

We recall that in the single particle case the l-th Fourier component of the energy band (coefficient of e^{ikld} in the Fourier expansion) is given by the matrix element of the Hamiltonian between Wannier functions at distance ld. In the tight binding regime this immediatly yields the $\cos$-dependence on the quasi-momentum. The situation is different in the presence of interactions. For instance, also next-neighbour overlap can lead to higher frequency contributions to the energy band since the term $\int dz f_l^2 f_{l\pm1}^2$, neglected here, would yield a $\cos(2kd)$-dependence.

Group velocity, current and effective mass

Exactly as in the single particle case, the knowledge of the form of the considered energy band (6.29) in the tight binding regime, immediately permits to write down explicit expressions for the group velocity (6.18), the current density (6.17) and the effective mass (6.19).

The group velocity (6.18) takes the simple form

$$\bar{v}_j(k) = \frac{d\delta_j}{\hbar} \sin(kd)\,, \tag{6.39}$$

and correspondingly, the current density reads

$$I_j(k) = \frac{d\delta_j}{\hbar L} \sin(kd)\,. \tag{6.40}$$

Both quantities are proportional to the tunneling parameter δ.

The effective mass (6.19) turns out to be inversely proportional to the tunneling parameter

$$\boxed{\frac{1}{m^*} = \frac{d^2\delta}{\hbar^2}\,.} \tag{6.41}$$

Thus, the exponential increase of m^* as a function of s in an optical lattice (see Fig.6.8) reflects the exponential decrease of the tunneling parameter. We can now discuss why the effect of interaction on m^* can not be neglected, not even at very large s (see Fig. 6.9): This is

mainly due to the explicit dependence of the tunneling parameter on gn in (6.31) and secondly to the dependence of the Wannier function f on the density. In Fig. 6.9 one can see that the deviation of $m^*(gn)$ from the single particle effective mass is approximately proportional to gn. The departure from this linear law in gn is due to the density dependence of the Wannier function f. For the considered interaction $gn = 0.5E_R$ it has a small effect of about 5% on the effective mass, to be compared with the 30% shift due to the explicit dependence on gn.

The generalized k-dependent effective mass (6.22) takes the form

$$\frac{1}{m_j^*(k)} = \frac{d^2\delta_j}{\hbar^2}\cos(kd)\,. \tag{6.42}$$

In Figs. 6.10 and 6.11 we compare the tight binding expressions for the lowest energy band and the associated group velocity with the respective numerical solution. To evaluate (6.29) and (6.39), the tunneling parameter (6.31) is obtained by inserting the numerical results for m^* in Eq.(6.41). We find that the tight binding results provide a good description already at $s = 10$ for $gn = 0.5E_R$. To obtain the same degree of agreement at a higher value of gn/E_R one has to go to larger s.

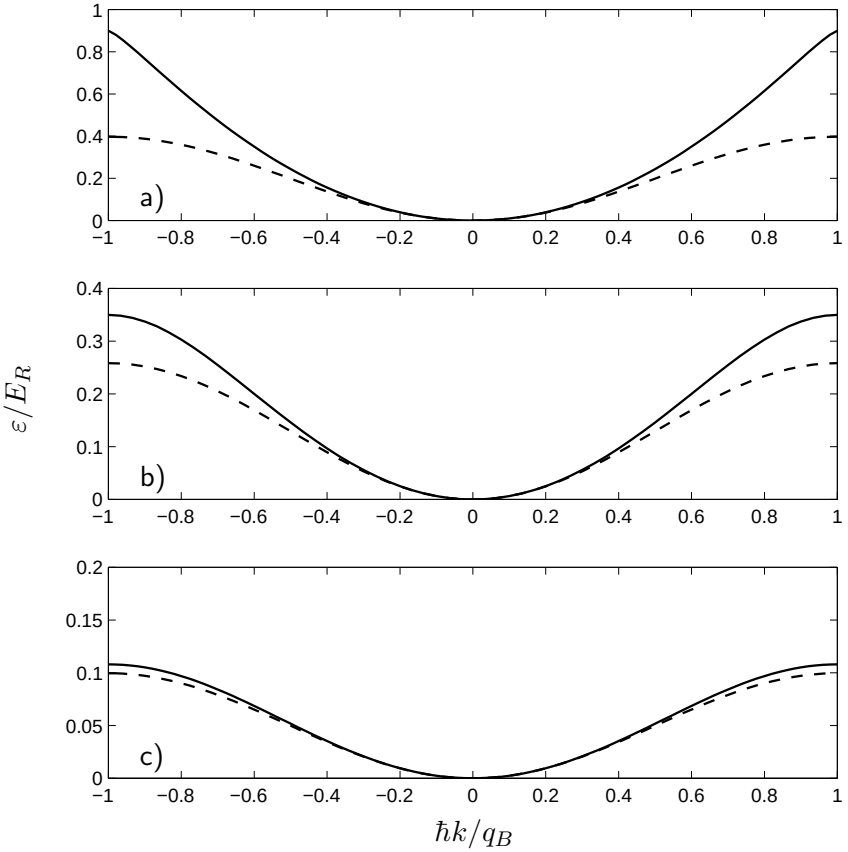

Figure 6.10: Comparison of the tight binding expression (6.29) for the lowest energy band with the respective numerical solution for $gn = 0.5E_R$ at a) $s = 1$, b) $s = 5$ and c) $s = 10$.

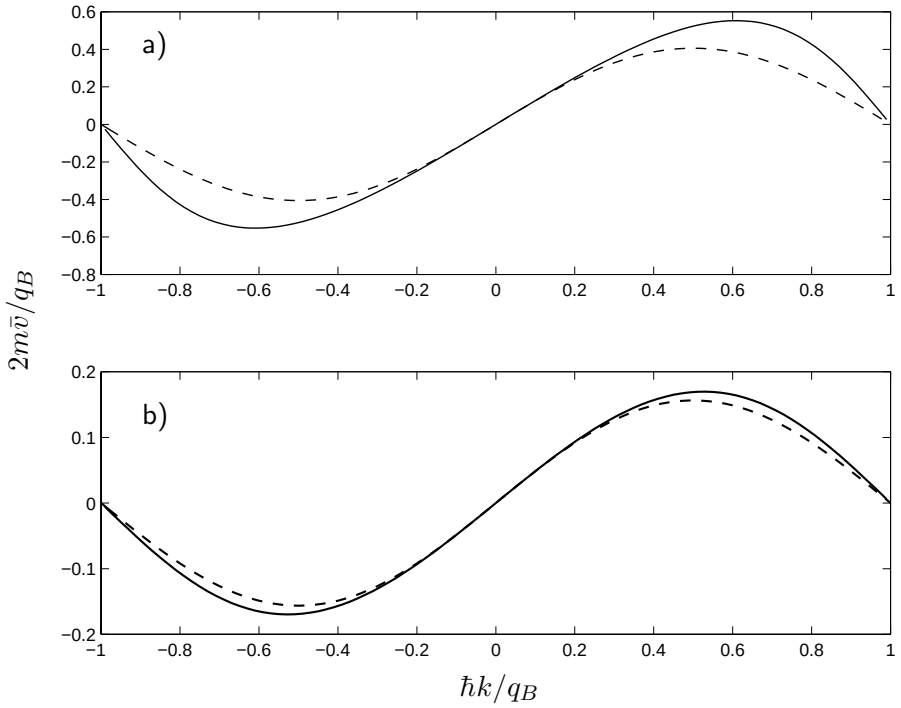

Figure 6.11: Comparison of the tight binding expression (6.39) for the group velocity in the lowest band with the respective numerical solution for $gn = 0.5E_R$ at a) $s = 5$, b) $s = 10$.

Compressibility and effective coupling

The compressibility κ in the tight binding regime can be calculated by inserting the tight binding expression for the chemical potential (6.32) with $j = 1, k = 0$ into the definition $\kappa^{-1} = n\partial\mu/\partial n$. Taking into account result (6.38) and (6.36), we find

$$\kappa^{-1} = gnd \int_{-L/2}^{L/2} f^4(z) + 8gnd \int_{-L/2}^{L/2} f^3(z) f(z-d) dz \,, \tag{6.43}$$

where μ_0 was defined in Eq.(6.33). The first term is the leading order on-site contribution, while the second contribution is due to the small overlap of neighbouring Wannier functions and can be often neglected. In deriving (6.43) we also discarded terms involving the derivating $\partial f(z;n)/\partial n$. This presupposes the lattice to be deep enough to ensure that the effect of interactions on the wavefunction is negligible. Expression (6.43) then takes the form

$$\kappa^{-1} = gnd \int_{-L/2}^{L/2} f_{gn=0}^4(z) \tag{6.44}$$

where $f_{gn=0}$ is the single particle Wannier function for the lowest band. This expression is expected to give a good account of the compressibility in a sufficiently deep lattice. It follows

that the effective coupling constant (5.15) in the tight binding regime reads

$$\boxed{\tilde{g} = gd \int_{-L/2}^{L/2} f_{gn=0}^4(z)\,.} \tag{6.45}$$

A quantitative estimate of the validity of this expression will be given in the following section using a gaussian ansatz for the Wannier function.

Gaussian approximation to the Wannier function of the lowest band

In the limit of zero tunneling ($s \to \infty$), Wannier functions become eigenstates. In particular, a single particle in the groundstate can be described by the corresponding harmonic oscillator wavefunction. If $s \gg 1$ and as long as the single-well condensate is far from being correctly described by the TF-approximation inside each well, it is reasonable to approximate the Wannier function by a gaussian

$$\varphi(z) \equiv f(z) = \frac{1}{\pi^{1/4}\sqrt{\sigma}} \exp(-z^2/2\sigma^2)\,. \tag{6.46}$$

The gaussian (6.46) is a useful variational ansatz for the calculation of on-site quantities as the compressibility, but fails to describe properties which crucially depend on the overlap between neighbouring Wannier functions, as the effective mass. In fact, when tunneling is possible, but its effects only small, we expect the Wannier function of the lowest band to be still similar to the gaussian (6.46) inside a well, but to have oscillating tails in the barrier region in order to ensure orthogonality.

At a given lattice depth s and interaction gn/E_R, the value of the gaussian width σ is fixed by requiring the ansatz (6.46) to minimize the energy of the system. Since contributions due to tunneling go beyond the accuracy of this description, it is consistent to consider only the on-site energy ε_0 (see Eq.(6.30)). Moreover, we expand the lattice potential (3.6) around its minima

$$V(z)/E_R \approx s\left(\frac{\pi z}{d}\right)^2 - \frac{s}{3}\left(\frac{\pi z}{d}\right)^4\,, \tag{6.47}$$

where the first term corresponds to a harmonic potential of oscillator frequency

$$\tilde{\omega} = 2\sqrt{s}E_R/\hbar\,, \tag{6.48}$$

while the second term allows for anharmonicity effects of $\mathcal{O}(z^4)$. The solution σ has to satisfy the equation

$$-\frac{d^3}{\pi^3}\frac{1}{\sigma^3} + s\frac{\pi}{d}\sigma - s\frac{\pi^3}{d^3}\sigma^3 - \frac{1}{2}\frac{gn}{E_R}\sqrt{\frac{\pi}{2}}\frac{d^2}{\pi^2}\frac{1}{\sigma^2} = 0\,. \tag{6.49}$$

Since in we are interested in the large-s limit, we neglect the interaction term. Using $s \gg 1$, $\sigma\pi/d << 1$ we obtain the explicit expression

$$\sigma = \frac{1}{s^{1/4}}\left(1 + \frac{1}{4\sqrt{s}}\right)\frac{d}{\pi}\,. \tag{6.50}$$

The leading contribution yields the single particle harmonic oscillator groundstate where $\sigma = s^{-1/4}d/\pi = \sqrt{\hbar/m\tilde{\omega}}$ for the harmonic well with frequency $\tilde{\omega} = 2\sqrt{s}E_R/\hbar$, while the second term is a small correction arising from the anharmonicity which slightly increases the width σ of the groundstate.

Inserting the gaussian ansatz into the expressions (6.30) and (6.33) for the on-site contribution to the energy and the chemical potential, we obtain

$$\frac{\varepsilon_0}{E_R} = \frac{d^2}{2\pi^2}\frac{1}{\sigma^2} + s\left(\frac{1\pi^2}{2d^2}\sigma^2 - \frac{1\pi^4}{4d^4}\sigma^4\right) + \frac{1}{\sqrt{8\pi}}\frac{gn}{E_R}\frac{d}{\pi}\frac{1}{\sigma}\,, \tag{6.51}$$

$$\frac{\mu_0}{E_R} = \frac{\varepsilon_0}{E_R} + \frac{1}{\sqrt{8\pi}}\frac{gn}{E_R}\frac{d}{\pi}\frac{1}{\sigma}\,. \tag{6.52}$$

Within the gaussian approximation, the inverse compressibility (6.44) can be rewritten as

$$\kappa^{-1} = \frac{gnd}{\sqrt{2\pi}\sigma} \tag{6.53}$$

and the tight binding effective coupling constant (6.45) takes the form

$$\tilde{g} = \frac{gd}{\sqrt{2\pi}\sigma} \tag{6.54}$$

with σ given by (6.50). For $s = 10, gn = 0.5E_R$ the approximation $\kappa^{-1} = \tilde{g}n$ with $\tilde{g}$ given by Eq.(6.54) differs from the exact value of κ^{-1} by less than 1%.

In section 5.4, we have found that the average density at the central site of a condensate loaded in the combined potential of optical lattice and harmonic trap decreases like $n_{l=0} \sim (\tilde{g}/g)^{-3/5} \sim s^{-3/20}$. As already mentioned there, the decrease of the *average* density at the trap center (5.31) is to be contrasted with the increase of the non-averaged peak density $n(r_\perp = 0, z = 0) \sim (\tilde{g}/g)^{2/5} \sim s^{1/10}$. We can now prove the latter statement using the gaussian ansatz (6.46) with σ given by (6.49): The peak density then reads

$$n(r_\perp = 0, z = 0) = f(z = 0)^2 n_{l=0}(r_\perp = 0; s) = \frac{1}{\pi^{1/2}\sigma}\frac{(\mu - \mu_{gn=0})}{\tilde{g}}\,, \tag{6.55}$$

where we have used the approximative solution $(\mu - \mu_{gn=0})/\tilde{g}$ for the average density profile (see Eq.(5.31)) with $\mu - \mu_{gn=0}$ and $\tilde{g}$ given by Eqs.(5.29) and (6.54) respectively. At $s = 0$, the density at the center is given by $n(r_\perp = 0, z = 0) = \mu/g$ where μ is the usual TF-value of the chemical potential (see Eq.(5.29) with $\tilde{g} = g$ and $\mu_{gn=0} = 0$). It follows that the ratio between the peak densities at large s and at $s = 0$ equals $\sqrt{2}\,(\tilde{g}/g)^{2/5}$. For $s = 20$ and $s = 50$, this amounts to a 32% and 46% increase respectively.

Chapter 7

Bogoliubov excitations of Bloch state condensates

Small perturbations of a stationary Bloch state condensate can be analyzed in terms of its Bogoliubov excitations. We show that these excitations have Bloch symmetry and hence are labeled by their band index j and their quasi-momentum $\hbar q$ (see section 7.2). Accordingly, the Bogoliubov dispersion takes the form of a band spectrum ("Bogoliubov band spectrum") which depends on the stationary condensate Bloch state whose excitations are considered.

The physical meaning underlying the Bogoliubov band spectrum is very different from the one of the energy Bloch bands discussed in the previous chapter: The Bloch bands refer to states which involve a motion of the whole condensate through the lattice. In contrast, the Bogoliubov bands describe small perturbations which involve only a small portion of atoms. The non-perturbed condensate acts as a carrier or, in other words, as a medium through which the perturbed portion is moving. This physical picture explains why interaction effects on the Bogoliubov spectrum are more significant than on the Bloch energies.

We calculate the Bogoliubov bands of the groundstate condensate (see section 7.2). The lowest band exhibits a phononic regime at small quasi-momenta while higher Bogoliubov bands are found to be little affected by interactions. An analysis of the Bogoliubov amplitudes of the lowest band shows that the v-amplitude becomes comparable to the u-amplitude in the whole Brillouin zone as the lattice is made deeper. Hence, all excitations of the lowest band acquire quasi-particle character, even in the range of quasi-momenta where the dispersion is not linear and excitations are not phonons.

We develop a formalism which is suitable to describe the lowest Bogoliubov band in the tight binding regime (see section 7.3). Analytic formulas for the lowest Bogoliubov band and the respective Bogoliubov amplitudes are found. They involve the tunneling parameter δ describing the lowest energy Bloch band in the tight binding regime (see chapter 6.2 above) and the compressibility κ of the groundstate. When the lattice is made very deep, the band takes the form of the modulus of a $\sin$-function. The band height is given by $2\sqrt{\delta\kappa}$ and decreases much more slowly as a function of the lattice depth as the height 2δ of the lowest energy Bloch band (see chapter 6.2 above). The relative difference between Bogoliubov u and v-amplitude at the boundary of the Brillouin zone goes to zero like $\sqrt{2\delta\kappa}$, indicating the quasi-particle character of excitations.

The sound velocity in the groundstate condensate drops strongly as a function of lattice depth (see section 7.4). This behavior is directly linked to the increase of the effective mass which overcompensates the decrease of the compressibility. We also discuss the sound velocity in a condensate with non-zero group velocity. In contrast to a moving uniform system, the sound velocity in a condensate moving in a lattice is not simply given by the sum of the sound velocity in a condensate at rest and the group velocity of the condensate with respect to the lattice.

In [102], we have reported the numerical results for the Bogoliubov band spectra and the sound velocity of the groundstate, as well as the analytical tight binding expressions for the lowest Bogoliubov band and the respective Bogoliubov amplitudes. There, we also discussed the hydrodynamic results for the sound velocity in a slowly moving condensate. This thesis adds the discussion of the numerical Bogoliubov amplitudes, their comparison with the tight binding expressions and the analysis of the ratio between the u and v-amplitude in the limit of a very deep lattice, as well as the discussion of the gap between first and second Bogoliubov band and the comparison of the heights of the lowest Bogoliubov and energy Bloch band.

7.1 Bogoliubov equations

The dynamics of a coherent zero-temperature condensate in a 1D optical lattice is described by the time-dependent GPE (TDGPE)

$$i\hbar\frac{\partial\Psi(z,t)}{\partial t} = \left(-\frac{\hbar^2}{2m}\frac{\partial^2}{\partial z^2} + sE_R\sin^2\left(\frac{\pi z}{d}\right) + g\,|\Psi(z,t)|^2\right)\Psi(z,t)\,, \tag{7.1}$$

where we have excluded dynamics involving the transverse direction and $\int_{-L/2}^{L/2} d\mathbf{r}|\Psi|^2 = N_{\mathrm{tot}}$.

Stationary state solutions of Bloch form are given by

$$\begin{aligned}\Psi_{jk}(z,t) &= \sqrt{\frac{N}{L^2}}e^{-i\mu_j(k)t/\hbar}\varphi_{jk}\\ &= \sqrt{\frac{N}{L^2}}e^{-i\mu_j(k)t/\hbar}e^{ikz}\tilde{\varphi}_{jk}\,,\end{aligned} \tag{7.2}$$

where L is the transverse size of the system, N is the number of particles per well and $\mu_j(k)$, φ_{jk} is a solution of the form (6.2) of the stationary GPE (5.4) (Recall that in sections 5 and 6 we have already made use of the rescaled order parameter (5.2)). To explore small time-dependent deviations from such stationary states, we write

$$\Psi(z,t) = e^{-i\mu_j(k)t/\hbar}e^{ikz}\left[\sqrt{\frac{N}{L^2}}\tilde{\varphi}_{jk}(z) + \delta\Psi(z,t)\right]\,, \tag{7.3}$$

where $\delta\Psi$ is a small perturbation of the Bloch state $\Psi_{jk}(z,t)$. We linearize the TDGPE (7.1) in $\delta\Psi(z,t)$ and obtain

$$i\hbar\frac{\partial\delta\Psi(z,t)}{\partial t} = \left(-\frac{\hbar^2}{2m}\frac{\partial^2}{\partial z^2} + sE_R\sin^2\left(\frac{\pi z}{d}\right) + 2d\,gn\,|\tilde{\varphi}_{jk}(z,t)|^2 - \mu_j(k)\right)\delta\Psi(z,t) + gnd\tilde{\varphi}_{jk}^2\delta\Psi^*\,. \tag{7.4}$$

Using the expansion

$$\delta\Psi(z,t) = \sum_{\sigma} \left(u_\sigma(z) e^{-i\omega_\sigma t} + v_\sigma^*(z) e^{i\omega_\sigma t} \right) , \tag{7.5}$$

where σ labels the elementary excitations of this stationary state, we find the set of equations

$$\left(-\frac{\hbar^2}{2m}\frac{\partial^2}{\partial z^2} + sE_R \sin^2\left(\frac{\pi z}{d}\right) + 2d\, gn\, |\tilde{\varphi}_{jk}(z)|^2 - \mu_j(k) \right) u_\sigma(z) + gnd\tilde{\varphi}_{jk}^2(z) v_\sigma(z) \;=\; \hbar\omega_\sigma u_\sigma(z) \tag{7.6}$$

$$\left(-\frac{\hbar^2}{2m}\frac{\partial^2}{\partial z^2} + sE_R \sin^2\left(\frac{\pi z}{d}\right) + 2d\, gn\, |\tilde{\varphi}_{jk}(z)|^2 - \mu_j(k) \right) v_\sigma(z) + gnd\tilde{\varphi}_{jk}^{*2}(z) u_\sigma(z) \;=\; -\hbar\omega_\sigma v_\sigma(z) \tag{7.7}$$

for the Bogoliubov amplitudes $u_\sigma(z)$, $v_\sigma(z)$ and the excitation energies $\hbar\omega_\sigma$.

We require

$$\int dz \left(|u_\sigma|^2 - |v_\sigma|^2 \right) = 1 \, . \tag{7.8}$$

Moreover, the Bogoliubov amplitudes must satisfy the orthogonality relations

$$\int dz \, (u_\sigma^* u_{\sigma'} - v_\sigma^* v_{\sigma'}) = 0 \, , \tag{7.9}$$

$$\int dz \, (u_\sigma^* v_{\sigma'} - v_\sigma u_{\sigma'}) = 0 \, , \tag{7.10}$$

for $\sigma \neq \sigma'$.

The normalization condition (7.8) implies that for an energetically stable state φ_{jk} the spectrum $\hbar\omega_\sigma$ is positive, while negative values $\hbar\omega_\sigma$ signify that the stationary state φ_{jk} is energetically unstable (see [1], chapter 5.6). The occurrence of complex frequencies ω_σ with a negative imaginary part reveals the dynamical instability of the stationary state φ_{jk}. The stability analysis of condensate Bloch states commented on in the previous chapter is thus based on the solution of the Bogoliubov equations (7.6,7.7).

The presence of a harmonic trap can changes significantly the low energy excitations of the system. In fact, in chapter 9 we will show that small amplitude collective oscillations occurring on a length scale of the system size are strongly affected both by the harmonic trap and the lattice. The excitation spectrum obtained from (7.6,7.7) does not account for the presence of a harmonic trap. Still, the solution of (7.6,7.7) is relevant also for trapped systems: It yields a local Bogoliubov band spectrum given by $\hbar\omega_\sigma(n_M(\mathbf{r}))$ where $n_M(\mathbf{r})$ is the macroscopic density profile introduced above in chapter 5.4. This approach is valid for excitations whose characteristic length scale is small compared to the size of the system.

7.2 Bogoliubov bands and Bogoliubov Bloch amplitudes

Since $\tilde{\varphi}_{jk}(z)$ is periodic, we can apply the Bloch theorem as in section 4.1 and write the Bogoliubov amplitudes in the form

$$u_{j'q}(z) \;=\; \frac{1}{\sqrt{N_w}} e^{iqz} \tilde{u}_{j'q}(z) \, , \tag{7.11}$$

$$v_{j'q}(z) \;=\; \frac{1}{\sqrt{N_w}} e^{iqz} \tilde{v}_{j'q}(z) \, , \tag{7.12}$$

where $\tilde{u}_{j'q}(z)$, $\tilde{v}_{j'q}(z)$ are periodic with period d and the index σ in Eqs.(7.6,7.7) is replaced by the band index j' and the quasi-momentum q of the excitation. Because the Eqs.(7.6,7.7) are linear, the set of Bogoliubov Bloch amplitudes (7.11,7.12) represents all possible solutions, in contrast to the case of the nonlinear equation (5.4), where states of Bloch form constitute only the class of solutions which are associated with a density profile of period d. The set of solutions (7.11,7.12) is associated with a band spectrum $\hbar\omega_{j'}(q)$ of the energies of elementary excitations ("Bogoliubov band spectrum"). In order to conform with periodic boundary conditions, the quasi-momentum q must belong to the spectrum

$$q = \frac{2\pi}{L}\nu\,, \qquad \nu = 0, \pm 1, \pm 2, \ldots\,. \tag{7.13}$$

The solutions (7.11,7.12) and the corresponding Bogoliubov band spectrum $\hbar\omega_{j'}(q)$ depend on the particular stationary condensate φ_{jk}. In the following, we will restrict ourselves to discussing small perturbations of the groundstate φ. The Bogoliubov equations (7.6,7.7) for this case read

$$\left(-\frac{\hbar^2}{2m}\frac{\partial^2}{\partial z^2} + sE_R\sin^2\left(\frac{\pi z}{d}\right) + 2d\,gn\,|\tilde{\varphi}(z)|^2 - \mu\right)u_{jq}(z) + gnd\tilde{\varphi}^2(z)v_{jq}(z) \;=\; \hbar\omega_j(q)u_{jq}(z) \tag{7.14}$$

$$\left(-\frac{\hbar^2}{2m}\frac{\partial^2}{\partial z^2} + sE_R\sin^2\left(\frac{\pi z}{d}\right) + 2d\,gn\,|\tilde{\varphi}(z)|^2 - \mu\right)v_{jq}(z) + gnd\tilde{\varphi}^{*2}(z)u_{jq}(z) \;=\; -\hbar\omega_j(q)v_{jq}(z) \tag{7.15}$$

where we have replaced the index σ by the band index j and the quasi-momentum q of the excitation. Evidently, the Bogoliubov band spectrum takes only positive values in this case. The numerical solution of Eqs.(7.14,7.15) is conveniently obtained by expanding the periodic functions $\tilde{u}_{jq}, \tilde{v}_{jq}, \tilde{\varphi}$ in a Fourier series.

The Bogoliubov equations (7.14,7.15) have been solved for example by [119, 120]. Numeric solution for the bands $\hbar\omega_j(q)$ of (7.6,7.7) with values of the condensate quasi-momentum $k \neq 0$ has been reported in [118]. The damping of Bogoliubov excitations in optical lattices at finite temperatures has been studied by [121].

Bogoliubov band spectrum

Similarities and differences with respect to the well-known Bogoliubov spectrum in the uniform case ($s = 0$) are immediate. As in the uniform case, interactions make the compressibility finite, giving rise to a phononic regime for long wavelength excitations ($q \to 0$) in the lowest band. In high bands the spectrum of excitations instead resembles the Bloch dispersion (see Eq.(6.4)), as it resembles the free particle dispersion in the uniform case. The differences are that in the presence of the optical lattice the lattice period d and the Bragg momentum $q_B = \hbar\pi/d$ emerge as an additional physical length and momentum scale respectively and that the Bogoliubov spectrum develops a band structure. As a consequence, the dispersion is periodic as a function of quasi-momentum and different bands are separated by an energy gap. In particular, the phononic regime present in the lowest band at $q = 0$ is repeated at every even multiple of the Bragg momentum q_B.

In Fig.7.1 we compare the Bologoliubov bands at $s = 1$ for $gn = 0$ and $gn = 0.5E_R$. In the interacting case, one notices the appearance of the phononic regime in the lowest band,

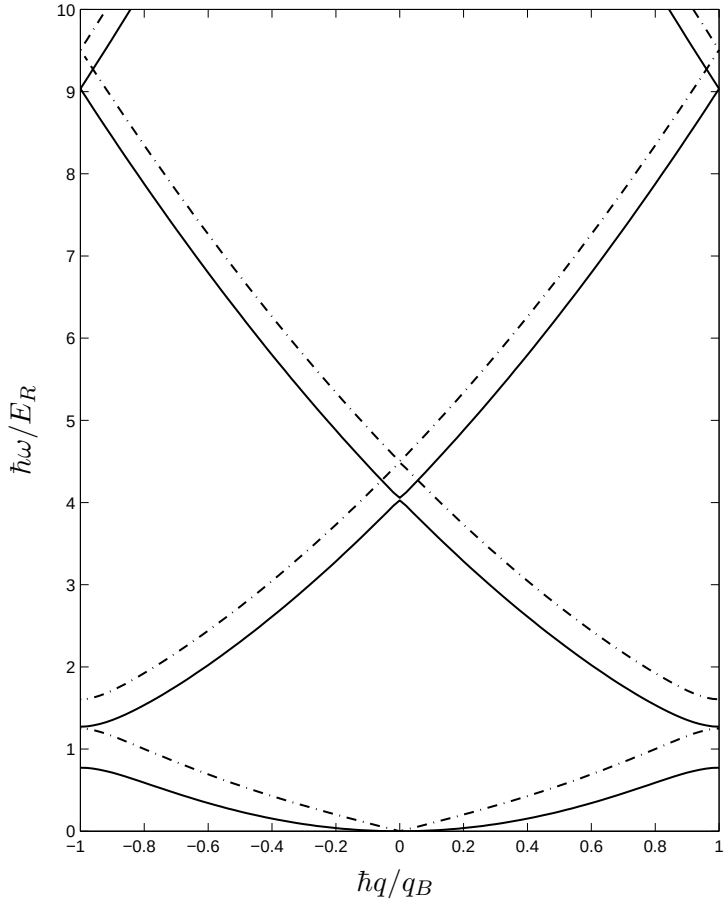

Figure 7.1: Bogoliubov bands $\hbar\omega_j(q)$ obtained from the solution of (7.14,7.15) in the first Brillouin zone for $s = 1$, $gn = 0$ (solid line) and $gn = 0.5E_R$ (dash-dotted line). Note that for such a small potential, the gap between second and third band is still very small.

while high bands differ from the non-interacting ones mainly by an energy shift gn. This is a general feature: For a given gn and s, sufficiently high bands are not affected by the lattice, but are governed by the behavior of the Bogoliubov spectrum of the uniform gas at momenta much larger than the inverse healing length $\hbar/\xi$

$$\hbar\omega_{\rm uni}(q) = \sqrt{q^2/2m(q^2/2m + 2gn)} \approx \hbar q^2/2m + gn\,, \tag{7.16}$$

where momenta lying in the j-th Brillouin zone are mapped to the j-th band.

In Fig.7.2 we compare the lowest Bogoliubov and Bloch bands with the single particle energy. Clearly, the lowest Bloch band is less affected by the presence of interactions than the Bogoliubov band. Similarly, in the uniform case the Bogoliubov dispersion is strongly affected by interactions while the Bloch dispersion, obtained simply from a Galilei transformation, does not involve interaction effects at all. The enhanced effect of interaction on the Bogoliubov bands can be understood by recalling that the Bogoliubov band gives the energy of a small perturbation propagating in a large background condensate while the Bloch band gives the energy per particle related to the motion of the condensate as a whole.

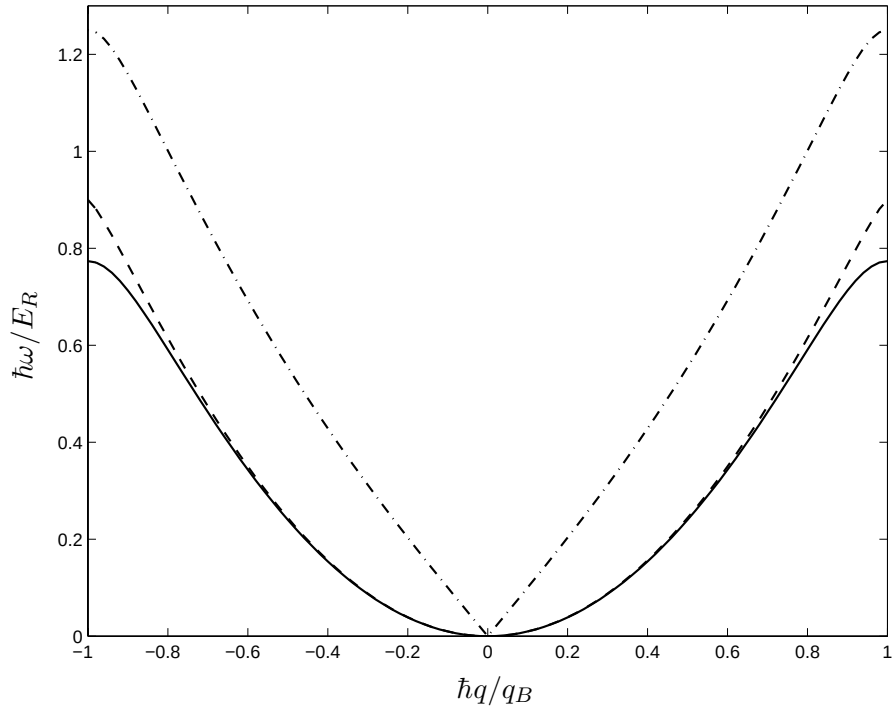

Figure 7.2: Lowest Bloch band (dashed line) and lowest Bogoliubov band (dash-dotted line) for $s = 1$ and $gn = 0.5E_R$ compared with the single particle Bloch band (solid line). In the case of the Bloch bands (solid and dashed line) the groundstate energy has been subtracted .

The solid lines in Fig.7.3 show how the lowest Bogoliubov band changes when the lattice depth is increased at fixed interaction. At $s = 1$ (Fig.7.3a), apart from the formation of the energy gap close to $q = q_B$, the curve still resembles the dispersion in the uniform case: both the phononic linear regime at small q and the quadratic regime at larger q are visible. When the potential is made deeper ($s = 5, 10$; Fig.7.3b,c), the band becomes flatter. As a consequence, the quadratic regime disappears and the slope of the phononic regime decreases. This reflects the strong decrease of the velocity of sound as the lattice is made deeper (see discussion below in section 7.4).

In Fig.7.4, we plot the energy gap between lowest and first excited band as a function of lattice depth for $gn/E_R = 1$. For comparison, we display the corresponding curve for the energy gap in the Bloch band spectrum of a single particle (see Fig.6.6). In addition, we plot the gap $2\sqrt{s}E_R$ between the vibrational levels obtained when approximating the bottom of a lattice well by a harmonic potential (see Eq.(6.48)). It turns out that the gap in the Bogoliubov band spectrum approaches the one in the single particle spectrum as s is tuned to large values. This is the case because in a very deep lattice the first excited band is almost not affected by interactions and is hence essentially given by the single particle Bloch band while the lowest Bogoliubov band becomes so flat that the excitation energy at the zone boundary is negligibly small compared to the energies of the second band. Note that the convergence to the gap $2\sqrt{s}E_R$ of the harmonic approximation is very slow, reflecting mainly the role of the anharmonicity of the potential wells.

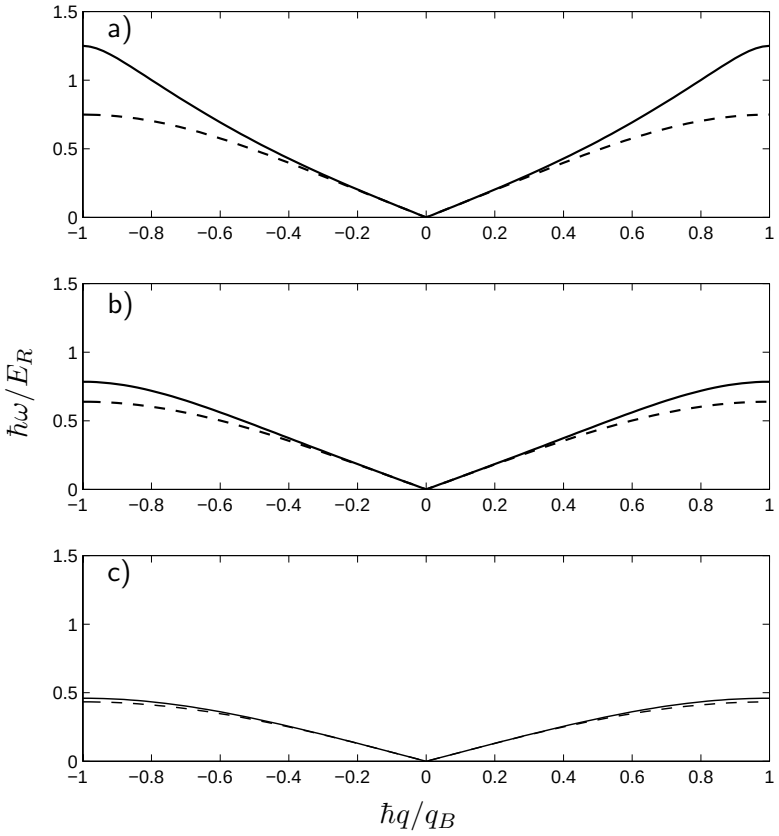

Figure 7.3: Lowest Bogoliubov band at $gn = 0.5E_R$ for different values of the potential depths: $s = 1$ (a), $s = 5$ (b) and $s = 10$ (c). The solid lines are obtained from the numerical solution of Eqs.(7.14,7.15) while the dashed lines refer to the tight-binding expression (7.38).

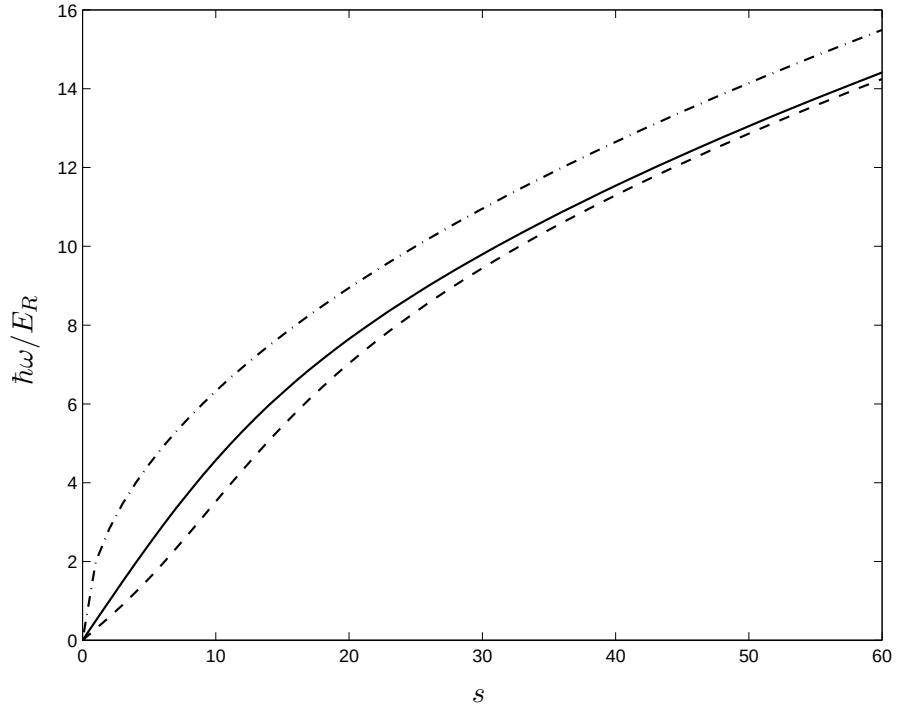

Figure 7.4: Energy gap at the zone boundary between lowest and first excited Bogoliubov band as a function of lattice depth for $gn = 0$ (solid line) and $gn = 1E_R$ (dashed line). For comparison, we also plot the gap $2\sqrt{s}E_R$ between the vibrational levels obtained when approximating the bottom of a lattice well by a harmonic potential (dash-dotted line).

Bogoliubov amplitudes

The functions $\tilde{u}_{jq}(z)$ and $\tilde{v}_{jq}(z)$ in (7.11,7.12) are periodic with period d. Their Fourier expansion reads

$$\tilde{u}_{jq}(z) = \sum_l b_{jql}\, e^{il\frac{2\pi z}{d}}\,, \tag{7.17}$$

$$\tilde{v}_{jq}(z) = \sum_l c_{jql}\, e^{il\frac{2\pi z}{d}}\,. \tag{7.18}$$

The normalization condition requires

$$d\sum_l \left(b^*_{jql}b_{j'ql} - c^*_{jql}c_{j'ql}\right) = \delta_{jj'}\,. \tag{7.19}$$

With q satisfying periodic boundary conditions this is sufficient to ensure the orthonormalization conditions (7.8,7.9) where the index σ is replaced by the band index j and the quasi-momentum q of the excitations.

In Figs. 7.5 and 7.6 we plot the square modulus of the Fourier coefficients b_{jql} and c_{jql} at different values of q in the first and the second Bogoliubov band for $gn = 0.5E_R$ at a lattice depth of $s = 1$, $s = 5$ and $s = 10$ respectively.

At all considered lattice depth, the relative importance of the Bogoliubov v_{jq}-amplitude with respect to the u_{jq}-amplitude diminishes in the transition from the lowest to the first excited band. In fact, the contribution of the v_{jq}-amplitude is negligible in all considered cases in the second band. Hence, for $gn = 0.5E_R$, apart from an energy offset, essentially only the lowest Bogoliubov band differs from the Bloch bands of a single particle. This can be explained by the fact that for this choice of the parameter gn/E_R, the healing length of the system is comparable to the lattice period d, a setting which is typical of current experiments. As a consequence, when the lattice is off the v_{jq}-amplitude is relevant only at momenta $\hbar q << q_B$ and thus is negligible in higher bands. Switching on the lattice can change this situation only in the lowest band.

Figs. 7.5 and 7.6 show that within the lowest Bogoliubov band, the relative magnitude of the Bogoliubov v_q-amplitude with respect to the u_q-amplitude is most relevant at small values of the quasi-momentum q, associated with small excitation energies $\hbar\omega(q)$ and a phonon-character of the excitations $\hbar\omega(q) \sim q$. At low lattice depth the Bogoliubov v_q-amplitude becomes in fact completely irrelevant as q is tuned towards q_B, i.e. to values outside the phononic regime. Yet, the deeper the lattice the larger becomes the relative magnitude of the Bogoliubov v_q-amplitude also at values of q close to q_B. In particular, Fig. 7.6 demonstrates that at $s = 10$ the v_q-amplitude takes values comparable to those of the u_q-amplitude even at $q = 0.9q_B$ where the band spectrum does *not* have a linear dependence on q. We conclude that in a sufficiently deep lattice, the elementary excitations of the lowest Bogoliubov band have quasi-particle character even though they are phonons only for very small q.

The comparison of Figs. 7.5 and 7.6 also illustrates that the Bogoliubov amplitudes are more strongly modulated s the potential depth s is increased giving rise to an increase in the number of relevant fourier coefficients in the sums (7.17,7.18). Besides, they become larger in the lowest band. In fact, as we will discuss in more detail in the following section, the Bogoliubov amplitudes of the lowest band become proportional to the condensate wavefunction

as $s \to \infty$. The normalization (7.8) can then only be ensured if u_q and v_q grow to infinity in this limit.

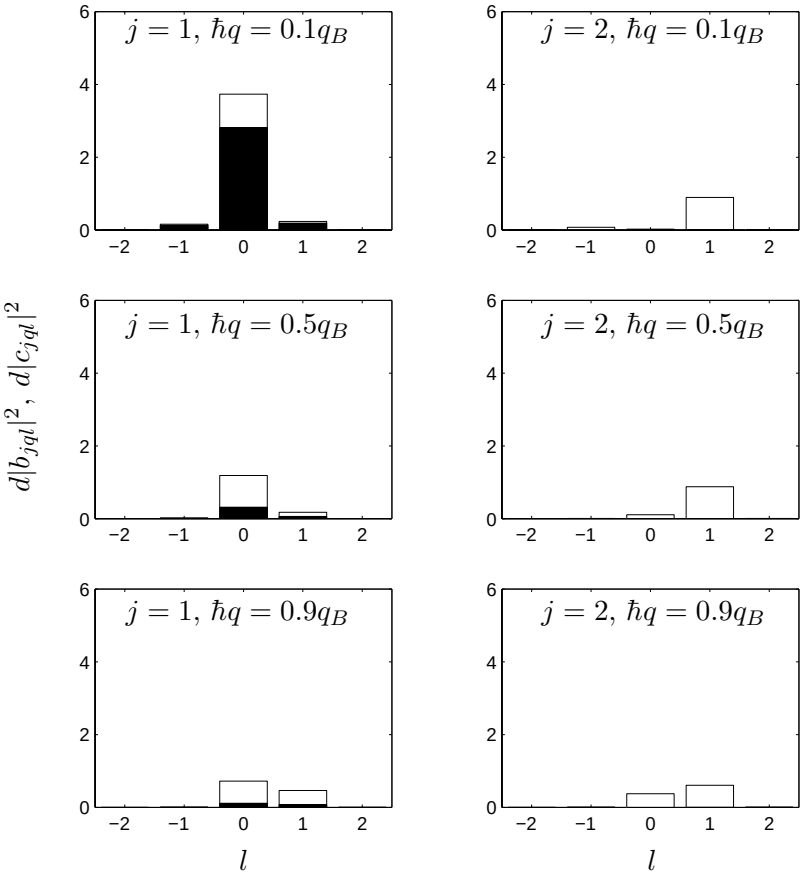

Figure 7.5: Square modulus of the Fourier coefficients b_{jql} (white bars) and c_{jql} (black bars) of $\tilde{u}_{jq}(z)$ and $\tilde{v}_{jq}(z)$ respectively as defined in (7.17,7.18) for the lowest Bogoliubov band ($j = 1$, left column) and the first excited Bogoliubov band ($j = 2$, right column) at $q = 0.1q_B, 0.5q_B, 0.9q_B$ as obtained from the numerical solution of Eqs.(7.14,7.15) with $gn = 0.5E_R$ and lattice depth $s = 5$.

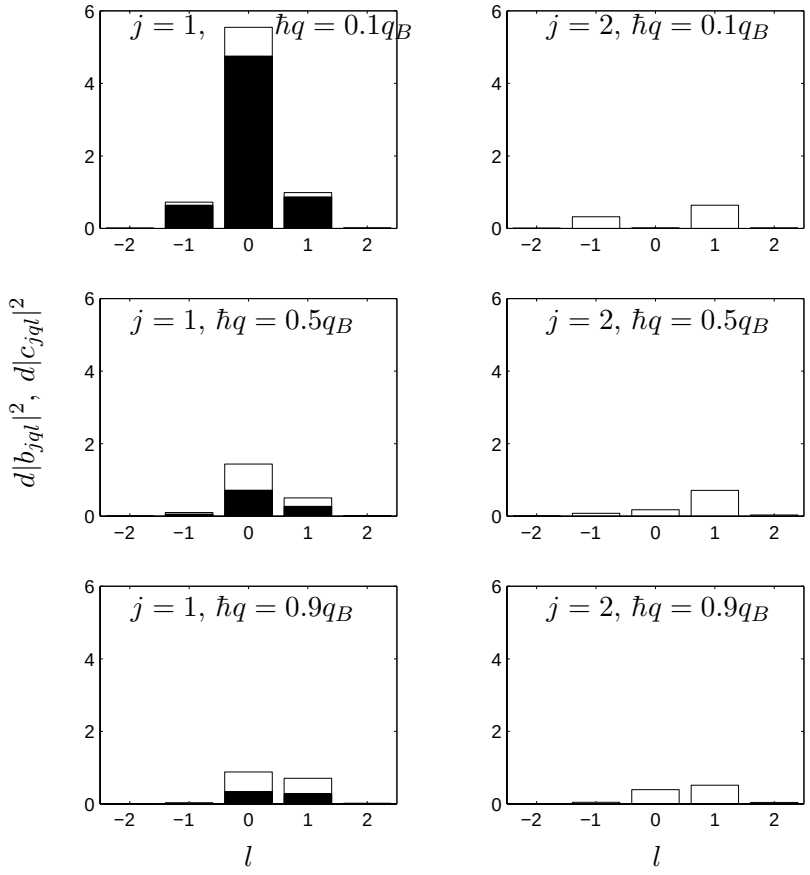

Figure 7.6: Square modulus of the Fourier coefficients b_{jql} (white bars) and c_{jql} (black bars) of $\tilde{u}_{jq}(z)$ and $\tilde{v}_{jq}(z)$ respectively as defined in (7.17,7.18) for the lowest Bogoliubov band ($j = 1$, left column) and the first excited Bogoliubov band ($j = 2$, right column) at $q = 0.1q_B, 0.5q_B, 0.9q_B$ as obtained from the numerical solution of Eqs.(7.14,7.15) with $gn = 0.5E_R$ and lattice depth $s = 10$.

7.3 Tight binding regime of the lowest Bogoliubov band

Since the Bogoliubov amplitudes have Bloch form (see Eqs.(7.11,7.12)), we can find Wannier functions $f_{u,j}(z)$ and $f^{(v)}_{l,j}(z)$ for the u_{jq} and the v_{jq}-amplitudes respectively. In their respective Wannier basis, the Bogoliubov amplitudes read

$$u_{jq}(z) = \frac{1}{\sqrt{N_w}} \sum_l f^{(u)}_{l,j}(z - ld) e^{iqld}\,, \tag{7.20}$$

$$v_{jq}(z) = \frac{1}{\sqrt{N_w}} \sum_l f^{(v)}_{l,j}(z - ld) e^{iqld}\,. \tag{7.21}$$

The Wannier functions $f^{(u)}_{l,j}$ and $f^{(v)}_{l,j}$ are in general different from each other and from the Wannier functions f_j (see Eq.(6.25)) of the condensate in a Bloch state. Yet, in the tight

binding regime, the situation is simpler in the case of the lowest band: Since the excitation energies go to zero as s is increased, the Bogoliubov amplitudes are approximately proportional to the condensate wavefunction of the groundstate. So we set

$$u_q(z) = \frac{1}{\sqrt{N_w}} U_q \varphi_q(z) \tag{7.22}$$

$$v_q(z) = \frac{1}{\sqrt{N_w}} V_q \varphi_q(z)\,, \tag{7.23}$$

where U_q and V_q are numbers that depend on the quasi-momentum q. The normalization condition (7.8) implies that

$$|U_q|^2 - |V_q|^2 = 1\,. \tag{7.24}$$

Expanding the condensate wavefunction in its Wannier basis we can write

$$u_q(z) = \frac{1}{\sqrt{N_w}} U_q \sum_l f_l(x) e^{iqld} \tag{7.25}$$

$$v_q(z) = \frac{1}{\sqrt{N_w}} V_q \sum_l f_l(x) e^{iqld}\,. \tag{7.26}$$

Our discussion of elementary excitations in the tight binding regime of the lowest Bogoliubov band will be based on these expressions for the Bogoliubov amplitudes. We presuppose the lowest Bloch band to be within the tight binding regime so that only next-neighbour overlap has to be considered.

Lowest Bogoliubov band

To solve for the lowest Bogoliubov band $\hbar\omega(q)$, we first add and subtract the two equations (7.14,7.15) yielding two coupled equations for $u_q + v_q$ and $u_q - v_q$

$$L_1(u_q + v_q) = \hbar\omega(q)(u_q - v_q)\,, \tag{7.27}$$

$$L_3(u_q - v_q) = \hbar\omega(q)(u_q + v_q)\,, \tag{7.28}$$

where

$$L_1 = -\frac{\hbar^2}{2m}\frac{\partial^2}{\partial z^2} + sE_R \sin^2\left(\frac{\pi z}{d}\right) + d\,gn\,|\varphi(z)|^2 - \mu\,, \tag{7.29}$$

$$L_3 = -\frac{\hbar^2}{2m}\frac{\partial^2}{\partial z^2} + sE_R \sin^2\left(\frac{\pi z}{d}\right) + 3d\,gn\,|\varphi(z)|^2 - \mu\,. \tag{7.30}$$

Eliminating $u_q + v_q$ or $u_q - v_q$ from (7.27,7.28), we obtain

$$L_3\,L_1(u_q + v_q) = \hbar^2\omega(q)^2(u_q + v_q)\,, \tag{7.31}$$

$$L_1\,L_3(u_q - v_q) = \hbar^2\omega(q)^2(u_q - v_q)\,. \tag{7.32}$$

The matrix elements of L_1 and L_3 take the form

$$\langle f_l|L_1|f_l\rangle = \delta\,, \qquad \langle f_l|L_1|f_{l\pm1}\rangle = -\frac{\delta}{2}\,, \tag{7.33}$$

$$\langle f_l|L_3|f_l\rangle = 3\delta - 2\delta_\mu + 2gnd\int dz f^4(z)\,, \qquad \langle f_l|L_3|f_{l\pm1}\rangle = \frac{\delta}{2} - \delta_\mu\,. \tag{7.34}$$

As in the previous chapter 6.2, we have neglected next-neighbour terms of the kind $\int dz f_l^2 f_{l\pm1}^2$ and we have used the definitions of the tunneling parameters δ and δ_μ (see Eqs.(6.31,6.34)). Eqs.(7.27,7.28) become

$$(U_q - V_q) 2\delta \sin^2\left(\frac{qd}{2}\right) = \hbar\omega(q)(U_q + V_q)\,, \tag{7.35}$$

with

$$\hbar\omega(q) = \sqrt{2\delta \sin^2\left(\frac{qd}{2}\right)\left(2\left(2\delta_\mu - \delta\right)\sin^2(\frac{qd}{2}) + 2dgn\int dz f^4(z) + 4\left(\delta - \delta_\mu\right)\right)} \tag{7.36}$$

Comparison of the tight binding expression for the compressibility (6.43) with $\delta - \delta_\mu$ (6.36) and $n\partial\delta/\partial n$ (6.38) allows us to rewrite (7.36) in the form

$$\boxed{\hbar\omega(q) = \sqrt{2\delta \sin^2\left(\frac{qd}{2}\right)\left(2\left(\delta + 2n\frac{\partial\delta}{\partial n}\right)\sin^2\left(\frac{qd}{2}\right) + 2\kappa^{-1}\right)}\,.} \tag{7.37}$$

The density dependence of this spectrum shows up in three different ways:

- in the density dependence of δ discussed in section 6.2 and shown in Fig.6.8 (where the quantity $m^* \propto 1/\delta$ (see relation (6.41)) is plotted);
- in the density dependence of κ^{-1} which in the tight binding regime can be usually approximated by the linear law $\tilde{g}n$ (see Fig.5.5);
- a contribution due to the density derivative of δ appears. However its effect in the Bogoliubov band (7.37) is always small: for small interactions one has $n\partial\delta/\partial n \ll \delta$; instead, for larger interactions the inverse compressibility κ^{-1} dominates both δ and $n\partial\delta/\partial n$. Hence, we rewrite (7.37) neglecting this term

$$\hbar\omega(q) = \sqrt{2\delta \sin^2\left(\frac{qd}{2}\right)\left(2\delta \sin^2\left(\frac{qd}{2}\right) + 2\kappa^{-1}\right)} \tag{7.38}$$

  Note that, as is discussed below in section 7.4 and shown in [116, 118] contributions due to $n\partial\delta/\partial n$ can significantly affect the excitation frequency calculated on top of a moving condensate.

Fig.7.3 compares the numerical data with the approximate expression (7.38), evaluated using the quantity κ^{-1} calculated in section 5.2 and the tunneling parameter δ calculated in section 6.1. As already found for the lowest Bloch band, for this value of gn, the agreement with the tight binding expression is already good for $s = 10$.

It is possible to identify two regimes, where the lowest Bogoliubov band (7.38) can be described by further simplified expressions:

- for very large potential depth, the spectrum is dominated by the compressibility term. In fact, $\delta \to 0$ while κ^{-1} becomes larger and larger as s increases. Hence, for large enough

s with fixed gn, we can neglect the term of $\mathcal{O}(\delta^2)$ under the squareroot in Eq.(7.38) and the spectrum takes the form

$$\hbar\omega(q) = 2\sqrt{\delta\kappa^{-1}}\left|\sin\left(\frac{qd}{2\hbar}\right)\right|, \tag{7.39}$$

Of course for large gn, the proper density-dependence of δ and κ^{-1} has to be taken into account in evaluating (7.39). Note that the Bogoliubov band becomes very flat since δ decreases exponentially for large lattice depth s. Yet, its height decreases more slowly than the one of the lowest Bloch band (6.29) whose width decreases linearly in δ. To illustrate this characteristic difference in the behaviour of the lowest Bogoliubov and Bloch bands, we compare in Fig.7.7 the numerically obtained band heights.

- for small enough gn, one can neglect the density dependence of δ and use the approximation $\kappa^{-1} = \tilde{g}n$ for the compressibility, where $\tilde{g}$ takes the form (6.45) in the tight binding regime. This yields

$$\hbar\omega(q) = \sqrt{2\,\delta_0\,\sin^2\left(\frac{qd}{2\hbar}\right)\left[2\,\delta_0\,\sin^2\left(\frac{qd}{2\hbar}\right) + 2\tilde{g}n\right]}, \tag{7.40}$$

which was first obtained in [122] (see also [115, 123, 124]). Eq.(7.40) has a form similar to the well-known Bogoliubov spectrum of uniform gases, the energy $2\delta_0\sin^2(qd/2\hbar)$ replacing the free particle energy $q^2/2m$.

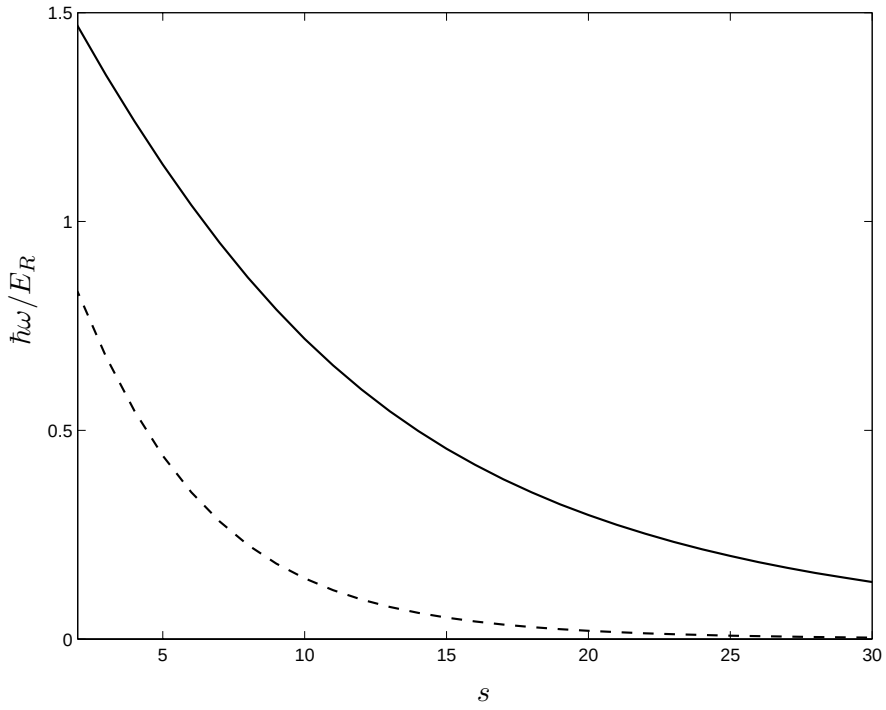

Figure 7.7: Height of the lowest Bogoliubov band $\hbar\omega(q)$ (solid line) and the lowest Bloch energy band (6.4) (dashed line) for $gn = 1E_R$ as a function of lattice depth s.

Bogoliubov Bloch amplitudes of the lowest band

Using the normalization conditon for the Bogoliubov amplitudes (7.24), Eq.(7.35) yields

$$U_q = \frac{\varepsilon_q + \hbar\omega_q}{2\sqrt{\hbar\omega_q \varepsilon_q}}, \tag{7.41}$$

$$V_q = \frac{\varepsilon_q - \hbar\omega_q}{2\sqrt{\hbar\omega_q \varepsilon_q}}, \tag{7.42}$$

where $\varepsilon_q = 2\delta \sin^2(qd/2)$ is the lowest energy Bloch band (6.29) from which the groundstate energy has been subtracted.

According to (7.22,7.23) the coefficients of the Fourier expansion of the Bogoliubov Bloch waves $\tilde{u}$, $\tilde{v}$ read

$$b_{ql} = U_q a_{ql}\,, \tag{7.43}$$

$$c_{ql} = V_q a_{ql}\,, \tag{7.44}$$

where a_{ql} are the coefficients of the Fourier expansion of the condensate Bloch wave $\tilde{\varphi}_q$. In Fig. 7.8 we compare the square moduli $|b_{ql}|^2$, $|c_{ql}|^2$ obtained from the approximation (7.43,7.44) with those obtained from the exact Fourier expansion (7.17,7.18) of the numerical solutions of the Bogoliubov equations (7.14,7.15). As previously, we evaluate the expressions (7.41,7.42) for U_q, V_q using the numerical results for κ and m^*. We find that the agreement between the full numerical and the tight binding results is very good.

The large-s limit of the ratio of U_q/V_q for non-zero interaction gn/E_R reads

$$\boxed{\frac{U_q}{V_q} \approx -\left(1 + \sqrt{2\delta\kappa}\,|\sin(qd/2)|\right)\,.} \tag{7.45}$$

The second term is small and decreases rapidly as a function of s implying that in the tight binding regime U_q and V_q are of the same order of magnitude in the whole Brillouin zone. This shows that all excitations of the lowest Bogoliubov band acquire quasi-particle character. For large gn/E_R (small κ) this behavior is enhanced. Note that the second term decreases with increasing s like the band height of the lowest Bogoliubov band in the large-s limit (see Eq.(7.39) and Fig. 7.7).

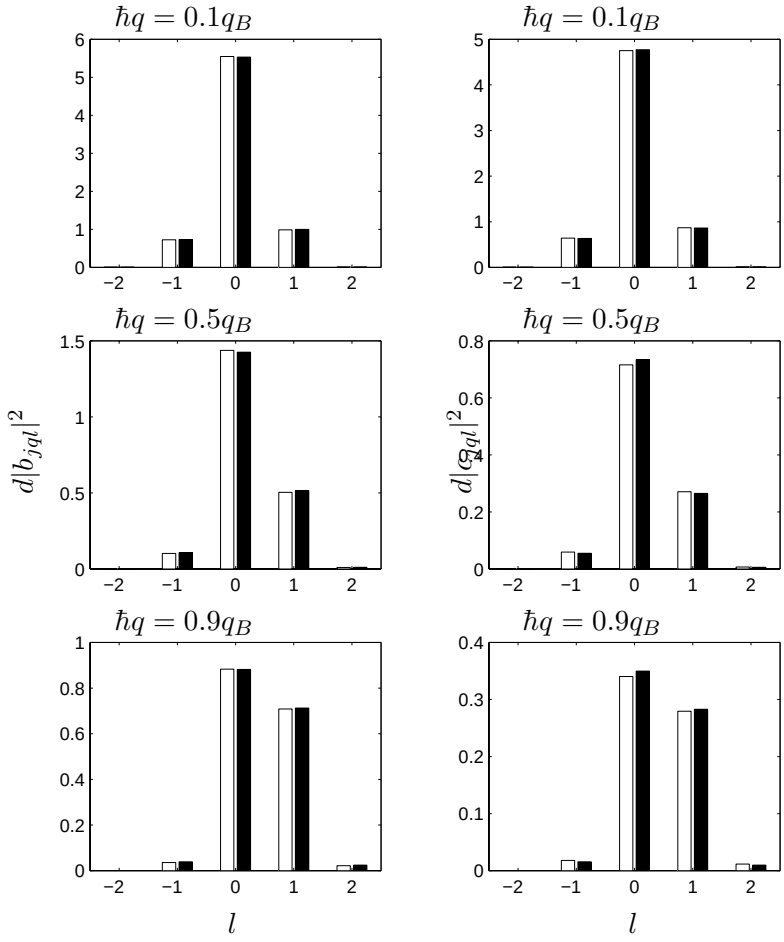

Figure 7.8: Fourier coefficients b_{ql}, c_{ql} of the Bogoliubov Bloch waves $\tilde{u}_q$ and $\tilde{v}_q$ respectively: Comparison of the tight binding approximation (7.43,7.44) (black bars) with the restults obtained from the numerical solutions of the Bogoliubov equations (7.14,7.15) (white bars) at lattice depth $s = 10$ for $gn = 0.5E_R$. Left column: $|b_{ql}|^2$. Right column: $|c_{ql}|^2$.

7.4 Velocity of sound

The low energy excitations of a stable stationary Bloch state φ_{jk} are sound waves. The corresponding dispersion law is linear in the quasi-momentum $\hbar q$ of the excitation. In general, the spectrum $\hbar\omega(q)$ is not symmetric with respect to $q = 0$ giving rise to two sound velocities c_+ and c_-

$$\hbar\omega(q) \to c_+ \hbar q\,, \qquad \text{for } q \to 0^+\,, \tag{7.46}$$

$$\hbar\omega(q) \to c_- \hbar q\,, \qquad \text{for } q \to 0^-\,. \tag{7.47}$$

For a carrier condensate with quasi-momentum $\hbar k > 0$, the velocities c_+ and c_- refer to sound waves propagating in the same and in the opposite direction as stationary current respectively. Their values depend on the quantum numbers j, k of the stationary condensate, on lattice depth s and interaction strength gn. They can be determined from the slope of the lowest Bogoliubov band at $q = 0$. We first address in detail the case $k = 0$ and then discuss $k \neq 0$.

Sound in a condensate at rest

In section 7.2, we have presented the results for the Bogoliubov bands of a condensate in the groundstate. By determining the slope of the lowest Bogoliubov band at $q = 0$, we obtain the sound velocity as a function of s and gn/E_R. The results are presented in Fig.7.9 where we plot the ratio $c(s)/c(s = 0)$ for different values of gn/E_R. The presence of the lattice leads to a slow-down of sound. For $gn = 0.5E_R$ the decrease of the sound velocity amounts to about 34% and 71% at $s = 10$ and $s = 20$ respectively. In fact, the hydrodynamic formalism developed below in section 9 allows us to derive the relation

$$\boxed{c = \frac{1}{\sqrt{m^*\kappa}}\,.} \tag{7.48}$$

Hence, the decrease of the sound velocity is a consequence of the exponential increase of the effective mass m^*. which overcompensates the decrease of the compressibility κ. It is not the enhanced rigidity which governs the sound velocity, but the fact that the atoms are slowed down by the potential barriers. To underline this point we also display in Fig. 7.9 the function $\sqrt{m/m^*}$ obtained for $gn = 0.5E_R$. Clearly, this quantity reproduces the characteristic features of the ratio $c(s)/c(s = 0)$.

Fig.7.9 shows that the density-dependencies of m^* and κ^{-1} lead to a slight increase of the ratio $c(s)/c(s = 0)$ with gn/E_R for fixed s which can be understood in terms of the screening effect of interactions. This effect is due to the decrease of m^* with increasing density which overcompensates the decrease of $1/gn\kappa$ (see Figs. 5.5 and 6.8). For small but nonzero interaction gn one obtains the law $c(s)/c(s = 0) = \sqrt{(m/m^*)(\tilde{g}/g)}$ with the effective coupling constant $\tilde{g}$ as defined in Eq.(5.15).

Note that in the tight binding regime the sound velocity (7.48) can also be obtained from the low-q limit of the expression for the lowest Bogoliubov band (7.38).

The results for the sound velocity presented in this section concern sound waves of small amplitude. Such sound waves exist as long as the system is superfluid and hence at all lattice depths for which GP-theory can be applied. Yet, it remains a question whether sound waves of finite amplitude can propagate at a certain s. This problem will be discussed in chapter 11.

Sound in a moving condensate

The energy of a sound wave excitation in a moving uniform condensate observed from the lab frame is related to its energy in the rest frame by the Galilei transformation

$$\hbar\omega(q) = c\hbar|q| \pm \frac{\hbar|k|}{m}\hbar|q|\,. \tag{7.49}$$

Here, c is the sound velocity in the rest frame, $\hbar k$ is the momentum associated with the relative motion of the two frames and q is the wave number of the sound wave in the rest frame. The plus- and minus-sign hold when the sound wave propagates in the same and in the opposite direction as the condensate respectively. Hence, the sound velocities observed in the lab frame are obtained by simply adding or subtracting c to/from the velocity $\hbar|k|/m$ of the moving

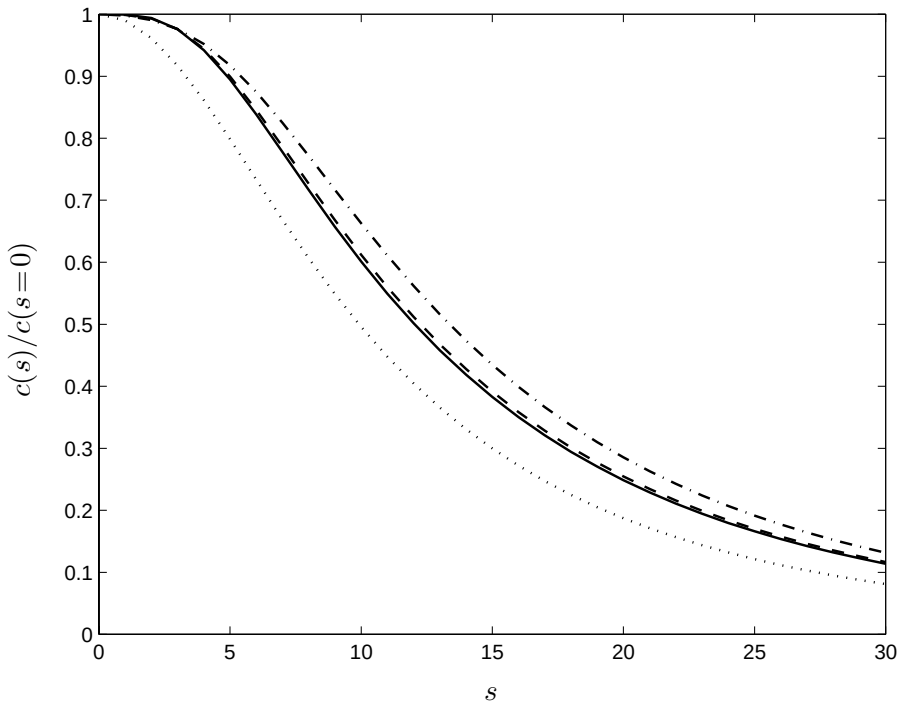

Figure 7.9: Ratio between the sound velocity $c(s)$ at lattice depth s and the sound velocity $c(s=0)$ for $gn = 0.02E_R$ (solid line), $gn = 0.1E_R$ (dashed line) and $gn = 0.5E_R$ as a function of lattice depth s. The dotted line depicts the quantity $\sqrt{m/m^*}$ for $gn = 0.5E_R$.

condensate

$$c_k = c \pm \frac{\hbar|k|}{m}\,. \tag{7.50}$$

To generalize this result to account for the presence of a lattice, we first consider a condensate in a Bloch state of the lowest band moving with a *small* group velocity $\bar{v}$ with respect to the lab frame (see discussion section 6.1)

$$\bar{v} = \frac{\hbar k}{m^*}\,, \tag{7.51}$$

where $\hbar k$ is the quasi-momentum of the condensate and m^* is its effective mass in the lowest band at $k = 0$ for a given lattice depth s. As mentioned above, the sound velocity in such a condensate can be obtained by solving the Bogoliubov equations (7.6,7.7) with $j = 1$ and small k and by extracting the slopes of the resulting lowest Bogoliubov band $\hbar\omega(q)$ for $q \to \pm 0$. As in the case $s = 0$ (see Eq.(7.50)), the Bogoliubov bands are asymmetric with respect to $q = 0$ if $k \neq 0$ and the sound velocity depends on the sign of q.

An alternative to the numeric solution of (7.6,7.7) is offered by the hydrodynamic formalism developed below in chapter 9. Its application allows us to derive the analytic result

$$\hbar\omega(q) = c\hbar|q| \pm \frac{\hbar|k|}{m^*_\mu}\hbar|q|\,, \tag{7.52}$$

where c is the sound velocity (7.48) in the condensate at rest and m^*_μ is the effective mass obtained from the chemical potential band spectrum (see Eq.(6.23)). Hence, in the lab frame the sound velocity is given by

$$c_k = c \pm \frac{\hbar|k|}{m^*_\mu} \,. \tag{7.53}$$

The plus- and minus-sign hold when the sound wave propagates in the same and in the opposite direction as the condensate respectively. Since the quantity $\hbar k/m^*_\mu$ is generally different from the group velocity $\bar{v} = \hbar k/m^*$, the sound velocity is not generally obtained by adding $\bar{v}$ and c in the case of copropagating sound waves, or by subtracting $\bar{v}$ from c in the case of counterpropagation. This is the case only for $s = 0$ where $m^* = m^*_\mu = m$. It is interesting to note that the result (7.53) gives a physical meaning to the quantity m^*_μ.

In the tight binding regime, we can write $c_k = c \pm (\bar{v} + (\delta_\mu - \delta)d^2k/\hbar)$, where $\delta_\mu - \delta = n\partial\delta/\partial n$ (see Eqs.(6.38,6.36)), in order to show that the density-derivative of δ plays an important role. We remind that, in contrast, contributions arising from this quantity are negligible as far as excitations of groundstate condensate are concerned (see discussion in section 7.3).

Expression (7.53) has been derived assuming a small value of the condensate quasi-momentum k. The hydrodynamic formalism can also be employed to calculate the sound velocity for any value of k. The result reads [107, 125] (see also section 9 below)

$$c_k = \sqrt{\frac{n}{m^*(k)}\frac{\partial\mu(k)}{\partial n}} \pm \left|\frac{\partial\mu(k)}{\partial k}\right| \,, \tag{7.54}$$

where $m^*(k)$ is the generalized effective mass (6.22) with $j = 1$. Expanding this expression up to $\mathcal{O}(k)$ at $k = 0$, we recover result (7.53).

Chapter 8

Linear response - Probing the Bogoliubov band structure

The Bogoliubov band structure can be probed by exposing the condensate to a weak external perturbation: The linear response of the system involves transitions between the initial groundstate and the excited states of the Bogoliubov spectrum. The spectrum of excitations is determined by scanning both transferred energy and momentum and by recording the encountered resonances.

In this chapter we will consider the particular case in which the external probe generates a density perturbation in the system. This can be achieved experimentally by doing Bragg spectroscopy where the system is illuminated with two laser beams. The absorption of a photon from one beam initiates the stimulated emission of a photon into the second beam. The difference between the wavevectors of the two beams and their detuning fixes the momentum and the energy transferred to sample. So far, this technique has been used successfully to investigate condensates without lattice [126, 127, 128, 129, 130, 131]. A method equivalent to Bragg spectroscopy is offered by the possibility to manipulate the lattice itself in a time-dependent way [132, 79, 91]: A modulation of the lattice depth transfers momentum $0, \pm 2q_B$ and energy $\hbar\omega$, where ω is the frequency of the modulation.

The presence of the lattice brings about significant changes with respect to the linear response of the uniform system: Not only does the spectrum of excitations change (see previous chapter 7) and therefore the resonance conditon for a probe to transfer momentum and energy, but also the excitation strengths for a particular momentum transfer feature a strong dependence on lattice depth and density.

In section 8.1 we present results for the dynamic structure factor of a condensate loaded into a one-dimensional lattice: We show that when keeping the momentum transfer fixed while scanning the energy transfer a resonance is encountered for each Bogoliubov band. This implies that the j-th band can be excited even if the transferred momentum does not lie in the j-th Brillouin zone. Due to phononic correlations the excitation strength towards the lowest Bogoliubov band develops a typical oscillating behaviour as a function of the momentum transfer, and vanishes at even multiples of the Bragg momentum. Even though the excitation energies $\hbar\omega_j(p)$ are periodic as a function of p, this is not true for the excitation strength to the j-th band.

The effects of interactions on the static structure factor are found to be significantly amplified by the presence of the optical potential (see section 8.2). Using a sum rule approach, we prove that the static structure factor vanishes like $p/2m^*c$ for $p \to 0$, where m^* and c are the effective mass and the sound velocity at a given lattice depth respectively.

In [133], we have reported the numerical and analytical results for the excitation strengths of the lowest band and for the static structure factor. The discussion of the excitation strengths of higher bands is added here.

8.1 Dynamic structure factor

The capability of the system to respond to an external density probe transferring momentum $\mathbf{p}$ and energy $\hbar\omega$ is described by the dynamic structure factor

$$S(\mathbf{p},\omega) = \sum_{\sigma} \left|\langle\sigma|\delta\hat{\rho}^{\dagger}_{\mathbf{p}}|0\rangle\right|^2 \delta\left(\omega-\omega_{\sigma}\right) . \tag{8.1}$$

Here, σ labels low energy excitations, $|0\rangle$ is the groundstate and $\delta\hat{\rho}_p$ is defined as

$$\delta\hat{\rho}_{\mathbf{p}} = \hat{\rho}_{\mathbf{p}} - \langle\hat{\rho}_{\mathbf{p}}\rangle_{eq} , \tag{8.2}$$

where $\hat{\rho}_{\mathbf{p}}$ is the Fourier transform of the density operator $\hat{n}(\mathbf{r})$

$$\hat{\rho}_{\mathbf{p}} = \int d\mathbf{r} e^{-i\mathbf{p}\cdot\mathbf{r}/\hbar}\hat{n}(\mathbf{r}) \tag{8.3}$$

and $\langle\ldots\rangle_{eq}$ denotes the expectation value at equilibrium. For a weakly interacting Bose gas, the matrix elements involved in (8.1) take the form ([1], chapter 5.7 and 7.2)

$$\left|\langle\sigma|\delta\hat{\rho}^{\dagger}_{\mathbf{p}}|0\rangle\right| = \left|\int d\mathbf{r}\left[e^{i\mathbf{p}/\hbar\cdot\mathbf{r}}\left(u^*_{\sigma}(\mathbf{r})+v^*_{\sigma}(\mathbf{r})\right)\Psi(\mathbf{r})\right]\right| , \tag{8.4}$$

where $\int d\mathbf{r}\left(u^*_{\sigma'}u_{\sigma}-v^*_{\sigma'}v_{\sigma}\right)=\delta_{\sigma',\sigma}$ and Ψ is the condensate wavefunction normalized such that $\int d\mathbf{r}|\Psi|^2 = N_{\mathrm{tot}}$. The modulus squared of this quantity yields the excitation strength for the state $|\sigma\rangle$. The response of a harmonically trapped condensate to a density probe has been theoretically studied in [134, 135, 136, 137].

To study the excitation of the system in presence of an optical lattice, we will assume $\mathbf{p}$ to be oriented along the z-axis. Rescaling the condensate wavefunction according to (5.2) and using the solutions of the Bogoliubov equations (7.14,7.15) with the orthonormalization relations (7.8,7.9,7.10) the matrix element (8.4) takes the form

$$\left|\langle\sigma|\delta\hat{\rho}^{\dagger}_{\mathbf{p}}|0\rangle\right| = \sqrt{N}\left|\int dz\left[e^{ipz/\hbar}\left(u^*_{jq}(z)+v^*_{jq}(z)\right)\varphi(z)\right]\right| . \tag{8.5}$$

Inserting the Bloch forms (7.11,7.12) for the Bogoliubov amplitudes and noting that $\left(\tilde{u}^*_{jq}(z)+\tilde{v}^*_{jq}(z)\right)\varphi(z)$ is periodic with period d, we find that the expression (8.5) is non-zero only for

$$q = p \pm l\frac{2\pi}{d} , \tag{8.6}$$

with q lying in the first Brillouin zone and l integer. In fact, since excitations with the same j and q differing by a multiple of $2\pi/d$ are physically equivalent, the quasi-momenta of one Brillouin zone exhaust all possible excitations. Yet, note that p can not be restricted to one zone, being the momentum transferred by the external probe.

Inserting (8.5) into (8.1) the dynamic structure factor (8.1) takes the form

$$S(p,\omega) = \sum_j Z_j(p)\delta(\omega - \omega_j(p))\,. \tag{8.7}$$

The quantity $Z_j(p)$ is the excitation strength to the j-th band for a given momentum transfer p.

$$Z_j(p) = N\left|\int dz\left[e^{ipz/\hbar}\left(u^*_{jq}(z)+v^*_{jq}(z)\right)\varphi(z)\right]\right|^2, \tag{8.8}$$

where q lies in the first Brillouin zone and is fixed by the relation $q = p + l2\pi/d$.

The expression (8.7) reveals some interesting properties of the dynamic structure factor in the presence of an optical lattice:

- When scanning ω for fixed momentum transfer p a resonance is encountered for each Bogoliubov band. In contrast, when the lattice is switched off only one resonance exists for a given p. An important consequence is that on one hand it is possible to excite high energy states with small values of p, and on the other hand one can excite low energy states, belonging to the lowest band, also with high momenta p outside the first Brillouin zone. This difference with respect to the uniform case can be understood by noting that the excitations created by the external probe have well-defined quasi-momentum $\hbar q$ and accordingly many momentum components $\hbar q + l2\pi/d$. The external probe couples to the component which corresponds to the momentum transfer.
- While the excitation energies $\hbar\omega_j(p)$ are periodic as a function of p, this is not true for the excitation strengths $Z_j(p)$ (see Eq.(8.8)). This reflects the difference between quasi-momentum and momentum:

To illustrate these two characteristic features of the excitation strengths in the presence of an optical lattice we plot in Fig.8.1 the three lowest Bogoliubov bands in the first three Brillouin zones for $s = 10$, $gn = 0.5E_R$ and indicate the values of the excitation strengths $Z_j(p)$ at specific values of p.

For comparison we plot in Fig. 8.2 the strengths $Z_1(p)$, $Z_2(p)$, $Z_3(p)$ for the uniform system ($s = 0$) where the Bogoliubov dispersion does not form a band structure. Yet, in order to facilitate the comparison with $s \neq 0$ we can formally map excitations for momenta lying in the j-th Brillouin zone onto the j-th band. The corresponding excitation strengths are given by (see [1] chapter 7.6)

$$Z_j(p) = N_{\rm tot}\frac{p^2/2m}{\hbar\omega_{\rm uni}(p)}\,, \tag{8.9}$$

with p lying in the jth Brillouin zone and

$$\hbar\omega_{\rm uni}(p) = \sqrt{\frac{p^2}{2m}\left(\frac{p^2}{2m}+2gn\right)} \tag{8.10}$$

the Bogoliubov dispersion of the uniform system. For p lying outside the jth Brillouin zone the strength $Z_j(p)$ is zero.

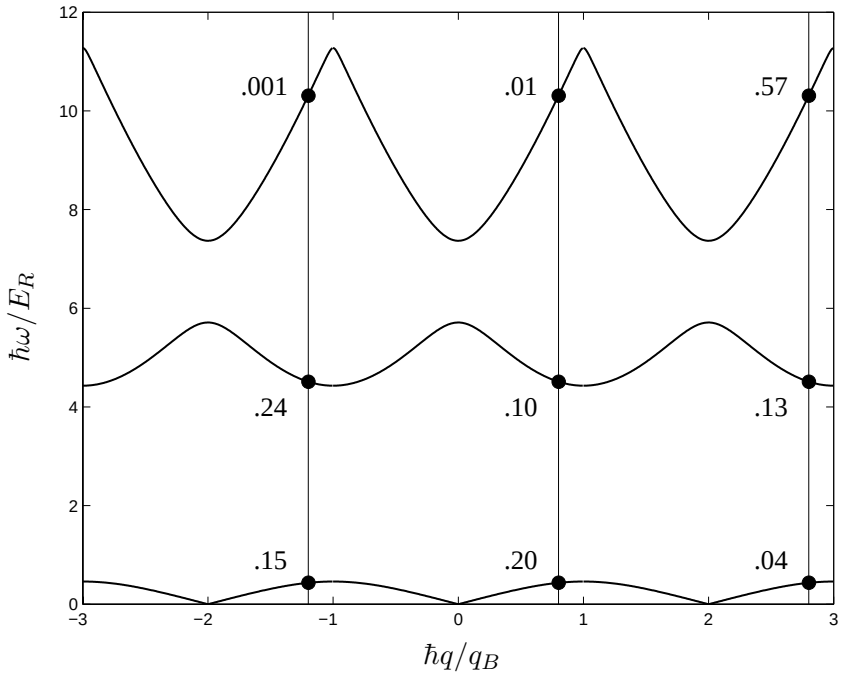

Figure 8.1: Bogoliubov bands for $s = 10$ and $gn = 0.5E_R$ in the first three Brillouin zones. Excitation strengths $Z_j/N_{\rm tot}$ (8.8) towards the states in the first three bands for $p = -1.2q_B$, $p = 0.8q_B$ and $p = 2.8q_B$.

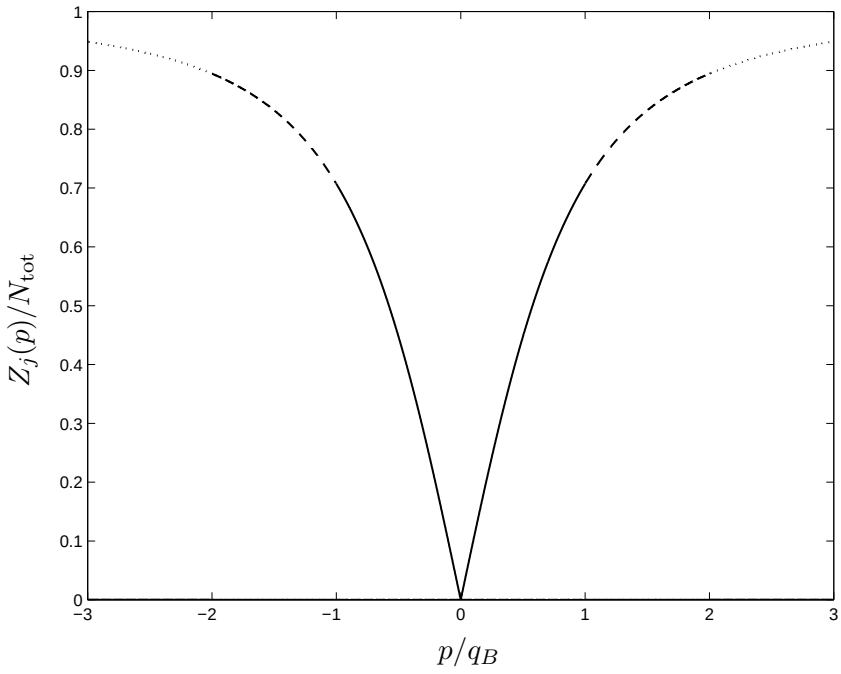

Figure 8.2: Excitation strength (8.9) to the first ($j = 1$; solid line), second ($j = 2$; dashed line) and third Bogoliubov band ($j = 3$; dotted line) without lattice ($s = 0$) for $gn = 0.5E_R$.

The excitation strength to the lowest Bogoliubov band - Numerical results

The study of the excitation strength to the lowest Bogoliubov band $Z_1(p)$ requires the evaluation of (8.8) with the solutions $u_{1q}(z)$, $v_{1q}(z)$ and $\varphi(z)$ for a given lattice depth s and interaction parameter gn/E_R. Numeric results are depicted in Figs.8.3 and 8.4 for $s = 5,\ 10$ and $gn = 0E_R, 0.02E_R$ and $gn = 0.5E_R$.

In general, we find the following characteristics:

- $Z_1(p)$ features an overall decay for increasing $|p|$. This is due to the fact that the momentum components of the created excitations are smaller at large momenta.
- Provided that $gn/E_R \neq 0$, $Z_1(p)$ exhibits characteristic oscillations: $Z_1(p)$ is suppressed in the vicinities of $p = l2\pi/d$ where the excitations contributing to the strength have phonon character and is exactly zero at $p = l2\pi/d$ (l integer) where the energy of the contributing excitation vanishes.
- Increasing gn/E_R at fixed s *or* increasing s at fixed $gn/E_R \neq 0$ leads to an overall decrease of $Z_1(p)$.

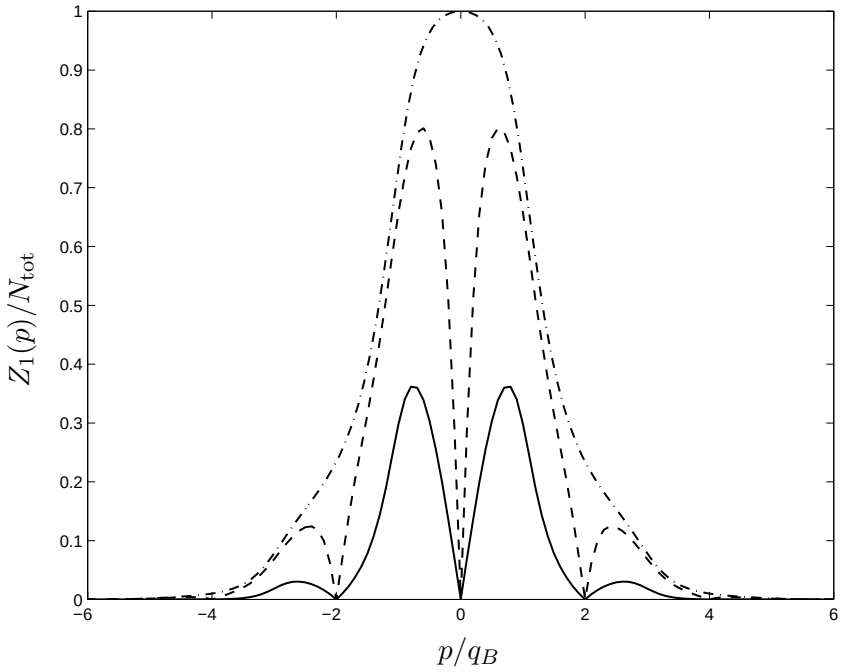

Figure 8.3: Excitation strength to the lowest Bogoliubov band $Z_1(p)$ (8.8) at lattice depth $s = 5$ for $gn = 0.5E_R$ (solid line), $gn = 0.02E_R$ (dashed line) and $gn = 0$ (dash-dotted line).

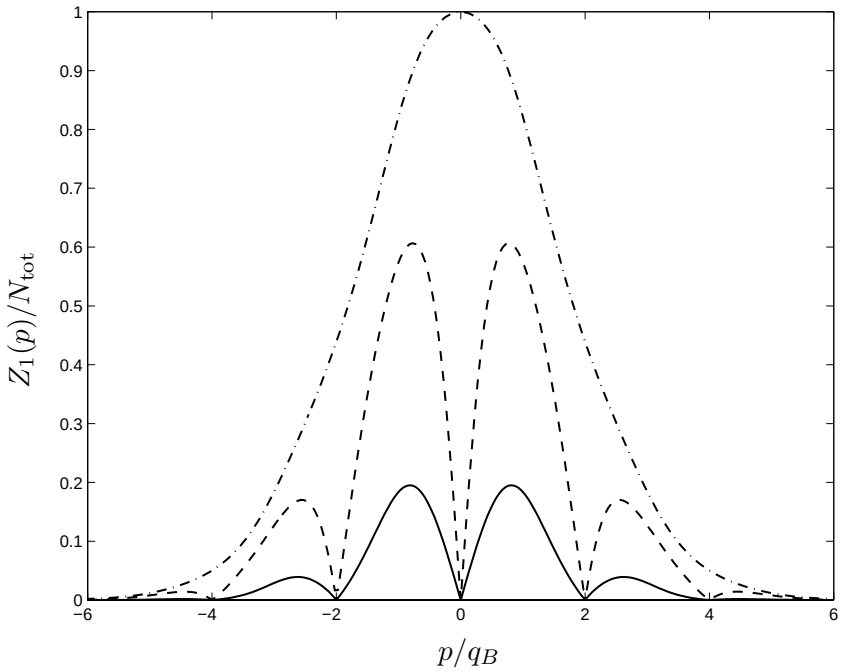

Figure 8.4: Excitation strength to the lowest Bogoliubov band $Z_1(p)$ (8.8) at lattice depth $s = 10$ for $gn = 0.5E_R$ (solid line), $gn = 0.02E_R$ (dashed line) and $gn = 0$ (dash-dotted line).

The excitation strength to the lowest Bogoliubov band - Analytic results

The characteristic behaviour described above can be understood by considering the lowest Bogoliubov band in the tight binding regime where an analytic expression can be derived for $Z_1(p)$: Using the expression (6.26) with $j = 1, k = 0$ for the condensate and the tight binding ansatz (7.25,7.26) for the Bogoliubov amplitudes, the expression for the strength $Z_1(p)$ (8.8) takes the form

$$Z_1(p) = N_{\rm tot}|U_p + V_p|^2 \left| \int dz \left(|f(z)|^2 e^{ipz/\hbar} \right) \right|^2 , \tag{8.11}$$

where we have neglected contributions due to the overlap of neighbouring Wannier functions. In chapter 7.3 we have found that

$$(U_p + V_p)^2 = \frac{2\delta \sin^2 (pd/2)}{\hbar\omega(p)} \tag{8.12}$$

Thus, expression (8.11) takes the form

$$\boxed{Z_1(p) = N_{\rm tot} \frac{2\delta \sin^2 (pd/2\hbar)}{\hbar\omega(p/\hbar)} \left| \int dz \left(|f(z)|^2 e^{ipz/\hbar} \right) \right|^2} \tag{8.13}$$

The integral mainly depends on the properties of the Wannier function near the center of the well and can hence be evaluated within the gaussian approximation discussed in section 6.2. Replacing the integral limits by $-\infty$ and $+\infty$, we obtain

$$Z_1(p) = N_{\mathrm{tot}} \frac{2\delta \sin^2(pd/2)}{\hbar\omega(p)} \exp\left(-\frac{1}{2}\sigma^2 \frac{p^2}{\hbar^2}\right). \tag{8.14}$$

This expression for the excitation strength to the lowest band in a deep lattice exhibits all the characteristics mentioned above with respect to the numeric results:

- The gaussian dependence on the momentum transfer p describes the overall decay of the excitation strength at large p. This behavior is also present in the absence of interactions ($gn = 0$). Note that σ is smaller in a deeper lattice, yielding a broader envelope of the strength (8.14). This reflects that at larger s the excitations have more momentum components.

- Provided that $gn/E_R \neq 0$, the ratio between the Bloch and the Bogoliubov dispersion gives rise to the characteristic oscillations of $Z_1(p)$ in the vicinities of $p = l2q_B$ where the excitations contributing to the strength have phonon character: Near the points $p = l2q_B$, we have

  $$Z_1(p) \approx N_{\mathrm{tot}} \sqrt{\delta\kappa} \frac{d}{2\hbar} |p - l2q_B| \exp(-\frac{1}{2}\sigma^2 \frac{(2lq_B)^2}{\hbar^2}), \tag{8.15}$$

  and hence the strength (8.14) vanishes approximately linearly.

  If $gn/E_R = 0$, Bloch and Bogoliubov dispersion coincide and we are left with the non-oscillating behavior $Z_1(p) = \exp\left(-\frac{1}{2}\sigma^2 p/\hbar^2\right)$. Note that $\sigma \to 0$ for $s \to \infty$ and hence $Z_1(p) \to 1$.

- Increasing gn/E_R at fixed s *or* increasing s at fixed $gn/E_R \neq 0$ leads to an overall decrease of $Z_1(p)$: This behavior can be explained by considering the ratio between Bloch and Bogoliubov dispersion appearing in (8.14). Using Eq.(7.38) for the Bogoliubov dispersion, we can write

  $$\frac{2\delta \sin^2(pd/2)}{\hbar\omega(p)} = \frac{\sqrt{\delta\kappa \sin^2(pd/2\hbar)}}{\sqrt{1 + 2\delta\kappa \sin^2(pd/2\hbar)}}. \tag{8.16}$$

  Increasing gn/E_R at fixed s leads to a decrease of κ which dominates the slight increase of δ. So, $\delta\kappa \to 0$ and hence the ratio (8.16) and accordingly the strength (8.14) diminuish. Moreover, increasing s at fixed $gn/E_R \neq 0$ both δ and κ diminish, $\delta\kappa \to 0$, and thus brings about an overall decrease of $Z_1(p)$. Hence, from (8.16) it follows that for increasing gn/E_R *or* increasing s the excitation strength to the lowest band (8.14) is reduced according to the law

  $$Z_1 \sim \sqrt{\delta\kappa}. \tag{8.17}$$

Looking at expression (8.11), we note that in the presence of interactions the strength is suppressed whenever $U_p \sim -V_p$. This must always be the case in the vicinity of $p = l\,2\pi/d$ where the excitations are phonons. Yet, also the *overall* suppression of Z_1 is a consequence of such a behavior of the Bogoliubov amplitudes since $U_p \sim -V_p$ can be achieved for all p if the lattice is made sufficiently deep.

The excitation strength to the lowest Bogoliubov band - Conclusions

In the presence of an optical lattice, it is possible to excite the lowest band $\hbar\omega(q)$ with a momentum transfer $p = q + l\,2\pi/d$ lying outside the first Brillouin zone since the excitation has many momentum components. This is in contrast to the behaviour of a uniform system where the excitation $\hbar\omega(q)$ can only be created provided p exactly equals q.

Furthermore, we find dramatic effects due to the *combined* presence of lattice and interaction: First of all, the excitation strength to the lowest band is not only suppressed when the external perturbation couples to excitations of phononic type close to $p = 0$, as in the uniform case, but vanishes whenever $p = l\,2\pi\hbar/d$. This repeated suppression can be explained by the periodicity of the Bogoliubov excitations featuring a phononic regime in the vicinity of $q = l\,2\pi/d$.

Apart from the periodic suppression of $Z_1(p)$ close to $p = l\,2\pi/d$, the strength diminishes rapidly for all values of p as s is increased and goes to zero in the limits $s \to \infty$. For a larger gn/E_R this reduction is enhanced. This effect is a consequence of the excitations in the lowest band acquiring quasi-particle character associated with $|u_q| \sim |v_q|$ at all values of q, even beyond the phononic regime. If $\hbar/\xi \ll q_B$, this implies that the presence of the lattice extends the role of correlations in the system to length scales below the healing length.

The suppression of $Z_1(p)$ goes along with a suppression of the imaginary part of the response function and hence of the energy transfer between system and external probe. Hence, we can say that due to the lattice it becomes difficult to transfer energy to the system by means of a weak external probe in the range of energies below the second Bogoliubov band, in particular for momentum transfer $p \approx l\,2\pi/d$.

In a recent experiment [91], the amplitude of a one-dimensional optical lattice was modulated to transfer momenta $\pm 2q_B$ to an ultracold Bose gas confined in the tubes of a two-dimensional lattice. A strong response of the system was observed for energy transfers lying in the range of the lowest Bogoliubov band and within the gap between lowest and second band, in disagreement with our prediction. There are two reasons for this discrepancy: The one-dimensional lattice along the tubes was deep enough to enter a regime of strong coupling between the atoms, rendering a Bogoliubov theory approach for weakly interacing systems invalid. Furthermore, the excitation was strong enough to produce a nonlinear response of the system.

The excitation strength to the higher Bogoliubov bands

To study the excitation strength to the higher Bogoliubov bands we evaluate (8.8) with $j > 1$ and the solutions $u_{j>1,q}(z)$, $v_{j>1,q}(z)$ of (7.14,7.15) for a given choice of the lattice depth s and the interaction parameter gn/E_R. Numeric results for the excitation strength to the second band $Z_2(p)$ are depicted in Figs.8.5 for $s = 5$ and $gn = 0.5E_R$ while Figs.8.6 display the strength to the third band $Z_3(p)$ for the same lattice depth and interaction parameter.

These examples illustrate again that the j-th band can be excited by means of a momentum lying outside the j-th Brillouin zone, in contrast with the case $s = 0$ (see Fig. 8.2): Even though Z_j still has its peak values in the j-th Brillouin zone, it takes non-zero values outside that zone with local maxima forming in the zones $j + 2l$. At $s = 5$ the curves in the j-th

Brillouin zone still resembles the curve in the case $s = 0$. Yet, they are smoothed out. This is more evident in the third band which is less affected by the presence of the optical lattice than the second band.

The strengths $Z_{j>1}$ decrease in the j-th Brillouin zone when s is increased, while increasing outside. This reflects the growth of momentum components of the excitations in the j-th band outside the respective Brillouin zone. Very differently from the case of the lowest band, there is no qualitative difference between the curves for $gn = 0$ and $gn \neq 0$. Also, an increase in gn/E_R brings along only minor changes in the strengths: The values of the strength Z_j outside the j-th Brillouin zone is reduced which corresponds to the screening of the lattice by interactions. These observations confirm the statement made in section 7 that interactions have a small effect on the higher Bogoliubov bands.

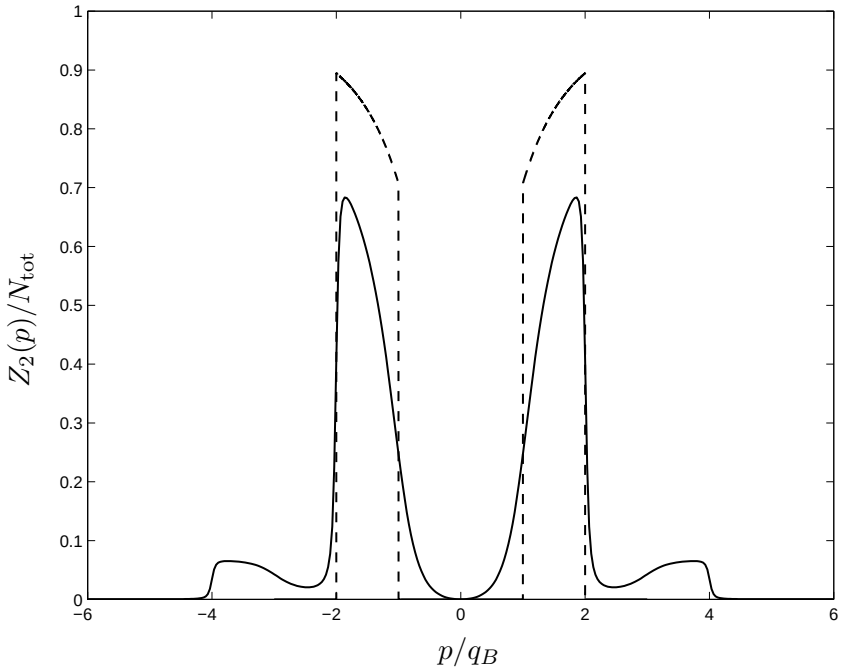

Figure 8.5: Excitation strength to the second Bogoliubov band $Z_2(p)$ (8.8) for $gn = 0.5E_R$ at lattice depth $s = 5$ (solid line) and $s = 0$ (dashed line).

8.2 Static structure factor and sum rules

The integral of the dynamic structure factor provides the static structure factor

$$S(p) = \frac{1}{N_{\rm tot}} \int S(p, \omega) d\omega. \tag{8.18}$$

The static structure factor is a quantity of primary importance in many-body theory since it is closely related to the Fourier transform of the two-body correlation function (see [1] chapter 7.2). Eq.(8.18) is also referred to as non-energy weighted sum-rule of the dynamic structure

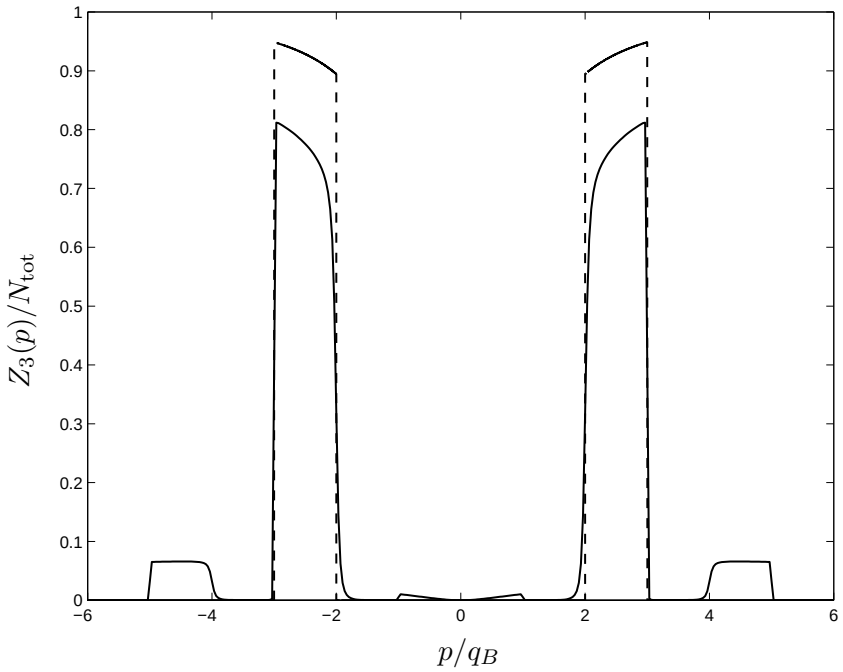

Figure 8.6: Excitation strength to the third Bogoliubov band $Z_3(p)$ (8.8) for $gn = 0.5E_R$ at lattice depth $s = 5$ (solid line) and $s = 0$ (dashed line).

factor. Notice that in the absence of two-body interactions ($gn = 0$), $S(p) = 1$ for any value of p (see dash-dotted lines in Figs.8.7 and 8.8). As we will see, $S(p)$ is strongly affected by the combined presence of two-body interactions and optical lattice.

A second important sum-rule obeyed by the dynamic structure factor is the model independent f-sum rule

$$\int \hbar\omega S(p,\omega)d\omega = N_{\rm tot}\frac{p^2}{2m}. \tag{8.19}$$

Another important sum-rule is the compressibility sum-rule corresponding to the low-p limit of the inverse-energy weighted sum-rule

$$\int \frac{S(p,\omega)}{\hbar\omega}\, d\omega \,\Big|_{p\to 0} = N_{\rm tot}\frac{\kappa}{2}, \tag{8.20}$$

where κ is the compressibility (5.11) (see section 5.2). As discussed above in section (7.4) the compressibility of a condensate loaded in an optical lattice is naturally expressed in terms of the sound velocity c, characterizing the low-q phononic behaviour of the dispersion law ($\hbar\omega(q) = c\hbar q$), through the relation (see Eq.(7.48))

$$\kappa = \frac{1}{m^* c^2}\,. \tag{8.21}$$

Static structure factor of the uniform system

In the uniform system, the sum (8.7) is exhausted by a single mode with the energy $\hbar\omega_{\rm uni}(p)$ (8.10). In this case the static structure factor obeys the Feynman relation

$$S_{\rm uni}(p) = \frac{\frac{p^2}{2m}}{\hbar\omega_{\rm uni}(p)}, \tag{8.22}$$

which can be derived using the f-sum rule (8.19) (see [1] chapter 7.6). For $p \to 0$ the static structure factor (8.22) behaves like

$$S_{\rm uni}(p) \to \frac{|p|}{2mc_{\rm uni}}\,, \tag{8.23}$$

while the compressibility sum-rule (8.20) becomes

$$\int \frac{S(p,\omega)}{\hbar\omega}\, d\omega \,\Big|_{p\to 0} = \frac{N_{\rm tot}}{2mc_{\rm uni}^2}\,, \tag{8.24}$$

where $c_{\rm uni} = \sqrt{gn/m}$ is the sound velocity of the uniform system. The suppression of $S_{\rm uni}(p)$ at small momenta is a direct consequence of phononic correlations between particles. For large momenta, instead, the static structure factor (8.22) approaches unity (see dotted lines in Figs.8.7 and 8.8).

Static structure factor of the system in a lattice

The structure factor (8.18) is obtained by summing up the excitation strengths $Z_j(p)$ (8.8) of all bands

$$S(p) = \frac{1}{N_{\rm tot}} \sum_j Z_j(p)\,. \tag{8.25}$$

Results are presented in Figs.8.7 and 8.8 for $gn = 0,\ 0.02E_R,\ 0.5E_R$ at lattice depth $s = 5$ and $s = 10$ respectively. For weak interactions (dashed lines) the static structure factor exhibits characteristic oscillations, reflecting the contribution $Z_1(p)$ from the first band. This effect is less pronounced for larger values of gn (solid lines) due to the suppression of $Z_1(p)$. In both cases one observes a big difference with respect to the behaviour of $S(p)$ in the uniform gas (8.22) (dotted lines) and with respect to the non-interacting system (dash-dotted lines).

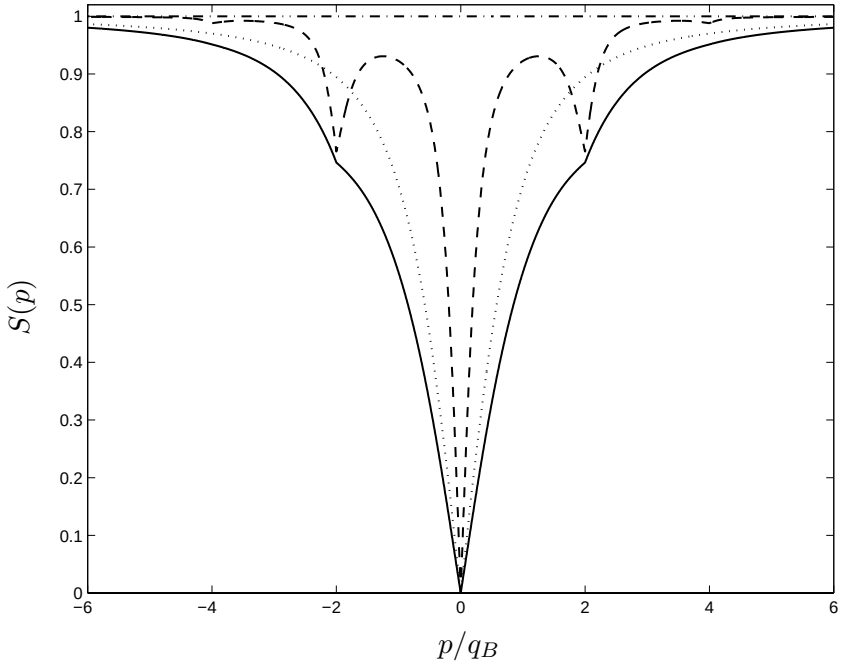

Figure 8.7: Static structure factor (8.25) at lattice depth $s = 5$ for $gn = 0.5E_R$ (solid line), $gn = 0.02E_R$ (dashed line), $gn = 0$ (dash-dotted line) and at lattice depth $s = 0$ for $gn = 0.5$ (dotted line; see also Eq.(8.22).

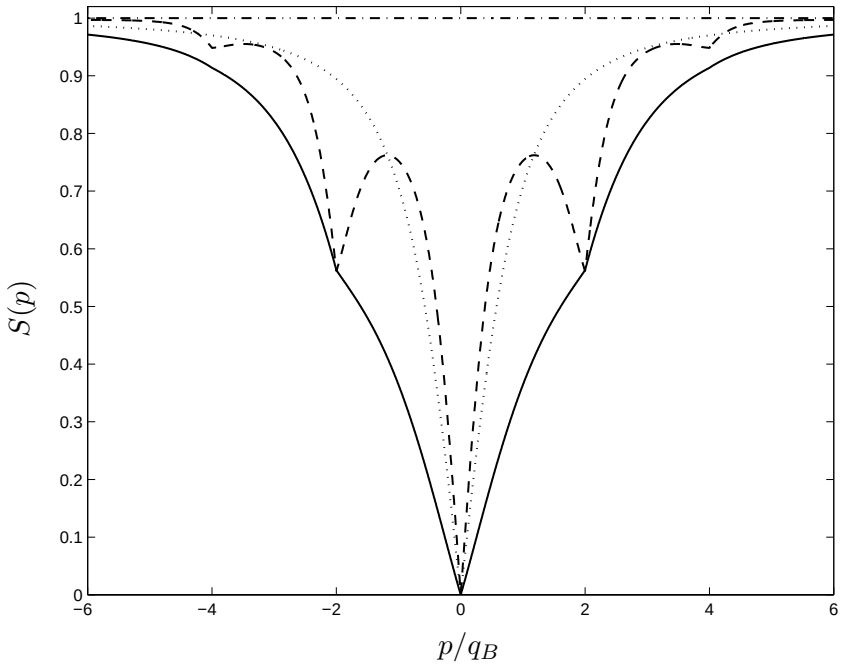

Figure 8.8: Static structure factor (8.25) at lattice depth $s = 10$ for $gn = 0.5E_R$ (solid line), $gn = 0.02E_R$ (dashed line), $gn = 0$ (dash-dotted line) and at lattice depth $s = 0$ for $gn = 0.5$ (dotted line; see also Eq.(8.22).

The behaviour of $S(p)$ at small momenta can be described exactly using sum-rule arguments. Inserting (8.8) into (8.19) and (8.20) we can write

$$\sum_j Z_j(p)\hbar\omega_j(p) = N_{\rm tot}\frac{p^2}{2m}\,, \tag{8.26}$$

$$\sum_j \frac{Z_j(p)}{\hbar\omega_j(p)}\bigg|_{p\to 0} = N_{\rm tot}\frac{\kappa}{2}\,. \tag{8.27}$$

In lowest order in p the Bogoliubov bands $\hbar\omega_j(p)$ behave like

$$\hbar\omega_1(p)|_{p\to 0} \;=\; cp\,, \tag{8.28}$$

$$\hbar\omega_{j>1}(p)|_{p\to 0} \;=\; const\,. \tag{8.29}$$

Hence, the f-sum rule (8.26) can only be ensured at small p if

$$Z_1(p) \;\sim\; p\,, \tag{8.30}$$

$$Z_{j>1}(p) \;\sim\; p^2\,. \tag{8.31}$$

Inserting this result and (8.28,8.29) into (8.18,8.27) we find that both the non-energy weighted sum rule (8.18) and the compressibility sum rule (8.20) are exhausted by the contribution from the first band when $p \to 0$, high energy bands giving rise to contributions of $\mathcal{O}(p^2)$. Thus, we can rewrite (8.18,8.20) in the form

$$S(p)|_{p\to 0} \;=\; \frac{1}{N_{\rm tot}}Z_1(p) \sim p\,, \tag{8.32}$$

$$\frac{Z_1(p)}{\hbar\omega_1(p)}\bigg|_{p\to 0} \;=\; N_{\rm tot}\frac{\kappa}{2}\,. \tag{8.33}$$

Combining these two equations and using $\kappa = 1/m^*c^2$ we obtain

$$\boxed{S(p) \;\underset{p\to 0}{\longrightarrow}\; \frac{|p|}{2m^*c}} \tag{8.34}$$

This shows that in the presence of 2-body interactions the low-p behaviour of the static structure factor is entirely determined by phonon correlations. This result holds for any value of s as long as $gn \neq 0$. In the absence of the optical lattice $m^* = m$ and c coincides with the Bogoliubov sound velocity $c_{\rm uni} = \sqrt{gn/m}$ of the uniform system. Since we can write $m^*c = \sqrt{m^*\kappa^{-1}}$ and both m^* and κ^{-1} increase with s, we find that the presence of the lattice results in an enhanced suppression of the static structure factor at low values of p, as clearly shown in Figs.8.7 and 8.8.

Chapter 9

Macroscopic Dynamics

In this chapter, we show how to describe the long length scale GP-dynamics of a condensate in a one-dimensional optical lattice by means of a set of hydrodynamic equations for the macroscopic density and the macroscopic superfluid velocity (see sections 9.2 and 9.3). Within this formalism, we can account for the presence of additional external fields, as for example a harmonic trap, provided they vary on length scales large compared to the lattice spacing d. As an input the equations require the energy and chemical potential Bloch band spectra calculated in presence of the optical lattice only (see chapter 6.1 above). In the case of a groundstate condensate in the presence of harmonic trapping, the hydrodynamic equations reproduce the results obtained in chapter 5.4 for the smoothed density profile.

As an application we derive an analytic expression for the sound velocity in a Bloch state condensate (see section 9.4, see also discussion in chapter 7.4 above). The sound velocity in the groundstate condensate is determined by the effective mass and the compressibility. In a moving condensate the sound velocity also involves information about the chemical potential band spectrum discussed above in chapter 6.1.

In the combined presence of optical lattice and harmonic trap, the hydrodynamic equations can be solved for the frequencies of small amplitude collective oscillations (see section 9.5). Our treatment relies on the assumption that the effective mass is density-independent and that the change in the compressibility brought about by the lattice can be accounted for by the effective coupling constant $\tilde{g}$ (see chapter 5). It turns out that in a trap with axial frequency ω superimposed to the lattice, the condensate oscillates as if it was confined in a harmonic trap of axial trapping frequency $\sqrt{m/m^*}\omega_z$ with the lattice off. The slow-down of the collective oscillations observed in the experiment [75] for increasing lattice depth has confirmed our prediction.

The frequency $\omega = \sqrt{m/m^*}\omega_z$ for the small amplitude center-of-mass motion is independent of the equation of state (see section 9.6), i.e. it can be derived without knowing how the chemical potential depends on density. The large amplitude center-of-mass motion is described by a set of equations which does not involve the equation of state and is valid at any lattice depth. As an input it requires the single particle Bloch band spectrum calculated with the lattice potential only. Using these equations of motion we show that the deeper the lattice the harder it is to fulfill the condition on the initial trap displacement for the observation of harmonic dipole oscillations. In the tight binding regime, these equations also have a simple

analytical solution in the limit of a large initial displacement of the center-of-mass from the trap center. We comment on the instability of the center-of-mass motion which has been the subject of recent experimental and theoretical work.

In [138] we have presented the hydrodynamic description of large current dynamics in the tight binding regime assuming that the effective mass is density-independent and that the change in the compressibility brought about by the lattice can be accounted for by the effective coupling constant $\tilde{g}$. In [102] we reported the hydrodynamic equations for small currents which are valid at all lattice depths and allow for a density-dependent effective mass and a chemical potential which has a nonlinear dependence on density. Here, we generalize these hydrodynamic equations to account for large currents. They coincide with the ones we presented in [138] in the limit considered there and which, previously to [102], have been reported in [107].

Our result for the sound velocity in a condensate at rest is derived in [138] within the hydrodynamic framework developed there. The generalization to all lattice depth, general effective mass and compressibility, and to a condensate in slow motion is included in [102] (see also [107]). Our results for small amplitude collective oscillations were derived in [138] for the tight binding regime. In this thesis, their discussion is generalized to all lattice depths maintaining the assumptions made in [138] concerning the effective mass and the equation of state. The demonstration of the irrelevance of the equation of state for the dipole mode frequency and the derivation of the equations describing large amplitude center-of-mass oscillations at any lattice depth is added.

9.1 Macroscopic density and macroscopic superfluid velocity

Our guiding idea is to retain from time-dependent GP-theory only the information necessary to describe the dynamics occurring on length scales much larger than the lattice spacing d. More precisely, we will assume that the state of the system in a window of size $D >> d$ resembles a stationary state solution of the system without any external potential in addition to the optical lattice. Note that in order to describe non-stationary dynamics, D has to be much smaller than the size of the system. Accordingly, the dynamics we will be able to capture has non-stationary character only on length scales much larger than D.

We set out by generalizing definition (5.21) of the average density at site l to the case of a time-dependent density

$$n_l(r_\perp, t) = \frac{1}{d}\int_{ld-d/2}^{ld+d/2} n(r_\perp, z, t)\, dz \ , \tag{9.1}$$

where $n(r_\perp, z) = |\Psi(r_\perp, z)|^2$ is the density obtained by solving the time-dependent GP-equation in the presence of optical lattice and an additional slowly varying external potential as for example a harmonic trap. With l replacing the continous variable z, expression (5.21) defines an average density profile of the condensate in the trap, as pointed out in section 5.4 for the static case. It is a smooth function of $r_\perp$ and varies slowly as a function of the index l. We obtain a smooth macroscopic density profile $n_M(r_\perp, z)$ by replacing the discrete index l by the continous variable $z = ld$

$$l \to z = ld \qquad \Rightarrow \qquad n_l(r_\perp, t) \to n_M(r_\perp, z, t)\,. \tag{9.2}$$

In accordance with the basic idea introduced above, we assume n_M to be approximately constant on the length scale D in the z-direction at any given time t.

In analogy to the definition of the average density $n_l(r_\perp)$, we introduce the average z-component of the superfluid velocity field at site l

$$\begin{aligned} v_{zl}(r_\perp,t) &= \frac{1}{d}\int_{ld-d/2}^{ld+d/2} dz \left[\frac{\hbar}{m}\partial_z S(r_\perp,z,t)\right] \\ &= \frac{\hbar}{m}\frac{1}{d}\left[S(r_\perp,ld+d/2,t)-S(r_\perp,ld-d/2,t)\right] , \end{aligned} \tag{9.3}$$

where $S(r_\perp,z,t)$ is the phase of the order parameter and $(\hbar/m)\partial_z S(r_\perp,z,t)$ is the z-component of the superfluid velocity field obtained by solving the time-dependent GP-equation in the presence of optical lattice and an additional slowly varying external potential as for example a harmonic trap. The quantity (9.3) is required to be approximately constant over a distance D. Hence, we can rewrite (9.3) in the form

$$v_{zl}(r_\perp,t) = \frac{\hbar}{m}\frac{1}{D}\left[S(r_\perp,ld+D/2,t)-S(r_\perp,ld-D/2,t)\right] . \tag{9.4}$$

Now, we go a step further and require the approximate stationary state in the window of size D around the site l to be of the Bloch form $\varphi_k = \exp(ik_l z)\tilde{\varphi}_k$ (6.2) with quasi-momentum $k_l(r_\perp,t)$. Note that $k_l(r_\perp,t)$ must be a slowly varying function of the index l and the variable $r_\perp$. The phase S in the window of size D around the site l is then approximately given by

$$S(r_\perp,z,t) = k_l(t)z + \tilde{S}_k(r_\perp,z,t)\,, \tag{9.5}$$

where the second contribution $\tilde{S}_k$ is the phase of the Bloch wave $\tilde{\varphi}_k$ and thus $\tilde{S}_k(r_\perp,z,t) = \tilde{S}_k(r_\perp,z+ld,t)$. Inserting (9.5) into (9.4) we find

$$v_{zl}(r_\perp,t) = \frac{\hbar k_l(t)}{m} + \frac{\hbar}{m}\frac{\tilde{S}_{jk}(r_\perp,ld+D/2,t)-\tilde{S}_{jk}(r_\perp,ld-D/2,t)}{D} . \tag{9.6}$$

Since $\tilde{S}_{jk}$ is periodic in z with periodicity d, the second contribution becomes small for $D >> d$. It can consequently be neglected for sufficiently large D and we are left with

$$v_{zl}(r_\perp,t) = \frac{\hbar k_l(r_\perp,t)}{m} . \tag{9.7}$$

We smooth (9.7) in the z-direction in the same way as the average density profile

$$l \to z = ld \qquad \Rightarrow \qquad v_{zl}(r_\perp,t) \to v_{Mz}(r_\perp,z,t)\,, \tag{9.8}$$

where the z-component of the *macroscopic superfluid velocity* field $\mathbf{v}_M$ is given by

$$\boxed{v_{Mz}(r_\perp,z,t) = \frac{\hbar k(r_\perp,z,t)}{m} .} \tag{9.9}$$

The x, y-components v_{Mx}, v_{My} are given by the usual expressions $(\hbar/m)\partial_{x,y}S(r_\perp,z,t)$.

It is important to note that $v_{Mz} = \hbar k/m$ does not coincide with the group velocity $\bar{v}_k$ of a Bloch state condensate with quasi-momentum $\hbar k$. This is a very peculiar feature of a

condensate in a lattice. Note that group velocity and superfluid velocity are related to the superfluid current I by the relations $I = n\bar{v}$ and $I = n_s v_M$ respectively, where n is the total density and n_s is the superfluid density. The decrease of the superfluid current I due to the lattice brings about a decrease of the group velocity and of the superfluid density rather than of the superfluid velocity. It is this effect which underlies the difference between the expression (9.7) and the group velocity.

We can also define a macroscopic phase S_M through the relation

$$\mathbf{v}_M(r_\perp, z) = \frac{\hbar}{m} \nabla S_M(r_\perp, z) \tag{9.10}$$

This fixes the quantity S_M up to an irrelevant constant.

The introduction of the quantities n_M and S_M allows us to speak of an effective macroscopic order parameter

$$\Psi_M = \sqrt{n_M}\, e^{iS_M}\,, \tag{9.11}$$

whose evolution in time we are interested in.

9.2 Hydrodynamic equations for small currents

Using the notions of macroscopic density and macroscopic superfluid velocity we devise a hydrodynamic formalism which is valid to the dynamics involving only small currents. This restriction signifies that only small quasimomenta $\hbar k$ are involved in the dynamics which are associated with currents $n_M \hbar k/2m^*$. The generalization to large currents is done in the subsequent section.

Macroscopic energy functional

The energy change per particle due to the presence of a small constant current in z-direction is $\hbar^2 k^2/2m^* = m^2 v_{Mz}^2/2m^*$, where we have used the expression (9.9) for the macroscopic superfluid velocity. Using this fact, the total energy of the system can be written in terms of the macroscopic density n_M and superfluid velocity field $\mathbf{v}_M$

$$E = \int d\mathbf{r} \left[\frac{m}{2} n_M v_{Mx}^2 + \frac{m}{2} n_M v_{My}^2 + \frac{m}{2} \frac{m}{m^*(n_M)} n_M v_{Mz}^2 + n_M \varepsilon(n_M) + n_M V_{\rm ext} \right], \tag{9.12}$$

for the total energy of the system. Here, $V_{\rm ext}$ is an external potential supposed to vary on length scales much larger than D and $\varepsilon(n_M)$ and $m^*(n_M)$ are, respectively, the groundstate energy and the effective mass calculated at the average density n_M in absence of the external potential (see sections 5.1 and 6.1). We can rewrite the integrand of (9.12) in terms of the density n_M and the phase S_M defined in (9.10). This yields

$$E = \int d\mathbf{r} \left[n_M \frac{\hbar^2}{2m} \left(\frac{\partial S_M}{\partial x} \right)^2 + n_M \frac{\hbar^2}{2m} \left(\frac{\partial S_M}{\partial y} \right)^2 + \frac{m}{m^*} n_M \frac{\hbar^2}{2m} \left(\frac{\partial S_M}{\partial z} \right)^2 + n_M \varepsilon(n_M) + n_M V_{\rm ext} \right]. \tag{9.13}$$

Even though this expression is written in terms of macroscopic variables, the energy change brought about by the lattice is implicitly accounted for by the effective mass $m^*(n_M)$ and by the function $\varepsilon(n_M)$, which have been calculated microscopically solving the stationary GP-equation in presence of the optical lattice.

Action principle

Our derivation of the equations of motion for the macroscopic density n_M and the macroscopic velocity field v_M is based on the requirement that the action

$$A = \int_0^{t'} dt \left[E - i\hbar \left\langle \frac{\partial}{\partial t} \right\rangle \right] \tag{9.14}$$

is stationary and hence satisfies the condition

$$\delta A = 0\,. \tag{9.15}$$

The integrand in (9.14) contains the quantity

$$\begin{aligned} \left\langle \frac{\partial}{\partial t} \right\rangle &= \int d\mathbf{r} \left[\Psi_M^* \frac{\partial}{\partial t} \Psi_M \right] \\ &= \int d\mathbf{r} \left[\frac{1}{2} \frac{\partial}{\partial t} n_M + i n_M \frac{\partial}{\partial t} S_M \right] . \end{aligned} \tag{9.16}$$

The first term does not contribute to δA since the variation at $t = 0$ and $t = t'$ is zero by assumption.

Imposing (9.15) on the variation of the action with respect to S_M and using (9.10) for the relation between S_M and the macroscopic superfluid velocity, we find the equation of continuity

$$\frac{\partial}{\partial t} n_M + \partial_x (v_{Mx} n_M) + \partial_y (v_{My} n_M) + \partial_z \left(\frac{m}{m^*} v_{Mz} n_M \right) = 0\,. \tag{9.17}$$

On the other hand, upon variation of the action with respect to n_M and imposing (9.15), we obtain an Euler equation for the macroscopic density

$$m \frac{\partial}{\partial t} \mathbf{v}_M + \nabla \left[V_{\rm ext} + \mu_{\rm opt}(n_M) + \frac{m}{2} v_{Mx}^2 + \frac{m}{2} v_{My}^2 + \frac{\partial}{\partial n_M} \left(\left(\frac{m}{m^*} n_M \right) \frac{m}{2} v_{Mz}^2 \right) \right] = 0\,, \tag{9.18}$$

where $\mu_{\rm opt}(n_M) = \partial \left[n_M \varepsilon(n_M) \right] / \partial n_M$ denotes the groundstate chemical potential for $V_{\rm ext} = 0$ (see Eq.(5.9)).

It is interesting to note that in (9.17), the current in the lattice direction is modified by the factor m/m^*. Since the respective current component can be written as the product of the superfluid velocity component and the superfluid density

$$I = n_s v_{Mz}\,, \tag{9.19}$$

the superfluid density results to be

$$\boxed{n_s = n_M \frac{m}{m^*}\,.} \tag{9.20}$$

The appearance of this quantity in the Euler equation (9.18), confirms this statement: There, the quantity $\partial/\partial n_M\,((m/m^*)n_M(m/2)v_z^2)$ replaces the term $\partial/\partial n_M\,(n_M(m/2)v_z^2)$ we would obtain without lattice where $n_M = n_s$.

The hydrodynamic equations (9.17,9.18) can be further generalized to account for larger condensate velocities. This is the topic of the subsequent section.

9.3 Hydrodynamic equations for large currents

In order to derive the hydrodynamic equations (9.17,9.18) for larger condensate velocities, we need to generalize the energy functional (9.12). This is done by modifying the energy contribution due to the current in lattice direction: The contribution $(m/2)(m/m^*(n_M))v_{zM}^2 + \varepsilon(n_M)$ is replaced by the more general expression $\varepsilon(v_{zM} = \hbar k/m; n_M)$, the latter being the energy of a Bloch state condensate (6.4) at average density n_M, quasi-momentum $\hbar k$ and macroscopic superfluid velocity $v_{Mz} = \hbar k/m$. Note that, for convenience, we include the groundstate energy $\varepsilon(n_M)$ in the term $\varepsilon(v_{zM} = \hbar k/m; n_M)$. In this way, we obtain the energy functional

$$E = \int d\mathbf{r}\left[\frac{m}{2}n_M v_{Mx}^2 + \frac{m}{2}n_M v_{My}^2 + n_M\varepsilon(v_{Mz} = \hbar k/m; n_M) + n_M V_{\rm ext}\right], \qquad (9.21)$$

which in terms of the phase defined in (9.10) can be rewritten in the form

$$E = \int d\mathbf{r}\left[\frac{m}{2}n_M\left(\frac{\partial S_M}{\partial x}\right)^2 + \frac{m}{2}n_M\left(\frac{\partial S_M}{\partial y}\right)^2 + n_M\varepsilon(\partial_z S_M = k; n_M) + n_M V_{\rm ext}\right] \qquad (9.22)$$

In writing this expression we have used the fact that according to (9.7,9.10)

$$\partial_z S_M = k\,. \qquad (9.23)$$

Using this identity and the action principle employed above, we find the following hydrodynamic equations

$$\frac{\partial}{\partial t}n_M + \partial_x(v_{Mx}n_M) + \partial_y(v_{My}n_M) + \partial_z\left(\frac{1}{\hbar}\partial_k\varepsilon(k; n_M)n_M\right) = 0\,. \qquad (9.24)$$

$$m\frac{\partial}{\partial t}\mathbf{v}_M + \nabla\left[V_{\rm ext} + \frac{m}{2}v_{Mx}^2 + \frac{m}{2}v_{My}^2 + \mu_{\rm opt}(k; n_M)\right] = 0\,. \qquad (9.25)$$

The second equation involves the chemical potential (6.5) of a Bloch states condensate with quasi-momentum $\hbar k$ at average density n_M for $V_{\rm ext} = 0$. When using the hydrodynamic equations (9.24,9.25) it is important to keep in mind that k is a function of $\mathbf{r}$ and essentially represents the z-component of the macroscopic velocity field $v_{Mz} = \hbar k/m$.

The generalized hydrodynamic equations (9.24,9.25) have been reported in [138] for the tight binding regime with the density-dependent effective mass and the equation of state $\mu_{\rm opt} = \tilde{g}n_M$ and in [107] for a general equation of state $\mu_{\rm opt}(n_M)$ and general dispersion $\varepsilon(k; n_M)$, hence for any lattice potential depth.

9.4 Sound Waves

For $V_{\rm ext} = 0$, the small-current hydrodynamic equations (9.17,9.18) have sound wave solutions. These correspond to small amplitude plane wave perturbations $\Delta n(\mathbf{r},t)$, $\Delta \mathbf{v}(\mathbf{r},t)$ of a Bloch state associated with constant macroscopic density $\bar{n}_M$ and macroscopic velocity $\bar{\mathbf{v}}_M$. Here, we restrict ourselves to sound waves moving in the lattice direction in a Bloch state condensate with quasi-momentum $\hbar k$ and velocity $\bar{v}_M = \hbar k/m$ oriented in the same direction. In this case, the perturbation takes the form

$$\Delta n(z,t) \propto \Delta n(z)\, e^{i(qz-\omega(q)t)} \tag{9.26}$$

$$\Delta v(z,t) \propto \Delta v(z)\, e^{i(qz-\omega(q)t)} \tag{9.27}$$

To find the dispersion $\omega(q)$, we linearize Eqs.(9.17,9.18) in $\Delta n(z,t)$, $\Delta v(z,t)$ with $V_{\rm ext} = 0$. The resulting equations read

$$\frac{\partial}{\partial t}\Delta n(z,t) + \frac{m}{m^*(\bar{n})}\bar{n}\partial_z \Delta v(z,t) + \frac{k}{m^*_\mu(\bar{n})}\partial_z \Delta n(z,t) = 0\,, \tag{9.28}$$

$$\frac{\partial}{\partial t}\Delta v(z,t) + \frac{1}{m}\left(\frac{\partial \mu_{\rm opt}}{\partial n}\right)_{\bar{n}} \partial_z \Delta n(z,t) + \frac{k}{m^*_\mu(\bar{n})}\partial_z \Delta v(z,t) = 0\,, \tag{9.29}$$

where m^* and m^*_μ are the effective masses obtained from the lowest energy and chemical potential Bloch band respectively (see Eqs.(6.19,6.23)) and we have neglected terms of order higher than $\mathcal{O}(k)$. Inserting (9.26,9.27) into (9.28,9.29), we find

$$\omega(q) = \frac{\hbar|k|}{m^*_\mu(\bar{n}_M)}|q| \pm \frac{1}{\sqrt{\kappa m^*}}|q|\,, \tag{9.30}$$

where κ is the groundstate compressibility (see Eq.(5.11)). According to this result, sound waves in a groundstate condensate ($k = 0$) travel at velocity

$$c = \frac{1}{\sqrt{\kappa m^*}}\,. \tag{9.31}$$

This expression and in particular the implied dependence of the sound velocity on average density and on lattice depth has been discussed above in section 7.4. On the other hand, if the condensate carrying the sound wave has non-zero quasi-momentum $\hbar k$, Eq.(9.30) yields the sound velocity

$$c_k = c \pm \frac{\hbar|k|}{m^*_\mu}\,, \tag{9.32}$$

where the plus- and minus-sign hold for k parallel and anti-parallel q respectively. This expression has been discussed above in chapter 7.4 (see Eq.(7.53)).

The result (9.30) describes the excitation energy spectrum associated with small perturbations of a Bloch state condensate at any lattice depth in the limit of small q and k. Using the set of hydrodynamic equations (9.24,9.25) valid also for large currents, the spectrum for small q and any k has been obtained in [107]. The result reads [107, 125]

$$\boxed{c_k = \sqrt{\frac{n}{m^*(k)}\frac{\partial \mu(k)}{\partial n}} \pm \left|\frac{\partial \mu(k)}{\partial k}\right|\,,} \tag{9.33}$$

where $m^*(k)$ is the generalized effective mass (6.22) with $j = 1$.

9.5 Small amplitude collective oscillations in the presence of harmonic trapping

In current experiments, the external potential $V_{\rm ext}$ is provided by a harmonic trap

$$V_{\rm ext} = \frac{m}{2}\left(\omega_x^2 x^2 + \omega_y^2 y^2 + \omega_z^2 z^2\right) \tag{9.34}$$

to which the optical lattice is superimposed. In the following, we will assume the groundstate to be adequately described by the LDA developed in section 5.4, implying that the size of the condensate is much larger than the lattice spacing d (see Eq.(5.20)). In accordance with the discussion above, this is a necessary condition for the use of (9.17,9.18). Moreover, we presuppose the chemical potential in absence of the harmonic confinement to exhibit the linear dependence on average density (see Eq.(5.13))

$$\mu_{\rm opt} = \tilde{g} n + \mu_{gn=0}\,. \tag{9.35}$$

The validity of this approximation has been discussed in section 5.2. Within LDA, the groundstate macroscopic density profile $\bar{n}_M$ is then defined by the relation (see discussion in section 5.4)

$$\mu = \tilde{g}\bar{n}_M(\mathbf{r}) + \mu_{gn=0} + V_{\rm ext}\,. \tag{9.36}$$

The dynamic equations (9.17,9.18) do not only require the equation of state $\mu_{\rm opt}(n_M)$ as an input, but also the effective mass $m^*(n_M)$. As a simplification, we will consider the effective mass to be density-independent and thus to be given by the single particle effective mass

$$m^* = m^*(gn/E_R = 0)\,. \tag{9.37}$$

The applicability of this approximation has been discussed in section 6.1.

With $V_{\rm ext}$ given by the harmonic potential (9.34) and the approximations (9.35,9.37), the hydrodynamic equations (9.17,9.18) take the form

$$\frac{\partial}{\partial t} n_M + \partial_x(v_{Mx} n_M) + \partial_y(v_{My} n_M) + \frac{m}{m^*}\partial_z\left(v_{Mz} n_M\right) = 0\,, \tag{9.38}$$

$$m\frac{\partial}{\partial t}\mathbf{v}_M + \nabla\left[V_{\rm ext} + \tilde{g} n_M + \mu_{gn=0} + \frac{m}{2}v_{Mx}^2 + \frac{m}{2}v_{My}^2 + \frac{m}{m^*} n_M \frac{m}{2} v_{Mz}^2\right] = 0\,. \tag{9.39}$$

These equations are expected to give a correct description of the dynamics occurring on a length scale of the order of the system size. In particular, we will explore here the limit of small amplitude collective oscillations which comply with this condition.

Hydrodynamic equations for small amplitude oscillations

Small amplitude collective oscillations are associated with an oscillating perturbation in the groundstate density $\bar{n}_M$ and a small oscillating velocity field

$$\Delta n(\mathbf{r}, t) \propto \Delta n(\mathbf{r})\, e^{-i\omega t}\,, \tag{9.40}$$

$$\Delta \mathbf{v}(\mathbf{r}, t) \propto \Delta \mathbf{v}(\mathbf{r})\, e^{-i\omega t}\,. \tag{9.41}$$

To find the frequencies ω, we linearize Eqs.(9.38,9.39) in $\Delta n(\mathbf{r},t)$, $\Delta\mathbf{v}(\mathbf{r},t)$

$$\frac{\partial}{\partial t}\Delta n + \partial_x(\Delta v \bar{n}_M) + \partial_y(\Delta v \bar{n}_M) + \frac{m}{m^*}\partial_z\left(\Delta v_z \bar{n}_M\right) = 0\,. \tag{9.42}$$

$$m\frac{\partial}{\partial t}\Delta\mathbf{v} + \tilde{g}\nabla\Delta n = 0\,, \tag{9.43}$$

where we have made use of (9.36). After differentiating (9.42) with respect to time and inserting (9.43), we obtain

$$\frac{\partial^2}{\partial t^2}\Delta n - \partial_x\left(\frac{\tilde{g}\bar{n}_M}{m}\partial_x\Delta n\right) - \partial_y\left(\frac{\tilde{g}\bar{n}_M}{m}\partial_y\Delta n\right) - \frac{m}{m^*}\partial_z\left(\frac{\tilde{g}\bar{n}_M}{m}\partial_z\Delta n\right) = 0\,. \tag{9.44}$$

Using (9.36) this equation can be rewritten in the form

$$\frac{\partial^2}{\partial t^2}\Delta n - \partial_x\left(\frac{\mu-\mu_{gn=0}-V_{\rm ext}}{m}\partial_x\Delta n\right) - \partial_y\left(\frac{\mu-\mu_{gn=0}-V_{\rm ext}}{m}\partial_y\Delta n\right) - \frac{m}{m^*}\partial_z\left(\frac{\mu-\mu_{gn=0}-V_{\rm ext}}{m}\partial_z\Delta n\right) = 0\,. \tag{9.45}$$

Its form is affected by the lattice only through the appearance of the factor m/m^* and the irrelevant constant $\mu_{gn=0}$. This formal difference can be eliminated by replacing the trap frequency ω_z, the z-coordinate and the chemical potential μ by

$$\tilde{\omega}_z = \sqrt{\frac{m}{m^*}}\omega_z\,, \tag{9.46}$$

$$\tilde{z} = \sqrt{\frac{m^*}{m}}z\,, \tag{9.47}$$

$$\tilde{\mu} = \mu - \mu_{gn=0}\,. \tag{9.48}$$

Using these new quantities we can rewrite Eq.(9.45) in the form

$$\frac{\partial^2}{\partial t^2}\Delta n - \partial_x\left(\frac{\tilde{\mu}-\tilde{V}_{\rm ext}}{m}\partial_x\Delta n\right) - \partial_y\left(\frac{\tilde{\mu}-\tilde{V}_{\rm ext}}{m}\partial_y\Delta n\right) - \partial_{\tilde{z}}\left(\frac{\tilde{\mu}-\tilde{V}_{\rm ext}}{m}\partial_{\tilde{z}}\Delta n\right) = 0\,, \tag{9.49}$$

where $\tilde{V}_{\rm ext}$ is a harmonic potential with frequency $\tilde{\omega}_z$ along the $\tilde{z}$-direction

$$\tilde{V}_{\rm ext} = \frac{m}{2}\left(\omega_x^2x^2 + \omega_y^2y^2 + \tilde{\omega}_z^2\tilde{z}^2\right)\,. \tag{9.50}$$

At this stage, the differential equation (9.49) is formally identical with the one describing small amplitude collective oscillations of a condensate with chemical potential $\tilde{\mu}$ in a harmonic trap with frequencies ω_x, ω_y, $\tilde{\omega}_z$ *without* a lattice being superimposed to it.

Frequencies of small amplitude collective oscillations

The above derivation has shown that the condensate in the combined potential of harmonic trap and lattice oscillates *as if* there was no lattice and *as if* the harmonic trap frequency along the z-direction was $\tilde{\omega}_z = \sqrt{m/m^*}\omega_z$ instead of ω_z and the chemical potential $\tilde{\mu} = \mu - \mu_{gn=0}$ instead of μ. This conclusion allows us to apply results obtained for a purely harmonically trapped condensate to the case when a lattice is added (see [1] chapter 12.2-12.3 and references therein): We obtain the correct frequency by replacing ω_z by $\tilde{\omega}_z$ and μ by $\tilde{\mu}$.

Let us consider the example of a cylindrically symmetric trap with $\omega_x = \omega_y = \omega_\perp$: For $\omega_\perp \gg \tilde{\omega}_z$ the system behaves like an elongated cigar shaped condensate for which the lowest frequency solutions are given by the center-of-mass motion ("dipole mode")

$$\boxed{\omega_D = \sqrt{\frac{m}{m^*}}\omega_z} \tag{9.51}$$

and by the axial breathing mode ("quadrupole mode")

$$\boxed{\omega_Q = \sqrt{\frac{5}{2}}\sqrt{\frac{m}{m^*}}\omega_z\,.} \tag{9.52}$$

These frequencies do not depend on the chemical potential, and therefore on the coupling constant. Still, the occurrence of the factor $\sqrt{5/2}$ in the quadrupole frequency ω_Q is a non-trivial consequence of the mean-field interaction [43]. In addition to the low frequency axial motion the system exhibits radial oscillations at high frequency, of the order of $\omega_\perp$. The most important ones are the transverse breathing and quadrupole oscillations occuring at $\omega = 2\omega_\perp$ and $\omega = \sqrt{2}\omega_\perp$ respectively. For elongated traps with $\omega_\perp \gg \tilde{\omega}_z$ we predict the frequencies of these modes not to be affected by the optical lattice. Note that the result for the dipole frequency (9.51) was obtained for the tight binding regime in [73].

A different scenario is obtained for $\tilde{\omega}_z \gg \omega_\perp$. In such a setting the system moves like a disk shaped condensate: While the dipole mode, of course, still has the frequency (9.51), the breathing mode oscillates at

$$\omega_Q = \sqrt{3}\sqrt{\frac{m}{m^*}}\omega_z \tag{9.53}$$

instead of (9.52). The low frequency modes involving the radial direction are, apart from the dipole mode $\omega = \omega_\perp$ given by $\omega = \sqrt{10/3}\omega_\perp$ and $\omega = \sqrt{2}\omega_\perp$ respectively.

Effective change of geometry

In chapter 5.4 we have found that the aspect ratio of a static harmonically trapped condensate does not change when a lattice is superimposed, i.e. its shape of the condensate remains the same. Yet, the above discussion shows that the dynamics of the system is governed by an effective change of geometry: The condensate oscillates *as if* it was a condensate without lattice in a trap with the frequencies $\tilde{\omega}_z = \sqrt{m/m^*}\omega_z$. Accordingly, an elongated condensate ($\omega_z << \omega_\perp$) oscillates like an even more elongated sample, while a disc-shaped condensate ($\omega_z >> \omega_\perp$) can behave as an effectively spherical ($\sqrt{m/m^*}\omega_z = \omega_\perp$) or even cigar-shaped system ($\sqrt{m/m^*}\omega_z >> \omega_\perp$). In the latter example, the effective change of geometry manifests itself in a change of the axial breathing mode frequency from $\sqrt{3}\sqrt{m/m^*}\omega_z$ to $\sqrt{5/2}\sqrt{m/m^*}\omega_z$.

The results obtained in this section can easily be generalized to cubic two-dimensional lattices. The frequencies of the low energy collective modes are then obtained from those in

the absence of the lattice [43] by simply replacing

$$\omega_x \to \sqrt{m/m^*}\omega_x\,, \tag{9.54}$$

$$\omega_y \to \sqrt{m/m^*}\omega_y\,, \tag{9.55}$$

where we have assumed the lattice two be set up in the x, y plane and ω_x, ω_y are the harmonic trapping frequencies in these directions. If $\omega_z >> \omega_x\sqrt{m/m^*}, \omega_y\sqrt{m/m^*}$, the lowest energy solutions involve the motion in the $x-y$ plane. The oscillations in the z-direction are instead fixed by the value ω_z of the harmonic trap. These include the center-of-mass motion ($\omega = \omega_z$) and the lowest compression mode ($\omega = \sqrt{3}\omega_z$). The frequency $\omega = \sqrt{3}\omega_z$ coincides with the value obtained by directly applying the hydrodynamic theory to 1D systems [139, 140] and reveals the 1D nature of the tubes generated by the 2D lattice. If the radial trapping generated by the lattice becomes too strong the motion along the tubes can no longer be described by the mean field equations and one enters into more correlated 1D regimes associated with a modification of the equation of state which affects the frequencies of the collective oscillations [141]. It is interesting to note that the study of the macroscopic behavior of a Bose-Einstein condensate in a two-dimensional lattice and the investigation of one-dimensional Bose gases can be merged: The equation of state entering the hydrodynamic equations for a two-dimensional lattice can be chosen such as to reflect the one-dimensional nature of the gas strongly confined in the tubes of the lattice. This allows to identify signatures of strong correlations in the macroscopic 3D properties (density profile, collective modes) of the sample [142].

Comparison with experiment

The predictions (9.51) and (9.52) for the center-of-mass oscillation and the axial breathing mode in an elongated condensate have been confirmed experimentally in [73, 75]. In these experiments $gn \approx 0.2E_R$ at the center of the harmonic trap at $s = 0$. For this relatively low value of the parameter gn/E_R it is reasonable to work with the approximations (9.35,9.37) neglecting the density dependence of m^* and supposing the chemical potential to be linear in the density.

Fig. 9.1 displays both the experimental data reported in [73] and the theoretical curve (9.51) for the dipole frequency as a function of lattice depth. Note that experimentally it is difficult to measure this frequency in a very deep lattice since the system enters a regime of nonlinear oscillations (see discussion below in section 9.6). For this reason, oscillations with the frequency (9.51) can be observed only if the oscillations amplitude is kept very small. In fact, it has turned out to be difficult to excite measurable harmonic center-of-mass oscillations at lattice depths $s > 9$.

In [75] experimental data for the frequencies of the axial breathing mode and the dipole mode have been compared with each other. By plotting ω_Q as a function of ω_D (see Fig. 9.2) the ratio of the two frequencies is determined to be 1.57 ± 0.01 in good agreement with the value $\sqrt{5/2}$ predicted based on the results (9.51,9.52). Furthermore, assuming the theoretical prediction to be true, the value of the effective mass m^* at a given lattice depth s can be extracted and compared to the calculated value. The results are depicted in Fig. 9.3 which also includes data obtained from the GP-simulation reported in [143] for the two types of oscillations. In contrast with the s-dependence of ω_D and ω_Q, the frequency of the transverse

breathing mode is found to be $2\omega_\perp$ independent of the lattice depth. This is in agreement with the theory described above. The respective experimental data is presented in Fig. 9.4.

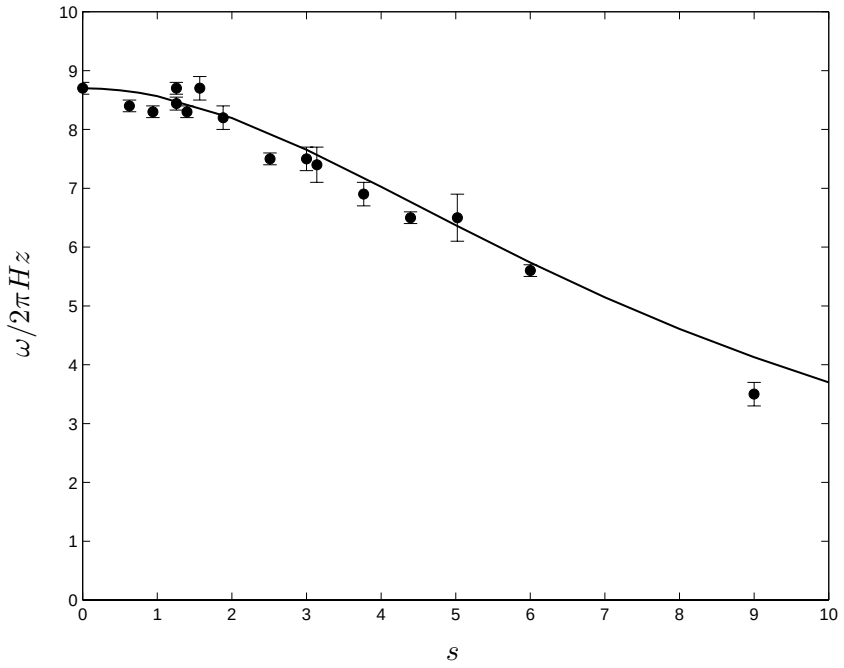

Figure 9.1: Frequency of the small amplitude center-of-mass oscillation as a function of lattice depth s for the experimental setting [73]. The circles display the experimental data reported in [73]. The solid line refers to the theoretical prediction (9.51).

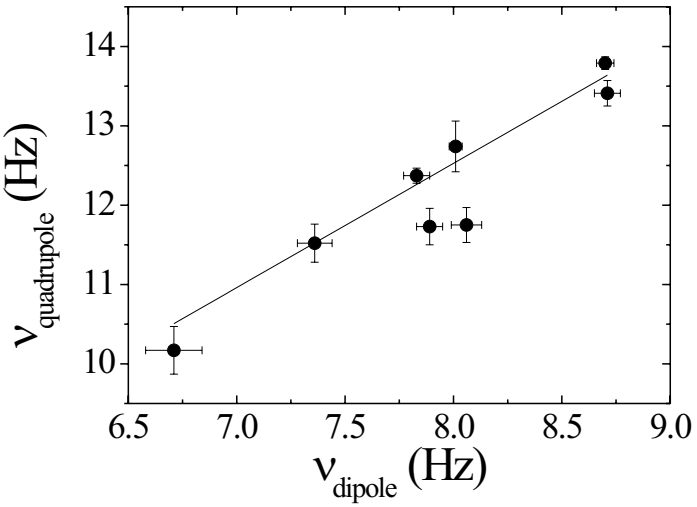

Figure 9.2: Frequency of the axial quadrupole mode of an elongated condensate trapped in the combined potential of harmonic magnetic trap and 1D optical lattice as a function of the axial dipole mode frequency measured for different values of the optical lattice depth from $0E_R$ to $4.1E_R$ in the experiment [75]. The line represents a linear fit with a slope of 1.57 ± 0.01. Figure taken from [75].

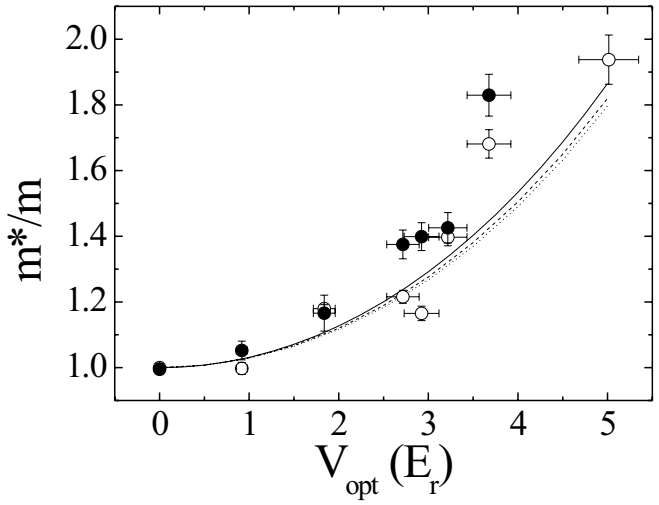

Figure 9.3: Effective mass extracted from the axial dipole mode frequency (open circles) and from the axial quadrupole mode frequency (closed circles) using Eqs. (9.51,9.52) as a function of lattice depth $V_{opt} \equiv s$ in the experiment [75]. The continuous line represents the theoretical curve (9.51), while dashed and dotted lines correspond to the values obtained in [143] by numerically solving the GPE and evaluating the effective mass from the quadrupole and the dipole mode frequencies. Figure taken from [75].

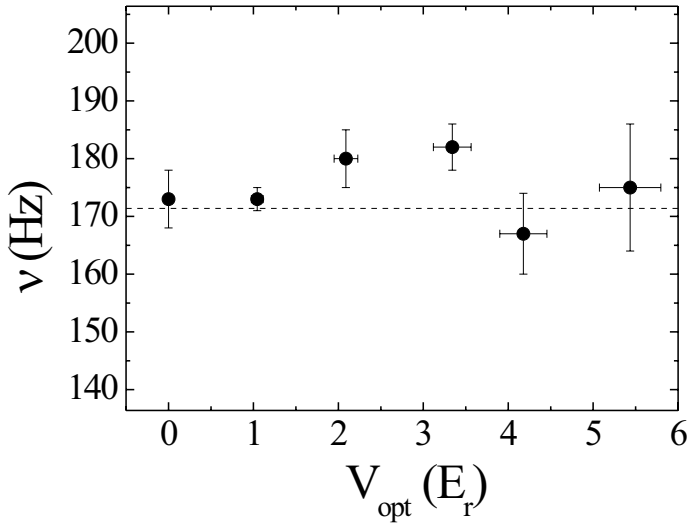

Figure 9.4: Frequency of the transverse breathing mode of the condensate measured in the experiment [75] as a function of the optical lattice depth $V_{opt} \equiv s$. The dashed line corresponds to the expected value $2\nu_\perp$. Figure taken from [75].

9.6 Center-of-mass motion: Linear and nonlinear dynamics

The result

$$\omega_D = \sqrt{\frac{m}{m^*}}\omega_z \tag{9.56}$$

for the frequency of small amplitude dipole oscillations in the presence of the harmonic potential (9.34) has been obtained in the previous section 9.5 under the condition that the chemical potential without harmonic trap can be approximated by the linear law $\mu_{\rm opt} = \tilde{g} n_M + \mu_{gn=0}$. Now, we will show that in the particular case of the dipole, no knowledge about the density dependence of the chemical potential is required in order to derive the result (9.56). As previously, we require the effective mass to be density-independent $m^* = m^*(gn = 0)$.

The center-of-mass motion in the lattice direction is associated with a uniform macroscopic superfluid velocity in the z-direction

$$v_{Mz} = \hbar k(t)/m\,, \tag{9.57}$$

associated with a quasi-momentum which depends only on time, but not on postion. The hydrodynamic equations for small currents (9.17,9.18) with this choice for v_{Mz}, $v_{Mx} = v_{My} = 0$, and $V_{\rm ext}$ given by the harmonic potential (9.34) read

$$\frac{\partial}{\partial t} n_M + \frac{m}{m^*}\frac{\hbar k}{m}\partial_z n_M = 0\,, \tag{9.58}$$

$$\hbar\frac{\partial}{\partial t} k + m\omega_z^2 z = 0\,. \tag{9.59}$$

These equations can be recast to describe the motion of the center-of-mass

$$Z(t) = \frac{1}{N}\int d\mathbf{r}\,(z n_M)\ , \tag{9.60}$$

yielding

$$\frac{\partial}{\partial t} Z - \frac{m}{m^*}\frac{\hbar k}{m} = 0\,, \tag{9.61}$$

$$\hbar\frac{\partial}{\partial t} k + m\omega_z^2 Z = 0\,. \tag{9.62}$$

These equation allow for a solution $Z \propto e^{i\omega_D t}$ with

$$\omega_D = \sqrt{\frac{m}{m^*}}\omega_z\,, \tag{9.63}$$

in agreement with (9.51). This result is independent of the equation of state of the system since the equations (9.58,9.61) do not contain $\mu_{\rm opt}(n_M)$ at all. Actually, it is a general property of the center-of-mass oscillation in a harmonic potential not to be affected by the interactions between particles. This reflects the fact that this particular type of oscillation does not involve a compression of the sample.

Large amplitude dipole oscillations

Large amplitude dipole oscillations can be described using the large-current hydrodynamic equations (9.24,9.25). We consider the velocity field in z-direction to be given by (9.57) as in the case of small amplitudes, while $v_{Mx} = v_{My} = 0$. The assumption of a density-independent effective mass is replaced by the more general requirement that the energy $\varepsilon(k)$ is independent of density. This is equivalent to setting it equal to the single particle band

$$\varepsilon(k, gn/E_R) \approx \varepsilon(k, gn/E_R = 0)\,. \tag{9.64}$$

The hydrodynamic equations for large currents (9.24,9.25) for the center-of-mass as defined in (9.60) then take the form

$$\frac{\partial}{\partial t} Z - \frac{1}{\hbar}\partial_k \varepsilon(k) = 0\,, \tag{9.65}$$

$$\hbar \frac{\partial}{\partial t} k + m\omega_z^2 Z = 0\,. \tag{9.66}$$

containing the dispersion $\varepsilon(k)$, or more precisely, the momentary group velocity $\bar{v}(t) = \partial_k \varepsilon(k(t))$ (see Eq.(6.18)) as a crucial ingredient. Small currents or, equivalently, small group velocities are associated with small deviations of k from $k = 0$. In this case, the dispersion is given by $\varepsilon = \hbar^2 k^2/2m^*$ and the equations (9.65,9.66) reduce to those for small amplitude dipole oscillations (9.61,9.62).

In the tight binding regime, $\partial_k \varepsilon(k) = \delta d \sin(kd)$ (see Eq.(4.29)). Thus, the center-of-mass obeys the equations of motion [73]

$$\frac{\partial}{\partial t} Z - \frac{\delta d}{\hbar} \sin(kd) = 0\,, \tag{9.67}$$

$$\hbar \frac{\partial}{\partial t} k + m\omega_z^2 Z = 0\,. \tag{9.68}$$

They describe a nonlinear pendulum. Its small amplitude oscillation is harmonic with frequency (9.63), as discussed previously (recall that δ is related to the effective mass through (4.33)). This regime is reached for

$$Z \ll \sqrt{\frac{\delta}{m\omega_z^2}}\,. \tag{9.69}$$

Hence, the deeper the lattice the smaller the initial displacement has to be in order to stay in the regime of harmonic oscillations. For initial values of Z larger than $\sqrt{2\delta/m\omega_z^2}$ the solutions of (9.67,9.68) correspond to a full rotation of k. If the initial value $Z = Z_0$ is much larger than $\sqrt{\delta/m\omega_z^2}$, one can treat the center-of-mass as constant and the solution takes the simple form

$$k = -tZ_0 m\omega_z^2/\hbar\,, \tag{9.70}$$

implying a constant increase of the quasi-momentum. This is analogous to the behavior of the quasi-momentum during Bloch-oscillations driven by a constant force. The time evolution for small displacement $Z - Z_0$ from is given by

$$Z = Z_0 + \frac{\delta}{m\omega_z^2 Z_0} \cos\left(\frac{dm\omega_z^2 Z_0}{\hbar} t\right)\,. \tag{9.71}$$

This solution corresponds to an oscillation of Z around Z_0 with amplitude much smaller than Z_0. Hence, the center-of-mass is always displaced from the center of the trap.

Breakdown of large amplitude dipole oscillations

The above discussion of dipole oscillations associates the dynamics of the condensate quasi-momentum $k(t)$ with its dynamics in real space $Z(t)$. Two limits have been considered explicitly: We have found that a harmonic center-of-mass motion goes along with a small amplitude oscillation of the condensate quasi-momentum around $k = 0$. In contrast, very large initial displacements Z_0 lead to a monotonic increase of k with time while in real space the condensate exhibits an off-centered oscillation. This latter case indicates that the stability analysis of condensate Bloch states commented on at the end of chapter 6.1 is relevant to understand the response of a condensate to the displacement of the harmonic trap in the lattice direction: Once $k(t)$ takes values corresponding to unstable Bloch states we can't be sure any more whether the condensate will actually exhibit the dynamics exemplified above. The breakdown of the superfluid current due to a dynamical instability has been predicted in [115]. The role played by dynamical instabilities has also been investigated by numerically solving the time-dependent Gross-Pitaevskii equation in the presence of both optical lattice and harmonic trapping potential. This has been done in [118] for a one-dimensional system and in [144, 145] including also the radial degrees of freedom, confirming that the occurence of dynamical instabilities leads to a breakdown of the center-of-mass motion. On the experimental side, it hs been found that beyond a critical displacement of the trap, which decreases as a function of lattice depth, the condensate does not exhibit oscillations and stops at a position displaced from the trap center [74, 76].

Chapter 10

Array of Josephson junctions

In a deep lattice, the time-evolution of the system can be described in terms of the dynamics of the number of particles and the condensate phase at each lattice site. This formulation incorporates a particularly clear physical picture: The system is considered as an array of weakly linked condensates, each of which contains a time-dependent number of particles and is characterized by a time-dependent phase. The coupling between the condensates is provided by the tunneling of atoms between neighbouring lattice wells. From this point of view, the system constitutes a particular realization of an array of Josephson junctions. This approach is particularly valuable because it allows for a link between the regime of validity of GP-theory with a regime, described by a quantum Josephson Hamiltonian, where quantum fluctuations of phases and site occupations are important. The link is established by quantizing the Josephson Hamiltonian obtained from GP-theory.

Within the regime of validity of GP-theory, the occupation and phase of each site is well-defined at any time. We derive the dynamical equations governing their time evolution in the purely periodic potential (see section 10.1). In the most general case, they are characterized by the appearance of time-dependent tunneling parameters.

We show how to reproduce the tight binding expression for the lowest Bogoliubov band found in chapter 7.3 above (see section 10.2). The Josephson junction array description allows for a particularly clear physical interpretation: Bogoliubov excitations are associated with the exchange of a small amount of atoms between the lattice sites. The quasi-momentum $\hbar q$ of the excitation is a measure of the number of lattice sites over which this exchange takes place. At the maximal value $q = \pi/d$ atoms move back and forth only between neighbouring sites. We show that in the limit of very deep lattices, the spectrum can be determined neglecting the difference in the occupation of neighbouring sites and retaining only the phase difference.

Under certain simplifying assumptions the dynamical equations for phases and site occupations of the array can be recast in the form of Hamiltonian equations (see section 10.3). We present the corresponding Josephson Hamiltonian and discuss the governing Josephson parameters. The plasma oscillation frequency of a single Josephson junction is compared with the corresponding Bogoliubov excitation in an array. The equations of motion governing a single Josephson junction bear certain analogies with those for the center-of-mass motion in the combined trap of lattice and harmonic trap in the tight binding regime (see chapter 9.6 above).

The formalism developed in this chapter is useful in understanding the propagation of sound signals in a condensate subject to a lattice potential (see the subsequent chapter 11).

In [102], we presented the dynamical equations for the occupations and phases of each site, as well as the result for the lowest Bogoliubov band. The discussion of the Josephson Hamiltonian is added here.

10.1 Current-phase dynamics in the tight binding regime

In section 6.1 we have discussed Bloch state solutions of the stationary GP-equation in the periodic potential of the optical lattice. We have shown that the condensate Bloch functions $\Psi_{jk}(z)$ can be written in terms of the condensate Wannier functions $f_{j,l}(z)$ in the following way

$$\Psi_{jk}(z) = \sum_l \sqrt{nd} f_{j,l}(z) e^{ikld} \,. \tag{10.1}$$

Note that Ψ_{jk} is normalized to the total number of atoms $N_{\rm tot}$ and apart from the normalization coincides with the Bloch function φ_{jk} (see Eq.(5.2)). In this section we will use an ansatz similar to (10.1) for the time-dependent condensate wavefunction $\Psi(z,t)$, allowing for the time-dependence of site occupation and phase. In the tight binding regime the time-dependent phases and populations of each lattice site emerge as the dynamical variables.

Let us consider a stationary Bloch state of the lowest band ($j = 1$) in the tight binding regime. For convenience, we will choose the corresponding Wannier functions f_l to take only real values. Since f_l is well localized at site l we can say that the condensate at site l has phase

$$S_l = kld - \frac{\mu(k)}{\hbar} t \,. \tag{10.2}$$

The density of particles at site l is simply given by

$$n_l = n \,, \tag{10.3}$$

where, as previously, n is the average density of the system. Hence, in this state the population of each site is constant across the sample at any time t, while the phases S_l vary with the site index and have the simple time dependence $\mu(k)t/\hbar$. Furthermore, recall that two Wannier functions f_l, $f_{l'}$ can be obtained from each other by a simple displacement

$$f_l(z) = f_{l'}(z - (l - l')d) \tag{10.4}$$

and that the set $\{f_l\}$ is found for a given average density n

$$f_l(z) = f_l(z; n) \,. \tag{10.5}$$

Ansatz for the time-dependent wavefunction

We are interested in time-dependent solutions $\Psi(z,t)$ of (3.14). We focus on states whose form is obtained by releasing the restriction of the phases S_l and the average densities n_l to

the values (10.2,10.3) and allow them to undergo a general time-dependent evolution

$$S_l = kld - \frac{\mu(k)}{\hbar}t \to S_l(t)\,, \tag{10.6}$$

$$n_l = n \to n_l(t)\,. \tag{10.7}$$

Furthermore, we require the shape of the wavefunction at site l to be well approximated by the Wannier function f_l obtained for a Bloch state (10.1) with average density $n = n_l(t)$. This presupposes an adiabatic adaptation of the shape of the wavefunction to the instantaneous value of $n_l(t)$. Given these assumptions the time-dependent state $\Psi(z,t)$ is written in the form

$$\Psi(z,t) = \sum_l f_l(z; n_l(t))\sqrt{n_l(t)d}e^{iS_l(t)}\,. \tag{10.8}$$

This ansatz must ensure that the quantities n_l indeed have the meaning of the average density at site l. Thus, (10.8) must satisfy the equation

$$\int_{ld-d/2}^{ld+d/2} dz\,|\Psi(z,t)|^2 = n_l d\,. \tag{10.9}$$

This is achieved by requring $f_l(z;n_l)$ to be very well localized at the site l such that $f_{l\pm1}$ have a negligible contribution to the population of site l ($\int_{ld-d/2}^{ld+d/2} dz f_{l\pm1}^2 = 0$). In addition, we require the orthogonalization condition

$$\int dz f_l(z; n_l(t)) f_{l'}(z; n_{l'}(t)) = \delta_{l,l'}\,, \tag{10.10}$$

to be approximately satisfied. Exact orthogonality is guaranteed of course only for a stationary state where $n_l = n_{l'}$.

Dynamical equations phases and site occupations

The wavefunction $\Psi(z,t)$ evolves according to the time-dependent GP-equation (3.14). To obtain dynamical equations for the phases S_l and average densities n_l, we insert (10.8) into the GPE. Upon multiplication of (3.14) by Ψ^* and integration over the total volume, using (10.10) we obtain

$$\dot{n}_l = \sum_{l'=l+1,l-1} \frac{\delta^{l,l'}}{\hbar}\sqrt{n_l n_{l'}}\,\sin(S_l - S_{l'})\,, \tag{10.11}$$

$$\dot{S}_l = -\frac{\mu_l}{\hbar} + \sum_{l'=l+1,l-1} \frac{\delta_\mu^{l,l'}}{2\hbar}\sqrt{\frac{n_{l'}}{n_l}}\,\cos(S_l - S_{l'})\,, \tag{10.12}$$

where

$$\mu_l = \int f_l\left[-\frac{\hbar^2\partial_z^2}{2m} + V(z) + gn_l d|f_l|^2\right] f_l dz\,, \tag{10.13}$$

while the time-dependent tunneling parameters $\delta^{l,l'}$ and $\delta_\mu^{l,l'}$ are directly related to the overlap between two neighbouring Wannier functions

$$\begin{aligned}\delta^{l,l'} &= -2\int dz\left[f_l\left(-\frac{\hbar^2\partial_z^2}{2m}+V\right)f_{l'} + gn_l d\, f_l|f_l|^2 f_{l'} + gn_{l'} d\, f_l|f_{l'}|^2 f_{l'}\right],\\ \delta_\mu^{l,l'} &= \delta^{l,l'} - 4gn_l d\int f_l|f_l|^2 f_{l'} dz.\end{aligned} \tag{10.14}$$

Note that at equilibrium $\delta^{l,l'} = \delta$ and $\delta_\mu^{l,l'} = \delta_\mu$, where δ and δ_μ have been previously defined in Eq.(6.31) and in Eq.(6.34). At equilibrium they do not depend on the sites l and l' since the wavefunctions f_l are related to each other through (10.4).

In deriving the dynamical equations (10.11,10.12) we have retained contributions from the nonlinear term involving $\int f_l^3 f_{l\pm1} dz$, but discarded terms arising from $\int f_l^2 f_{l\pm1}^2 dz$, as in previous chapters. It can be easily checked that the latter contributions are much smaller than the former.

An approach equivalent to the Josephson formalism presented in this section, based on the ansatz

$$\Psi(\mathbf{r}, t) = \sum_l \psi_l(t) f_l(\mathbf{r}; N_l(t)) \tag{10.15}$$

has been developed in [116, 117]. Here, N_l is the time-dependent occupation of the site l and $f_l(\mathbf{r}; N_l(t))$ is the corresponding Wannier function at site l. In practize, ψ_l is a discrete wavefunction which corresponds to our $\sqrt{n_l d} e^{iS_l}$. Replacing this nonlinear tight binding ansatz into the time-dependent GP-equation and integrating out the spatial degrees of freedom, a discrete nonlinear equation for the $\psi_l(t)$ is obtained. The authors find that it is justified to approximate the Wannier functions in (10.15) by their solution at equilibrium. In our case, this corresponds to setting $\delta^{l,l'} = \delta$ and $\delta_\mu^{l,l'} = \delta_\mu$ in the dynamical equations (10.11,10.12). Moreover, in this approximation the on-site chemical potential (10.13) depends linearly on the time-dependent deviation $n_l - n$ from the average density.

Lowest chemical potential Bloch band

Let us assume the system to be in a Bloch state of the lowest band. This corresponds to setting S_l and n_l equal to (10.2,10.3) in the equations of motion (10.11,10.12). While the equation for $\dot{n}_l$ is solved trivially, the equation for $\dot{S}_l$ yields

$$\mu(k) = \mu_0 - \delta_\mu \cos(kd)\,, \tag{10.16}$$

where μ_0 is obtained by evaluating (10.13) for $n_l = n$. This is exactly the expression for the lowest chemical potential Bloch band in the tight binding regime discussed in section 6.2 (see Eq.(6.32)).

10.2 Lowest Bogoliubov band

In order to recover the tight binding expression (7.38) for the lowest Bogoliubov band in the tight binding regime we consider small deviations of the phases S_l and the average densities n_l from the groundstate

$$S_l = \Delta S_l\,, \tag{10.17}$$

$$n_l = n + \Delta n_l\,, \tag{10.18}$$

where we used that $S_l = 0$ at equilibrium. We then linearize Eqs.(10.11,10.12) in ΔS_l, Δn_l. The result reads

$$\dot{\Delta n_l} = n\frac{\delta}{\hbar}\left(2\Delta S_l - \Delta S_{l+1} - \Delta S_{l-1}\right)\,, \tag{10.19}$$

$$\dot{\Delta S}_l = -\left[\frac{\mu_l}{\hbar}+\frac{\delta_\mu}{\hbar}\right]_{n_l=n} - \left[\frac{1}{\hbar}\frac{\partial\mu_l}{\partial n_l}\right]_{n_l=n}\Delta n_l + \sum_{l'=l+1,l-1}\left[\frac{\delta+2n\frac{\partial\delta}{\partial n}}{4n\hbar}\Delta n_{l'} - \frac{\delta-2n\frac{\partial\delta}{\partial n}}{4n\hbar}\Delta n_l\right] . \quad (10.20)$$

To obtain (10.19) we have taken the value of $\delta^{l,l'}$ at equilibrium since the dependence on ΔS_l is of first order. Instead, to get Eq.(10.20) one has to expand $\delta_\mu^{l,l'}$ to first order in the density fluctuations Δn_l

$$\begin{aligned}\delta_\mu^{l,l'} &\approx \delta_\mu + \left.\frac{\partial\delta_\mu^{l,l'}}{\partial n_l}\right|_{n_l=n}\Delta n_l + \left.\frac{\partial\delta_\mu^{l,l'}}{\partial n_{l'}}\right|_{n_l=n}\Delta n_{l'} \\ &= \delta_\mu + \frac{3}{2}\frac{\partial\delta}{\partial n}\Delta n_l + \frac{1}{2}\frac{\partial\delta}{\partial n}\Delta n_{l'} ,\end{aligned} \quad (10.21)$$

where in the last step we have neglected terms involving $\partial f/\partial n$, as done previously in sections 6.2 and 7.3. Taking the derivative of (10.20) with respect to time and and inserting (10.19) we find

$$\begin{aligned}\ddot{\Delta S}_l = &-\left[\frac{1}{\hbar}\frac{\partial\mu_l}{\partial n_l}\right]_{n_l=n}\frac{n\delta}{\hbar}\left(2\Delta S_l - \Delta S_{l+1} - \Delta S_{l-1}\right) \\ &+\frac{n\delta}{\hbar^2}\left(\frac{\delta+2n\frac{\partial\delta}{\partial n}}{4n}\right)\left[(2\Delta S_{l+1} - \Delta S_{l+2} - \Delta S_l) + (2\Delta S_{l-1} - \Delta S_l - \Delta S_{l-2})\right] \\ &-2\frac{n\delta}{\hbar^2}\left(\frac{\delta-2n\frac{\partial\delta}{\partial n}}{4n}\right)\left(2\Delta S_l - \Delta S_{l+1} - \Delta S_{l-1}\right) .\end{aligned} \quad (10.22)$$

This equation is solved by

$$\Delta S_l \propto e^{i(lqd-\omega(q)t)} , \quad (10.23)$$

with

$$\hbar\omega(q) = \sqrt{2\delta\sin^2\left(\frac{qd}{2}\right)\left[2\left(\delta+2n\frac{\partial\delta}{\partial n}\right)\sin^2\left(\frac{qd}{2}\right)+2n\frac{\partial\mu_l}{\partial n}-4n\frac{\partial\delta}{\partial n}\right]} . \quad (10.24)$$

Recalling the tight binding expression for the inverse compressibility (see Eq.(6.43)) we can rewrite (10.24) in the form

$$\hbar\omega(q) = \sqrt{2\delta\sin^2\left(\frac{qd}{2}\right)\left[2\left(\delta+2n\frac{\partial\delta}{\partial n}\right)\sin^2\left(\frac{qd}{2}\right)+2\kappa^{-1}\right]} , \quad (10.25)$$

in agreement with the result (7.38) obtained from the solution of the Bogoliubov equations (7.14,7.15).

It is interesting to note that if we initially set $\sqrt{n_l n_{l'}} = n_l$ in Eq.(10.11) we obtain the result

$$\hbar\omega(q) = 2\sqrt{\delta\kappa^{-1}}\left|\sin\left(\frac{qd}{2}\right)\right| \quad (10.26)$$

for the dispersion of small groundstate perturbations. This proves that the first term in the brackets of Eq.(10.25) has its physical origin in the fluctuations of the site occupations occurring on a few-sites length scale which are excluded when setting $\sqrt{n_l n_{l'}} = n_l$. Note that

the expression (10.26) coincides with the large-s limit of (10.25) (see Eq.(7.39) and respective discussion) indicating that short length scale fluctuations of the average density are suppressed in a deep lattice.

The formalism based on the dynamical equations (10.11,10.12) assigns a simple physical picture to small groundstate perturbations: They correspond to small amplitude plane wave variations of the phases S_l and the average densities n_l

$$\Delta S_l \propto e^{i(lqd-\omega(q)t)}\,, \tag{10.27}$$

$$\Delta n_l \propto e^{i(lqd-\omega(q)t)}\,. \tag{10.28}$$

The phase difference of the perturbation at neighbouring sites equals qd. Since the wavelength of such excitations can't be smaller than twice the lattice period d, the wavenumber q corresponding to the quasi-momentum of the Bogoliubov amplitudes used in section 7, has its maximal physically relevant value at π/d. For this maximal value the phase difference is π implying that the perturbation at neighbouring sites is exactly out of phase: One site takes the minimal values of phase and population when the neighbouring sites reach the maxima. This is just another way of saying that the perturbation has wavelength $2d$ and that a particle exchange takes place between neighbouring wells. In contrast, at the minimal value of $q = 2\pi/L$ the wavelength of the perturbation equals the size of the system and thus, particles involved in the perturbation can be carried across half of the system length L.

10.3 Josephson Hamiltonian

Let us neglect the density dependence of $\delta^{l,l'}$ and $\delta^{l,l'}_{\mu}$ appearing in the dynamical equations (10.11,10.12). This corresponds to setting both quantities equal to the time-independent single particle tunneling matrix element (4.30)

$$\delta^{l,l'} = \delta^{l,l'}_{\mu} = \delta_{gn=0} \;=\; -2\int dz\, f^{*}_{gn=0}(z)\left(-\frac{\hbar^2}{2m}\frac{\partial^2}{\partial z^2} + V(z)\right) f_{gn=0}(z-d)\,, \tag{10.29}$$

where $f_{gn=0}$ is the single particle Wannier function of the lowest band. Consistently with this step, we replace in μ_l as defined in (10.13) the density-dependent Wannier function by $f_{gn=0}$. In this way, we get

$$\mu_l = \varepsilon_{0\mathrm{sp}} + n_l g d \int f^4_{gn=0} dz\,, \tag{10.30}$$

where $\varepsilon_{0\mathrm{sp}}$ is the time-independent term

$$\varepsilon_{0\mathrm{sp}} = \int f_{gn=0}\left[-\frac{\hbar^2\partial_z^2}{2m} + V(z)\right] f_{gn=0} dz\,, \tag{10.31}$$

which we omit in the following. It is common to write the dynamical equations in terms of the populations N_l rather than the average densities n_l and to replace the one-dimensional Wannier function $f_{gn=0}(z)$ by the corresponding three-dimensional one $f_{gn=0}(\mathbf{r}) = f(z)/L$. Note that the latter step affects only the g-dependent term in the equation for $\dot{S}_l$. We obtain

$$\hbar\dot{N}_l \;=\; \sum_{l'=l+1,l-1} \delta_{gn=0}\sqrt{N_l N_{l'}}\;\sin(S_l - S_{l'})\,, \tag{10.32}$$

$$\hbar\dot{S}_l \;=\; -N_l\frac{E_C}{2} + \sum_{l'=l+1,l-1} \frac{\delta_{gn=0}}{2}\sqrt{\frac{N_{l'}}{N_l}}\;\cos(S_l - S_{l'})\,, \tag{10.33}$$

where we have introduced the charging or capacitative energy

$$E_C = 2g \int f_{gn=0}(\mathbf{r})^4 d^3\mathbf{r}\,. \tag{10.34}$$

We note that E_C is closely related to the compressibility of the system

$$\kappa^{-1} = \tilde{g}n = N\frac{E_C}{2}\,, \tag{10.35}$$

where $\tilde{g}$ is the effective coupling constant introduced in section 5.2 and N, as previously, is the number of particles per well at equilibrium.

The equations of motion (10.32,10.33)) can be rewritten in the Hamiltonian form

$$\hbar\dot{\Delta}N_l = -\frac{\partial H_J}{\partial S_l}\,, \tag{10.36}$$

$$\hbar\dot{S}_l = \frac{\partial H_J}{\partial \Delta N_l}\,, \tag{10.37}$$

where $\Delta N_l = N_l - N$ is the deviation of the population at site l from its equilibrium value N (Note that $\sum_l \Delta N_l = 0$). These equations are governed by the Josephson Hamiltonian (see for example [1], chapter 16)

$$H_J = -\frac{E_C}{4}\sum_l (\Delta N_l)^2 + \delta_{gn=0}\sum_l \sqrt{(N+\Delta N_{l+1})\,(N+\Delta N_l)}\,\cos(S_{l+1}-S_l)\,. \tag{10.38}$$

This Hamiltonian describes an array of Josephson junctions with on-site charging energy E_C arising from 2-body interaction and a next-neighbour tunneling parameter $\delta_{gn=0}$ which does not depend on the site index and is solely determined by the external lattice potential.

A double-well system with just two lattice sites is a physical realization of a single Josephson junction. The respective Hamiltonian is given by (10.38) with ($l = 1, 2$). It reads

$$H_J = -\frac{E_C}{2}m^2 + \delta_{gn=0}\sqrt{N-m^2}\,\cos\Phi\,, \tag{10.39}$$

where we have introduced the quantities

$$m = \frac{N_1 - N_2}{2}\,, \tag{10.40}$$

$$\Phi = S_1 - S_2\,. \tag{10.41}$$

In this case, the difference between populations suffices to describe the dynamics of the system since $\Delta N_1 = -\Delta N_2$. The equations of motion for m and Φ can be obtained from this Hamiltonian

$$\hbar\dot{m} = -\frac{\partial H_J}{\partial \Phi}\,, \tag{10.42}$$

$$\hbar\dot{\Phi} = \frac{\partial H_J}{\partial m}\,. \tag{10.43}$$

They read

$$\hbar\dot{m} = \delta_{gn=0}\sqrt{N^2-m^2}\,\sin(\Phi)\,, \tag{10.44}$$

$$\hbar\dot{\Phi} = -E_C m - \delta_{gn=0}\frac{m}{\sqrt{N^2-m}}\,\cos(\Phi)\,. \tag{10.45}$$

For a typical double well system, the m-dependence in front of the $\cos\Phi$ of the Hamiltonian (10.39) is not important. The gas must be very dilute for it to be relevant (see [1] chapter 15 for a discussion of this issue). Neglecting this contribution, the Hamiltonian and the equations of motion read

$$H_J = -\frac{E_C}{2}m^2 + E_J \cos\Phi\,, \tag{10.46}$$

$$\hbar\dot{m} = E_J \sin(\Phi)\,, \tag{10.47}$$

$$\hbar\dot{\Phi} = -E_C m\,, \tag{10.48}$$

with the Josephson tunneling energy

$$E_J = N\delta_{gn=0}\,. \tag{10.49}$$

A characteristic property of such a Josephson junction is its possibility to exhibit plasma oscillations of frequency

$$\omega_P = \frac{\sqrt{E_C E_J}}{\hbar}\,. \tag{10.50}$$

They correspond to harmonic small amplitude oscillations around $m = 0, \Phi = 0$ of the pendulum described by the equations (10.47,10.48). The existence of such oscillations was first proposed by Josephson with respect to tunneling currents between superconductors [146]. Using (10.35,10.49) we can rewrite ω_P in the form

$$\omega_P = \frac{\sqrt{2\delta_{gn=0}\tilde{g}n}}{\hbar}\,. \tag{10.51}$$

The junction described by the more complicated Hamiltonian (10.39) exhibits plasma oscillations with the frequency

$$\omega_P = \frac{\sqrt{\delta_{gn=0}(\delta_{gn=0} + NE_C)}}{\hbar} = \frac{\sqrt{\delta_{gn=0}\,(\delta_{gn=0} + 2\tilde{g}n)}}{\hbar}\,. \tag{10.52}$$

It is interesting to note that the lowest Bogoliubov band excitation with $q = \pi/d$ is the physical analogue for a lattice of the plasma oscillations for a single Josephson junction: As discussed above, the excitation at this value of q involves a particle exchange between neighbouring sites. The corresponding frequency is given by (see Eq.(10.25))

$$\hbar\omega(q = \pi/d) = \sqrt{2\delta_{gn=0}\,[2\delta_{gn=0} + 2\tilde{g}n]}\,, \tag{10.53}$$

where consistenly with the discussion of the Josephson Hamiltonian we have set $\delta = \delta_{gn=0}$ and $\kappa^{-1} = \tilde{g}n$. This frequency coincides with (10.52) apart from a factor $\sqrt{2}$. This difference is due the fact that each site of the lattice exchanges particles with two neighbouring wells instead of with just one as in the double well case.

A further interesting connection between the lattice and the double well case emerges when comparing the equations of motion (10.47,10.48) with those for the center-of-mass motion in the tight binding regime given the combined presence of lattice and harmonic trap (see Eqs.(9.67,9.68)): The two sets of equations are formally identical if one identifies

$$m \leftrightarrow \frac{NZ}{d}\,, \tag{10.54}$$

$$\Phi \leftrightarrow kd\,, \tag{10.55}$$

$$E_C \leftrightarrow \frac{m\omega_z^2 d^2}{N}\,. \tag{10.56}$$

For both systems the second crucial parameter apart from E_C is given by $E_J = N\delta_{gn=0}$ setting an upper bound to the current that can flow through the lattice. Note that also the analogies between m, Z and Φ, kd go along with a physical resemblance. Yet, a clear difference consists in the fact that the "charging energy" in the case of the center-of-mass motion is not provided by interactions but by the external trapping potential. The plasma frequency $\omega_P = \sqrt{E_C E_J}/\hbar$ of the single Josephson junction (10.46) corresponds to the dipole frequency $\omega_D = \sqrt{\pi^2\delta/2E_R}\omega_z$ of the harmonically confined lattice in the tight binding regime (see section 9.6 Eq.(9.51) and use (6.41)).

Note that a double well system with a TF-condensate in each well is not well described within the framework presented here. The Josephson Hamiltonian for such a system should involve a density-dependent tunneling parameter and a compressibility which is non-linear in the density. In fact, it is easy to see that if the condensate has a TF-profile in each well, $E_C = 2\partial\mu/\partial N \sim N^{-3/5}$ indeed depends on N. Moreover, the tails of the wavefunction in the region of the barrier are obtained by matching the TF-profile to an exponential decaying function. This matching procedure makes δ sensitive to N. Since for a larger N the TF-profile becomes steeper at the barrier boundary, δ can in fact *de*crease for increasing N [57], in contrast to the behavior of δ discussed in section 7.3 where the wavefunction of the condensate at each site resembles the single particle wavefunction.

Within GP theory, the phases and occupation numbers are classical quantities. One can go beyond this description by quantizing the appropriate Josephson Hamiltonian, replacing the classical dynamical variables with operators (see discussion in [1] chapter 15.6). This shows that the parameters $E_J = N\delta$ and E_C (10.34) play an important role in evaluating the quantum fluctuations of phases and site occupations: The inequality $E_C \ll E_J$, corresponding to strong tunneling, turns out to be the conditon for applying GP-theory. In this limit the qunatum phase fluctuations are small while the occupation number fluctuations are large. In the opposite case of weak tunneling $E_C \gg E_J$ the relative phases are distributed in a random way, while fluctuations in the occupations numbers are small.

Discrete nonlinear Schrödinger equation

The dynamical equations (10.11,10.12) with the quantities $\delta^{l,l'}$, $\delta^{l,l'}_{\mu}$, μ_l evaluated using $f_{gn=0}$ are equivalent to the Discrete Nonlinear Schrödinger Equation (DNLS) for the discrete wavefunction ψ_l

$$i\hbar\dot{\psi}_l = -\frac{\delta_{gn=0}}{2}\left(\psi_{l+1} + \psi_{l-1}\right) + U|\psi_l(t)|^2\psi_l(t), \tag{10.57}$$

which can be obtained using the ansatz (10.15) with the single particle Wannier functions. Here, $\delta_{gn=0}$ governs the tunneling between neighbouring wells and $U = \tilde{g}n$ describes on-site interactions. The DNLS has been used for example in [147] to investigate nonlinear phenomena like solitons and breathers. In the next chapter, we will use it to study sound propagation in the presence of a lattice.

Chapter 11

Sound propagation in presence of a one-dimensional optical lattice

The propagation of sound in a harmonically trapped condensate without lattice, has been observed in the experiment [148]. We study the effect of a one-dimensional optical lattice on sound propagation in a set-up analogous to this experiment, yet without harmonic trap.

The spectrum of elementary excitations shows a linear behavior $\hbar\omega = c\hbar|q|$ in the lowest Bogoliubov band at small quasi-momenta $\hbar q$, indicating the existence of phonons (see chapter 7.2 above). The sound velocity c decreases for increasing lattice depth, due to reduced tunneling or equivalently to increased effective mass (see chapter 7.4 above). In the regime of validity of the linearized GP-equation, sound propagation is expected to be possible. We confirm numerically that for sufficiently small sound signal amplitude the sound velocity decreases by increasing the lattice depth, as predicted by Bogoliubov theory.

However, it is not obvious a priori whether a sound signal of finite amplitude is able to propagate also in deep lattices, where the tunneling rate is very small. For deep lattices, nonlinear effects are very different from the uniform case: first of all, shock waves propagate slower than sound waves (see section 11.3). This is due to the negative curvature of the Bogoliubov dispersion relation in the lowest Bogoliubov band. The most striking effect is that non-linearities can play a role also at very small density variations and induce a saturation of the sound signal, which goes along with dephased currents in the back of the signal (see section 11.3). This effect has no analogon in the uniform case.

In conclusion we find that sound signals propagate, but that the maximal attainable signal amplitude (density variation) decreases very strongly with the optical lattice depth, making it in practise observable only up to a certain lattice depth which depends on the interaction strength. We show that there exists a range of optical potential depths where the signal is still large enough and where the change in sound velocity induced by the lattice can be measured (see section 11.4).

A paper containing the results presented in this chapter is in preparation.

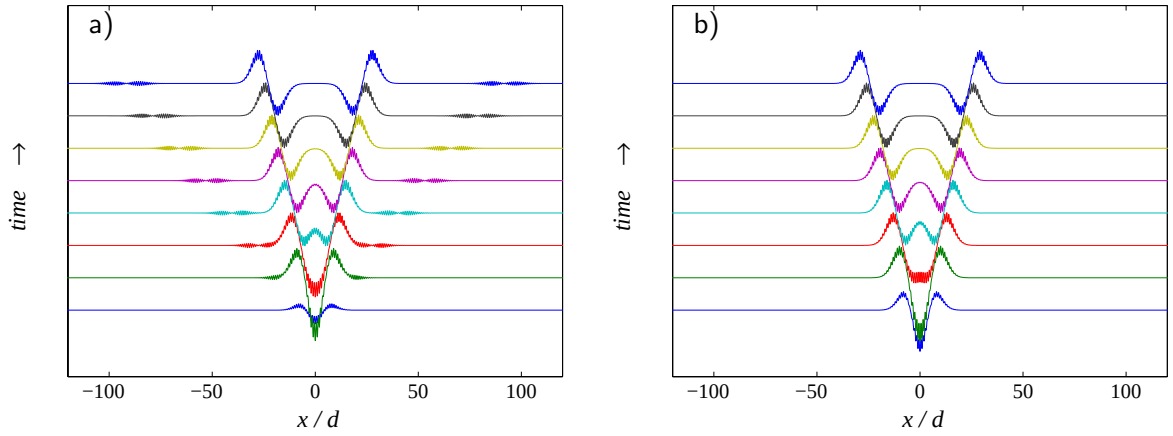

Figure 11.1: Wavepackets produced by a) a fast ($T_p = 1$) and b) a slow ($T_p = 10$) external perturbation of the type (11.1) in presence of an optical lattice. In a) the first, the second and the third band is excited leading to the formation of two pairs of wavepackets. In b) only the slow pair composed of phonons of the lowest band is created.

11.1 Generation of Sound Signals

For usual densities, scattering lengths and lattice spacings, the healing length is of the same order of magnitude as the lattice spacing which implies that the center of the lowest Bogoliubov band has phononic character, while higher bands describe excitations which are mainly particle-like (see discussion in chapter 7).

One can address excitations with low quasi-momentum, by raising and/or lowering a sufficiently large barrier at the center of the trap. Such a procedure generates a pair of wavepackets propagating symmetrically outwards. If the width of the barrier is much larger than the lattice spacing, only quasi-momenta much smaller than the Bragg momentum q_B will be addressed. Moreover, only Bogoliubov bands with energy lower than the inverse time scale T_p of the perturbation will be excited. In particular, since the gap between first and second Bogoliubov band at the center of the Brillouin zone is order of $4E_R$, one has multiple band excitations if $T_p < \hbar/4E_R$, otherwise if $T_p \gg \hbar/4E_R$ only the lowest band will be addressed. The result of a fast perturbation ($T_p = \hbar/E_R$) at low lattice depth is shown in Fig.11.1(a). One finds two pairs of wavepackets propagating at two different velocities. The velocity of the slower ones is given by the sound velocity (7.48), while the velocity of the faster ones is given approximatively by $2q_B/m$, which is close to the derivative of the second and third band of the spectrum at small q. Those fast wave packets are not sound signals but are composed of single particle excitations: they disappear in absence of the lattice, but if the lattice is present they are found also in a non-interacting gas. At first sight, they seem to travel without changing shape, because the curvature of the spectrum is too small to observe their dispersion on the time scale of our simulation. In order to avoid their excitation it is enough to use a slower perturbation, as shown in Fig.11.1(b) where $T_p = 10\hbar/E_R$. In the following, we restrict ourselves to this kind of situation and concentrate on the lowest band dynamics.

The details of the wave packets depend on the excitation scheme with which they are produced. Yet, the main features are general. The observation of sound signals without lattice

[148] was achieved by employing two different excitations methods: The first one consisted in raising a barrier in the center of a harmonically trapped condensate. The second method instead consisted in letting the condensate equilibrate in presence of a barrier, which was then removed. The first method produces a density bump in the center of the trap, which splits into two *bright* sound wavepackets; the second method on the contrary gives rise to a dip in the density which splits into two *dark* sound wavepackets.

The excitation method we adopt is a combination of these two: The initial condensate is at equilibrium in a one-dimensional optical lattice superimposed to a simple box potential. We then switch on and off a gaussian potential barrier in the center. This procedure has the advantage that the ground states of the initial and final potential are identical. For zero lattice depth, we get two composed *bright-dark* sound signals propagating symmetrically outwards.

The potential creating the barrier is written as a product of its spatial and temporal dependence

$$V_B(x,t) = V_{Bx}(x)V_{Bt}(t)\,, \tag{11.1}$$

where

$$V_{Bx}(x) \;=\; bE_R \exp\left[-x^2/(wd)^2\right]\,, \tag{11.2}$$

$$V_{Bt}(t) \;=\; \sin^4\left(\frac{\pi E_R t}{\hbar T_p}\right)\,. \tag{11.3}$$

The tunable parameters are the width of the barrier w, its height b and the time scale T_p. They are subject to the constraints

$$w \gg 1\,, \tag{11.4}$$

in order to address only the quasi-momenta in the central part of the Brillouin zone,

$$wd \gg \xi\,, \tag{11.5}$$

to ensure that the produced excitations are phonons, and

$$T_p > 1 \tag{11.6}$$

in order to excite the lowest Bogoliubov band only. Note that for typical densities and lattice spacings, $w \gg 1$ automatically implies $wd \gg \xi$.

11.2 Current-Phase dynamics

In order to study sound propagation in presence of the lattice, we use the GP-equation

$$i\hbar\dot{\varphi} = \left[-\frac{\hbar^2\partial_x^2}{2m} + V_{tot}(x,t) + gnd|\varphi(x,t)|^2\right]\varphi(x,t) \tag{11.7}$$

and the discrete nonlinear Schrödinger equation (DNLS)

$$i\hbar\dot{\psi}_\ell = -\frac{\delta}{2}\left(\psi_{\ell+1} + \psi_{\ell-1}\right) + \left[V_\ell(t) + U|\psi_\ell(t)|^2\right]\psi_\ell(t), \tag{11.8}$$

valid in the tight binding limit (see chapter 10). In the GPE, the external potential $V_{tot}(x,t)$ is given by the sum of the lattice potential $V = sE_R \sin^2(\pi x/d)$ and the time-dependent barrier potential $V_B(x,t)$ (11.1). In the DNLS (11.8) instead, the potential is just given by the barrier $V_\ell = V_B(ld,t)$, since the presence of the optical potential is included in the assumption that space is discretized.

The GP-equation (11.7) is governed by two parameters: the optical lattice depth s and the interaction strength gn (see chapter 5). These two quantities determine the parameters δ and U in the DNLS, describing respectively the tunneling coupling between two neighboring wells (corresponding to the height of the lowest Bloch band, see chapter 6.2) and the on-site interaction U (see chapter 10).

For future use, it is important to rewrite the equations (11.7,11.8) in terms of the density and the phase of the condensate wavefunction. In continuous space, the condensate wavefunction can be written as $\varphi(x,t) = \sqrt{n(x,t)/n}\exp[iS(x,t)]$ and the GP-equation (11.7) becomes

$$\begin{aligned} \dot{n}(x) &= -\partial_x\left[n(x)\frac{\hbar}{m}\partial_x S(x)\right], \\ \dot{S}(x) &= -\frac{1}{\hbar}\left[V_{tot}(x,t) + gn(x) - \frac{\hbar^2}{2m\sqrt{n}}\partial_x^2\sqrt{n} + \frac{\hbar^2}{2m}\left(\partial_x S(x)\right)^2\right]. \end{aligned} \tag{11.9}$$

In the discrete case, we write $\psi_\ell = \sqrt{n_\ell(t)/n}\exp[iS_\ell(t)]$ and obtain

$$\begin{aligned} \dot{n}_\ell &= \sum_{\ell'=\ell\pm1}\frac{\delta}{\hbar}\sqrt{n_\ell(t)n_{\ell'}(t)}\sin[S_\ell(t) - S_{\ell'}(t)], \\ \dot{S}_\ell &= -\frac{\mu_\ell}{\hbar} + \sum_{\ell'=\ell\pm1}\frac{\delta}{2\hbar}\sqrt{\frac{n_{\ell'}(t)}{n_\ell(t)}}\cos[S_\ell(t) - S_{\ell'}(t)], \end{aligned} \tag{11.10}$$

where $\mu_\ell = Un_\ell + V(\ell)$. Note that apart from the additional potential $V(\ell)$, these are the equations of motion (10.11,10.12) derived in chapter 10 with the density dependent Wannier function replaced by the single particle solution. Already at this stage, an important difference between the uniform case and the deep lattice case can be pointed out: The $\sin$ and $\cos$-terms in the DNLS correspond to the terms involving $\partial_x S$ and $(\partial_x S)^2$ in the GPE for the uniform case respectively. Hence, the presence of a deep lattice is associated with a dependence of the current on the gradient of the phase analogous to the one in the absence of the lattice only if $S_\ell(t) - S_{\ell'}(t) \ll \pi$. When this condition is not fulfilled nonlinear effects arise which have no analogue in the uniform case.

11.3 Nonlinear propagation of sound signals

We solve numerically the GP-equation (11.7) and the DNLS (11.8) for various values of the barrier height b, the barrier width w and the perturbation time T_p. We also vary the parameters s and gn in the case of the GP-equation and the parameters δ and U in the case of the DNLS to explore different regimes of lattice depth and interaction strength. The effect produced by the perturbation can be made visible by looking at the ratio between the density at a certain time $n(x,t)$ and the equilibrium density distribution $n(x,t=0)$. A sound signal emerges as a wavepacket in the ratio $n(x,t)/n(x,t=0)$. It maintains a compact shape and, after an initial

formation time, propagates with a constant speed which we "measure" and compare with the prediction obtained from Bogoliubov theory. Nonlinearities can lead to a deformation of the signal and modify the speed at which it propagates. Yet, as we will see below, this need not be the case in the presence of a lattice, provided that $\delta \ll U/3$. Moreover, nonlinear effects lead to the formation of dephased currents in the back of the signal. In correspondence to this the signal's amplitude saturates while it keeps propagating at the Bogoliubov sound velocity.

Apart from the relative density, we also look at the evolution of the relative phase $\phi_{\ell+1/2}$ between neighbouring wells. The quantity $\phi_{\ell+1/2}$ is defined as

$$\phi_{\ell+1/2} = S_{\ell+1} - S_\ell \tag{11.11}$$

in the case of the DNLS, while in the case of the GP-equation we define

$$\phi_{\ell+1/2} = S(x = (l+1)d) - S(x = ld) \tag{11.12}$$

Note that in a deep lattice the phase distribution within each well is found to be flat to a good degree. An example for $n_l(t)/n_l(t=0)$ and $\phi_{\ell+1/2}$ is plotted in Fig.11.2. We call Δn the amplitude of the sound wave packet in the relative density and $\Delta\phi$ the amplitude of the wavepacket in the relative phase, as shown in Fig.11.2.

Our first result is that sound signals of measurable amplitude can be observed also in deep lattices where the sound velocity is considerably lower than in the uniform system. This is illustrated in Fig. 11.3 which depicts the sound velocity obtained from the simulation (circles) with the respective signal amplitudes Δn together with the Bogoliubov prediction (solid line). Up to $s = 20$ relatively large signal amplitudes can be obtained at this value of g. Note that the signal amplitudes obtained from the simulation at $s = 20,\ 30$ correspond to their saturated values as discussed further below.

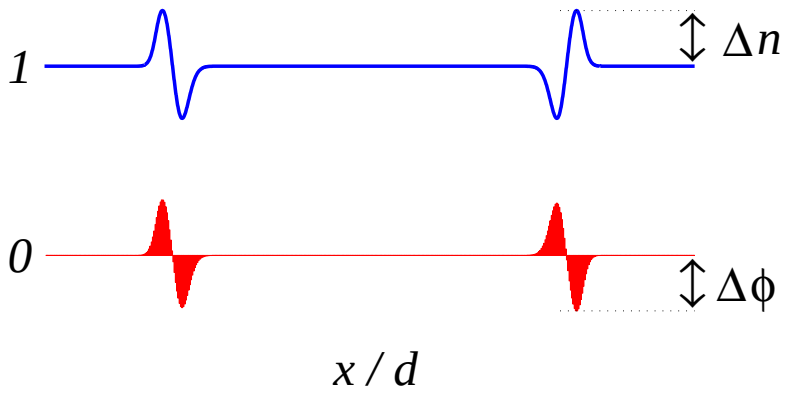

Figure 11.2: Example for sound signals as obtained from the DNLS (11.8). The signals are created in the center with a relatively weak external perturbation of the form (11.1). They move outward to the left and to the right at the Bogoliubov sound velocity. Upper panel: Ratio between the density at a long time t after the perturbation and the equilibrium density. Lower panel: Phase difference between neighbouring wells $\phi_{\ell+1/2}$ as defined in (11.12). The signal amplitude in the relative density and in the relative phase is denoted by Δn and $\Delta\phi$ respectively.

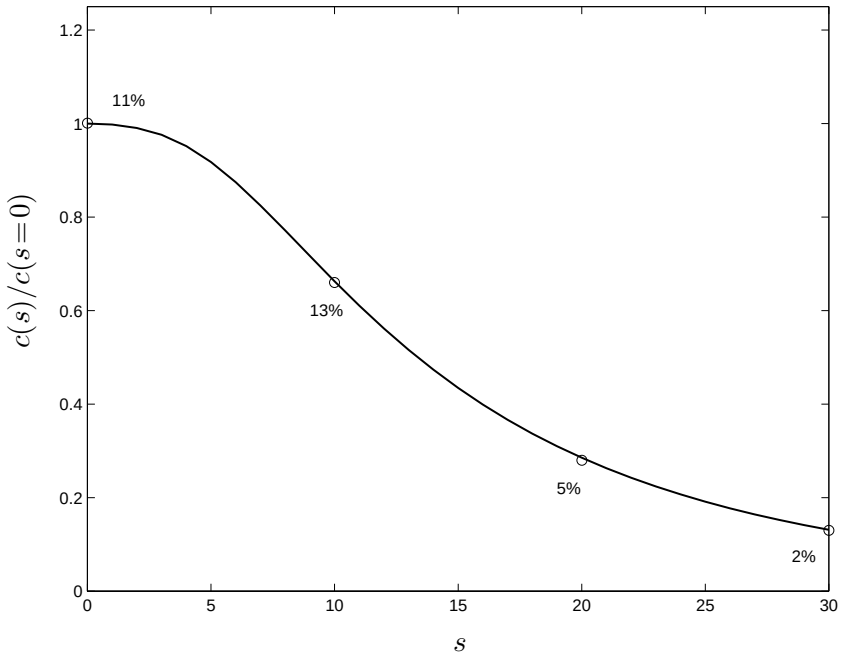

Figure 11.3: Sound velocity as a function of lattice depth s. Bogoliubov prediction (solid line) and results "measured" based on the simulation (circles) with respective signal amplitudes Δn for $gn = 0.5E_R$. The signal amplitude Δn is defined as indicated in Fig. 11.2.

In Fig. 11.4 we plot the relative density at the final stage of our GP-simulation for the lattice depths $s = 0,\, 10,\, 20$ with $gn = 0.5E_R$ for a large perturbation. From these simulations we extract the sound velocity included in Fig.11.3. These results show that the measured signals already involve significant nonlinear effects, even in the uniform case. We will now discuss in more detail what nonlinear effects can occur and how they affect the sound signal. By keeping lattice depth and interaction fixed while increasing the strength of the external perturbation the role of nonlinearities increases and we pass through three regimes:

1. linear regime, where the Bogoliubov description holds and the variations of density and relative phases are small;

2. shock wave regime, where density variations induce mode–coupling among Bogoliubov excitations, giving rise to the formation of shock waves. Depending on the curvature of the Bogoliubov dispersion beyond the phononic regime, shock waves emerge in front of the wavepacket (uniform system, shallow lattice), both in the front and in the back (intermediate lattice depth) or only in the back (deep lattice with $\delta \ll U/3$). In the case in which shock waves form only in the back, the signal maintains a compact shape and propagates at the sound velocity predicted by Bogoliubov theory. In the other two cases, the sound signal deforms and disperses.

3. saturation regime in a deep lattice, where there exists a non–trivial dependence of the current on the relative phase. The sound signal amplitude saturates, leaves behind a

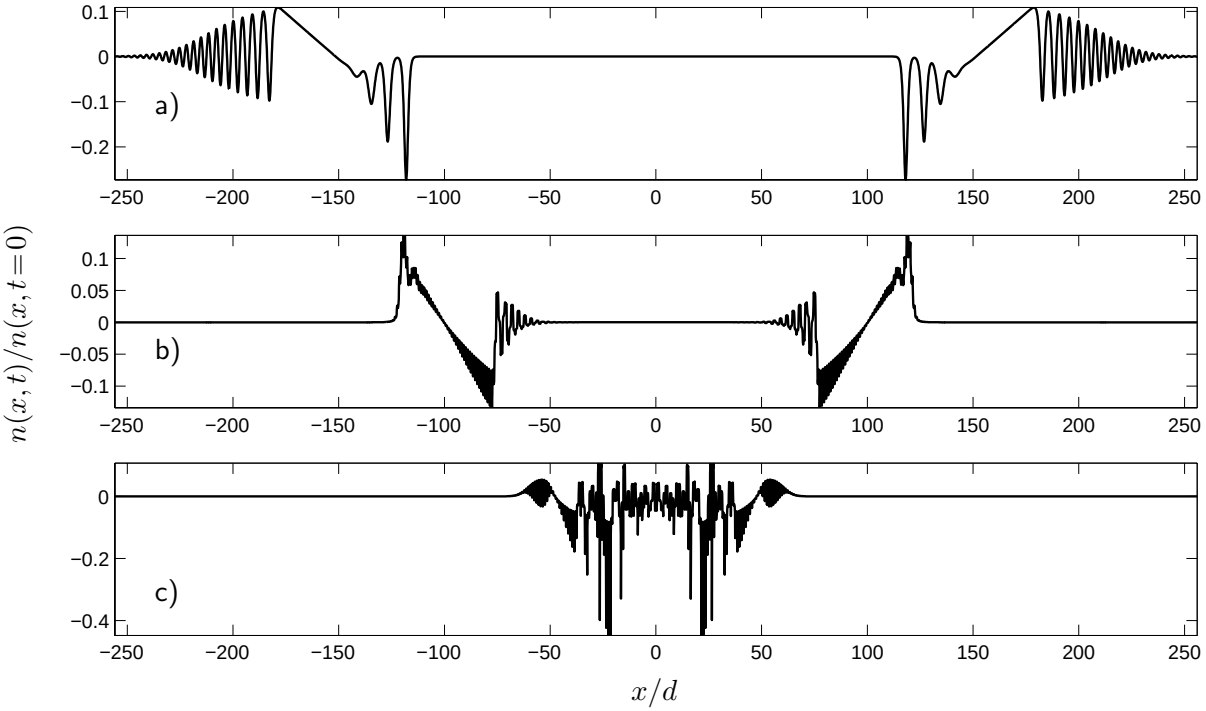

Figure 11.4: Relative density at $t = 480\hbar/E_R$ in the GP-simulation with $gn = 0.5E_R$ at lattice depths a) $s = 0$, b) $s = 10$ and c) $s = 20$ yielding the sound velocities included in Fig.11.3.

wake of noise, but still propagates at the sound velocity predicted by Bogoliubov theory. This regime exists only in the presence of the lattice and requires $\delta \ll U/3$ to ensure that shock waves form in the back of the signal as in regime (2).

The signal amplitudes attainable in each regime and the perturbation parameters b, w, T_P needed to reach a certain regime depend on the lattice depth s and on the interaction strength gn, or equivalently, on δ and U. As a general trend, in the presence of a lattice a stronger perturbation is needed to obtain the same signal amplitude as without lattice. This reflects the fact that the condensate is less compressible in a lattice. As already mentioned, regime (3) exists only in the presence of the lattice and provided that $\delta \ll U/3$, which for fixed gn or U can be ensured by making the lattice sufficiently deep.

1. Linear Regime

In Figs.11.5 and 11.6 we present examples for sound signals produced with a weak external perturbation of the form (11.1) in the uniform case and for a lattice with $s = 10$. The signal amplitudes Δn and $\Delta\phi$ are small and do not change during the propagation. The shape of the signals remains constant and it moves with the sound velocity obtained from Bogoliubov theory. In fact, all points of the signal move with the same speed. For example, the sound velocity can be extracted equally well by measuring the position of the signal maximum, minimum or center of mass as a function of time.

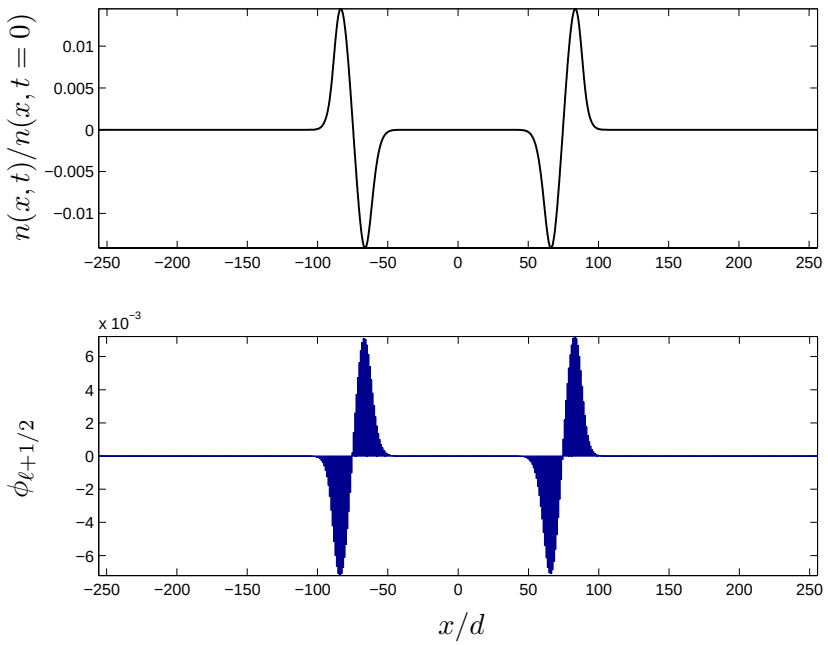

Figure 11.5: Sound propagation in the linear regime without lattice for $gn = 0.5E_R$. Upper panel: Relative density $n(x,t)/n(x,t=0)$ at $t = 480\hbar/E_R$ of the GP-simulation. Lower panel: Relative phase as defined in (11.12) at $t = 480\hbar/E_R$ of the GP-simulation

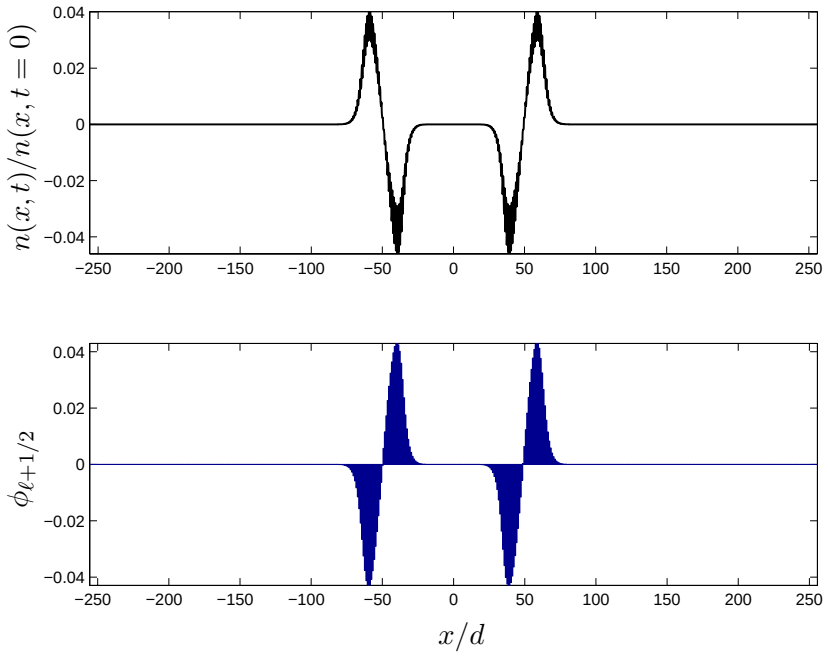

Figure 11.6: Sound propagation in the linear regime with a lattice of depth $s = 10$ for $gn = 0.5E_R$. Upper panel: Relative density $n(x,t)/n(x,t=0)$ at $t = 480\hbar/E_R$ of the GP-simulation. Lower panel: Relative phase as defined in (11.12) at $t = 480\hbar/E_R$ of the GP-simulation

2. Shock Wave Regime

The peculiarity of region (2) is the formation of shock waves. In the uniform case, a wave front emits shock waves in the forward direction (see Fig.11.4). The stronger the external perturbation, the more the sound signal deforms and spreads due to the shock waves. A measurement of the position of the signal maximum or minimum yields a velocity which deviates from the Bogoliubov prediction for the velocity of sound. To obtain the value of the sound velocity included in Fig.11.3 we have done a convolution of the signal over a few lattice sites, mimicking the limited resolution of a detection system. In this way the signal is less distorted by the shock waves. We then determine the center-of-mass position of the signal as a function of time. This method allows to extract the exact sound velocity thanks to our specific excitation method. On the contrary, a similar measurement done with a bright (dark) sound signal would lead to a higher (lower) value for the sound velocity. The formation of shock waves in front of a bright sound wave packet (positive density variation) in a uniform system is predicted analytically and numerically [149]. An analytic solution describing shock waves in a uniform system has been found by [150]. Their formation has also been discussed in [151].

In a shallow lattice, shock waves form in the front as in the uniform case. This is because the formation of a gap in the Bogoliubov spectrum does affect only a small range of quasi-momenta close to q_B. Hence, the mode–coupling among Bogoliubov excitations leads to the creation of excitations outside the phononic regime which travel at a speed larger than the sound velocity.

In a deep lattice, in contrast, shock waves are formed behind the sound packet. (see Fig. 11.7). In fact the lowest band tight binding Bogoliubov dispersion law, given by (see chapter 7.3)

$$\hbar\omega_q \approx \sqrt{2\delta \sin^2\left(\frac{\pi q}{2q_B}\right)\left[2\delta \sin^2\left(\frac{\pi q}{2q_B}\right)+2U\right]}, \tag{11.13}$$

has a negative curvature for all q as long as $\delta/U < 1/3$. If the ratio δ/U is larger than $1/3$ the Bogoliubov dispersion has a positive curvature in a small range of quasimomenta and becomes negative closer to the zone boundary. Only in deep lattices (where $\delta/U \ll 1/3$), wavepackets composed by quasi-momenta out of the phononic regime will propagate slower than the sound packets. In this case shock wave formation takes place both in the front and in the back of the sound wavepacket. Note that for typical values of the density δ/U lies between zero and one. In a deep lattice where shock waves are formed behind the sound packet, we observe that the relative phase distribution can approach $\phi_{\ell+1/2} \sim \pi/2$, as shown in Fig. 11.8 which refers to an early stage of the evolution shown in Fig. 11.7. Then, it becomes strongly deformed indicating that higher orders of the sine–function in (11.10) are important. However this behaviour does not become critical up to the point where the relative phase of two neighboring lattice sites $\phi_{\ell+1/2} = \pi$, which defines the onset of regime (3).

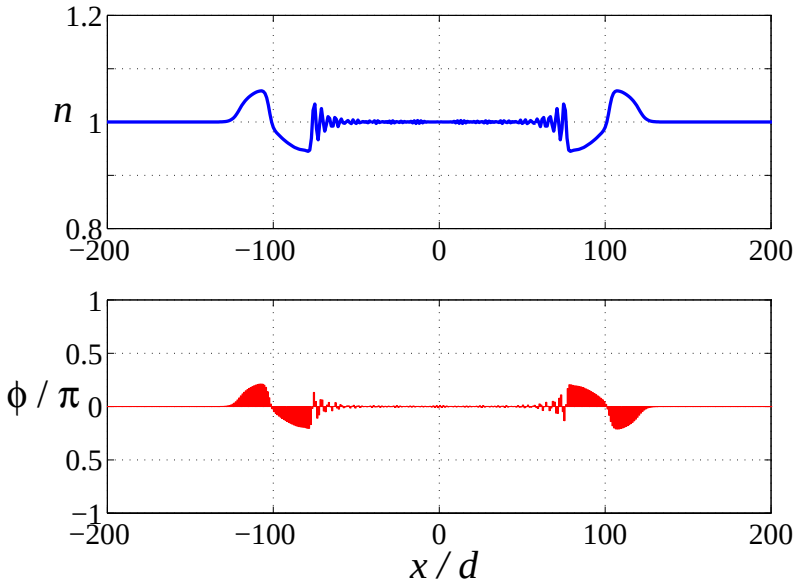

Figure 11.7: Sound signals with shock waves in the back for a deep lattice with $\delta/U \ll 1/3$. Upper panel: Relative density $n_\ell(t)/n_\ell(t=0)$ obtained from the DNLS-simulation. Lower panel: Relative phase (11.11) obtained from the DNLS-simulation

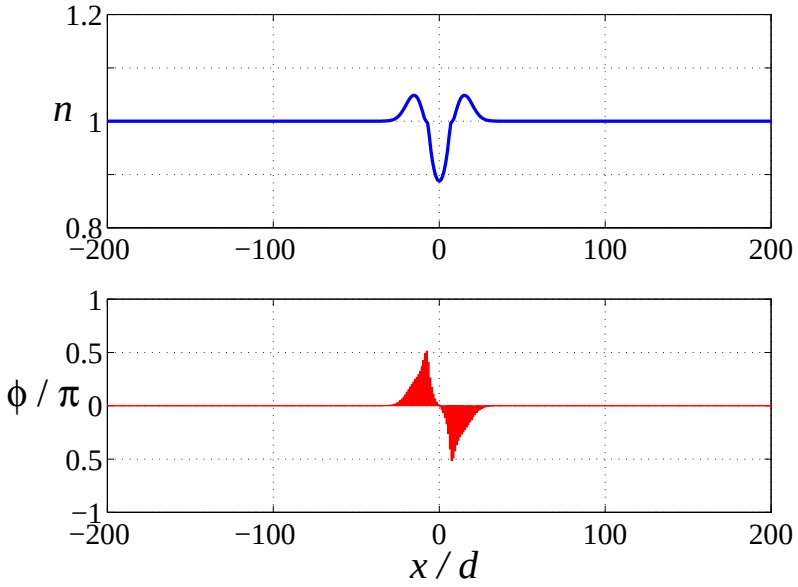

Figure 11.8: At an early stage of the simulation depicted also in Fig. 11.7 the relative phase touches $\pi/2$.

3. Saturation Regime in deep lattices

Provided that the lattice is deep enough to satisfy $\delta \ll U/3$, shock waves form only in the back of the signal, as discussed above. If under this condition we further increase the strength of the external perturbation, the relative phase $\phi_{\ell+1/2}$ at some site reaches π (see Fig.11.9, upper two panels) and there the current starts flowing in the opposite direction (see Eq.(11.10)). As a consequence, a wake of noise is left behind the sound packets and saturation in the amplitude of the propagating signal is found (see Fig.11.9, lower two panels). The interesting feature is that the noise has average zero velocity, since the oscillations of population between different wells are completely dephased. Hence it never overtakes the sound signal, which is always able to "escape" from the noise. The system is in an interesting state, where the outer part is phase coherent, while the part between the two sound signals has lost coherence. We stress that in the uniform case, in presence of strong nonlinearities, we can observe a strong deformation of the signal, but in the central region the system is always able to recover the ground state after the sound wave has passed by (see Fig.11.4 a)).

To demonstrate the saturation of the signal, we let the system evolve for a long time after the external perturbation and look at the amplitudes Δn and $\Delta\phi$ which are defined as indicated in Fig. 11.2. We find an interesting scaling behavior that helps to distinguish the three regimes mentioned above in the case of deep lattices and renders evident the saturation of the signal amplitude. Both in the GPE simulations (for relatively deep lattices) and in the DNLS simulations, we find a very interesting scaling law of the results, shown in Fig.11.10: The effect of the barrier is universal when:

- the barrier parameters are combined in the form $T_P b/w$ which reflects the capability of the system to react to an external perturbation;
- the relative density variation is rescaled as $\Delta n\sqrt{U/\delta}$, while the amplitude of the relative phase signal $\Delta\phi$ need not be rescaled.

The phenomenology of the system as summarized in Fig.11.10 shows that for small barrier parameter $T_p b/w$, the perturbation produced in the system is small, and depends linearly on $T_p b/w$. Increasing the barrier parameter $T_p b/w$, the signal amplitude Δn saturates quite suddenly. The three regions indicated in Fig.11.10 correspond to the three regimes (1-3) listed above.

Based on the DNLS equation (11.10) one can give a quantitative estimate of the saturation value for Δn. Assuming small density and relative phase variations, the first of Eqs.(11.10) becomes

$$\dot{n}_\ell \approx \frac{n\delta}{\hbar}\left[\sin(\phi_{\ell+1/2}) - \sin(\phi_{\ell-1/2})\right] \approx \frac{n\delta}{\hbar} d\frac{\partial\phi}{\partial\ell}. \tag{11.14}$$

Now, we make the ansatz $n = 1 + \Delta n[f_+(\ell d - ct) + f_-(\ell d + ct)]$ and $\phi = -\Delta\phi[f_+(\ell d - ct) + f_-(\ell d + ct)]$ for the density and relative phase variation, where f_+ and f_- describe respectively the packets moving to the left and to the right. Using that $c = (d/\hbar)\sqrt{\delta U}$,we get

$$\boxed{\Delta n = \sqrt{\frac{\delta}{U}}\Delta\phi.} \tag{11.15}$$

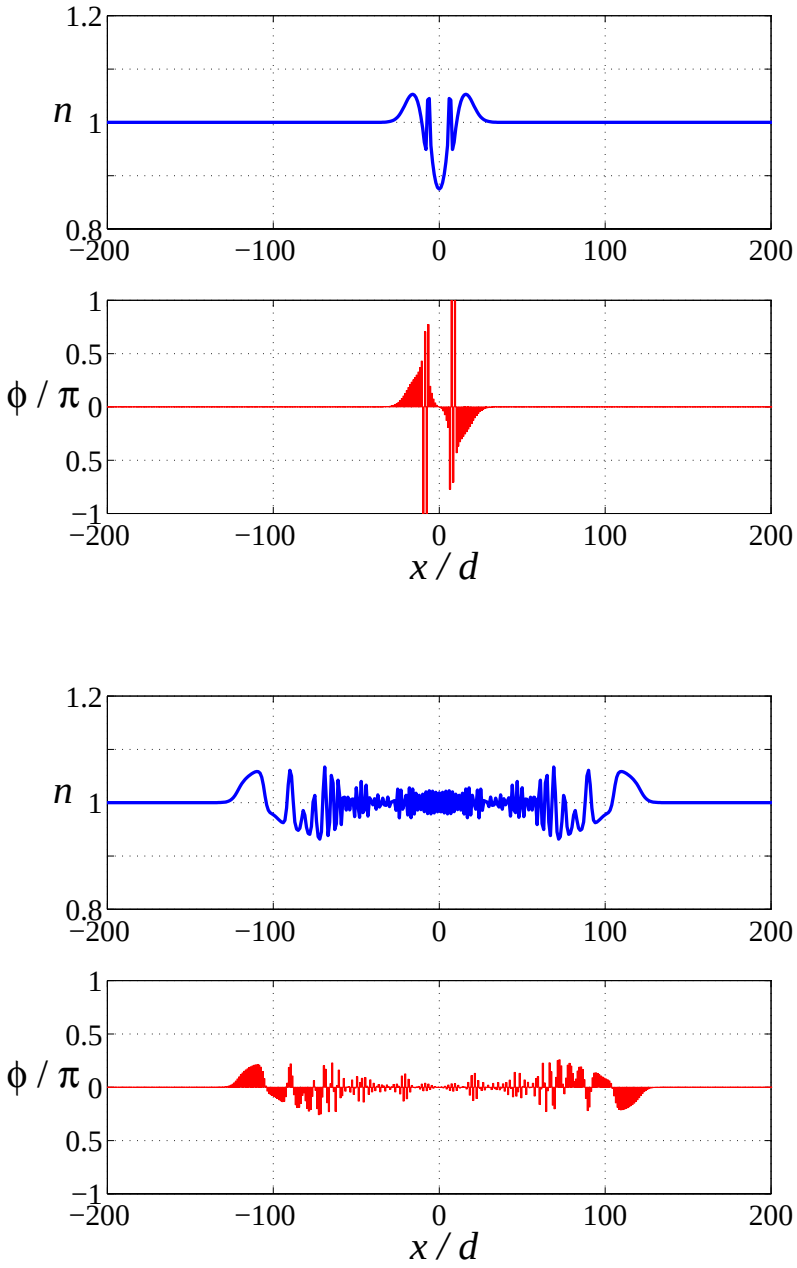

Figure 11.9: Sound signals in the saturation regime at an early ($t = 16\hbar/E_R$; upper two panels) and a late stage ($t = 200\hbar/E_R$; lower two panels) for a deep lattice with $\delta/U \ll 1/3$. First and third panel from top: Relative density $n_\ell(t)/n_\ell(t=0)$ obtained from the DNLS-simulation. Second and forth panel from top: Relative phase (11.11) obtained from the DNLS-simulation.

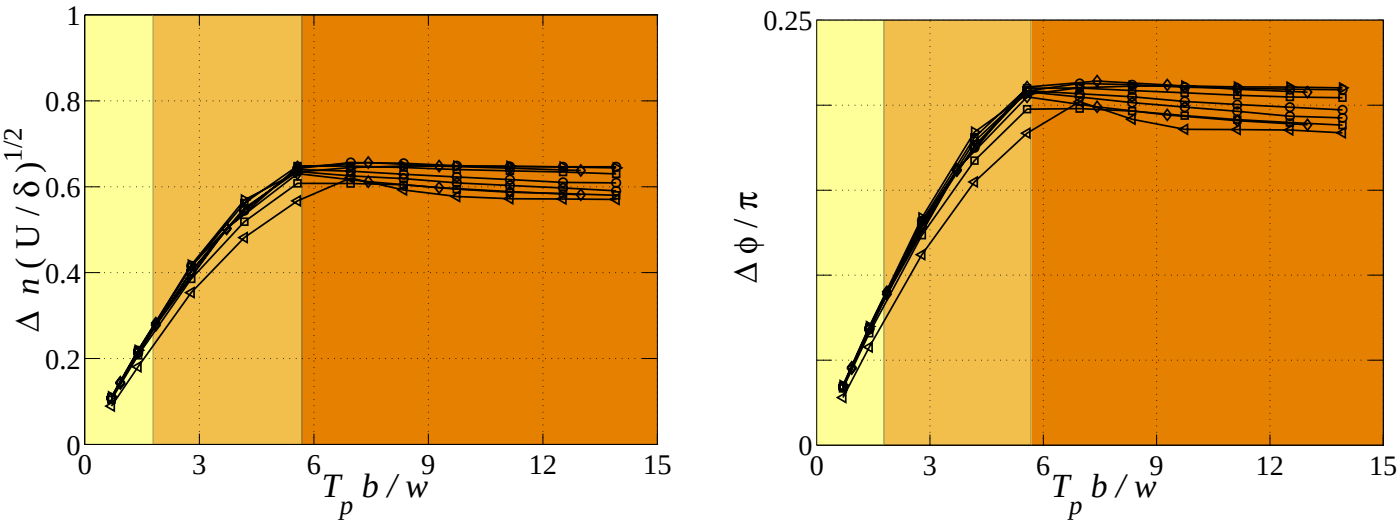

Figure 11.10: Results for the density and relative signal amplitudes Δn and $\Delta\phi$ obtained from DNLS simulations for varying barrier parameters T_P, b, w (see Eq.(11.1)), tunnel coupling δ and on-site interaction U (see Eq.(11.8)) with $\delta \ll U/3$.

This is in agreement with the behavior we find for Δn in the first (linear) and even in the second (shockwave) regime as summarized in Fig. 11.10. The first order approximation to $\sin(\phi_{\ell\pm1/2})$ in $\phi_{\ell\pm1/2}$ is valid for $\Delta\phi < 0.2\pi$, which implies $\Delta n_{\max} = 0.2\pi\sqrt{\delta/U}$. This is in agreement with our observation that nonlinear effects play a minor role for signal amplitudes $\Delta n \ll 0.2\pi\sqrt{\delta/U}$ (region (1) in Fig.11.10). In region (3) of Fig. 11.10 we find that a very good estimate for the saturated signal amplitude is given by $\Delta n_{\max} = 0.2\pi\sqrt{\delta/U}$

Saturation does not occur in the uniform system or at low lattice depth. To demonstrate this we plot in Fig. 11.11 the signal amplitude Δn measured after different propagation times for $s = 0$ (dashed lines) and $s = 15$ (solid lines) as a function of barrier height b for fixed barrier width w and perturbation time T_p. For $s = 15$ the signal amplitude takes exactly the same values at $t = 100,\, 200,\, 300,\, 400\hbar/E_R$ (The corresponding four lines in Fig. 11.11 perfectly overlap!). The saturated value is reached around $b = 200$ in this setting. In contrast, the signal amplitudes in the uniform system at different times ($t = 100,\, 200\hbar/E_R$) differ from each other: At earlier times the signal amplitude increases as a function of the strength of the external perturbation and does not saturate. The amplitude measured at later times coincides with the one measured at earlier times only for small barrier heights b for which the propagation dynamics is linear. When nonlinear effects are presented, Δn becomes lower during the evolution as a consequence of the dispersion of the signal.

It is interesting to note that in the linear regime, the signal amplitudes Δn and $\Delta\phi$ in the uniform case obey the relation (11.15) with $\delta = 2E_R/\pi^2$ and $U = gn$. In Fig. 11.12 we accordingly rescale the data of Fig. 11.11 and find that all curves coincide in the linear regime.

The applicability of the relation (11.15) also in the uniform case or in a shallow lattice is due to the fact that in the linear limit the lattice induced effects on the macroscopic dynamics can be accounted for by the replacement $m \to m^*$ and $gn \to \kappa^{-1}$ (see chapter 9.4, in particular Eqs.(9.28,9.29) with $k = 0$). Apart from this modification, the linearized dynamical equations take the same form at all lattice depths.

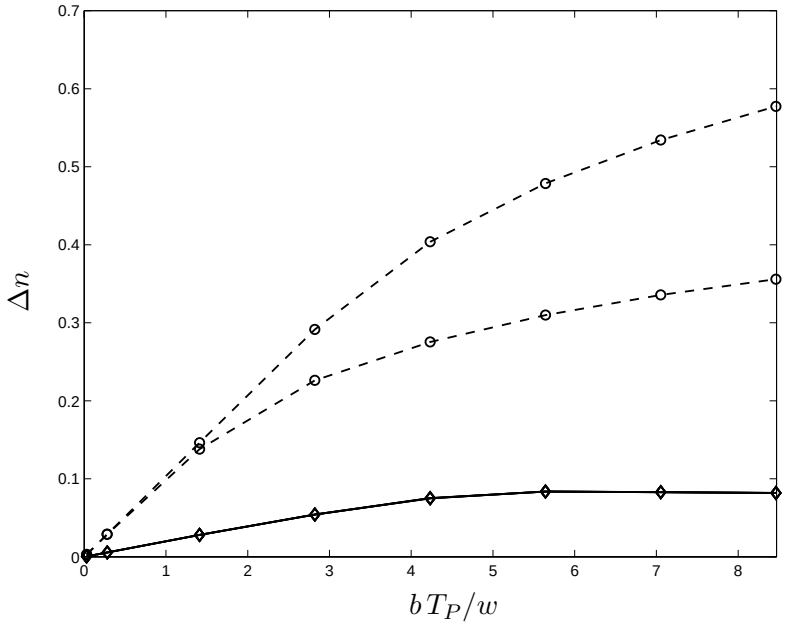

Figure 11.11: The signal amplitude Δn as a function of the barrier parameter bT_P/w at $gn = 0.5E_R$. Dashed lines: $s = 0$ measured at $t = 100\hbar/E_R$ (upper dashed line) and $t = 200\hbar/E_R$ (lower dashed line). Solid lines: $s = 15$ measured at $t = 100,\ 200,\ 300,\ 400\hbar/E_R$ for $s = 15$. The corresponding four lines exactly overlap.

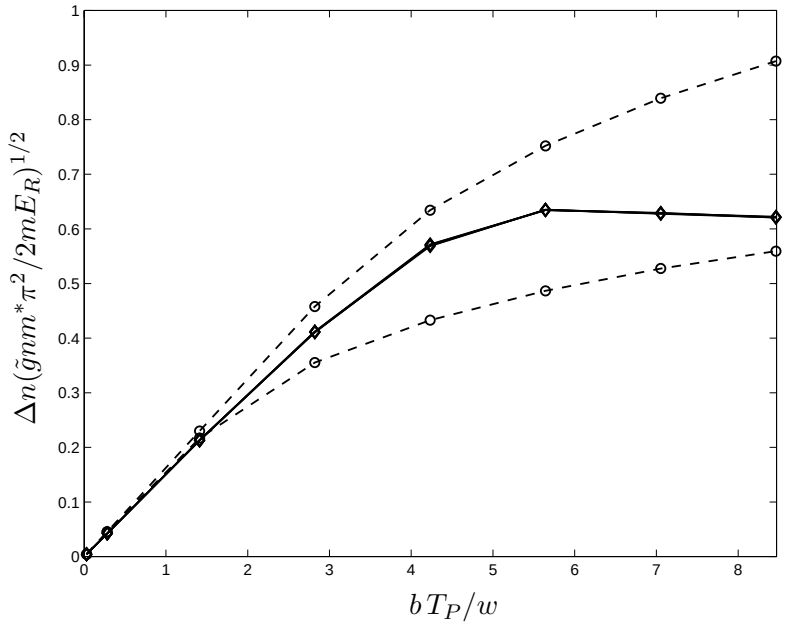

Figure 11.12: Same data as in Fig. 11.11. The amplitudes are rescaled to demonstrate the universal behavior in the linear regime.

11.4 Experimental observability

In order to discuss the experimental observability of the discovered effects, a few things need to be considered: first of all, an experimental set-up involves a trapping potential in the longitudinal and radial directions. In our model, we have neglected completely the radial degrees of freedom, which might play an important role in sound propagation. First of all, even in the uniform case, a radial TF-density distribution can change the sound velocity to $c = \sqrt{gn/2m}$ [152, 153, 154, 139]. Such effects can be simply taken into account by correctly changing the density dependence of the interaction term in our equations [116]. The second important thing to consider is the external harmonic potential along the direction of sound propagation. One should require that the time needed by the sound packet to travel along an observable distance $L >> d$ is shorter than the oscillation period in the trap. For example for ^{87}Rb atoms, for $s = 10 \div 20$, $gn = 0.5E_R$ and $L = 50d$, trapping frequencies smaller than $2\pi \times 25 \div 80$ Hz are required. Last but not least, one should of course require that the signal is measurable. In order to mimic the experimental resolution of the detection system, one has to perform a convolution over a few lattice sites of the GPE solution. This gives a maximum observable amplitude for the density variation which is in good agreement with our DNLS prediction $\Delta n_{\max} = 0.2\pi\sqrt{\delta/U}$. For $gn = 0.5E_R$, the density variations which can be observed for a few different values of the optical potential depth are: for $s = 10$, $\Delta n_{\max} = 0.13$; $s = 15$, $\Delta n_{\max} = 0.08$; $s = 20$, $\Delta n_{\max} = 0.05$. Finally, one should also keep in mind, that the saturation effect is clearly evident only if the shock waves move with a velocity much lower than the sound velocity, which requires $\delta/U \ll 1/3$. Obtaining a clear saturation effect (small δ/U) associated with a large signal amplitude Δn (large δ/U) at fixed lattice depth requires a compromise in the choice of lattice depth s and interaction strength gn.

Chapter 12

Condensate fraction

The presence of the optical potential may introduce phase fluctuations which reduce the degree of coherence of the sample. This effect yields spectacular consequences such as number squeezing [89] and the occurence of a quantum phase transition from the superfluid to the Mott insulator phase [155, 90, 91]. In the presence of a one-dimensional optical lattice with large N at relatively low lattice depth one can predict interesting effects on the condensate fraction. The determination of the quantum depletion also serves as a check for the validity of GP-theory.

In a shallow lattice, the quantum depletion of the condensate is slightly enhanced (see section 12.3). It still has the form of the standard Bogoliubov result for the uniform system (see review in section 12.2), with g replaced by the effective coupling constant $\tilde{g} > g$ and the mass by the effective mass m^*.

In the tight binding regime, the situation is very different (see section 12.4): The deeper the lattice the more the system acquires the character of an array of condensates. In the thermodynamic limit coherence is maintained across the whole system and the quantum depletion is only little enhanced with respect to the shallow lattice. However, its dependence on the scattering length changes with respect to the case of a shallow lattice: Reflecting the two-dimensional character of each condensate of the array, the expression for the quantum depletion takes the same form as for a disc-shaped condensate whose motion is frozen in the tightly confined axial direction. In this configuration, the increase of the quantum depletion with respect to the shallow lattice is due to its larger value in each disc and fails to capture the loss of coherence between the discs. The loss of overall coherence has to be demonstrated in a different way: Considering a large, but finite system we single out the contribution to the depletion without transverse excitations corresponding to the depletion in a one-dimensional system. This contribution grows logarithmically with the number of lattice sites. Moreover, it becomes larger with increasing effective mass and with decreasing number of particles per site. As the lattice is made deeper this 1D contribution becomes dominant and indicates the transition to a regime where the condensate fraction is small and the long range order behavior is modified.

The results included in this chapter were published in [102].

12.1 Quantum depletion within Bogoliubov theory

Let us consider the problem in a 3D box of size L in x, y-direction and an optical lattice with N_w sites oriented along z Note that the quantum depletion of the condensate has been calculated in [123, 124] for different geometries. The quantum numbers of the elementary excitations are the band index j and the quasi-momentum q along the z direction and the momenta p_x and p_y in the transverse directions.

Within the framework of Bogoliubov theory, the quantum depletion of the condensate is given by

$$\frac{\Delta N_{\rm tot}}{N_{\rm tot}} = \frac{1}{N_{\rm tot}} \sum_j \sum_{q,p_x,p_y,|p|\neq 0} \int dz \int dx \int dy \, |v_{j,q,p_x,p_y}(\mathbf{r})|^2, \tag{12.1}$$

where $N_{\rm tot}$ denotes the total number of atoms, $\Delta N_{\rm tot}$ is the number of non-condensed particles, $|p| = \sqrt{p_x^2 + p_y^2 + \hbar^2 q^2}$ and $v_{j,q,p_x,p_y}(\mathbf{r})$ are the Bogliubov v-amplitudes of the elementary excitations. The sum runs over all bands j, over the quasi-momenta q in the first Brillouin zone and the momenta of elementary excitations in the transverse directions p_x, p_y allowed by the periodic boundary conditions

$$q = \frac{2\pi}{N_w d}\nu\,, \qquad \nu = 0, \pm 1, \pm 2, \ldots, \pm\frac{N_w}{2}\,, \tag{12.2}$$

$$p_x, p_y = \hbar\frac{2\pi}{L}\nu\,, \qquad \nu = 0, \pm 1, \pm 2, \ldots\,. \tag{12.3}$$

The Bogoliubov amplitudes $v_{j,q,p_x,p_y}(\mathbf{r})$ in Eq. (12.1) solve the Bogoliubov equations

$$\left(-\frac{\hbar^2}{2m}\nabla^2 + sE_R \sin^2\left(\frac{\pi z}{d}\right) + 2d\,gn\,|\tilde{\varphi}(z)|^2 - \mu\right) u_{jqp_xp_y}(\mathbf{r}) + gnd\tilde{\varphi}^2 v_{jqp_xp_y}(\mathbf{r}) \;=\; \hbar\omega_j(q) u_{jqp_xp_y} \tag{12.4}$$

$$\left(-\frac{\hbar^2}{2m}\nabla^2 + sE_R \sin^2\left(\frac{\pi z}{d}\right) + 2d\,gn\,|\tilde{\varphi}(z)|^2 - \mu\right) v_{jqp_xp_y}(\mathbf{r}) + gnd\tilde{\varphi}^{*2} u_{jqp_xp_y}(\mathbf{r}) \;=\; -\hbar\omega_j(q) v_{jqp_xp_y}\,. \tag{12.5}$$

They can be obtained from the three-dimensional time-dependent GPE

$$i\hbar\frac{\partial\Psi(\mathbf{r},t)}{\partial t} = \left(-\frac{\hbar^2}{2m}\nabla^2 + sE_R\sin^2\left(\frac{\pi z}{d}\right) + g\,|\Psi(\mathbf{r},t)|^2\right)\Psi(\mathbf{r},t)\,, \tag{12.6}$$

where the order parameter Ψ fulfills the normalization condition

$$\int d\mathbf{r}\,|\Psi(\mathbf{r},t)|^2 = N_{\rm tot}\,, \tag{12.7}$$

by considering small time-dependent perturbations $\delta\Psi(\mathbf{r},t)$ of the groundstate $\Psi_0(\mathbf{r})$

$$\Psi(\mathbf{r},t) = e^{-i\mu t/\hbar}\left[\Psi_0(\mathbf{r}) + \delta\Psi(\mathbf{r},t)\right]\,, \tag{12.8}$$

where

$$\delta\Psi(\mathbf{r},t) = u_\sigma(\mathbf{r})e^{-i\omega_\sigma t} + v_\sigma^*(\mathbf{r})e^{i\omega_\sigma t} \tag{12.9}$$

as exemplified in section 7 for the case $p_x = p_y = 0$.

The Bogoliubov amplitudes must comply with the normalization condition

$$\int dz \int dx \int dy \left[|u_{q,p_x,p_y}(\mathbf{r})|^2 - |v_{q,p_x,p_y}(\mathbf{r})|^2 \right] = 1 \,. \tag{12.10}$$

Eq. (12.1) adquately describes the quantum depletion provided

$$\frac{\Delta N_{\rm tot}}{N_{\rm tot}} \ll 1 \,. \tag{12.11}$$

Otherwise it is necessary to go beyond Bogoliubov theory.

12.2 Uniform case

At lattice depth $s = 0$, Eq. (12.1) yields the quantum depletion of the weakly interacting uniform Bose gas. In this case the sum $\sum_{j,q}$ with q belonging to the first Brillouin zone can be replaced by $\sum_q$ with

$$q = \frac{2\pi}{L}\nu \,, \qquad \nu = 0, \pm 1, \pm 2, \ldots \,. \tag{12.12}$$

The correctly normalized Bogoliubov amplitudes are given by

$$u_{q,p_x,p_y}(\mathbf{r}) \;=\; U_{q,p_x,p_y} \frac{e^{i(p_x x + p_y y)/\hbar}}{L^{3/2}} e^{iqz} \,, \tag{12.13}$$

$$v_{q,p_x,p_y}(\mathbf{r}) \;=\; V_{q,p_x,p_y} \frac{e^{i(p_x x + p_y y)/\hbar}}{L^{3/2}} e^{iqz} \,, \tag{12.14}$$

with

$$U_{q,p_x,p_y} \;=\; \frac{\frac{p^2}{2m} + \hbar\omega_{\rm uni}}{2\sqrt{\frac{p^2\hbar\omega_{\rm uni}}{2m}}} \,, \tag{12.15}$$

$$V_{q,p_x,p_y} \;=\; \frac{\frac{p^2}{2m} - \hbar\omega_{\rm uni}}{2\sqrt{\frac{p^2\hbar\omega_{\rm uni}}{2m}}} \,, \tag{12.16}$$

where $p^2 = p_x^2 + p_y^2 + \hbar^2 q^2$ and ω is the dispersion relation of the elementary excitations

$$\hbar\omega_{\rm uni} = \sqrt{\frac{p^2}{2m}\left(\frac{p^2}{2m} + 2gn\right)} \,. \tag{12.17}$$

We insert (12.13,12.14) into Eq.(12.1). To obtain the result in the thermodynamic limit $N_{\rm tot},\, L \to \infty,\, n = const.$ we make use of the continuum approximation

$$\sum_{p_x,p_y,q} \to \frac{L^3}{(2\pi)^3}\frac{1}{\hbar^2} \int dp_x \int dp_y \int dq \,. \tag{12.18}$$

This leads to

$$\begin{aligned} \frac{\Delta N_{\rm tot}}{N_{\rm tot}} \;&=\; \frac{1}{N_{\rm tot}} \frac{L^3}{(2\pi)^3}\frac{1}{\hbar^2} \int dp_x \int dp_y \int dq |V_{q,p_x,p_y}|^2 \\ &=\; \frac{1}{N_{\rm tot}} \frac{L^3}{(2\pi)^3}\frac{1}{\hbar^2} \int_0^\infty 4\pi p^2 dp \frac{1}{2} \left[\frac{\frac{p^2}{4g_2 n_2 m} + 1/2}{\sqrt{\frac{p^2}{4g_2 n_2 m}(\frac{p^2}{4g_2 n_2 m} + 1)}} - 1 \right] . \end{aligned} \tag{12.19}$$

This expression can be evaluated analytically. One obtains the well known result

$$\frac{\Delta N_{\rm tot}}{N_{\rm tot}} = \frac{8}{3}\frac{1}{\pi^{1/2}}(a^3 n)^{1/2}\,. \tag{12.20}$$

In view of the discussion of the case $s \neq 0$ below, it is important to point out that the integrand in (12.19) contributes most at $p \sim mc$ where the dispersion (12.17) passes from the phononic regime $\hbar\omega \sim p$ to the single particle regime $\hbar\omega \sim p^2$. Yet the convergence is very slow and the integral is saturated by momenta much larger than mc [156], where elementary excitations have single particle character.

Quantum depletion of the 2D uniform gas

Let us consider a uniform system of axial size d and transverse size L and let us assume that the motion is frozen in the z-direction. We set $\Psi(\mathbf{r}) = \frac{1}{\sqrt{d}}\Psi_2(x,y)$. Under these conditions the stationary GPE takes the form

$$\left(-\frac{\hbar^2}{2m}\nabla_\perp^2 + \frac{g}{d}|\Psi_2|^2\right)\Psi_2 = \mu\Psi_2\,. \tag{12.21}$$

The 2D density is given by

$$n_2 = |\Psi_2|^2 = N_{\rm tot}/L^2\,. \tag{12.22}$$

The 2D coupling constant emerges as

$$g_2 = \frac{g}{d} = 4\pi\frac{\hbar^2}{m}\frac{a}{d}\,. \tag{12.23}$$

The groundstate solution is given by

$$\mu = g_2 n_2\,. \tag{12.24}$$

The calculation of the Bogoliubov spectrum is analogous to the 3D case. The result for the depletion changes only because of the change in the dimensionality of the integral over momenta. We rewrite the derivation here for clarity. The Bogoliubov equations for the system in the groundstate read

$$\left(\frac{p^2}{2m} + 2g_2|\Psi_2|^2 - \mu\right)u_p + g_2|\Psi_2|^2 v_p\,, \;=\; \hbar\omega(p)u_p \tag{12.25}$$

$$\left(\frac{p^2}{2m} + 2g_2|\Psi_2|^2 - \mu\right)v_p + g_2|\Psi_2|^2 u_p \;=\; -\hbar\omega(p)v_p\,, \tag{12.26}$$

where $p^2 = p_x^2 + p_y^2$ and we have assumed that the Bogoliubov amplitudes take the form

$$u_p(x,y) = U_p\frac{1}{\sqrt{d}}\frac{1}{L}e^{i(p_x x + p_y y)/\hbar}\,, \tag{12.27}$$

$$v_p(x,y) = V_p\frac{1}{\sqrt{d}}\frac{1}{L}e^{i(p_x x + p_y y)/\hbar}\,. \tag{12.28}$$

The solution for the excitation spectrum is found to be

$$\hbar\omega(p) = \sqrt{\frac{p^2}{2m}\left(\frac{p^2}{2m} + 2g_2 n_2\right)}\,, \tag{12.29}$$

and the square of the V_p-amplitude is given by

$$V_p^2 = \frac{1}{2}\left[\frac{\frac{p^2}{4g_2n_2m} + 1/2}{\sqrt{\frac{p^2}{4g_2n_2m}(\frac{p^2}{4g_2n_2m} + 1)}} - 1\right]\,, \tag{12.30}$$

where we have used the fact that the amplitudes should be normalized to $\int d\mathbf{r}\,(|u_p|^2 - |v_p|^2) = 1$.

We then find that in the thermodynamic limit the depletion of this 2D uniform gas is given by

$$\begin{aligned}\frac{\Delta N_{\rm tot}}{N_{\rm tot}} &= \frac{1}{N_{\rm tot}}\frac{L^2}{(2\pi\hbar)^2}\int_0^\infty 2\pi p dp \frac{1}{2}\left[\frac{\frac{p^2}{4g_2n_2m} + 1/2}{\sqrt{\frac{p^2}{4g_2n_2m}(\frac{p^2}{4g_2n_2m} + 1)}} - 1\right] \\ &= \frac{1}{4\pi}\frac{m}{\hbar^2}g_2 \\ &= \frac{a}{d}\,,\end{aligned} \tag{12.31}$$

where we have used (12.22) and (12.23). Note that the integral differs from (12.19) only due to the replacement of $4\pi p^2 dp$ by $2\pi p dp$.

If the axial profile of the order parameter is given by a gaussian of width σ which is normalized to one in the z-direction, the 2D coupling constant is given by

$$g_2 = \frac{g}{\sqrt{2\pi}\sigma}\,. \tag{12.32}$$

In this case, the result for the depletion reads

$$\frac{\Delta N_{\rm tot}}{N_{\rm tot}} = \frac{a}{\sqrt{2\pi}\sigma}\,, \tag{12.33}$$

Quantum depletion of the 1D uniform gas

In a one-dimensional uniform system the one-body density exhibits a power law decay at large distances. This rules out Bose-Einstein condensation in an infinite, but not in large but finite system. Considering the latter case and supposing that Bogoliubov theory is applicable we calculate the quantum depletion in analogy with the calculations above. This requires evaluating the expression

$$\frac{\Delta N_{\rm tot}}{N_{\rm tot}} = \frac{1}{N_{\rm tot}}\sum_q V_q^2\,, \tag{12.34}$$

with

$$V_q^2 = \frac{1}{2}\left[\frac{\frac{\hbar^2q^2}{2m} + g_{1d}n_{1d}}{\sqrt{\frac{\hbar^2q^2}{2m}\left(\frac{\hbar^2q^2}{2m} + 2g_{1d}n_{1d}\right)}} - 1\right]\,, \tag{12.35}$$

where

$$g_{1d} = \frac{g}{L^2}\,, \tag{12.36}$$

$$n_{1d} = nL^2\,, \tag{12.37}$$

are the effective 1D coupling constant and 1D density in a system with radial extension L and 3D density n whose motion is frozen in the radial direction. Supposing that the system is very long, we make use of the continuum approximation in the z-direction. This yields

$$\frac{\Delta N_{\rm tot}}{N_{\rm tot}} = \frac{1}{N_{\rm tot}}\frac{L}{2\pi}2\int_{q_{\rm min}=2\pi/L}^{\infty} dq\frac{1}{2}\left[\frac{\frac{\hbar^2q^2}{2m}+g_{1d}n_{1d}}{\sqrt{\frac{\hbar^2q^2}{2m}\left(\frac{\hbar^2q^2}{2m}+2g_{1d}n_{1d}\right)}}-1\right]. \tag{12.38}$$

We rewrite this expression in the form

$$\frac{\Delta N_{\rm tot}}{N_{\rm tot}} = \frac{1}{N_{\rm tot}}\frac{L}{2\pi}\frac{1}{\xi}2\int_{2\pi\xi/L}^{\infty} dq\frac{1}{2}\left[\frac{\xi^2q^2+1}{\sqrt{\xi^2q^2\left(\xi^2q^2+2\right)}}-1\right], \tag{12.39}$$

with the healing length $\xi = \sqrt{2mg_{1d}n_{1d}}$. The integral can be solved analytically yielding

$$\frac{\Delta N_{\rm tot}}{N_{\rm tot}} = \frac{1}{N_{\rm tot}}\frac{L}{2\pi}\frac{1}{\xi}\left[-\sqrt{4\pi^2\frac{\xi^2}{L^2}+2}+2\pi\frac{\xi}{L}+\frac{1}{\sqrt{2}}\mathrm{arctanh}\sqrt{\frac{1}{1+4\pi^2\frac{\xi^2}{2L^2}}}\right]. \tag{12.40}$$

Using $\xi \ll L$ this expression can be recast in the form

$$\begin{aligned}\frac{\Delta N_{\rm tot}}{N_{\rm tot}} &= \frac{1}{N_{\rm tot}}\frac{L}{2\pi}\frac{1}{\xi}\frac{1}{\sqrt{2}}\mathrm{arctanh}\left(1-4\pi^2\frac{\xi^2}{4L^2}\right)\\ &= \frac{1}{N_{\rm tot}}\frac{L}{2\pi}\frac{1}{\xi}\frac{1}{\sqrt{2}}\ln\left(\frac{\sqrt{2}L}{\pi\xi}\right)\end{aligned} \tag{12.41}$$

Using the formula $c = \sqrt{g_{1d}n_{1d}/m}$ for the sound velocity and defining

$$\nu = \frac{mc}{2\pi\hbar n_{1d}}\,. \tag{12.42}$$

we rewrite this result in the form

$$\frac{\Delta N_{\rm tot}}{N_{\rm tot}} = \nu\ln\left(\frac{\sqrt{2}L}{\pi\xi}\right) \tag{12.43}$$

This result is valid provided that the depletion is small which can be ensured by making ν sufficiently small. In this respect, it is interesting to note that the quantity ν becomes smaller when the 1D density $n_{1d} = N_{\rm tot}/L$ is made larger. The depletion diverges for $L \to \infty$. This follows from the power law decay behavior of the 1-body density: The condensate depletion measures to what extent the 1-body density drops on a distance of the system length.

12.3 Shallow lattice

In chapter 5 and 9 we have seen that a condensate loaded in a lattice can be effectively described as a uniform system of atoms whose motion in the z-direction occurs with effective mass m^* and whose interaction, at sufficiently low average density, is described by an effective coupling constant $\tilde{g}$. We can then pose the question under what condition this holds also for the calculation of the quantum depletion. According to the above discussion of the uniform case, the dispersion of the relevant elementary excitations must be well approximated by

$$\hbar\omega(p_x,p_y,q)=\sqrt{\left(\frac{p_x^2}{2m}+\frac{p_y^2}{2m}+\frac{\hbar^2q^2}{2m^*}\right)\left(\left(\frac{p_x^2}{2m}+\frac{p_y^2}{2m}+\frac{\hbar q^2}{2m^*}\right)+2\tilde{g}n\right)}\,. \tag{12.44}$$

Note that this dispersion implies different sound velocities in the axial z and transverse x, y-directions respectively:

$$c_z=\frac{\tilde{g}n}{m^*}\,, \tag{12.45}$$

$$c_{x,y}=\frac{\tilde{g}n}{m}\,. \tag{12.46}$$

As pointed out in section 12.2, the range of relevant momenta p_x, p_y and quasi-momenta q reaches up to values much larger than $mc_{x,y}$ and much larger than m^*c_z respectively. Hence, a necessary condition for the applicability of the approximation (12.44) is that

$$m^*c_z << \hbar q_B\,, \tag{12.47}$$

since near the zone boundary $q\sim q_B$ the dispersion certainly deviates from (12.44). This requirement can be rewritten in the form

$$\frac{m^*}{m}\frac{\tilde{g}}{g}\ll\frac{E_R}{gn}\,. \tag{12.48}$$

It can only be fulfilled for $gn/E_R<1$ since the left hand side is always larger than one. Moreover, for a given value of $gn/E_R<1$ it can only be satisfied for sufficiently low lattice depths s since both m^*/m and $\tilde{g}/g$ are monotonically increasing functions of s (see section 5.2 and 6.1).

Supposing that the approximation (12.44) is applicable, we can calculate the quantum depletion as in the uniform case: The effective mass can be eliminated from $|v_{q,p_x,p_y}(\mathbf{r})|^2$ by introducing the rescaled quasi-momentum $\tilde{q}=\sqrt{m/m^*}q$. Accordingly, we write $\int dq=\sqrt{m^*/m}\int d\tilde{q}$ and obtain

$$\boxed{\frac{\Delta N_{\rm tot}}{N_{\rm tot}}=\frac{8}{3}\frac{1}{\pi^{1/2}}\sqrt{\frac{m^*}{m}}(\tilde{a}^3n)^{1/2}\,,} \tag{12.49}$$

where we have defined the effective scattering length $\tilde{a}$ through the relation $\tilde{g}=4\pi\hbar^2\tilde{a}/m$. As pointed out above, this expression is valid only for low average densities and low lattice depths. In this regime, the quantum depletion is expected to differ only little from the one in the absence of the lattice. The situation becomes more interesting for larger optical potential depth, where the lattice is expected to affect the coherence properties of the system more strongly.

12.4 Tight binding regime

In the regime of deep optical lattices, one can neglect contributions to the depletion from higher bands, because high energy excitations are particle-like (see discussion section 7.2) and hence

$$\frac{v_{j\neq 1,q,p_x,p_y}(\mathbf{r})}{u_{j\neq 1,q,p_x,p_y}(\mathbf{r})} \approx 0\,. \tag{12.50}$$

We are then allowed to restrict the sum in (12.1) to $j = 1$.

In the tight binding limit, one can easily generalize expressions (7.25,7.26) for the Bogoliubov amplitudes in the lowest band to account for transverse excitations

$$u_{q,p_x,p_y}(\mathbf{r}) = \frac{e^{i(p_x x+p_y y)/\hbar}}{L}\frac{U_{q,p_x,p_y}}{\sqrt{N_w}}\sum_l e^{iqld/\hbar} f(z-ld), \tag{12.51}$$

$$v_{q,p_x,p_y}(\mathbf{r}) = \frac{e^{i(p_x x+p_y y)/\hbar}}{L}\frac{V_{q,p_x,p_y}}{\sqrt{N_w}}\sum_l e^{iqld/\hbar} f(z-ld), \tag{12.52}$$

where $f(z)$ is the condensate Wannier function (see Eq.(6.26) with $j = 1$). Starting from this ansatz and for simplicity neglecting contributions arising from $n\partial\delta/\partial n$ (see discussion section 7.2), Eq.(7.38) can be generalized to 3D in a straightforward way, yielding

$$\hbar\omega(p_\perp, q) = \sqrt{\varepsilon(p_\perp, q)(\varepsilon(p_\perp, q) + 2\kappa^{-1})}, \tag{12.53}$$

where

$$\varepsilon(p_\perp, q) = \frac{p_\perp^2}{m} + 2\delta\sin^2(qd/2) \tag{12.54}$$

and $p_\perp^2 = p_x^2 + p_y^2$. For the amplitudes U_{q,p_x,p_y} and V_{q,p_x,p_y} in (12.51,12.52) we find the result

$$U_{q,p_x,p_y} = \frac{\varepsilon + \hbar\omega}{2\sqrt{\hbar\omega\varepsilon}}, \tag{12.55}$$

$$V_{q,p_x,p_y} = \frac{\varepsilon - \hbar\omega}{2\sqrt{\hbar\omega\varepsilon}}, \tag{12.56}$$

ensuring the 3D normalization condition (12.10).

Omitting the sum over $j > 1$ in (12.1) we are left with the expression

$$\begin{aligned}\frac{\Delta N_{\rm tot}}{N_{\rm tot}} &= \frac{1}{N_{\rm tot}}\sum_{q,p_x,p_y}\frac{\left[\varepsilon(p_x,p_y,q) - \hbar\omega(p_x,p_y,q)\right]^2}{4\hbar\omega(p_x,p_y,q)\varepsilon(p_x,p_y,q)} \\ &= \frac{1}{N_{\rm tot}}\sum_{q,p_x,p_y}\frac{1}{2}\left[\frac{\varepsilon(p_x,p_y,q) + \kappa^{-1}}{\hbar\omega(p_x,p_y,q)} - 1\right]\end{aligned} \tag{12.57}$$

with $\varepsilon(p_x, p_y, q)$ and $\omega(p_x, p_y, q)$ given by (12.54) and (12.53) respectively. The spectrum of values of q and p_x, p_y is given by (12.2) and (12.3) to satisfy the correct boundary conditions.

3D thermodynamic limit

An analytic expression for (12.57) can be found in the thermodynamic limit employing the continuum approximation

$$\sum_{p_x,p_y,q} \rightarrow \frac{L^3}{(2\pi)^3}\frac{1}{\hbar^2}\int dp_x \int dp_y \int_{-\pi/d}^{\pi/d} dq\,. \tag{12.58}$$

The quantum depletion in the tight binding regime then becomes

$$\frac{\Delta N_{\rm tot}}{N_{\rm tot}} = \frac{1}{N_{\rm tot}}\frac{L^3}{(2\pi)^3}\frac{1}{\hbar^2}\times \\ \times\int_{-\pi/d}^{\pi/d} dq \int_0^\infty 2\pi p_\perp dp_\perp \frac{1}{2}\left[\frac{\frac{p_\perp^2}{2\kappa^{-1}2m}+1/2+\frac{\delta}{\kappa^{-1}}\sin^2(\frac{qd}{2})}{\sqrt{(\frac{p_\perp^2}{2\kappa^{-1}2m}+\frac{\delta}{\kappa^{-1}}\sin^2(\frac{qd}{2}))(\frac{p_\perp^2}{2\kappa^{-1}2m}+\frac{\delta}{\kappa^{-1}}\sin^2(\frac{qd}{2})+1)}}-1\right]. \tag{12.59}$$

The integral can be solved analytically and the final result reads

$$\frac{\Delta N_{\rm tot}}{N_{\rm tot}} = \frac{\pi}{4}\frac{1}{nd^3}\frac{\kappa^{-1}}{E_R}G\left(\frac{\delta}{\kappa^{-1}}\right), \tag{12.60}$$

where the function $G(b)$, given by

$$G(b) = \frac{1}{2}-\frac{\sqrt{b}}{\pi}+\frac{b}{2}-\frac{1}{\pi}\arctan(\sqrt{b})(1+b) \tag{12.61}$$

is depicted in Fig.12.1.

From Eq.(12.60), one recovers the result (12.49) in the limit $\delta/\kappa^{-1}\rightarrow\infty$, reflecting the fact that the case of a shallow lattice is approached by increasing δ. Yet, this limit is only of academic interest, since in the tight binding regime where (12.60) applies, the ratio δ/κ^{-1} becomes large only if interactions are vanishingly small. For example, for $gn = 0.02E_R$ and $s = 10$ one still finds $\delta/\kappa^{-1}\approx 1$. Thus, in the tight binding regime the ratio δ/κ^{-1} is usually small. It goes to zero as $s\rightarrow\infty$. Moreover, the incompressibility κ^{-1} approaches the expression $\kappa^{-1}=\tilde{g}n$. Hence, in the large-s limit the depletion (12.60) converges to

$$\boxed{\frac{\Delta N_{\rm tot}}{N_{\rm tot}} = \frac{\tilde{a}}{d}\,,} \tag{12.62}$$

where, as previously, we have defined an effective scattering length $\tilde{a}$ through the relation $\tilde{g}=4\pi\hbar^2\tilde{a}/m$. Note that the dependence on the interaction strength is stronger in this case than in a shallow lattice (see Eq.(12.49)), since the depletion scales like $\tilde{a}$ rather than $\tilde{a}^{3/2}$.

The result (12.62) coincides with the thermodynamic limit quantum depletion (12.33) of a disc shaped uniform system with strong axial harmonic confinement, freezing the wavefunction to a gaussian of width σ. The link between the result for the disc (12.33) and the lattice result (12.62) is established by noting that within the gaussian approximation to the Wannier function in a deep lattice we find $\tilde{a}=ad/\sqrt{2\pi}\sigma$ (see section 6.2, in particular Eq.(6.54)). Thus, the

depletion (12.62) can be rewritten in the form $\Delta N_{\rm tot}/N_{\rm tot} = a/\sqrt{2\pi}\sigma$ in coincidence with the expression for the depletion in a disc (12.33). This means that we are not dealing with an array of separated two-dimensional condensates, but with one condensate only being distributed over several sites. Equivalently, we can refer to the system as a *coherent* array of two-dimensional condensates, each of them containing a non-condensed fraction

$$\left(\frac{\Delta N}{N}\right)_l = \frac{\tilde{a}}{d}\,, \tag{12.63}$$

giving rise to a non-condensed fraction of the whole system

$$\begin{aligned}\frac{\Delta N_{\rm tot}}{N_{\rm tot}} &= \frac{1}{N_w}\sum_l \left(\frac{\Delta N}{N}\right)_l \\ &= \frac{\tilde{a}}{d}\,,\end{aligned} \tag{12.64}$$

where the fact that we can simply added up the number of non-condensed atoms at each site is a non-trivial step presupposing the coherence of the system as a whole.

It is interesting to note that the depletion (12.62) is obtained by letting the tunneling parameter go to zero ($\delta \to 0$). Still, the resulting depletion takes values much smaller than one provided that the confinement within each well does not become infinitely large giving rise to a diverging $\tilde{g}$ and hence $\tilde{a}$ [1]. The reason for this is that *before* letting $\delta \to 0$ we have taken the limit $N_{\rm tot}$, $L \to \infty$, $n = const.$. This forces the system as a whole to be coherent since the ratio between the Josephson tunneling energy E_J and the Josephson charging energy E_C (see Eqs.(10.34,10.49)) diverges

$$E_J/E_C = N\kappa\delta/2 \to \infty \tag{12.65}$$

for fixed κ, δ as $N \to \infty$, while the average density n is kept constant. This indicates that coherence is maintained across the whole sample (see discussion in section 10.1).

In conclusion, we can say that the result (12.62) does not tell us what happens to the condensate fraction when the system size and the total number of particles are kept fixed while the lattice is made very deep. Surely, we expect the true result to differ from (12.62) in this case: In connection with the occurence of number squeezing and the approach to the superfluid-insulator transition the condensed fraction should become small as a signature of the decoherence of the system breaking up into disconnected parts each one of them occupying one lattice site.

1D thermodynamic limit

We have seen that in the thermodynamic limit, the quantum depletion is upper-bounded by the usually very small quantity $\tilde{a}/d$. If the continuum approximation (12.58) in the radial

[1] If $\delta \to 0$ is achieved by letting $s \to \infty$, also $\tilde{g} \to \infty$ and thus $\tilde{a} \to \infty$ (see Eq.(6.54) with σ given by (6.50)). Yet, there are other ways of taking the limit $\delta \to 0$ which do not affect $\tilde{g}$: For example, the tunneling rate can be made zero by increasing d or by raising the barriers of the periodic potential while keeping the potential unchanged close to its minima.

direction is not applicable and it is crucial to take into account the discreteness of the sum over the quantum numbers p_x and p_y in Eq.(12.57), the results are different. This is the case if the number of particles in each well is sufficiently small, or if the longitudinal size of the system, fixed by the number of wells N_w, is sufficiently large. The limiting case is obtained when the contribution arising from the term with $p_x = p_y = 0$, $q \neq 0$ is the dominant one in Eq.(12.57) and we are thus left with

$$\frac{\Delta N_{\rm tot}}{N_{\rm tot}} = \frac{1}{N_{\rm tot}} \sum_{q\neq 0} \frac{1}{2} \left[\frac{2\delta \sin^2(\frac{qd}{2}) + \kappa^{-1}}{\sqrt{2\delta \sin^2(\frac{qd}{2}) \left(2\delta \sin^2(\frac{qd}{2}) + 2\kappa^{-1} \right)}} - 1 \right] . \qquad (12.66)$$

Supposing that the system is very long, we make use of the continuum approximation in the z-direction. This yields

$$\frac{\Delta N_{\rm tot}}{N_{\rm tot}} = \frac{1}{N_{\rm tot}} \frac{L}{2\pi} 2 \int_{q_{\rm min}}^{\pi/d} dq \frac{1}{2} \left[\frac{2\delta \sin^2(\frac{qd}{2}) + \kappa^{-1}}{\sqrt{2\delta \sin^2(\frac{qd}{2}) \left(2\delta \sin^2(\frac{qd}{2}) + 2\kappa^{-1} \right)}} - 1 \right] , \quad (12.67)$$

with $q_{\rm min} = 2\pi/L$. Since we are interested in particular in what happens in a very deep lattice, we expand the integrand to lowest order in the ratio δ/κ^{-1}. Replacing q by

$$s = q\frac{d}{\pi} , \qquad (12.68)$$

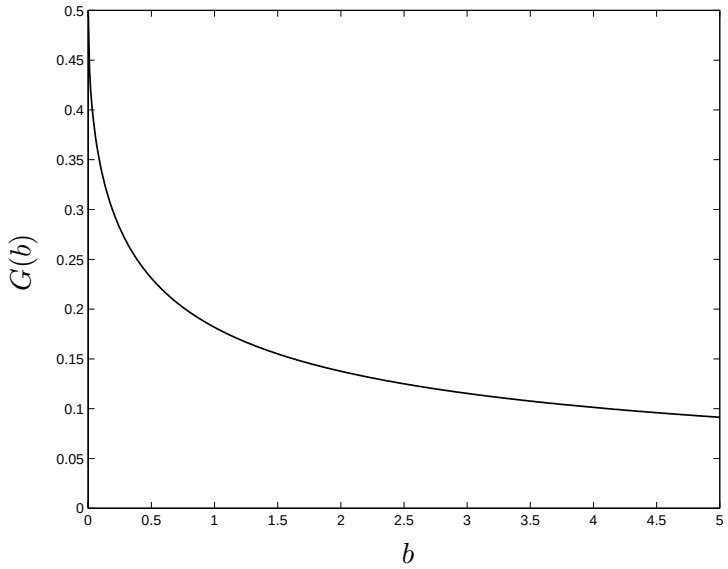

Figure 12.1: The function (12.61) involved in the result for the quantum depletion (12.60) obtained by considering the thermodynamic limit of the tight binding expression (12.57).

we obtain

$$\begin{aligned}\frac{\Delta N_{\rm tot}}{N_{\rm tot}} &= \frac{1}{N}\int_{s_{\rm min}}^{1} ds \frac{1}{4}\frac{1}{\sqrt{\delta\kappa}\sin(\frac{\pi s}{2})} \\ &= \frac{1}{N}\frac{1}{4}\frac{2}{\pi\sqrt{\delta\kappa}}\mathrm{arctanh}\left[\cos\left(\frac{\pi s_{\rm min}}{2}\right)\right] . \end{aligned} \tag{12.69}$$

Because $s_{\rm min} = 2/N_w \ll 1$, we expand

$$\begin{aligned}\frac{\Delta N_{\rm tot}}{N_{\rm tot}} &= \frac{1}{N}\frac{1}{4}\frac{2}{\pi\sqrt{\delta\kappa}}\mathrm{arctanh}\left(1-\frac{1}{8}\pi^2 s_{\rm min}^2\right) \\ &= \frac{1}{N}\frac{1}{2\pi\sqrt{\delta\kappa}}\ln\left(\frac{4}{\pi s_{\rm min}}\right) . \end{aligned} \tag{12.70}$$

and inserting $s_{\rm min} = 2/N_w$ we finally obtain

$$\frac{\Delta N_{\rm tot}}{N_{\rm tot}} = \frac{1}{N}\frac{1}{2\pi\sqrt{\delta\kappa}}\ln\left(\frac{2N_w}{\pi}\right) . \tag{12.71}$$

Using the relation between δ and the effective mass (6.41) and the relation between sound velocity, compressibility and effective mass (7.48) this result can also be written in the form

$$\boxed{\frac{\Delta N_{\rm tot}}{N_{\rm tot}} = \nu\ln\left(\frac{2N_w}{\pi}\right) ,} \tag{12.72}$$

with

$$\nu = \frac{m^* c d}{2\pi\hbar N} . \tag{12.73}$$

Hence, the quantum depletion can be made larger by increasing the lattice depth s (thereby increasing m^*c), decreasing the number of particles per well N, or by increasing the number of wells N_w. Yet, one can easily check that, unless N is of the order of unity or m^* is extremely large, the value of ν always remains very small. To illustrate this point we plot in Fig.12.2 the quantity $N\nu$ as a function of the lattice depth s as obtained for $gn = 0.5E_R$, showing that for a small number of particles per site the depletion (12.72) is large.

Note that in a deep lattice, we have $c = \sqrt{\tilde{g}n/m^*}$ and hence the depletion scales like $\tilde{a}^{1/2}$. This should be compared with the $\tilde{a}$ and $\tilde{a}^{3/2}$ dependence in the coherent array of 2D discs (12.62) and in the shallow lattice (12.49) respectively.

Result (12.72,12.73) has a form analogous to the quantum depletion (12.43) of 1D uniform gas. Yet, recall that strictly speaking (12.73) was obtained in the tight binding regime and assuming that $\delta/\kappa^{-1} \ll 1$. An interesting difference is given by the fact that the healing length ξ entering as relevant length scale in the argument of the logarithmic function in the case of the uniform system is replaced by the interwell spacing d in the case of a deep lattice.

Quantum depletion and decoherence

Result (12.72,12.73) is linked to the coherence theory of 1D systems, where the off-diagonal 1-body density exhibits the power law decay

$$\frac{n^{(1)}(|z-z'|)}{n} \to \left(\frac{|z-z'|}{\xi}\right)^{-\nu} \tag{12.74}$$

at large distances. If the exponent ν is much smaller than 1, the coherence survives at large distances

$$\frac{n^{(1)}(|z-z'|)}{n} \to \left(\frac{|z-z'|}{\xi}\right)^{-\nu} \approx 1 - \nu \ln\left(\frac{|z-z'|}{\xi}\right), \tag{12.75}$$

and the application of Bogoliubov theory is justified

$$\frac{\Delta N_{\rm tot}}{N_{\rm tot}} \approx \nu \ln\left(\frac{L}{\xi}\right) \ll 1\,. \tag{12.76}$$

For a superfluid, the value of ν in (12.74) is fixed by the hydrodynamic fluctuations of the phase and is given, at $T=0$, by the expression (12.73) [1].

In terms of the Josephson parameters (10.34,10.49) we can also write

$$\nu = \sqrt{\frac{E_C}{8\pi^2 E_J}}\,, \tag{12.77}$$

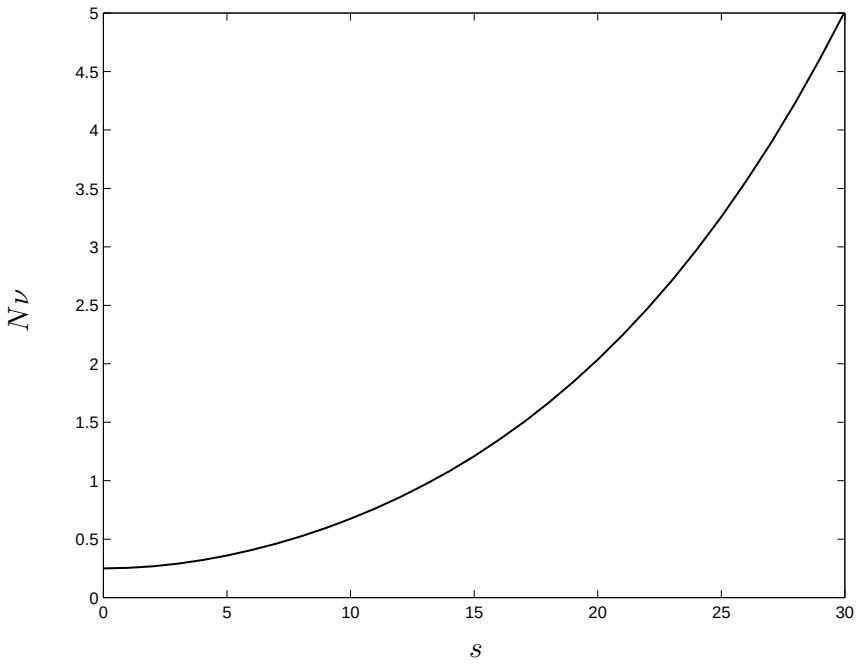

Figure 12.2: The quantity $N\nu$ (see Eq. (12.73) with N the number of particles per well) as a function of the lattice depth s with m^*c as obtained for $gn = 0.5E_R$.

confirming that the system is coherent as long as $E_J/E_C \ll 1$ (see section 10.1).

When the exponent of the power law takes the value $\nu = 0.14$, corresponding to $E_J = 1.62E_C$, the 1D system is expected to exhibit the Bradley-Doniach phase transition to an insulating phase where the 1-body density matrix decays exponentially [157]. Note however that before this transition is reached the depletion (12.72) becomes large and hence Bogoliubov theory is no longer applicable.

The transition from the regime where (12.62) is applicable to the regime where the 1D character of the fluctuations prevail (see Eq.(12.72) can be estimated by calculating at what lattice depth s the condition

$$\frac{\tilde{a}}{d} \approx \nu \ln\left(\frac{2N_w}{\pi}\right), \tag{12.78}$$

is fulfilled. As an example, for $gn = 0.2E_R$, $N_w = 200$ and $N = 500$, this transition is predicted to occur around $s = 30$ where the left and right side of the inequality become equal to $\sim 4\%$.

Quantum depletion in current experiments

To give an example, we set $gn = 0.2E_R, N = 200$ and $N_w = 500$ describing a setting similar to the experiment of [73]. Bogoliubov theory predicts a depletion of $\approx 0.6\%$ in the absence of the lattice ($s = 0$). At a lattice depth of $s = 10$ the evaluation of Eq.(12.1), using the tight binding result (12.57), and keeping the sum discrete yields a depletion of $\approx 1.7\%$. On the other hand, Eq.(12.60), obtained by replacing the sum in Eq.(12.57) by an integral, yields a depletion of $\approx 2\%$, in reasonable agreement with the full result $\approx 1.7\%$. The 2D formula (12.62) instead yields $\approx 2.9\%$ depletion, revealing that the system is not yet fully governed by 2D fluctuations. With the same choice of parameters, the power law exponent (12.73) has the value $\nu = 0.001$ and the 1D depletion (12.72) is predicted to be $\approx 0.6\%$, significantly smaller than the full value $\approx 1.7\%$. This reveals that the sum (12.57) is not exhausted by the terms with $p_x = p_y = 0$. In conclusion, one finds that for this particular setting, the character of fluctuations is intermediate between 3D and 2D, and still far from 1D. In particular, from the above estimates it emerges that in order to reach the conditions for observing the Bradley-Doniach transition one should work at much larger values of s.

A very different situation is encountered in the experiment [91]: There, a weak one-dimensional optical lattice of depth s_{ax} is set up along the tubes formed by a deep two-dimensional lattice. In this setting, the number of particles per site is very small $N \approx 3 - 4$. For $s_{ax} = 4$ and interaction strength $gn = 1E_R$ one finds $N\nu = 0.42$, yielding a large depletion of 0.55 for $N_w = 40$ sites and $N = 3$ particles per site. Hence, this setting prepares the gas in a regime of strong coupling beyond the validity of GP- and Bogoliubov theory. Note that in determining the interaction parameter gn we have taken into account the non-uniform confinement in the transverse directions.

Bibliography

[1] L. Pitaevskii and S. Stringari, *Bose-Einstein Condensation* (Oxford University Press, Oxford, 2003).

[2] M.H. Anderson, J.R. Ensher, M.R. Matthews, C.E. Wieman, and E.A. Cornell, Observation of Bose-Einstein Condensation in a Dilute Atomic Vapor, Science **269**, 198 (1995).

[3] K.B. Davis, M.-O. Mewes, M.R. Andrews, N.J. van Druten, D.S. Durfee, D.M. Kurn, and W. Ketterle, Bose-Einstein Condensation in a Gas of Sodium Atoms, Phys. Rev. Lett. **75**, 3969 (1995).

[4] C.C. Bradley, C.A. Sackett, J.J. Tollett, and R.G. Hulet, Evidence of Bose-Einstein Condensation in an Atomic Gas with Attractive Interactions, Phys. Rev. Lett. **75**, 1687 (1995).

[5] R. Onofrio, D.S. Durfee, C. Raman, M. Köhl, C.E. Kuklewicz, and W. Ketterle, Surface Excitations of a Bose-Einstein Condensate, Phys. Rev. Lett. **84**, 810 (2000).

[6] K.W. Madison, F. Chevy, W. Wohlleben, and J. Dalibard, Vortex Formation in a Stirred Bose-Einstein Condensate Phys. Rev. Lett. **84**, 806 (2000).

[7] F. Chevy, K.W. Madison, and J. Dalibard, Measurement of the Angular Momentum of a Rotating Bose-Einstein Condensate, Phys. Rev. Lett. **85**, 2223 (2000).

[8] K.W. Madison, F. Chevy, W. Wohlleben, and J. Dalibard, Vortices in a stirred Bose-Einstein condensate, J. Mod. Optics **47**, 2715 (2000).

[9] F. Chevy, K.W. Madison, V. Bretin, and J. Dalibard, in *Proceedings of trapped particles and fundamental physics workshop*, eds. S. Atutov, K. Kalabrese, and L. Moi (Les Houches 2001).

[10] K.W. Madison, F. Chevy, V. Bretin, and J. Dalibard, Stationary States of a Rotating Bose-Einstein Condensate: Routes to Vortex Nucleation, Phys. Rev. Lett.**86**, 4443 (2001).

[11] C. Raman, J.R. Abo-Shaeer, J.M. Vogels, K. Xu, and W. Ketterle, Vortex Nucleation in a Stirred Bose-Einstein Condensate, Phys. Rev. Lett.**87**, 210402 (2001).

[12] J.R. Abo-Shaeer, C. Raman, J.M. Vogels, and W. Ketterle, Observation of Vortex Lattices in Bose-Einstein Condensates, Science **292**, 476 (2001).

[13] E. Hodby, G. Hechenblaikner, S.A. Hopkins, O.M. Maragò, and C.J. Foot, Vortex Nucleation in Bose-Einstein Condensates in an Oblate, Purely Magnetic Potential, Phys. Rev. Lett. **88**, 010405 (2002).

[14] G. Hechenblaikner, E. Hodby, S.A. Hopkins, O.M. Maragò, and C.J. Foot, Direct Observation of Irrotational Flow and Evidence of Superfluidity in a Rotating Bose-Einstein Condensate, Phys. Rev. Lett. **88**, 070406 (2002).

[15] C.J. Pethick and H. Smith, *Bose-Einstein Condensation in Dilute Bose Gases* (Cambridge University Press, 2002).

[16] A. Recati, F. Zambelli, and S. Stringari, Overcritical Rotation of a Trapped Bose-Einstein Condensate, Phys. Rev. Lett. **86**, 377 (2000).

[17] S. Sinha and Y. Castin, Dynamic Instability of a Rotating Bose-Einstein Condensate, Phys. Rev. Lett. **87**, 190402 (2001).

[18] J. Garcia-Ripoll and V. Pérez-Garcia, Anomalous rotational properties of Bose-Einstein condensates in asymmetric traps, Phys. Rev. A **64**, 013602 (2001).

[19] E.M. Lifshitz and L.P. Pitaevskii, *Statistical Physics* (Butterworth-Heinemann, Oxford, 1999).

[20] L. Onsager, Nuovo Cimento **6**, suppl. 2, 249 (1949) (observation concerning C.J. Gorter, The two fluid model for Helium II, Nuovo Cimento **6**, suppl. 2, 245 (1949)).

[21] R.P. Feynman, Application of Quantum Mechanics to liquid Helium, in *Progress in Low Temperature Physics*, Vol. I, ed. C.J. Gorter (North-Holland, Amsterdam, 1955).

[22] A.A. Abrikosov, On the Magnetic Properties of Superconductors of the Second Group, JETP **5**, 1174 (1957).

[23] V.K. Tkachenko, On Vortex Lattices, JETP **22**, 1282 (1966).

[24] D. Butts and D. Rokshar, Predicted signatures of rotating Bose-Einstein condensates, Nature **397**, 327 (1999).

[25] Y. Castin and R. Dum, Bose-Einstein condensates with vortices in rotating traps, Eur. Phys. J. D **7**, 399 (1999).

[26] D.L. Feder, C.W. Clark, and B.I. Schneider, Vortex Stability of Interacting Bose-Einstein Condensates Confined in Anisotropic Harmonic Traps, Phys. Rev. Lett. **82**, 4956 (1999).

[27] A.L. Fetter and A.A. Svidzinsky, Vortices in a trapped dilute Bose-Einstein condensate, J. Phys.: Condens. Matter **13**, R135 (2001).

[28] M.R. Matthews, B.P. Anderson, P.C. Haljan, D.S. Hall, C.E. Wieman, and E.A. Cornell, Vortices in a Bose-Einstein Condensate, Phys. Rev. Lett. **83**, 2498 (1999).

[29] P.C. Haljan, B.P. Anderson, I. Coddington, and E.A. Cornell, Use of Surface-Wave Spectroscopy to Characterize Tilt Modes of a Vortex in a Bose-Einstein Condensate, Phys. Rev. Lett. **86**, 2922 (2001).

[30] P.C. Haljan, I. Coddington, P. Engels, and E.A. Cornell, Driving Bose-Einstein-Condensate Vorticity with a Rotating Normal Cloud, Phys. Rev. Lett. **87**, 210403 (2001).

[31] E. Lundh, C.J. Pethick, and H. Smith, Zero-temperature properties of a trapped Bose-condensed gas: Beyond the Thomas-Fermi approximation, Phys. Rev. A **55**, 2126 (1997).

[32] F. Dalfovo and M. Modugno, Free expansion of Bose-Einstein condensates with quantized vortices, Phys. Rev. A **61**, 023605 (2000).

[33] E. Hodby, S.A. Hopkins, G. Hechenblaikner, N.L. Smith, and C.J. Foot, Experimental Observation of a Superfluid Gyroscope in a Dilute Bose-Einstein Condensate, Phys. Rev. Lett. **91**, 090403 (2003).

[34] S. Inouye, S. Gupta, T. Rosenband, A.P. Chikkatur, A. Görlitz, T.L. Gustavson, A.E. Leanhardt, D.E. Pritchard, and W. Ketterle, Observation of Vortex Phase Singularities in Bose-Einstein Condensates, Phys. Rev. Lett. **87**, 080402 (2001).

[35] P. Engels, I. Coddington, P.C. Haljan, and E.A. Cornell, Nonequilibrium Effects of Anisotropic Compression Applied to Vortex Lattices in Bose-Einstein Condensates, Phys. Rev. Lett.**89**, 100403 (2002).

[36] P. Rosenbusch, V. Bretin, and J. Dalibard, Dynamics of a Single Vortex Line in a Bose-Einstein Condensate, Phys. Rev. Lett. **89**, 200403 (2002).

[37] J.R. Abo-Shaeer, C. Raman, and W. Ketterle, Formation and Decay of Vortex Lattices in Bose-Einstein Condensates at Finite Temperatures, Phys. Rev. Lett. **88**, 070409 (2002).

[38] V. Bretin, P. Rosenbusch, F. Chevy, G.V. Shlyapnikov, and J. Dalibard, Quadrupole Oscillation of a Single-Vortex Bose-Einstein Condensate: Evidence for Kelvin Modes, Phys. Rev. Lett. **90**, 100403 (2003).

[39] I. Coddington, P. Engels, V. Schweikhard, and E.A. Cornell, Observation of Tkachenko Oscillations in Rapidly Rotating Bose-Einstein Condensates, Phys. Rev. Lett. **91**, 100402 (2003).

[40] P. Rosenbusch, D.S. Petrov, S. Sinha, F. Chevy, V. Bretin, Y. Castin, G. Shlyapnikov, and J. Dalibard, Critical Rotation of a Harmonically Trapped Bose Gas, Phys. Rev. Lett. **88**, 250403 (2002).

[41] P. Engels, I. Coddington, P.C. Haljan, V. Schweikhard, and E.A. Cornell, Observation of Long-Lived Vortex Aggregates in Rapidly Rotating Bose-Einstein Condensates, Phys. Rev. Lett. **90**, 170405 (2003).

[42] V. Schweikhard, I. Coddington, P. Engels, V.P. Mogendorff, and E.A. Cornell, Rapidly Rotating Bose-Einstein Condensates in and near the Lowest Landau Level, Phys. Rev. Lett. **92**, 040404 (2004).

[43] S. Stringari, Collective Excitations of a Trapped Bose-Condensed Gas, Phys. Rev. Lett. **77**, 2360 (1996).

[44] M. Krämer, L. Pitaevskii, S. Stringari, and F. Zambelli, Vortex nucleation and quadrupole deformation of a rotating Bose-Einstein condensate, Laser Physics **12**, 113 (2002).

[45] G.B. Hess, Angular Momentum of Superfluid Helium in a Rotating Cylinder, Phys. Rev. **161**, 189 (1967).

[46] A.A. Svidzinsky and A.L. Fetter, Dynamics of a vortex in a trapped Bose-Einstein condensate, Phys. Rev. A **62**, 063617 (2000).

[47] J.J. Garcia-Ripoll and V. Pérez-Garcia, Vortex nucleation and hysteresis phenomena in rotating Bose-Einstein condensates, Phys. Rev. A **63**, 041603(R) (2001).

[48] J.J. Garcia-Ripoll and V. Pérez-Garcia, Vortex bending and tightly packed vortex lattices in Bose-Einstein condensates, Phys. Rev. A **64**, 053611 (2001).

[49] A.A. Svidzinsky and A.L. Fetter, Stability of a Vortex in a Trapped Bose-Einstein Condensate, Phys. Rev. Lett. **84**, 5919 (2000).

[50] F. Dalfovo and S. Stringari, Shape deformations and angular-momentum transfer in trapped Bose-Einstein condensates, Phys. Rev. A **63**, 011601(R) (2001).

[51] T. Isoshima and K. Machida, Instability of the nonvortex state toward a quantized vortex in a Bose-Einstein condensate under external rotation, Phys. Rev. A **60**, 3313 (1999).

[52] D.L. Feder, C.W. Clark, and B.I. Schneider, Nucleation of vortex arrays in rotating anisotropic Bose-Einstein condensates, Phys. Rev. A **61**, 011601(R) (1999).

[53] D.L. Feder, A.A. Svidzinsky, A.L. Fetter, and C.W. Clark, Anomalous Modes Drive Vortex Dynamics in Confined Bose-Einstein Condensates, Phys. Rev. Lett. **86**, 564 (2001).

[54] M. Tsubota, K. Kasamatsu, and M. Ueda, Vortex lattice formation in a rotating Bose-Einstein condensate, Phys. Rev. A **65**, 023603 (2002).

[55] E. Lundh, J.-P. Martikainen, and K.-A. Suominen, Vortex nucleation in Bose-Einstein condensates in time-dependent traps, Phys. Rev. A **67**, 063604 (2003).

[56] C. Lobo, A. Sinatra, and Y. Castin, Vortex Lattice Formation in Bose-Einstein Condensates, Phys. Rev. Lett. **92**, 020403 (2004).

[57] F. Dalfovo, L. Pitaevskii, and S. Stringari, Order parameter at the boundary of a trapped Bose gas, Phys. Rev. A **54**, 4213 (1996).

[58] A.A. Penckwitt, R.J. Ballagh, and C.W. Gardiner, Nucleation, Growth, and Stabilization of Bose-Einstein Condensate Vortex Lattices, Phys. Rev. Lett. **89**, 260402 (2002).

[59] J. E. Williams, E. Zaremba, B. Jackson, T. Nikuni, and A. Griffin, Dynamical Instability of a Condensate Induced by a Rotating Thermal Gas, Phys. Rev. Lett. **88**, 070401 (2002).

[60] J.E. Williams and M.J. Holland, Preparing topological states of a Bose-Einstein condensate, Nature (London) **401**, 568 (1999).

[61] A.E. Leanhardt, A. Görlitz, A.P. Chikkatur, D. Kielpinski, Y. Shin, D.E. Pritchard, and W. Ketterle, Imprinting Vortices in a Bose-Einstein Condensate using Topological Phases, Phys. Rev. Lett. **89**, 190403 (2002).

[62] A.E. Leanhardt, Y. Shin, D. Kielpinski, D.E. Pritchard, and W. Ketterle, Coreless Vortex Formation in a Spinor Bose-Einstein Condensate, Phys. Rev. Lett. **90**, 140403 (2003).

[63] B.P. Anderson, P.C. Haljan, C.A. Regal, D.L. Feder, L.A. Collins, C.W. Clark, and E.A. Cornell, Watching Dark Solitons Decay into Vortex Rings in a Bose-Einstein Condensate, Phys. Rev. Lett. **86**, 2926 (2001).

[64] F. Zambelli and S. Stringari, Quantized Vortices and Collective Oscillations of a Trapped Bose-Einstein Condensate, Phys. Rev. Lett. **81**, 1754 (1998).

[65] W. Zwerger, Mott-Hubbard transition of cold atoms in optical lattices, J. Opt. B: Quantum Semiclass. Opt. **5**, 9 (2003).

[66] B.P. Anderson and M.A. Kasevich, Macroscopic Quantum Interference from Atomic Tunnel Arrays, Science **282**, 1686 (1998).

[67] O. Morsch, J.H. Müller, M. Cristiani, D. Ciampini, and E. Arimondo, Bloch Oscillations and Mean-Field Effects of Bose-Einstein Condensates in 1D Optical Lattices, Phys. Rev. Lett. **87**, 140402 (2001).

[68] M. Cristiani, O. Morsch, J.H. Müller, D. Ciampini, and E. Arimondo, Experimental properties of Bose-Einstein condensates in one-dimensional optical lattices: Bloch oscillations, Landau-Zener tunneling, and mean-field effects, Phys. Rev. A **65**, 063612 (2002).

[69] M. Jona-Lasinio, O. Morsch, M. Cristiani, N. Malossi, J.H. Muller, E. Courtade,M. Anderlini, and E. Arimondo, Asymmetric Landau-Zener tunneling in a periodic potential, Phys. Rev. Lett. **91**, 230406 (2003).

[70] P. Pedri, L. Pitaevskii, S. Stringari, C. Fort, S. Burger, F.S. Cataliotti, P. Maddaloni, F. Minardi, and M. Inguscio, Expansion of a Coherent Array of Bose-Einstein Condensates, Phys. Rev. Lett. **87**, 220401 (2001).

[71] O. Morsch, M. Cristiani, J.H. Müller, D. Ciampini, and E. Arimondo, Free expansion of a Bose-Einstein condensate in a one-dimensional optical lattice, Phys. Rev. A **66**, 021601 (2002).

[72] O. Morsch, M. Cristiani, J.H. Muller, D. Ciampini, E. Arimondo, Dynamics and phase evolution of Bose-Einstein condensates in one-dimensional optical lattices, Laser Physics **13**, 594 (2003).

[73] F.S. Cataliotti, S. Burger, C. Fort, P. Maddaloni, F. Minardi, A. Trombettoni, A. Smerzi and M. Inguscio, Josephson junction arrays with Bose-Einstein condensates, Science **293**, 843 (2001).

[74] S. Burger, F.S. Cataliotti, C. Fort, F. Minardi, M. Inguscio, M.L. Chiofalo, and M.P. Tosi, Superfluid and Dissipative Dynamics of a Bose-Einstein Condensate in a Periodic Optical Potential, Phys. Rev. Lett. **86**, 4447 (2001).

[75] C. Fort, F.S. Cataliotti, L. Fallani, F. Ferlaino, P. Maddaloni, and M. Inguscio, Collective Excitations of a Trapped Bose-Einstein Condensate in the Presence of a 1D Optical Lattice, Phys. Rev. Lett. **90**, 140405 (2003).

[76] F.S. Cataliotti, L. Fallani, F. Ferlaino, C. Fort, P. Maddaloni, and M. Inguscio, Superfluid current disruption in a chain of weakly coupled Bose-Einstein condensates, New J. Phys. **5**, 71 (2003).

[77] M. Cristiani, O. Morsch, N. Malossi, M. Jona-Lasinio, M. Anderlini, E. Courtade, E. Arimondo, Instabilities of a Bose-Einstein condensate in a periodic potential: an experimental investigation, cond-mat/0311160.

[78] O. Morsch, J.H. Müller, D. Ciampini, M. Cristiani, P.B. Blakie, C.J. Williams, P.S. Julienne, and E. Arimondo, Decay and revival of phase coherence of a Bose-Einstein condensate in a one-dimensional lattice, Phys. Rev. A **67**, 031603 (2003).

[79] J.H. Denschlag, J.E. Simsarian, H. Häffner, C. McKenzie, A. Browaeys, D. Cho, K. Helmerson, S.L. Rolston and W.D. Phillips, A Bose-Einstein condensate in an optical lattice, J. Phys. B **35**, 3095 (2002).

[80] A.S. Mellish, G. Duffy, C. McKenzie, R. Geursen, A.C. Wilson, Nonadiabatic loading of a Bose-Einstein condensate into the ground state of an optical lattice, Phys. Rev. A **68**, 051601 (2003).

[81] B. Eiermann, P. Treutlein, T. Anker, M. Albiez, M. Taglieber, K.P. Marzlin, M.K. Oberthaler, Dispersion management for atomic matter waves, Phys. Rev. Lett. **91**, 060402 (2003).

[82] L. Fallani, F.S. Cataliotti, J. Catani, C. Fort, M. Modugno, M. Zawada, M. Inguscio, Optically-induced lensing effect on a Bose-Einstein condensate expanding in a moving lattice, cond-mat/0303626.

[83] Th. Anker, M. Albiez, B. Eiermann, M. Taglieber, M.K. Oberthaler, Linear and nonlinear dynamics of matter wave packets in periodic potentials, cond-mat/0401165.

[84] B. Eiermann, Th. Anker, M. Albiez, M. Taglieber, P. Treutlein, K.P. Marzlin, M.K. Oberthaler, Bright gap solitons of atoms with repulsive interaction, cond-mat/0402178.

[85] S. Burger, F.S. Cataliotti, C. Fort, P. Maddaloni, F. Minardi, M. Inguscio, Quasi-2D Bose-Einstein condensation in an optical lattice, Europhys. Lett. **57**, 1 (2002).

[86] F. Ferlaino, P. Maddaloni, S. Burger, F.S. Cataliotti, C. Fort, M. Modugno, M. Inguscio, Dynamics of a Bose-Einstein condensate at finite temperature in an atomoptical coherence filter, Phys. Rev. A **66**, 011604(R) (2002).

[87] M. Greiner, I. Bloch, O. Mandel, T.W. Hänsch, and T. Esslinger, Exploring Phase Coherence in a 2D Lattice of Bose-Einstein Condensates, Phys. Rev. Lett. **87**, 160405 (2001).

[88] H. Moritz, T. Stöferle, M. Köhl, and T. Esslinger, Exciting Collective Oscillations in a Trapped 1D Gas, Phys. Rev. Lett. **91**, 250402 (2003).

[89] C. Orzel, A.K. Tuchmann, M.L. Fenselau, M. Yasuda, and M.A. Kasevich, Squeezed States in a Bose-Einstein Condensate, Science **291**, 2386 (2001).

[90] M. Greiner, O. Mandel, T. Esslinger, T.W. Hänsch and I. Bloch, Quantum Phase Transition from a Superfluid to a Mott Insulator in a gas of ultracold atoms, Nature **415**, 39 (2002).

[91] T. Stöferle, H. Moritz, C. Schori, M. Köhl, and T. Esslinger, Transition from a strongly interacting 1D superfluid to a Mott insulator, to be published in Phys. Rev. Lett..

[92] M. Greiner, O. Mandel, T.W. Hänsch and I. Bloch, Collapse and Revival of the Matter Wave Field of a Bose-Einstein condensate, Nature **419**, 51 (2002).

[93] O. Mandel, M. Greiner, A. Widera, T. Rom, T.W. Hänsch, and I. Bloch, Coherent Transport of Neutral Atoms in Spin-Dependent Optical Lattice Potentials, Phys. Rev. Lett. **91**, 010407 (2003).

[94] O. Mandel, M. Greiner, A. Widera, T. Rom, T.W. Hänsch and I. Bloch, Controlled collisions for multi-particle entanglement of optically trapped atoms, Nature **425**, 937 (2003).

[95] A. Widera, O. Mandel, M. Greiner, S. Kreim, T.W. Hänsch and I. Bloch, Entanglement interferometry for precision measurement of atomic scattering properties, cond-mat/0310719.

[96] N.W. Ashcroft and N.D. Mermin, *Solid State Physics* (Harcourt Brace College Publishers, 1976).

[97] M. Ben Dahan, E. Peik, J. Reichel, Y. Castin, and C. Salomon, Bloch Oscillations of Atoms in an Optical Potential, Phys. Rev. Lett. **76**, 4508 (1996).

[98] M. Raizen, C. Salomon, and Q. Niu, New light on quantum transport, Physics today**50** (7), 30 (1997).

[99] L.D. Landau and E.M. Lifshitz, *Quantum Mechanics* (Butterworth-Heinemann, Oxford, 2000).

[100] J.C. Slater, A Soluble Problem in Energy Bands, Phys. Rev. **87**, 807 (1952).

[101] K.K. Likharev and A.B. Zorin, Theory of the Bloch-Wave Oscillations in Small Josephson Junctions, J. Low Temp. Phys. **59**, 347 (1985).

[102] M. Krämer, C. Menotti, L. Pitaevskii and S. Stringari, Bose-Einstein condensates in 1D optical lattices: Compressibility, Bloch bands and elementary excitations, Eur. Phys. J. D **27**, 247 (2003).

[103] D.I. Choi and Q. Niu, Bose-Einstein Condensates in an Optical Lattice, Phys. Rev. Lett. **82**, 2022 (1999).

[104] M. Machholm, A. Nicolin, C.J. Pethick, and H. Smith, Spatial period-doubling in Bose-Einstein condensates in an optical lattice, cond-mat/0307183.

[105] W.D. Li and A. Smerzi, On the nonlinear Kronig-Penney model, unpublished.

[106] B. Wu and Q. Niu, Nonlinear Landau-Zener tunneling, Phys. Rev. A **61**, 023402 (2000).

[107] M. Machholm, C.J. Pethick, and H. Smith, Band structure, elementary excitations, and stability of a Bose-Einstein condensate in a periodic potential Phys. Rev. A **67**, 053613 (2003).

[108] J.C. Bronski, L.D. Carr, B. Deconick, and J.N. Kutz, Bose-Einstein Condensates in Standing Waves: The Cubic Nonlinear Schrdinger Equation with a Periodic Potential, Phys. Rev. Lett. **86**, 1402 (2001).

[109] B. Wu, R.B. Diener, and Q. Niu, Bloch waves and bloch bands of Bose-Einstein condensates in optical lattices, Phys. Rev. A **65**, 025601 (2002).

[110] D. Diakonov, L.M. Jensen, C.J. Pethick, and H. Smith, Loop structure of the lowest Bloch band for a Bose-Einstein condensate, Phys. Rev. A **66**, 013604 (2002).

[111] E.J. Mueller, Superfluidity and mean-field energy loops: Hysteretic behavior in Bose-Einstein condensates, Phys. Rev. A **66**, 063603 (2002).

[112] Y.S. Kivshar and M. Peyrard, Modulational instabilities in discrete lattices, Phys. Rev. A **46**, 3198 (1992).

[113] J.C. Bronski, L.D. Carr, B. Deconick, J.N. Kutz and K. Promislow, Stability of repulsive Bose-Einstein condensates in a periodic potential, Phys. Rev. E. **63**, 036612 (2001).

[114] B. Wu and Q. Niu, Landau and dynamical instabilities of the superflow of Bose-Einstein condensates in optical lattices, Phys. Rev. A **64**, 061603 (2001).

[115] A. Smerzi, A. Trombettoni, P.G. Kevrekidis, and A.R. Bishop, Dynamical Superfluid-Insulator Transition in a Chain of Weakly Coupled Bose-Einstein Condensates, Phys. Rev. Lett. **89**, 170402 (2002).

[116] A. Smerzi and A. Trombettoni, Nonlinear tight-binding approximation for Bose-Einstein condensates in a lattice, Phys. Rev. A **68**, 023613 (2003).

[117] A. Smerzi and A. Trombettoni, Discrete nonlinear dynamics of weakly coupled Bose-Einstein condensates, Chaos **13**, 766 (2003).

[118] C. Menotti, A. Smerzi, and A. Trombettoni, Superfluid Dynamics of a Bose-Einstein condensate in a periodic potential, New J. Phys. **5**, 112 (2003).

[119] K. Berg-Sørensen and K. Mølmer, Bose-Einstein condensates in spatially periodic potentials, Phys. Rev. A **58**, 1480 (1998).

[120] M.L. Chiofalo, M. Polini and M.P. Tosi, Collective excitations of a periodic Bose condensate in the Wannier representation, Eur. Phys. J. D **11**, 371 (2000).

[121] S. Tsuchiya and A. Griffin, Damping of Bogoliubov Excitations in Optical Lattices, cond-mat/0311321.

[122] J. Javanainen, Phonon approach to an array of traps containing Bose-Einstein condensates, Phys. Rev. A **60**, 4902 (1999).

[123] D. van Oosten, P. van der Straten, and H. T. C. Stoof, Quantum phases in an optical lattice, Phys. Rev. A **63**, 053601 (2001).

[124] A.M. Rey, K. Burnett, R. Roth, M. Edwards, C.J. Williams, and C.W. Clark, Bogoliubov approach to superfluidity of atoms in an optical lattice, J. Phys. B **36**, 825 (2003).

[125] E. Taylor and E. Zaremba, Bogoliubov sound speed in periodically modulated Bose-Einstein condensates, Phys. Rev. A **68**, 053611 (2003).

[126] J. Stenger, S. Inouye, A.P. Chikkatur, D.M. Stamper-Kurn, D.E. Pritchard, and W. Ketterle, Bragg Spectroscopy of a Bose-Einstein Condensate, Phys. Rev. Lett. **82**, 4569 (1999).

[127] D.M. Stamper-Kurn, A.P. Chikkatur, A. Görlitz, S. Inouye, S. Gupta, D.E. Pritchard, and W. Ketterle, Excitation of Phonons in a Bose-Einstein Condensate by Light Scattering, Phys. Rev. Lett. **83**, 2876 (1999).

[128] J.M. Vogels, K. Xu, C. Raman, J.R. Abo-Shaeer, and W. Ketterle, Experimental Observation of the Bogoliubov Transformation for a Bose-Einstein Condensed Gas, Phys. Rev. Lett. **88**, 060402 (2002).

[129] J. Steinhauer, R. Ozeri, N. Katz, and N. Davidson, Excitation Spectrum of a Bose-Einstein Condensate, Phys. Rev. Lett. **88**, 120407 (2002).

[130] R. Ozeri, J. Steinhauer, N. Katz, and N. Davidson, Direct Observation of the Phonon Energy in a Bose-Einstein Condensate by Tomographic Imaging, Phys. Rev. Lett. **88**, 220401 (2002).

[131] J. Steinhauer, N. Katz, R. Ozeri, N. Davidson, C. Tozzo, and F. Dalfovo, Bragg Spectroscopy of the Multibranch Bogoliubov Spectrum of Elongated Bose-Einstein Condensates, Phys. Rev. Lett. **90**, 060404 (2003).

[132] M.L. Chiofalo, S. Succi, M.P. Tosi, Probing the energy bands of a Bose-Einstein condensate in an optical lattice, Phys. Rev. A **63**, 063613 (2001).

[133] C. Menotti, M. Krämer, L. Pitaevskii, and S. Stringari, Dynamic structure factor of a Bose-Einstein condensate in a 1D optical lattice, Phys. Rev. A **67**, 053609 (2003).

[134] A.L. Fetter and D. Rokshar, Excited states of a dilute Bose-Einstein condensate in a harmonic trap, Phys. Rev. A **57**, 1191 (1998).

[135] F. Zambelli, L. Pitaevskii, D.M. Stamper-Kurn and S. Stringari, Dynamic structure factor and momentum distribution of a trapped Bose gas, Phys. Rev. A **61**, 063608 (2000).

[136] A. Brunello, F. Dalfovo, L. Pitaevskii, S. Stringari and F. Zambelli, Momentum transferred to a trapped Bose-Einstein condensate by stimulated light scattering, Phys. Rev. A **64**, 063614 (2001).

[137] P.B. Blakie, R.J. Ballagh, and C.W. Gardiner, Theory of coherent Bragg spectroscopy of a trapped Bose-Einstein condensate, Phys. Rev. A **65**, 033602 (2002).

[138] M. Krämer, L. Pitaevskii and S. Stringari, Macroscopic Dynamics of a Trapped Bose-Einstein Condensate in the Presence of 1D and 2D Optical Lattices, Phys. Rev. Lett. **88**, 180404 (2002).

[139] S. Stringari, Dynamics of Bose-Einstein condensed gases in highly deformed traps, Phys. Rev. A **58**, 2385 (1998).

[140] T.-L. Ho and M. Ma, Quasi 1 and 2d Dilute Bose Gas in Magnetic Traps: Existence of Off-Diagonal Order and Anomalous Quantum Fluctuations, J. Low. Temp. Phys. **115**, 61 (1999).

[141] C. Menotti and S. Stringari, Collective oscillations of a one-dimensional trapped Bose-Einstein gas Phys. Rev. A **66**, 043610 (2002).

[142] P. Pedri and L. Santos, Three-dimensional quasi-Tonks gas in a harmonic trap, Phys. Rev. Lett. **91**, 110401 (2003).

[143] P. Massignan and M. Modugno, One-dimensional model for the dynamics and expansion of elongated Bose-Einstein condensates, Phys. Rev. A **67**, 023614 (2003).

[144] S.K. Adhikari, Dynamical classical superfluid-insulator transition in a Bose-Einstein condensate on an optical lattice, J. Phys. B **36**, 2725 (2003).

[145] F. Nesi and M. Modugno, Loss and revival of phase coherence in a Bose-Einstein condensate moving through an optical lattice, cond-mat/0310659.

[146] B.D. Josephson, Possible new effects in superconductive tunnelling, Phys. Lett. **1**, 251 (1962).

[147] A. Trombettoni and A. Smerzi, Discrete Solitons and Breathers with Dilute Bose-Einstein Condensates, Phys. Rev. Lett. **86**, 2353 (2001).

[148] M.R. Andrews, D.M. Kurn, H.-J. Miesner, D.S. Durfee, C.G. Townsend, S. Inouye, and W. Ketterle, Propagation of Sound in a Bose-Einstein Condensate, Phys. Rev. Lett. **79**, 553 (1997).

[149] B. Damski, Formation of shock waves in a Bose-Einstein condensate, cond-mat/0309421.

[150] A.V. Gurevich and A.L. Krylov, Dissipationless shock waves in media with positive dispersion, Sov. Phys. JETP **65**, 944 (1987).

[151] A.V. Gurevich and L.P. Pitaevskii, Nonstationary structure of a collisionless shock waves, Sov. Phys. JETP **38**, 291 (1974).

[152] M. R. Andrews, D. M. Stamper-Kurn, H.-J. Miesner, D. S. Durfee, C. G. Townsend, S. Inouye, and W. Ketterle, Erratum: Propagation of Sound in a Bose-Einstein Condensate, Phys. Rev. Lett. **80**, 2967 (1998).

[153] E. Zaremba, Sound propagation in a cylindrical Bose-condensed gas, Phys. Rev. A **57**, 518 (1998).

[154] G.M. Kavoulakis and C.J. Pethick, Quasi-one-dimensional character of sound propagation in elongated Bose-Einstein condensed clouds, Phys. Rev. A, **58** 1563 (1998).

[155] D. Jaksch, C. Bruder, J.I. Cirac, C.W. Gardiner and P. Zoller, Cold Bosonic Atoms in Optical Lattices, Phys. Rev. Lett. **81**, 3108 (1998).

[156] F. Dalfovo, S. Giorgini, M. Guilleumas, L. Pitaevskii, and S. Stringari, Collective and single-particle excitations of a trapped Bose gas, Phys. Rev. A **56**, 3840 (1997).

[157] R.M. Bradley and S. Doniach, Quantum fluctuations in chains of Josephson junctions, Phys. Rev. B **30**, 1138 (1984).

Acknowledgements

I would like to thank my advisors Sandro Stringari and Lev Pitaevskii for their guidance and support during my time as a PhD-student. It has been a great opportunity and pleasure to work with them. Grazie mille[3] a Chiara Menotti per essere stata una collega e guida energetica, simpaticissima e paziente durante una grande parte del dottorato e per il suo incoraggiamento e appoggio instancabile durante la preparazione della tesi. Vorrei ringraziare Francesca Zambelli per la sua collaborazione e per avermi aiutato a sistemarmi qua a Trento all'inizio. Grazie ad Augusto Smerzi. È stato un piacere lavorare con lui durante la parte finale del dottorato. Inoltre, vorrei ringraziare Franco Dalfovo per essere sempre stato disposto a discutere, dare consigli e condividere la sua esperienza. Grazie anche ad Andrea Brunello per avermi passato volentieri la sua competenza durante il primo anno. A big thanks to all members of the Trento group for discussions, suggestions and for the friendly company, especially for all the efforts to keep up my spirits during the preparation of the thesis. Ringrazio anche il personale amministrativo del Dipartimento di Fisica e dell'INFM, in particolare Luisa Rossi Doria, Daniela Zecca e Flavia Evandri. Inoltre, grazie a Valerio Varriale per il suo pronto aiuto nelle varie emergenze con il computer. Finally, I would like to thank family and friends for motivating and supporting me again and again in many ways.